Terahertz spectroscopy of molecules and molecular complexes of atmospheric interest exhibiting large amplitude motions

Prakash Gyawali

University of Lille

Doctoral School Sciences de la Matière, du Rayonnement et de l'Environnement **(EDSMRE)**

Laboratoire de Physique des Lasers, Atomes et Molécules **(PhLAM)**

Thesis by **Prakash GYAWALI**

Defended on December 20, 2023

With a view of obtaining the degree of Doctor of the Lille University

Speciality: Physics, Diluted Media and Fundamental Optics

Terahertz spectroscopy of molecules and molecular complexes of atmospheric interest exhibiting large amplitude motions

Committee members

L. Coudert	Research Director, CNRS-Université Paris-Saclay	Reporter
M. Rotger	Professor, Université de Reims Champagne-Ardennes	Reporter
G. Feraud	Associate Professor, Sorbonne Université	Examiner
A. Roucou	Associate Professor, Université du Littoral-Côte-d'Opale	Examiner
C. Toubin	Professor, Université de Lille (President)	Examiner
R. Motiyenko	Associate Professor, Université de Lille	Supervisor

Université de Lille

Ecole Doctorale Sciences de la Matière, du Rayonnement et de l'Environnement **(EDSMRE)**

Laboratoire de Physique des Lasers, Atomes et Molécules **(PhLAM)**

Thèse présentée par **Prakash GYAWALI**

Soutenue le 20 décembre 2023

En vue de l'obtention du grade de docteur de l'Université de Lille

Spécialité: Physique, Milieux dilués et optique fondamentale

Spectroscopie térahertz de molécules et de complexes moléculaires d'intérêt atmosphérique présentant des mouvements de grande amplitude

Composition du jury

L. Coudert	Directeure de recherche, CNRS - Université Paris-Saclay	Rapporteur
M. R. Languereau	Professeure, Université de Reims Champagne-Ardennes	Rapportrice
G. Feraud	Maitresse de conférence, Sorbonne Université	Examinatrice
A. Roucou	Maitre de conférences, Université du Littoral-Côte-d'Opale	Examinateur
C. Toubin	Professeure, Université de Lille (Présidente)	Examinatrice
R. Motiyenko	Maitre de conférence, Université de Lille	Directeur de thèse

Abstract

The atmosphere comprises a diverse array of molecules and species. Among these, water vapor and its complexes have a significant role in the phenomenon of global warming and climate change. Spectroscopic analysis of such complexes is essential for understanding various atmospheric processes. However, there is still a limited knowledge on weakly bounded water complexes in the terahertz wave range due to their complex spectral features and experimental challenges. Spectral complexity often results from the large amplitude motions limited by low potential barriers. We present the development of pulsed-jet emission spectrometer intended for studies of molecular complexes in the terahertz range. Experimental developments were accompanied by benchmarking large amplitude motions models on the molecules of atmospheric interest. We started with acetyl halides exhibiting a periodic torsional motion of methyl group. We obtained accurate models of the rotational spectra of acetyl chloride and acetyl bromide within experimental accuracy. Subsequently, the rotational spectra of methylamine in its first excited torsional state were studied. Methylamine is characterized by two large amplitude motions: torsion and inversion. The rotational spectrum of methylamine was analyzed using the so-called "hybrid" model that for the first time allowed accurate assignment and modeling of the lowest excited torsional states. Finally, the high-resolution rotational spectra of ammonia-water weakly bounded complex were measured using the newly built spectrometer. For the analysis of ammonia-water which exhibits two large amplitude motions similar to methylamine, we also applied the "hybrid" approach demonstrating thus its advantage in the application to excited states and low barrier cases.

Keywords: mm/sub-mm wave spectroscopy, large-amplitude motions, high-resolution, internal rotation, weakly bounded complex, pulse jet, chirped pulse

Résumé

L'atmosphère est composée d'un large éventail de molécules et d'espèces. Parmi celles-ci, la vapeur d'eau et ses complexes jouent un rôle important dans le phénomène du réchauffement de la planète et du changement climatique. L'analyse spectroscopique de ces complexes est essentielle pour comprendre divers processus atmosphériques. Cependant, les connaissances sur les complexes d'eau à faible liaison dans le domaine des ondes térahertz sont encore limitées en raison de leurs caractéristiques spectrales complexes et des défis expérimentaux. La complexité spectrale résulte souvent des mouvements de grande amplitude limités par de faibles barrières de potentiel. Nous présentons le développement d'un spectromètre d'émission à jet pulsé destiné à l'étude des complexes moléculaires dans la gamme des térahertz. Les développements expérimentaux ont été accompagnés d'une analyse comparative des modèles de mouvements de grande amplitude sur les molécules d'intérêt atmosphérique. Nous avons commencé avec des halogénures d'acétyle présentant un mouvement de torsion périodique du groupe méthyle. Nous avons obtenu des modèles précis des spectres de rotation du chlorure d'acétyle et du bromure d'acétyle avec une précision expérimentale. Nous avons ensuite étudié les spectres de rotation de la méthylamine dans son premier état excité de torsion. La méthylamine est caractérisée par deux mouvements de grande amplitude : la torsion et l'inversion. Le spectre rotationnel de la méthylamine a été analysé à l'aide du modèle dit "hybride" qui, pour la première fois, a permis d'attribuer et de modéliser avec précision les états de torsion excités les plus bas. Enfin, les spectres rotationnels à haute résolution du complexe à faible liaison ammoniac-eau ont été mesurés à l'aide du nouveau spectromètre. Pour l'analyse du complexe l'ammoniac-eau qui présente deux mouvements de grande amplitude similaires à ceux de la méthylamine, nous avons également appliqué l'approche "hybride" démontrant ainsi son avantage dans l'application aux états excités et aux cas à faible barrière.

Mots clés: spectroscopie d'ondes mm/sub-mm, mouvements de grande amplitude, haute résolution, rotation interne, complexe à faible liaison, impulsion de jet, impulsion chirpée

Acknowledgement

I would like to express my deep gratitude for the inspiration and collaboration that made the completion of this thesis possible in its present form. I extend my heartfelt thanks to my supervisor, Dr. Roman Motiyenko, whose guidance and unwavering support inspired me to undertake this research. His valuable suggestions and continuous assistance throughout the thesis work have been of immeasurable significance.

I would also like to express my gratitude to Dr. Isabelle Kleiner, Prof. Laurent Margulès, Dr. Luyao Zou, Dr. Eugene Alekseev, Dr. Brian Hays, and Prof. Chuanliang Li for their valuable scientific discussions and assistance with experimental work. Additionally, I extend my thanks to the entire PhLAM laboratory team for their collaboration and support.

My sincere appreciation goes to Dr. Laurent Coudert and Prof. Maud Rotger-Languereau for accepting to review this work, as well as to Prof. Céline Toubin, Dr. Anthony Roucou, and Dr. Géraldine Feraud for their participation in the Ph.D. committee and their evaluation of my research.

My profound indebtedness goes out to my friends, including Ram Ghimire, Anjana Kuinkel, Abdel Aziz, Modibo Camara, and my entire circle of friends, whose encouragement and assistance were invaluable throughout this journey. I am immensely grateful to my family for their enduring patience, love, and enthusiasm in supporting me at every step of this thesis work. They have been with me in every moment of my success.

Finally, I would like to express my gratitude to the Université de Lille and Labex CaPPA for their financial support and for providing me with this opportunity.

Contents

List of Figures

List of Tables

Introduction

The atmosphere is a complex and intricate system filled with a diverse array of gases, aerosols, molecules, and complexes [1, 2]. All of these components have critical roles in regulating global biodiversity and safeguarding our survival [3]. The atmosphere serves as a dynamic medium where a variety of chemical reactions take place. Certain atmospheric molecules and complexes, in particular, play a critical role in gas-phase chemical reactions with significant consequences for global warming and climate change [4]. The elevated levels of these gases result from both natural and anthropogenic processes, including volcanoes, wetlands, and geological processes, as well as human activities such as the combustion of fossil fuels, deforestation, and industrial processes. The emission of atmospheric gases, together with subsequent chemical processes, can lead to a worsening in air quality. Poor air quality, often attributable to the emission of pollutants into the atmosphere, can cause a range of health problems, including respiratory illnesses and cardiovascular issues. Furthermore, clusters and complexes are given special consideration due to their significant contributions to climate change and aerosol formation. Clusters and complexes, which are assemblages of molecules or atoms, play a critical role in atmospheric chemistry [5].

Molecular complexes including dimers and clusters can emerge in the atmosphere due to a variety of physical and chemical mechanisms. These phenomena can be affected by a number of variables, such as humidity, temperature, pressure, and the presence of different chemical compounds. The most common process for complex formation involves van der Waals forces, which are weak attractions between molecules or atoms caused by transient variations in electron distribution, giving rise to unstable dipoles. This force arranges molecules or atoms in close proximity, resulting in complex formation. Furthermore, hydrogen bonds also generate complexes in which a hydrogen atom bound to a strongly electronegative atom, such as oxygen or nitrogen, is attracted to another electronegative atom in a nearby molecule. Molecular complexes play a pivotal role in atmospheric chemistry by bridging the gap between individual gaseous molecules and the formation of nanoparticles. They act as intermediaries in the transition from the gaseous phase to the condensed phase, facilitating the formation of larger structures. One significant outcome of this process is the

production of aerosols that have complex and diverse effects on the Earth's climate, with both cooling and warming influences depending on their specific characteristics and interactions with the atmosphere [6, 7].

There are numerous approaches for characterizing molecules and determining reaction patterns. Spectroscopy is a commonly applied technique across many scientific disciplines. In spectroscopy, the interaction of light and matter at various wavelengths reveals both the physical and chemical properties of molecules. The spectroscopic study of atmospheric complexes holds a pivotal role in advancing our comprehension of various atmospheric processes. It empowers scientists to explore the behavior and properties of molecules and complexes present in the atmosphere and space. Such studies aid in the identification and quantification of the diverse gases in the atmosphere, enabling the detection and monitoring of atmospheric pollutants.

Rotational spectroscopy is one of the most powerful tools for studying molecular properties and structure of molecules. Rotational spectroscopy, in particular, is a branch of spectroscopy that focuses on the rotational motion of molecules. Molecules can rotate about their center of mass, and this rotational motion is quantized, which means it can only occur at specific energy levels. The energy levels are determined by the moment of inertia and the shape of the molecules. It is particularly useful for identifying molecules with permanent electric dipole moments, such as H_2O, CH_3COCl, CH_3NH_2, etc. Rotational spectroscopy is employed in laboratories to study molecular interactions [8], reaction kinetics [9], and the behaviour of molecules [10, 11] under varying conditions. Renowned for the unique rotational spectrum of each molecule, rotational spectroscopy permits the observation of various higher-order spectroscopic phenomena within the spectrum. Through the analysis of the rotational spectrum, one can determine rotational constants, centrifugal distortion coefficients, nuclear quadrupole coefficients, and so on, which hold valuable structural information about the molecule and provide a precise method for determining molecular geometries. Analysing the rotational spectrum in the ground and excited vibrational states also reveals information about energy differences between interacting vibrational states. In addition, large-amplitude motions (LAMs) also play a crucial role in rotational spectroscopy. LAM refers to the internal vibrations and rotations of particular

atoms within a molecule with respect to their overall rotation. These internal motions are also quantized and can affect the energy levels, spectral patterns, and overall structure of the molecules. Therefore, addressing LAMs is crucial for refining theoretical models and achieving accurate predictions. However, tackling LAMs poses considerable challenges as it complicates theoretical models, necessitates extensive computational resources, and adds complexity to the assignment and analysis processes. In this thesis, we specifically focus on addressing LAMs for all molecules to obtain precise information about them. The precise molecular properties obtained from rotational spectroscopy serve as valuable benchmarks for the development and validation of quantum chemistry methods.

The primary objectives of this dissertation are to thoroughly analyse the rotational spectra of molecules that exhibit large amplitude motions. The research aims to determine their important physical properties from derived observables and to provide accurate experimental data needed for atmospheric and astrophysical observations. The work conducted throughout this thesis and presented herein is composed mainly of two parts. The first is to contribute to the design and development of a new chirped-pulse supersonic-jet spectrometer. The second part includes the laboratory spectroscopy of non-rigid molecules and molecular complexes in the terahertz domain.

The first chapter is a detailed description of a new chirped-pulse supersonic-jet spectrometer that operates in the mm/sub-mm wave range. It also covers the technical specifications of each component used to develop the chirped-pulse spectrometer.

In Chapter 2, we provide a theoretical foundation for rotational spectroscopy, including all of the methods and computer programs required to assign and analyse the rotational spectrum of molecules exhibiting a periodic large maplitude motion.

Chapter 3 is devoted to a careful investigation of molecules with internal rotation (torsion) of the methyl group. A comparison of the experimental data for acetyl chloride and acetyl bromide is presented. This chapter also includes a comparison analysis of the principal isotopologues of each molecule.

The fourth chapter addresses the molecules that exhibit two large-amplitude motions: torsion and inversion. It also includes the measurement and interpretation of high-

resolution spectra of weakly bounded ammonia-water complexes. In the final chapter, I provided a condensed overview of the entire thesis.

I present the most efficient theoretical models in terms of analysis accuracy for each type of LAM. I used these models to analyse the spectral properties of different molecules, and I am able to fit the spectrum with experimental precision.

Part I

Instrumentation for the jet-nozzle mm/sub-mm wave emission spectrometer

Chapter 1

Development of a chirped-pulse supersonic jet spectrometer at mm/sub-mm wavelength

1.1 Chirped-pulse technique

A chirped signal is a waveform whose frequency changes over time. The frequency of a chirped pulse follows a linear sweep pattern throughout its duration. This linear variation in frequency allows the signal to span a broad range of frequencies within a single pulse. Mathematically, the instantaneous frequency of a chirped pulse $f(t)$ can be expressed as follows:

$$f(t) = f_{start} + \alpha t \tag{1.1}$$

where f_{start} is the starting frequency of the chirped pulse, and α is the linear sweep rate, which determines how quickly the frequency varies over time. When the linear sweep rate (α) is positive, the frequency of the chirped signal increases over time, which is also known as an up-chirp. In contrast, a negative linear sweep rate shows that the frequency of the chirped signal decreases over time, often known as a down-chirp. In the case of a chirp pulse, the sweep range of frequencies covered by the pulse is directly proportional to the pulse duration. This means that a longer chirp pulse covers a wider range of frequencies. The relationship between chirped pulse bandwidth Δf_C and duration Δt_{pulse} can be written as $\Delta f_C = \alpha \times \Delta t_{pulse}$. In contrast, the bandwidth of a transform-limited pulse Δf_T is inversely proportional to the pulse duration as $\Delta f_T = \dfrac{1}{\Delta t_{pulse}}$

In microwave spectroscopy, a typical emission experiment is composed of two phases:

- an excitation phase when the molecular gas sample is brought into interaction with a microwave pulse
- a detection phase when molecular free induction decay (FID) of macroscopic gas polarization is recorded

Once a molecular gas sample interacts with a microwave pulse, the gas molecules absorb the microwave radiation, excite to higher rotational energy levels, and then return to lower energy levels by emitting a signal. The relaxation process emits a signal known as FID, which can be detected and holds information about the molecules. The detected polarization signal $P(t)$ decays at a rate proportional to the sum of the population lifetime (T_1) and coherence lifetime and (T_2) whose typical values are on the order of microseconds.

Therefore, the excitation must occur on a timescale that is shorter compared to these time constants. It has been shown that for the chirped pulse excitation in the weak field case, the FID signal is proportional to the reciprocal square root of the bandwidth: $P(t) \propto \Delta f_C^{-1/2}$, whereas the signal from transform-limited pulse scales as the reciprocal of the bandwidth to the first power $P(t) \propto \Delta f_T^{-1}$ [12, 13]. As pointed out by Brown et al., [14] this means that the chirped-pulse signal scales favorably as bandwidth is increased. When needed, it is possible to achieve more polarization from a given transition by decreasing the bandwidth of the chirped or transform-limited pulses. However, for broadband measurements, the chirped pulse excitation has a clear advantage. Increasing the efficiency of spectral acquisition by decreasing the bandwidth of the chirped pulse excitation does not improve the measurement process, because the increase in signal is only proportional to $\Delta f_C^{-1/2}$. Breaking up a spectrum into more than one frequency region therefore does not decrease the averaging time needed to obtain a specified signal-to-noise level over a given frequency region, since the noise reduction also scales as the square root of the number of averages, and there is a cancellation between the signal increase and the required number of averages [13].

Brooks Pate and his team successfully implemented a chirped pulse technique in high-resolution microwave spectroscopy [15]. They achieved an impressive bandwidth of 11 GHz within a very short pulse duration of 1 µs using an Arbitrary Waveform Generator (AWG) for chirped pulse generation. In conventional cavity-enhanced microwave spectroscopy, the instantaneous bandwidth is limited by the cavity mode and typically does not exceed 1 MHz [16]. Therefore it also requires a point-by-point scan to cover a broad frequency range. The chirped pulse technique revolutionized microwave spectroscopy by simultaneous broadband excitation of molecules using a single microwave pulse that allows for the recording of multiple rotational transitions within a few microseconds.

In the first experiments, to generate chirped pulses, an AWG was used. It is still a dominant way of chirped pulse generation in modern microwave spectroscopy. AWG allows for the generation of a wide range of complex waveforms, including custom shapes, frequencies, and amplitudes. This versatility allows for precise control and customization of output signals. At the same time, broadband AWGs especially in microwaves can be significantly

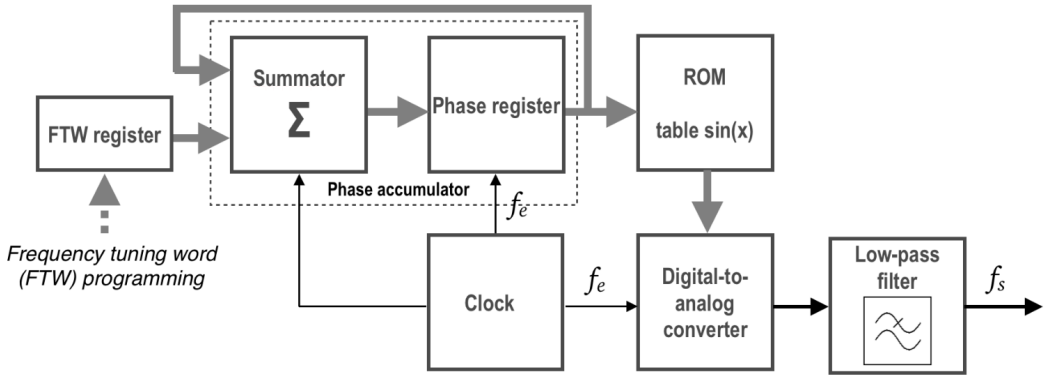

Figure 1.1: The schematic diagram of the direct digital synthesizer

expensive compared to other signal generators. The advanced technology and capabilities they possess contribute to their higher price tag.

About 10 years ago, it has been shown that the application of a direct digital synthesizer (DDS) is a valid alternative to the AWG [17] in the chirped pulse generation. DDS is capable of extremely fast frequency switching without any overshoot thus producing linear frequency sweeps with high frequency accuracy. The chirped signal generated by the DDS is similar to that generated by an AWG, but the DDS costs significantly less than an AWG and also consumes much less power[17]. In addition, the application of the DDS gives an indisputable advantage: due to frequency switching with the continuous phase, it allows us to build an intrinsically coherent receiving system and thus to provide extremely long-term averaging of time-domain records.

1.2 Direct Digital Synthesizer (DDS)

Direct digital synthesis is a technique to generate an analog waveform of a fixed or variable frequency using digital techniques [18]. It is widely used in many applications, such as signal generation, frequency synthesis, and various scientific and industrial applications. The simplified diagram of the direct digital synthesizer is shown in Figure 1.1. The major components of DDS and their operating principles are as follows:

Frequency Tuning Word (FTW) Register: The FTW is a digital register that sets the de-

sired output frequency of the DDS system. It is essentially a binary number that determines how fast the phase accumulator increments, which in turn controls the output frequency. The output frequency of the DDS system can be changed by altering the value in the FTW register.

Phase Accumulator: The core of a DDS system is a phase accumulator, which is actually a digital counter. This counter accumulates phase values over time. The phase value is represented digitally and is proportional to the desired output frequency. The phase value from the accumulator is then sent through a lookup table, also known as a sine lookup table, and stored in ROM.

Read-Only Memory (ROM): The ROM stores the values of the sine function for different phase angles, typically ranging from 0 to 2π. The phase value from the phase accumulator serves as an address to retrieve the corresponding sine value from the ROM. The ROM values represent discrete samples of the sine waveform consisting of N representing a range of values from $[0, 2^N]$.

Clock: The clock is the driving source for the DDS system. It determines the rate at which the phase accumulator increments, which in turn affects the output frequency of the waveform. The clock frequency f_c, along with the value in the FTW register, determines the output frequency of the DDS system f_{out} which may be expressed as

$$f_{out} = \frac{FTW \times f_c}{2^N} \tag{1.2}$$

where N is the length of the phase accumulator, in bits.

Digital-to-Analog Conversion (DAC): A DAC converts the amplitude values from the lookup table into an analog signal. This method converts discrete digital values into a continuous analog waveform.

Low-Pass Filtering: The DAC output is often a stair-stepped waveform with high-frequency components due to its digital nature. This output is processed through a low-pass filter to remove the high-frequency components and generate a continuous waveform in order to obtain a smooth analog signal.

An example of a digital sequence generated by a DDS and the result of the digital- to-

analog conversion with the successive filtration is presented in Figure 1.2.

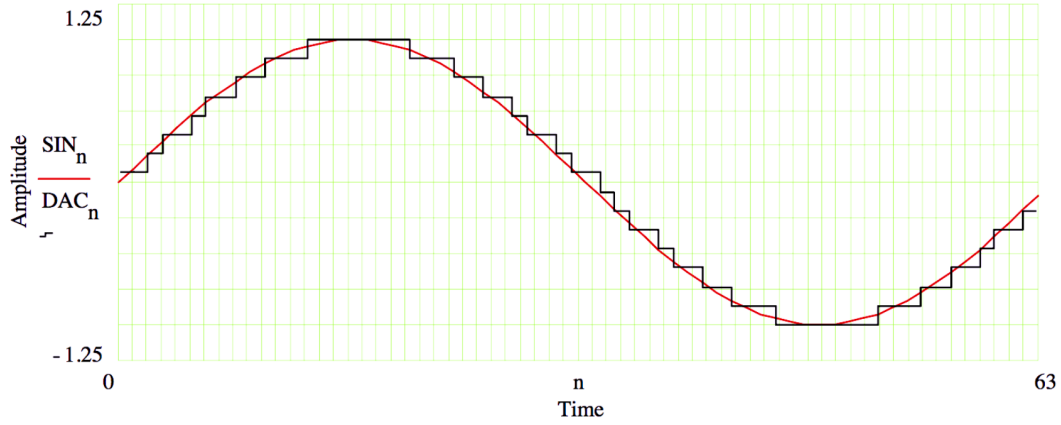

Figure 1.2: The digital time sequence representing the function sin(x) (in black) and the analog signal after the filtration (in red). The figure is taken from the technical tutorial on digital synthesis [19]

A DDS-based source can be used as an electromagnetic radiation source in high-resolution spectroscopic applications. When it comes to this application, DDS-based sources have various advantages:

- **Precision and Accuracy:** DDS sources provide precise and highly accurate frequency and phase control signals. It can generate stable signals that remain consistent throughout time; such stable signals are important in spectroscopic applications for spectrum purity and reliability.
- **Low Phase Noise:** DDS sources typically generates low phase noise signal, making them suitable for applications in high-resolution spectroscopy. Such signal allows the long-term average of the output signal to get a good signal-to-noise ratio.

  High-Frequency Resolution: DDS sources can generate signals with high-frequency resolution, making them suitable for high-resolution spectroscopic measurement.
- **Fast Frequency Switching Ability:** DDS sources can change frequencies almost instantaneously compared to traditional analog signal generators, which may require mechanical tuning or switching of components. The shorter switching time significantly reduces the spectral recording time.
- **Digital Control and Programmability:** DDS sources are digitally controlled and

programmable, which makes them highly versatile. It can easily implement complex modulation schemes, frequency sweeps, or other waveform manipulations, making them suitable for a wide range of spectroscopy experiments. The availability of two connecting interfaces (SPI, I^2C) allows for extremely quick data transmission.

- **Low Power Consumption and Cost-Effective:** Compared to other sources such as AWG, DDS consumes less power (≈ 3 W) and is less expensive. Which may be an attractive option for researchers and laboratories.

Besides these, there are some limitations and drawbacks of DDS in the context of high-resolution spectroscopy applications, particularly rotational spectroscopy in the terahertz frequency range:

- **Frequency Range Limitation:** The maximum output frequency of DDS commercial microcircuits, does not exceed 1.5 GHz, which is not sufficient for directly generating signals in microwaves or terahertz frequency range. To work in the terahertz frequency range, frequency multiplication is necessary. This introduces potential challenges, such as increased phase noise and reduced signal quality, when compared to directly generating signals within the target frequency range.
- **Spurious Signals:** DDS-based sources can produce spurious signals due to their internal architecture and digital signal processing techniques. These spurious signals can interfere with the desired signal and introduce noise into the spectroscopic measurements.

To overcome the inherent frequency limitations of DDS-based sources and extend their usability into higher frequency ranges, frequency multipliers can be used to achieve the appropriate output frequencies. At the same time, advanced signal processing techniques like spectral cleaning and phase noise reduction algorithms can be used to improve the purity of the spectrum. It also reduces the impact of spurious signals and phase noise. These methods make it possible to use DDS-based sources in the terahertz range while keeping the quality of the signal and the accuracy of spectroscopic measurements.

1.3 Fast Lille Adaptable Spectrometer of the Terahertz Range (FLASH)

The FLASH spectrometer employs two main methods for detecting and analyzing molecular interactions in the millimeter/submillimeter-wave and up to the terahertz range: absorption spectroscopy and emission spectroscopy.

Absorption spectroscopy measures the amount of radiation absorbed or attenuated by molecules at specific frequencies [20]. This method excels in accurately determining spectral line frequencies. It is also characterized by intrinsically higher spectral resolution compared to emission spectroscopy. However, absorption spectrometers have somewhat lower sensitivity due to inherent limitations relating to the source of radiation noise and baseline changes, which are fundamental constraints that absorption spectrometers cannot overcome [21].

On the other hand, emission spectroscopy provides an alternative approach. In emission spectroscopy, the inherent noise caused by the radiation source has less of an impact on the spectral measurement. Furthermore, instrumental and other factors that induce baseline changes have little effect on emission spectroscopy. In addition, emission spectroscopy requires the detection of molecular radiation in a coherent manner. This means that the radiation released by the molecules is properly measured and analyzed. Coherent detection enhances signal-to-noise ratios, allowing researchers to more precisely analyze molecular characteristics. In emission spectroscopy, it is possible to record multiple frequencies at once, which significantly speeds up the data gathering and interpretation processes. It also simplifies the experimental challenges of studying radicals and complexes [22]. One of the main drawbacks of emission spectroscopy is reduced spectral resolution. In emission spectroscopy one usually uses the magnitude Fourier transform of the FID directly, which combines the real (absorption) and imaginary (dispersion) parts of the Fourier transform. Although the line position is not altered by using magnitude Fourier transform, this practice intrinsically increases the linewidth of the Fourier transform spectra because of the extra contribution from the dispersion, creates wide wings on the line profile that deviate from a Voigt profile, and is sensitive to the initial phase because the dispersion causes line

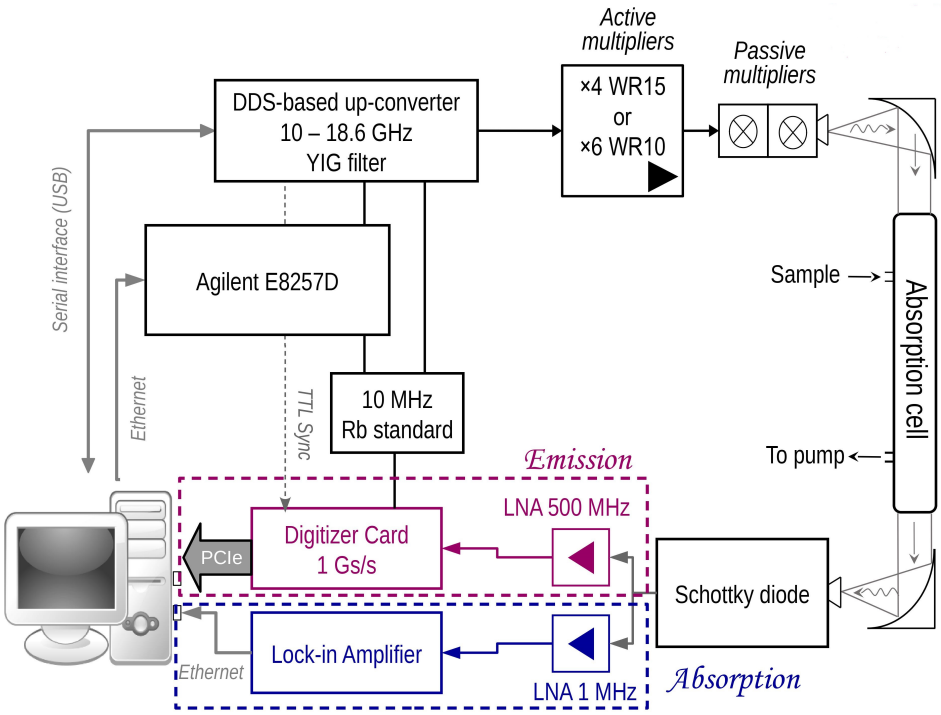

Figure 1.3: Schematic of the FLASH spectrometer.

asymmetry [21].

The schematic of the Lille hybrid spectrometer is shown in Figure 1.3. The main feature of the spectrometer is that it uses the same source radiation based on the up-converted and multiplied DDS AD9915 for absorption and emission experiments. Different multipliers permit to cover a broad frequency range: from 50 to 1520 GHz in absorption, and to 500 GHz in emission. Using only different detection channels it is thus possible to perform rapid switching between the two experiments taking advantage of both. The absorption part of the spectrometer has been described elsewhere [23, 24]. We will describe here the emission part in view of presenting the results of the upgrade carried out in the frame of this thesis.

1.3.1 DDS-bases up-converter

The up-conversion of the DDS output to the 10 – 18.5 GHz range is provided by the radio frequency (RF) mixing of the signal of DDS synthesizer f_s and of Agilent E8257D synthesizer f_{RF} with filtration and successive amplification. The diagram of the new fast-scanning microwave source is shown in Fig. 1.4.

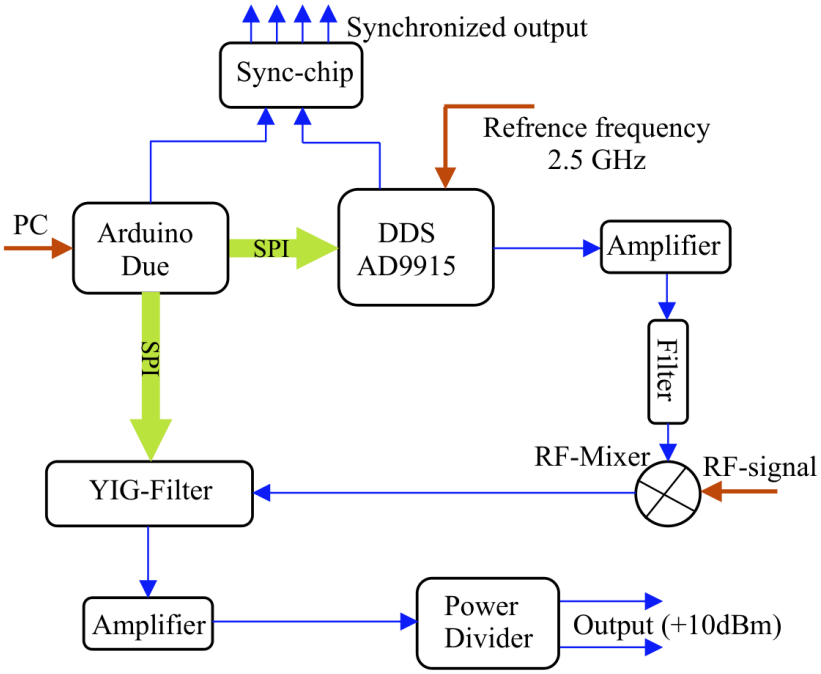

Figure 1.4: Schematic diagram of DDS-based radio frequency up-converter

The RF mixing produces the main signals: $f_{RF} \pm nf_s$ where $n = 0, 1, 2$ etc. Up-conversion is the process of isolating one of the two sideband signals $f_{RF} - f_s$ or $f_{RF} + f_s$. For this reason f_{RF} and one of the two signals of the conversion must be sufficiently spaced on the frequency scale for the filtration to be effective. This is the main reason to use AD9915 which output frequency may reach 1 GHz. The reference signal for the AD9915 synthesizer is provided by the 10 MHz Rb clock. The 10 MHz signal is multiplied internally in the microcircuit by the factor 250 to produce the clock of the DDS system at the frequency $f_e = 2.5$ GHz. To avoid the presence of spurious components in the spectrum of the DDS synthesizer, in the first step, its range of effective tunability is restricted within 320–420 MHz interval. The DDS microcircuit output signal is filtered by the fixed bandwidth bandpass filter and amplified thereafter. The radiofrequency mixing result of f_s and f_{RF} is filtered by the YIG bandpass filter (yttrium iron garnet, the magnetic resonance-based filter) tunable over the range of frequencies 8–20 GHz. The YIG filter on the one hand isolates the useful RF component and on the other hand represents a second step in the fight against spurious components in the spectrum of the DDS synthesizer. The bandwidth of the filter (rejection at 3dB) is about 20 MHz.

After the YIG filter, the signal is amplified by a very low noise RF amplifier to reach the 10 dBm power level needed to drive the active multiplier (x6) to the next level. The choice of this type of amplifier is dictated by the need to multiply the signal frequency of the system producing the up-conversion. With frequency multiplication by a factor of N, the phase noise typically increases by the factor $20 \log N$. Therefore, it is essential to have at the first stage of the multiplication chain a synthesizer with minimum possible phase noise. This was the main reason for choosing the Agilent E8257D synthesizer as the first level of the multiplication chain. The output of the amplifier is sent to the power divider which separates the signal path into two equivalent parts each having a power of 10 dBm approximately. One of the two channels may be used to control the signal produced by the up-conversion system. Slight variations in the power output of the RF synthesizer of the order of a few percent are possible because of the standing wave in the system. To reduce the effect of the standing wave we placed a 3 dB attenuator between the mixer and the YIG filter. Since the second stage of the frequency multiplication chain operates in saturation mode, the power variations at the output of the RF synthesizer do not influence the output power of the second stage.

The result of the mixture RF $f_{RF} + f_s$ is subsequently multiplied by different multiplication factors, N: 4, 6, 12, 18, 30, 36, 54 and 108. This allows to cover more than 80% of the 50–1520 GHz range.

The control of DDS and YIG filter bandwidth is performed by Arduino Due microcontroller. It also serves as an intermediate between the control PC and the up-converter. For sensitive measurements in emission spectroscopy, one had to acquire multiple records with subsequent data averaging. Therefore, the questions of the DDS phase stability and the data acquisition trigger jitter are of primary importance. The AD9915 DDS has an internal clock, which operates at 1/16 of the DDS clock frequency. In the initial setup, the reference frequency of 2500 MHz was obtained using the DDS internal phase-locked-loop multiplier of the 10 MHz Rb standard signal. The internal clock of the DDS (with 2500/16 = 156.25 MHz frequency or 6.4 ns period) is used to synchronize its many internal processes including frequency profile switching, pin state update, and frequency update during digital ramp generation. Each process is initiated on the rising edge of the internal clock. To synchro-

nize the DDS-based radiation source with the DAQ system, a special unit was designed and built. The unit takes on the input of the DDS internal clock and external trigger signals generated by Arduino and provides synchronized trigger signals for the DDS pins and for the ADC card.

1.3.2 Signal generation and detection scheme

In terahertz emission spectroscopy, detected FID signals are downconverted to microwaves since high-speed digitizers are either extremely expensive or not commercially available due to current technical limitations. For downconversion, usually, a heterodyne technique is used that consists of mixing FID signal and local oscillator (LO) signal at frequency close to FID to produce low-frequency difference pattern. The Lille hybrid spectrometer uses the same source for molecular excitation and as a LO for heterodyne downconversion. This is possible owing to the fact that as pointed out in Section 1.1, the two stages of the emission experiment are separated in time whereas DDS allows extremely rapid frequency switching down to a few nanoseconds.

The AD9915 DDS has five operational modes, two of which are used to generate pulse signals in the spectrometer: “profile mode” and “digital ramp mode”.

In profile mode, the frequency is synthesized using equation (1.2) for which the FTW value is stored in the so-called “profile register”. The AD9915 has eight profile registers that can be programmed in parallel. The DDS output frequency is then chosen by setting a bit sequence on three “profile selection” (PS) pins of the chip. Since $2^3 = 8$, by changing the state of three pins one can change the synthesized frequency value. To generate a single-frequency (transform-limited) pulse, two profiles are used, one set on the pumping frequency and the other on the LO frequency. The profile registers used are P0 with the simplest bit sequence 000, and P2 corresponding to 010 sequence. An external signal produced by Arduino microcontroller sets or clears one bit thus switching between two profiles. The DDS idle frequency corresponds to LO and is programmed in P0 register. During the excitation phase, the DDS is set to the pumping frequency for about 1 µs and then is set back to the LO frequency. The pin state change had to be synchronized with

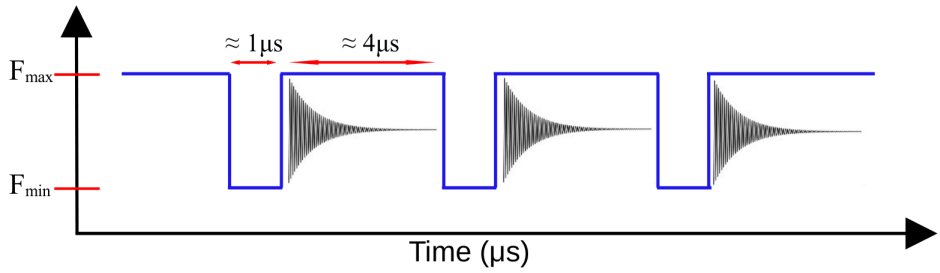

Figure 1.5: Time-domain siquence for generation of transform-limited pulse.

the rising edge of the internal clock of DDS. An example of the transform-limited pulse is shown in Figure 1.5.

In digital ramp mode, the digital ramp generator (DRG) of DDS controls all of the parameters associated with the frequency sweep. The characteristics of DRG are fully programmable, which allows for controlling the upper and lower frequency limits, step size, and step rate during the sweep. First, the frequency limits of the digital ramp are set in `DRUP` and `DRLO` registers. During frequency sweep, the frequency is progressively varied between the values set in the registers. The linear sweep rate α is then controlled by setting the number of frequency steps n_{steps} between `DRUP` and `DRLO`, and the idle time Δt between two consecutive steps.

The DRG AD9915 operates on the internal clock which rate is 1/16 of the clock frequency, as it was mentioned previously. Using 2.5 GHz clock, the minimum switching time Δt is defined as

$$\Delta t = \frac{16}{f_c} = 6.4\,\text{ns} \tag{1.3}$$

The number of steps (n_{steps}) taken within the pulse duration (t_{pulse}) may be then expressed as:

$$n_{steps} = \frac{t_{pulse}}{\Delta t} \tag{1.4}$$

Thus for a given chirped pulse width, between f_{min} and f_{max}, the control program of the spectrometer calculates the number of frequency steps, and then, the frequency step value as

$$\delta f = \frac{f_{max} - f_{min}}{n_{steps}} \tag{1.5}$$

and set into a specific register of DDS.

A specific pin, DRCTL, controls the direction of the ramp, whether it is increasing or decreasing in frequency. When DRCTL is set to logic 0, the DRG performs a frequency sweep with a negative slope, which means that the frequency decreases during the sweep. When DRCTL is set to logic 1, the DRG performs a frequency sweep with a positive slope, leading the frequency to increase during the sweep. Furthermore, the DRG includes a useful hold feature through DRHOLD pin, which allows a pause of the sweep at a given frequency for a defined length before continuing the next step of the sweep.

Using the DRG, chirped pulses can be generated in two ways: single-direction mode and dual-direction mode. The choice between single-direction and dual-direction mode depends upon the desired output and the experimental conditions.

The single-direction mode allowed either positive or negative slopes on the ramp. The frequency was initially set to the upper (lower) limit of the linear sweep range. When the chirped pulse began, the frequency immediately switched to the lower (upper) limit of the linear sweep range and remained there for a few microseconds ($\approx 1\,\mu s$). This holding time reduced the broadband stimulation caused by fast frequency changes. After this time, the DRG began the linear sweep, steadily raising the output frequency until it reached its maximum and repeating the same process.

The dual-direction mode allowed for both positive and negative slopes in the ramp. The frequency ramp initiated smoothly without a sudden jump, as seen in single-direction mode of Figure 1.6. The idle frequency corresponded to the final frequency of the previous sweep, serving as the upper limit for negative slope chirped signals and the lower frequency for positive slope chirped signals. The DRG initiates the frequency ramp smoothly without sudden jumps, regardless of whether there is a positive or negative slope. Since there were no significant frequency jumps, the dual-direction mode removes undesired broadband excitation. An example of single direction and dual direction chirped pulse is shown in Figure 1.6.

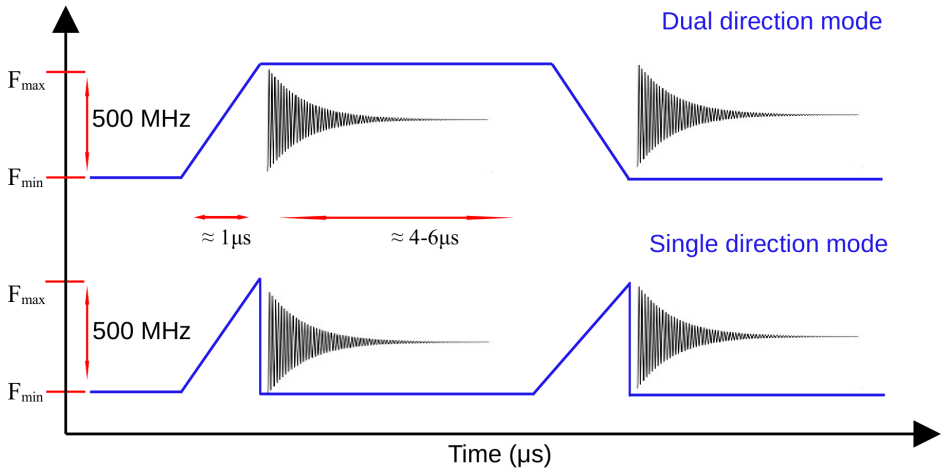

Figure 1.6: Time-domain sequence for generation of chirped-pulse in single and dual direction mode.

1.3.3 Limitations

The original design of the DDS-based up-converter was specifically adapted for absorption spectroscopy. It thus has some limitations when applied to emission experiment.

The main limitation is the bandwidth of the YIG-filter. In a lower part of millimeter-waves (50–150 GHz), after multiplication, the maximum chirped pulse bandwidth was only 80 MHz with $N = 4$ and 120 MHz with $N = 6$. In addition, the detection scheme imposes to cut the low frequency part of the heterodyne detected signal, that contains relatively strong features from relaxation processes of low-quality-factor resonances in the vacuum chamber and in receiving system. For these relaxation signals, typical cut-off frequency is set to 20 MHz. Thus, for all measurements, the effective exploitable bandwidth of recorded molecular spectrum is reduced by 20 MHz when using single direction mode chirped pulse generation, and by 40 MHz in dual-direction mode. At the same time, available output source power in lower part of millimeter-waves is high enough to provide sensitive measurements using significantly broader chirped pulses.

In the original design, the synchronizing unit was designed to have only one single synchronized output for data acquisition trigger. Coupling the spectrometer to pulsed supersonic jet system required another synchronized trigger. Overall, other potential applications of the spectrometer required more synchronized trigger outputs.

These limitations directly impacted the performance of the emission spectrometer. To address these limitations, it was important to upgrade the DDS-based up-converter in order to better suit the requirements for emission spectroscopy [17, 25]. This included the implementation of new YIG filter with larger bandwidth, enhancing synchronisation capabilities, and optimising the entire system for emission spectroscopy. The newly developed emission spectrometer is further coupled with a jet nozzle for carrying out spectroscopic studies of weakly bounded complexes.

A comprehensive description of the new up-converter is described in Section 1.4. The development and enhancements made to the DDS-based source are discussed in depth.

1.4 New DDS-based up converter for emission spectroscopy

The design of the new DDS-based up converter follows the guidelines of its previous version which schematic diagram is essentially the same as the one shown in Figure 1.4. The main modification is the implementation of new YIG-filter with larger badnwidth, and new synchronizing system with 4 fully synchronized outputs. Compared to the scheme of Figure 1.4, the new design includes 4 `ADAQ` outputs on Arduino card labeled in the new version `ADAQ1` to `ADAQ4` the produce 4 synchronized outputs `DAQ1` to `DAQ4`. Below we describe the key components of the new up-convereter and their characteristics.

DDS chip: we used the same DDS AD9915 from *Analog Devices* as in previous version. Along with AD9914, these are the two highest output frequency commercially available synthesizers. The DDS chip is controlled by Arduino Due microcontroller via SPI interface. The details of the SPI pin connections between Arduino and AD9915 are depicted in Figure 1.7. In addition to standard SPI pins (`CS`, `SCK`, `MISO`, and `MOSI`) for correct communication between the microcontroller and DDS evaluation board, one has to control the state of the following pins: IOUPDATE, RESET and SYNC-IO. For example, after a write cycle, the programmed data resides in the serial port buffer of DDS chip and is inactive. To transfer data from the serial port buffer to active registers, IOUPDATE pin should be triggered. It should be noted that Arduino SPI is also used to control the bandwidth of the YIG filter pro-

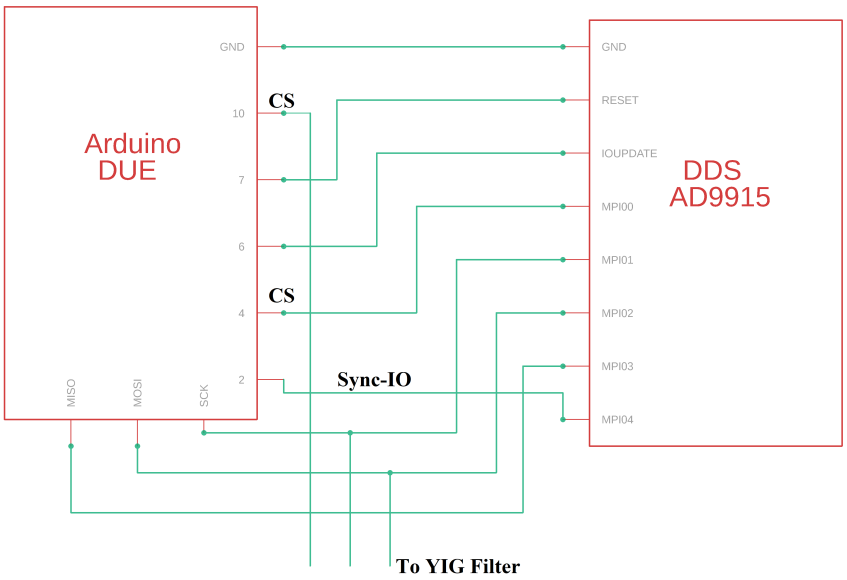

Figure 1.7: Detailed diagram of SPI communication connections between Arduino Due and AD9915 DDS evaluation board

viding thus a suitable way to completely control the output frequency of the up-converter. The advantage of using Arduino Due in this case is that this microcontroller has two independent SPI interfaces that can operate at different clock frequencies. We can therefore use the same microcontroller to set higher clock frequency and consequently data transfer rate communication with DDS and lower clock for YIG filter (as required by manufacturer).

ALN03G04G LNA: The output of AD9915 is amplified by low-noise amplifier from *Atlantic RF Lab.* The amplifier was specifically designed to operate within a frequency range of 300–400 MHz and provides a gain of 12 dB.

BPM20682 Low pass filter: To further restrict the bandwidth of the DDS output, the band pass filter from *Microtronics* is employed at the next stage. Its passband frequency range is 300–400 MHz incurring only a minimal 1.5 dB loss. When integrated into RF systems, this filter acts as a valuable tool for enhancing signal purity by acting as an additional layer of filtration. It ensures that only the desired signals within the specified frequency range are effectively transmitted.

M1-1020 double balanced mixer: At the next stage, the DDS output is mixed with RF signal in a double balanced mixer from *Marki Microwave.* It is a three-port device designed

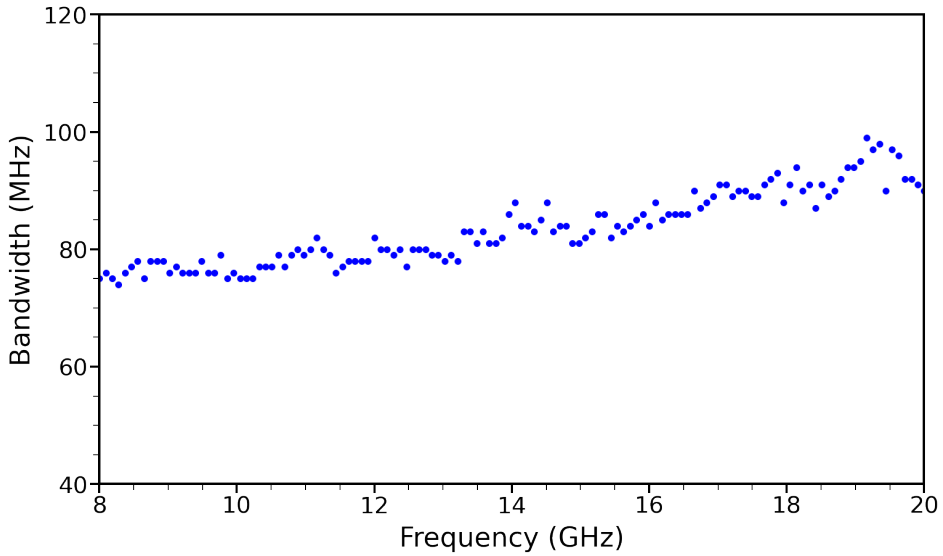

Figure 1.8: Examining the effective bandwidth of MLFP 1727 YIG filter at various frequencies in the 8–20 GHz range.

for up-converting DDS signals while maintaining a constant phase and amplitude. This mixer experiences a 6 dB conversion loss, which represents the reduction in signal power during the mixing process.

MLFP1727 YIG-filter & TWLNA10G20GA amplifier: The YIG bandpass filter from *Micro-Lambda* is characterized by high Q-factor, and consequently low energy loss. In general, YIG filters serve as magnetically tunable resonators for microwave frequencies, allowing the passage of resonance frequencies only. The MLFP1727 filter may be tuned within the frequency range of 8–20 GHz. The tuning consists in setting a desired value of DC current in a coil that produces magnetic field. The MLFP1727 filter was provided with a driver unit which is essentially a digitally controlled current source. As it was mentioned before, the YIG filter is controlled by SPI interface that allows digital setting of the current and consequently of the magnetic field. The control is performed in a simple way by sending a control word coded in 16 bits. Thus, the minimum value of the current and the center frequency (8 GHz) corresponds to the code 0 and the maximum value of the current and the frequency (20 GHz) corresponds to the code $2^{16} - 1 = 65535$. Numerical control allows very fine and continuous adjustment of the central frequency because the minimum step $\Delta f = \frac{20000-8000}{65535} = 0.1831$ MHz.

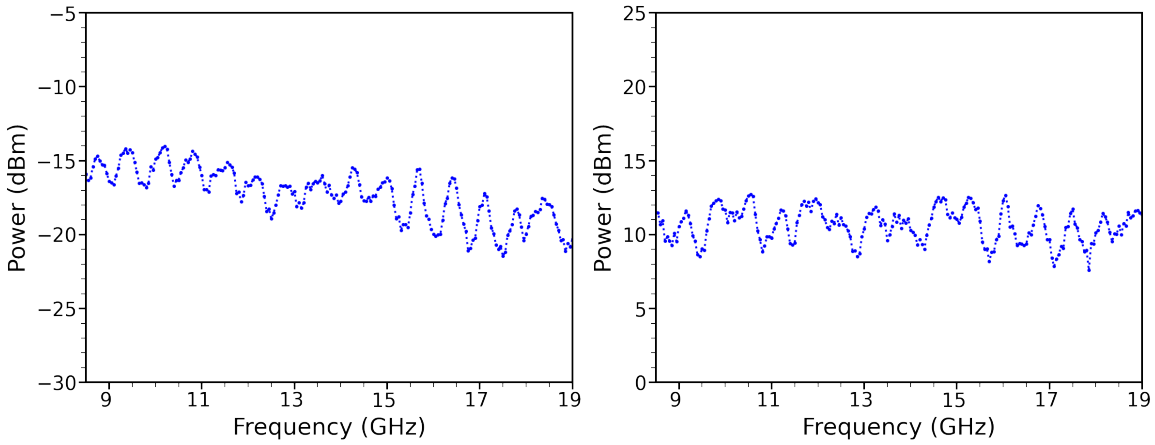

(a) (b)

Figure 1.9: Output power of DDS based source versus frequency (a) before amplification with LO input power of 0 dBm (b) after amplification and LO power correction

Before implementation in the up-converter, the bandwidth of YIG-filter was examined throughout the full frequency range of its operation. For this purpose, the input of the filter was connected to an RF synthesizer, and the output to a spectrum analyzer. Then, the digital code of the central frequency was set and the RF frequency was varied to observe 3 dB attenuation with respect to mean power value within the bandwidth. The difference between minimum and maximum frequencies at which 3 dB is produced corresponds thus to the filter bandwidth. The digital code was subsequently varied to measure the bandwidth as a function of central frequency. The results of the tests are shown in Figure 1.8. The minimum bandwidth is about 75 MHz at lower frequency limit and reaches up to 100 MHz at upper limit. It is 4 to 5 times larger compared to the bandwidth of the previous version of up-converter. Thus, the minimum bandwidth of the chirped pulse was increased from 80 MHz to 320 MHz.

Figure 1.9a illustrates the output power of the up-converted DDS signal at the output of the YIG filter. One can see periodical power variations due to standing waves in the system, and a decrease of the output power towards upper frequency limit due to increasing power attenuation at higher frequencies. To reduce the effect of standing waves, a 3 dB attenuator was installed between the mixer and the YIG filter. To account for power attenuation at higher frequencies, the input power of RF synthesizer was set to vary.

According to technical specifications, the first stage of frequency multiplication chain

requires 10 dBm input power. Taking power levels shown in Figure 1.9a into account, we had to install an amplifier at the output of the YIG filter. The gain factor of the amplifier (35 dB, TWLNA10G20GA from *Techniwave*) was chosen to obtain power level of about 20 dBm at its output since after the amplifier, a power divider is installed to provide two equivalent 10 dBm signals. The output signal of one of the two 10 dBm outputs is shown in Figure 1.9b. Compared to Figure 1.9a, one may notice slightly smoother mean output power value due to partial suppression of standing waves and to the power variation of the RF synthesizer to compensate attenuation losses. The empirically found equation that sets the output power of RF synthesizer P as a function of its frequency f, and that accounts for power attenuation at higher frequencies is :

$$P[\mathrm{dBm}] = 2.0 + 4.99 \times 10^{-4} \times f[\mathrm{MHz}] \tag{1.6}$$

Figure 1.10 shows a photo of the new version DDS-based up-converter installed in 19" rack box.

1.5 Reference synthesizer 2.5 GHz

For AD9915 DDS, the reference clock may be generated internally using built-in phase-locked-loop or can be supplied from an external source. The internal reference generation uses a 10 MHz signal that is multiplied in internal PLL of the DDS chip by the factors varying between 240 and 250 to produce a reference within 2.4–2.5 GHz. In this case, since the spectral purity is degraded as usual in the frequency multiplication process, additional constraints on the spectral purity of 10 MHz signal are introduced.

Instead of using internal DDS PLL we therefore decided to build a new external 2.5 GHz synthesizer which also multiplies 10 MHz reference signal. However, in this case, we had more flexibility to control the spectral purity of 10 MHz, for example, by applying a narrow band quartz filter at the input. The new synthesizer implements ADF4350 PLL chip from Analog Devices, along with an Erasable Programmable Read-Only Memory (EEPROM) controlled through an Arduino microcontroller. Figure 1.11 depicts the circuit connections for data transmission between the Arduino and the PLL chip using SPI communication, as well as the I2C communication between the Arduino and the EEPROM.

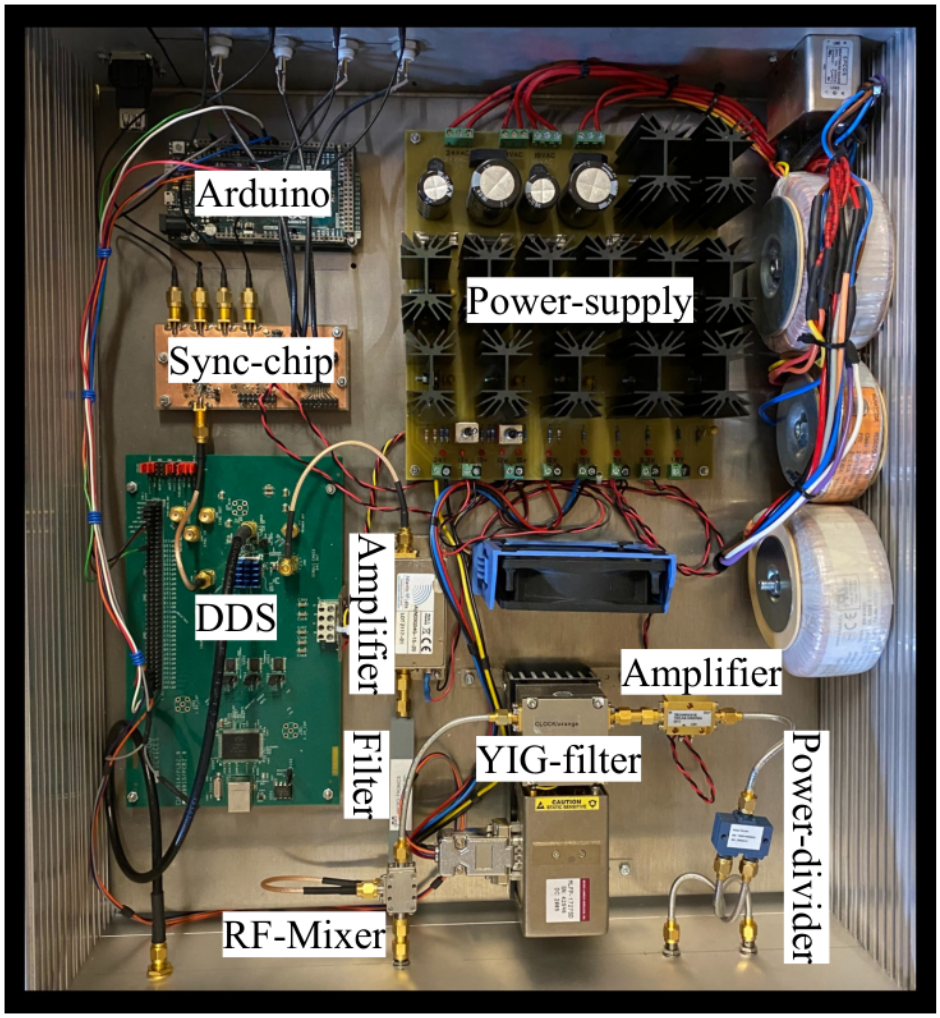

Figure 1.10: Photo of DDS based radio frequency up-converter installed into a standard 19" rack

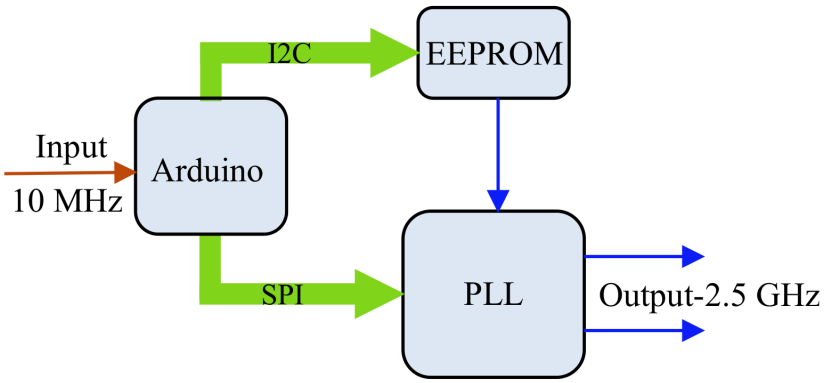

Figure 1.11: Schematic diagram of 2.5 GHz PLL-based reference synthesizer

The configuration of ADF4350 PLL synthesizer is performed via six 32-bit registers, that control all synthesizer parameters. The registers can be read/written using SPI interface, and for this purpose, in the design, an Arduino Due microcontroller is used. The particular feature of ADF4350 is that its six registers should be configured up upon each power up. Arduino Due does not have internal non-erasable memory (it's like a computer without a hard drive) in which one can store PLL registers configuration. Therefore we installed EEPROM chip 24FC02 with a capacity of 256 bytes (like an external hard drive) in which synthesizer configuration can be stored with the system powered down. The communication between Arduino and EEPROM is done using a simple two-wire serial interface known as I2C. Arduino and consequently PLL synthesizer can be controlled from a PC using standard serial interface. In the case, when the output frequency is changed by sending new configuration data to the registers, the data is also stored in EEPROM.

In Figure 1.12, we compare narrowband spectral purity of DDS-based up-converter at 15 GHz with 10 MHz reference (in blue), and 2.5 GHz reference (in red). One can clearly see that spurious components of the 10 MHz reference are completely removed by the application of the new 2.5 GHz reference. Although, the level of spurious components is relatively low, below −60 dB, the frequency multiplication would also lead to multiplication of the main signal and spurious components increasing thus the noise floor. We may therefore conclude that using the new 2.5 GHz reference we improved the signal-to-noise ratio of the DDS-based up converter signal after multiplication by at least 20 dB.

1.6 Optimal digital filtering of low-frequency resonances

Short pulse excitation results in the detection of molecular FID but also of a strong cavity mode decay signal due to direct detection of excitation signal by ZBD but also due to EM wave relaxation processes in the high-vacuum chamber which may be considered as low-quality-factor cavity because of reflections on the chamber windows. We may call the latter *chamber mode decay* (CMD). In absorption spectroscopy, the same phenomenon is often related to standing waves that may lead to rather significant background variations.

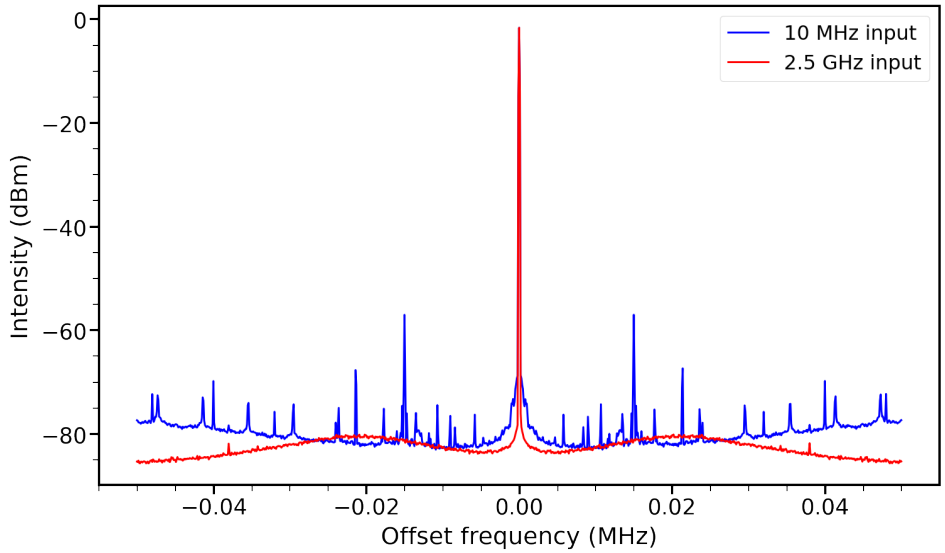

Figure 1.12: Narrow bandwidth spectral purity of the output signal of DDS-based up-converter at 15 GHz obtained from internal 10 MHz reference clock (blue), and external reference of 2.5 MHz (red)

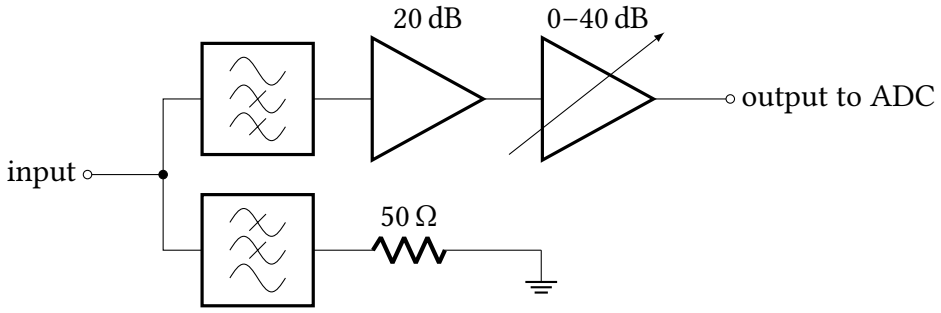

Figure 1.13: The schematic diagram of low noise amplifier and filter in the receiving system of emission spectrometer.

As shown in Figure 1.3, in the spectrometer design, the output of ZBD used as a harmonic mixer is amplified and sent to ADC for time-domain signal sampling. Because of the limited dynamic range of the amplifier, strong CMD signal may hamper the amplification of weak molecular FIDs. Therefore in the amplifier design, a low-pass and a high-pass filters were installed in parallel at the input (Figure 1.13). In our experiments, we found that the CMD frequency is typically below 15 MHz, so the two filters were designed with the same cut-off frequency of 15 MHz. However, due to uncertainties in the filters elements (inductors and capacitors) the cut-off frequencies of the two filters do not match exactly. In addition, the impedance of the filters do not match exactly 50 Ω which lead to non-zero

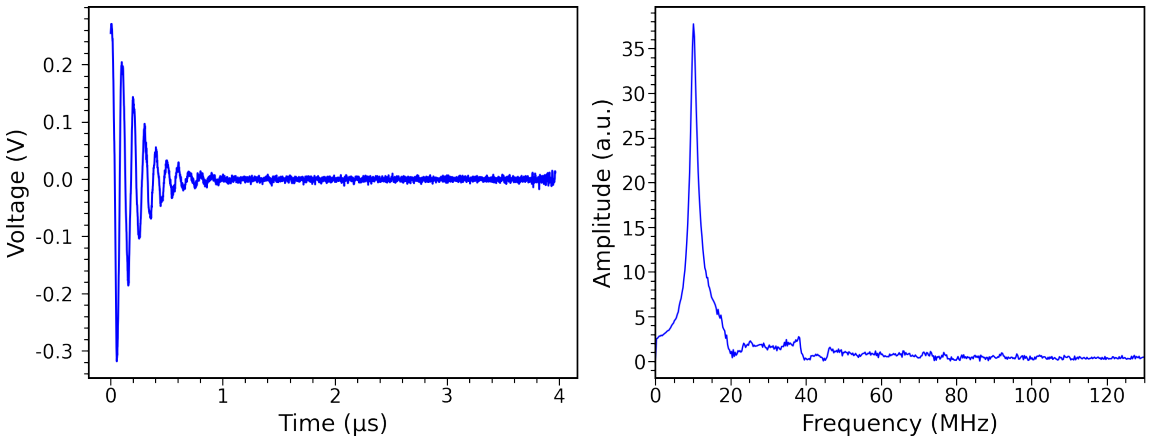

(a) (b)

Figure 1.14: Decay signal including low frequency parasitic resonances and molecular FID: (a) in time domain (b) in frequency domain

reflection coefficients. Thus, the two filters behave like a pseudo-resonant circuit. Such design permits to effectively suppress CMD signal but it is also the cause of new resonant signals which frequencies correspond to the values with highest reflection coefficients of the filters. The filter resonances are however much less stronger than CMD and usually do not saturate the amplifier. The quality factor of the pseudo-resonant circuit is also low, so its decay time is shorter compared to molecular FID. To ignore pseudo-resonant circuit decay (PRCD), one can introduce a delay time between the end of pulse excitation and the start of ADC sampling. However, in this case, the strongest part of molecular FID is also skipped, which results in lower SNR of molecular spectral lines after FFT.

The signal of chirped pulse excitation response (CPER) with dominant PRCD and its spectrum is shown in Figure 1.14. In the spectrum, one can also distinguish weak molecular lines. Throughout the experiments we noticed that the PRCD spectrum has constant characteristics independent of the parameters of the excitation: chirp or transform limited pulse, excitation frequency, or pulse width. Based on the assumption of constant PRCD spectrum, we developed time-domain optimal band-stop digital filter. In the time domain, PRCD signal may be represented as a sum of harmonics:

$$y(t) = \sum_{i=1}^{N} a_i \sin(\omega_i t + \phi_i) e^{-\gamma_i t} \tag{1.7}$$

where a is the amplitude, ω is the angular frequency, ϕ is the phase, and γ is the decay

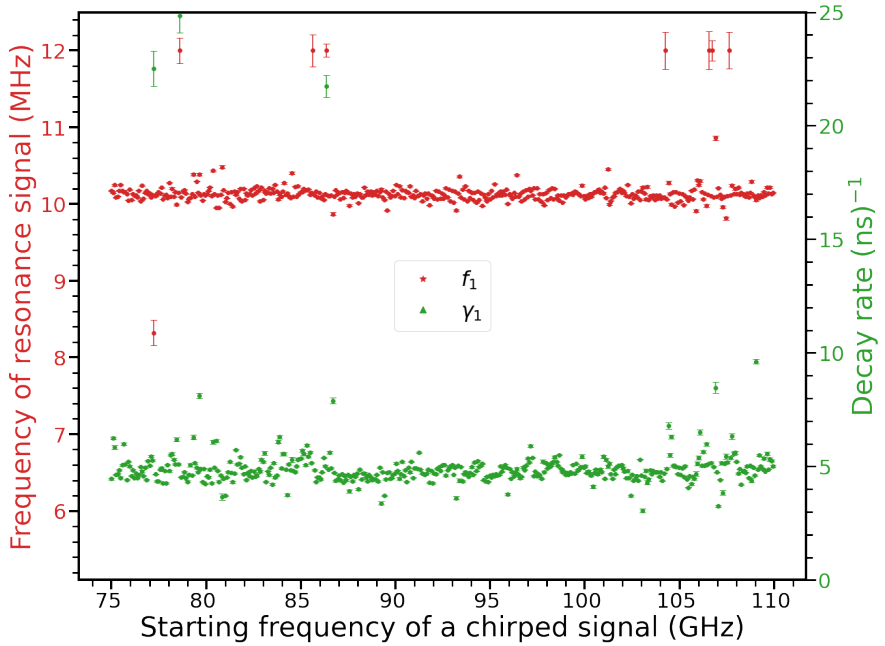

Figure 1.15: Principal resonant harmonic frequency f_1 and decay rate γ_1 determined from least-squares analysis of CPER signals in the frequency range 75–110 GHz plotted as a function of the chirped-pulse excitation frequency.

constant of the i-th PRCD harmonics. These 4 parameters may be derived from least squares fit of CPER signal to the model (1.7).

To test this approach, we recorded CPERs in the frequency range 75–110 GHz using an empty chamber, so no molecular FID signal could influence the least squares fit. At first, each time domain signal was fitted to (1.7) with $N = 1$. Figure 1.15 presents the fitted value of f_1 as a function of chirp pulse excitation frequency. One can see almost constant behaviour of f_1 which supports the assumption that PRCD spectrum does not depend on pulse excitation parameters. The mean value of the principal resonant harmonics frequency is $f_1 = \frac{\omega_1}{2\pi} = (10.13 \pm 0.14)$ MHz. One can also note several outliers, for which the determined resonant frequency was significantly lower or higher than the mean value of f_1. Close analysis of the outliers time domain residuals and their frequency domain spectra revealed the presence of second harmonics component. Therefore, on the next stage, each CPER was fitted to (1.7) with $N = 2$. The determined frequencies f_1 and f_2 of each time domain signal plotted as a function of chirp pulse excitation frequency are shown in Figure 1.16. From the analysis of Figure 1.16 it follows that using the model of (1.7) with two harmonics, one significantly reduced the outliers for f_1. The mean value of principal

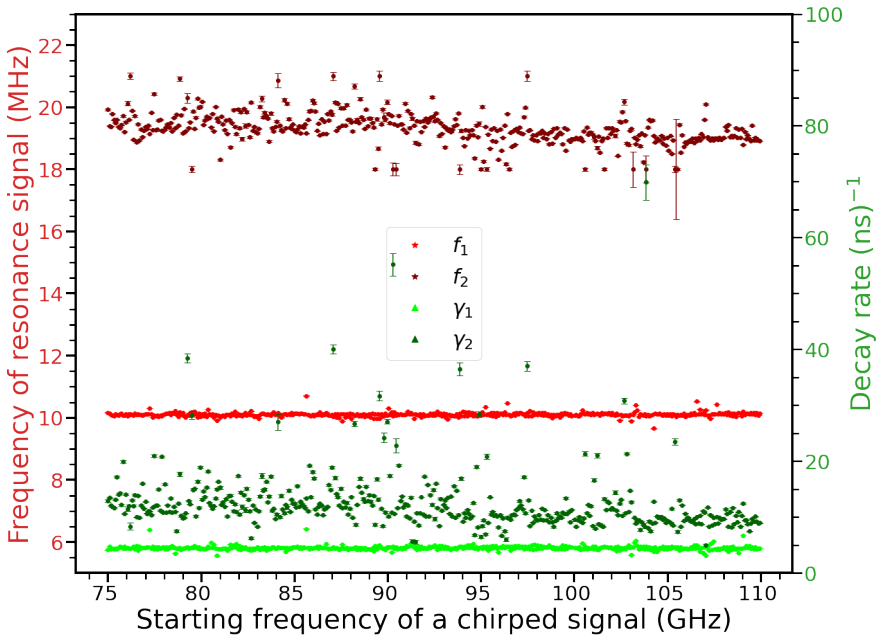

Figure 1.16: Harmonic frequencies f_1, f_2 and decay rates γ_1, γ_2 determined from least-squares analysis of CPER signals plotted as a function of the chirped-pulse excitation frequency.

harmonics is almost the same as in $N = 1$ model: $f_1 = (10.106 \pm 0.073)$ MHz. The mean value of the second harmonics is $f_2 = (18.55 \pm 0.32)$ MHz. One can also note that fitted f_2 and γ_2 values are more scattered around mean value. It is rather normal behaviour that can be explained by the fact that the amplitudes of the second harmonics signal are much lower and cause increased uncertainties of $i = 2$ parameters of (1.7) determined from the fit.

The scattering is also an indicator the limitations of the model applied to experimental time domain signals. In the present case, the recorded CPERs allowed us to determine the frequencies of the first two harmonics. However, ultimately, the number of harmonics N in (1.7) depends on the signal-to-noise ratio of the time domain signal.

Using the determined values of f_1 and f_2 harmonic frequencies, we developed a filtering procedure in the time domain to remove PRCD signals. The procedure consists in least-squares fitting of each CPER signal to (1.7) in which f_i and γ_i are fixed to the mean values determined from the fit. Thus only the amplitude and the initial phase which depend on experimental conditions are varied. Fixing two out of four parameters enables fast convergence of non-linear least squares algorithm. The fitted a and ϕ values along with fixed ω and γ are then used to build the model function (1.7) and to subtract it from the

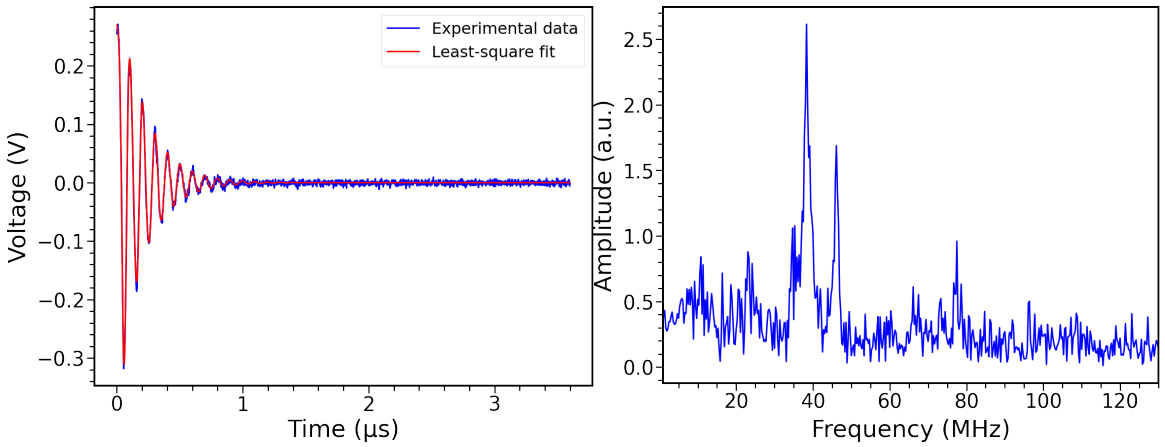

(a) (b)

Figure 1.17: (a) Time-domain decay signal (blue) and its optimally constructed filter response (red) (b) Spectrum of the decay signal after optimal filtration

time domain CPER signal. Figure 1.17a shows recorded CPER signal (in blue, the same as in Figure 1.14a) and the modeled function (1.7) with $N = 2$ (in red). The spectrum of filtered signal as a result of subtraction is shown in Figure 1.17b. By comparison with Figure 1.14b one can clearly see that PRCD was almost completely suppressed revealing the presence weak of molecular spectral lines.

The filtering procedure was implemented in the spectrometer control software written by my scientific supervisor. As explained in 1.3.3, because of PRCD, the effective exploitable bandwidth of recorded molecular spectrum is reduced by 20 MHz when using single direction mode chirped pulse generation, and by 40 MHz in dual-direction mode. The suppression of PRCD permits to exploit the frequency range of FID below 20 MHz for molecular line observation and thus to increase the effective frequency range of the chirped-pulse excitation which is especially useful in the case dual-direction mode excitation.

1.7 Conclusions

In the initial phase of my project, I focused on enhancing the performance of the existing Lille emission spectrometer. The DDS-based source used in this spectrometer was originally designed for absorption spectroscopy and had certain limitations when integrated with emission spectroscopy. To address these limitations, I developed a novel DDS-based

tunable terahertz source, enabling the generation of chirp pulses approximately five times broader than the previous DDS-based source. Additionally, a new synchronisation system was implemented to ensure precise alignment of the entire system with the DDS clock, including the jet pulse. Furthermore, to enhance spectral purity and signal stability, I developed a 2.5 GHz PLL synthesiser to serve as an input source for the DDS-based source. When an external 2.5 GHz source was applied to the DDS input, it significantly improved spectral purity and extended the operational life of the DDS source. In the detection phase, we encountered low-frequency resonance signals within the LNA, which overshadowed the molecular signals, making their identification and analysis challenging. To address this, I developed a comprehensive optimal digital filter model capable of subtracting the parasitic resonance signals. This modelling approach allowed us to effectively remove the low-frequency resonances, revealing clearer and more manageable molecular signals for simplified assignment and analysis.

Part II

Gas-phase pure rotational spectroscopy

Chapter 2

Theoretical background

Rotational spectroscopy stands as a highly potent means of obtaining precise insights into the chemical and physical properties of molecules. Over the past two to three decades, advancements in both experimental methodologies and theoretical frameworks have significantly expanded the capabilities of this spectroscopic technique. Well-known works by Gordy and Cook [26], Townes and Schawlow [27], and Kroto [28] give a lot of information about the theoretical techniques used in rotational spectroscopy. These works are useful for learning about the early stages of the theoretical and experimental development of microwave spectroscopy. The goal of this chapter is to cover all theoretical approaches within the field of rotational spectroscopy employed in this work. Within this chapter, the description starts with the Hamiltonian of a rotating system with a rigid-rotor approximation. In the next sections, different changes to the rotational Hamiltonian are looked at. Which includes corrections for centrifugal distortion, the Hamiltonian for molecules with periodic internal rotation LAM, the Hamiltonian for molecules with two LAMs, and nuclear quadrupole effects. Following this theoretical explanation, the chapter provides a comprehensive overview of the least squares approach used to fit experimental data, as well as an introduction to commonly used computer programs for the precise fitting of experimental data in rotational spectroscopy.

2.1 Rigid rotor molecules

In molecular physics, the rigid rotor approximation is commonly used to analyse the rotational energy levels and spectra of rotating molecules. It is based on the assumption that the bond length between the two atoms remains unchanged during rotation. This approach is very useful when analysing rotational energy levels and studying the spectroscopic characteristics of simple molecules. The rotational energy of a rigid body is given by:

$$E_{rot} = \frac{1}{2}\boldsymbol{\omega}.\mathbf{I}.\boldsymbol{\omega} \tag{2.1}$$

where $\boldsymbol{I}$ is the inertia tensor and $\boldsymbol{\omega}$ is the angular momentum.

In this approximation, the contribution of electrons to the inertia tensor is negligible since their mass is significantly smaller than that of the nucleus. For a molecule with N atoms, each having mass m_i and coordinates (x_i, y_i, z_i) in a molecule-fixed axis system, the

inertia tensor I can be expressed by:

$$I = \begin{pmatrix} I_{xx} & I_{xy} & I_{xz} \\ I_{yx} & I_{yy} & I_{yz} \\ I_{zx} & I_{zy} & I_{zz} \end{pmatrix} \tag{2.2}$$

Each inertia tensor component is defined as follows:

$$\begin{aligned} I_{xx} &= \sum m_i(y_i^2 + z_i^2) & I_{xy} &= I_{yx} = -\sum m_i x_i y_i \\ I_{yy} &= \sum m_i(z_i^2 + x_i^2) & I_{yz} &= I_{zy} = -\sum m_i y_i z_i \\ I_{zz} &= \sum m_i(x_i^2 + y_i^2) & I_{zx} &= I_{xz} = -\sum m_i z_i x_i \end{aligned} \tag{2.3}$$

Principal moments of inertia I_a, I_b, and I_c are obtained by diagonalizing the inertia tensor and always satisfy the condition $I_a \leq I_b \leq I_c$. The molecule fixed xyz axis system is attached to the molecule so that its origin coincides with the molecular center of mass. The (x, y, z) axes are taken parallel to the principal axes of the inertia tensor labeled (a, b, c). The molecule-fixed axes system (x, y, z) corresponds to the principal axes system (a, b, c) in six different ways [28], as shown in Table 2.1, which is necessary for calculating the rotational Hamiltonian.

Table 2.1: Possible mapping of the molecular axes systems x, y and z to the principal axes systems a, b and c. Superscripts r and l represent right-handed and left-handed coordinate systems.

	I^r	I^l	II^r	II^l	III^r	III^l
x	b	c	c	a	a	b
y	c	b	a	c	b	a
z	a	a	b	b	c	c

In quantum mechanics, the Hamiltonian of the rigid rotor is expressed as a function of the rotational constants with the rotational angular momentum operator $\hat{J}$ as follows:

$$H_{rot} = A\hat{J}_a^2 + B\hat{J}_b^2 + C\hat{J}_c^2 \tag{2.4}$$

The rotational constants A, B, and C are inversely proportional to the principal moments of inertia and are expressed as follows:

$$A = \frac{\hbar^2}{2I_a}; \qquad B = \frac{\hbar^2}{2I_b}; \qquad C = \frac{\hbar^2}{2I_c} \tag{2.5}$$

Where $\hbar = h/2\pi$ represents the modified form of Planck's constant. It is important to note that the rotational constants usually meet the condition $A \geq B \geq C$.

The rotation Hamiltonian depends solely on angular momentum operators. The quantum number J is a measure of total angular momentum, and the quantum numbers K and M are projections of total angular momentum on the z-axis of molecular system and Z-axis of laboratory system, respectively. The values of these quantum numbers are defined as follows:

- J is a positive integer starting from 0 $\rightarrow J = 0, 1, 2, ...$
- K can be any integer value between $-J$ and $J \rightarrow -J \leq K \leq J$
- M can be any integer value between $-J$ and $J \rightarrow -J \leq M \leq J$

The type of molecular rotor is defined by the relation between the principal moments of inertia. These relationships are used to classify molecules, as follows:

Table 2.2: The classification of molecules based on their moment of inertia

Moments of Inertia	Symmetry	Constants	Examples
I_a=0; I_b =I_c	Linear	$A = \infty; B = C$	HCl, CO_2
$I_a = I_b = I_c$	Spherical top	$A = B = C$	CH_4, SF_6
$I_a < I_b = I_c$	Prolate symmetric top	$A > B = C$	CH_3Cl, C_2H_6
$I_a = I_b < I_c$	Oblate symmetric top	$A = B > C$	CH_3CF_3, C_6H_6
$I_a < I_b < I_c$	Asymmetric top	$A > B > C$	CH_3NH_2, H_2O

Asymmetric top molecules: In this case, the molecule has three non-zero and unequal moments of inertia $i.e., I_a < I_b < I_c$. All the molecules studied in the present research (CH_3COCl, CH_3COBr, CH_3NH_2, $NH_3{-}H_2O$) belong to this group. In general, the patterns of the energy level of an asymmetric top can be defined by examining how they deviate from the prolate and the oblate symmetric top molecules [27]. Ray's asymmetric parameter is widely used to determine the degree of asymmetry in a molecule, which is expressed as:

$$\kappa = \frac{2B - A - C}{A - C} \tag{2.6}$$

The limiting cases are $\kappa = -1$ for the prolate symmetric molecule, $\kappa = 1$ for the oblate symmetric molecule, and $\kappa = 0$ for the highly asymmetric molecule. If the molecule is

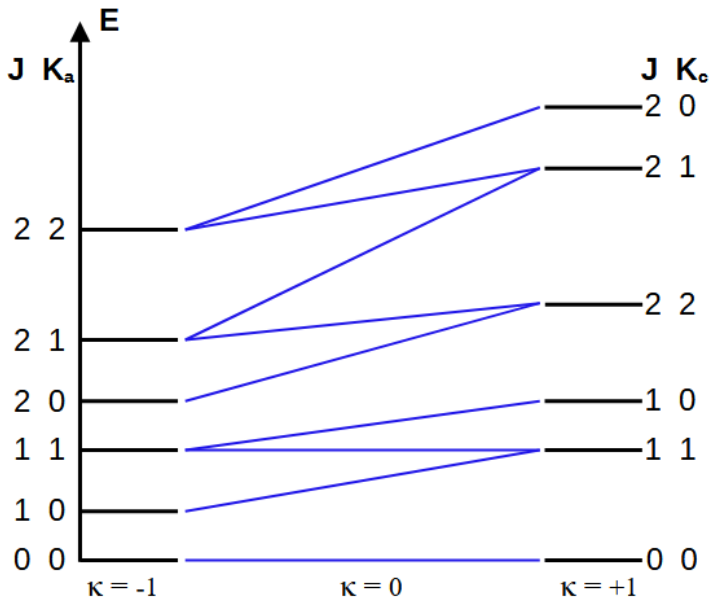

Figure 2.1: Representation of the rotational energy levels of an asymmetric-top molecule with respect to Ray's asymmetry parameter: the left side displays the J_{Ka} values, while the right side shows the J_{Kc} values, each associated with their respective vertical axes.

prolate-symmetric, the energy can be represented in the form:

$$E_{rot} = \frac{B+C}{2}J(J+1) + (A - \frac{B+C}{2})K^2 \tag{2.7}$$

Likewise, if the molecule is oblate-symmetric, the energy can be represented in the form:

$$E_{rot} = \frac{A+B}{2}J(J+1) + (C - \frac{A+B}{2})K^2 \tag{2.8}$$

The labeling of the rotational energy levels for asymmetric top molecules is no longer carried out by the two quantum numbers J and K. Instead, the King-Hainer-Cross notation introduces a more comprehensive description [29]. In this notation, an asymmetric top rotational level is characterized by three distinct quantum numbers: J, K_a, and K_c. These quantum numbers consistently adhere to the condition $K_a + K_c = J$ or $J+1$. The quantum numbers K_a and K_c represent the components of angular momentum along the principal axis of the molecule when it rotates in a prolate and oblate manner, respectively.

The rotational energy levels of an asymmetric top molecule with three different quantum numbers: J, K_a, and K_c, as well as for different Ray's asymmetric parameter values, are represented in Figure 2.1.

Table 2.3: Selection rules for asymmetric-top molecules

Type	Dipole	K_a , K_c	ΔJ	ΔK_a	ΔK_c
a-type	$\mu_a \neq 0$	$K_a = 0$	± 1	$0, \pm 2, ...$(even)	$\pm 1, \pm 3, ...$(odd)
		$K_a \neq 0$	$0, \pm 1$	$0, \pm 2, ...$(even)	$\pm 1, \pm 3, ...$(odd)
b-type	$\mu_b \neq 0$		$0, \pm 1$	$\pm 1, \pm 3...$(odd)	$\pm 1, \pm 3, ...$(odd)
c-type	$\mu_c \neq 0$	$K_c = 0$	± 1	$\pm 1, \pm 3, ...$(odd)	$0, \pm 2, ...$(even)
		$K_c \neq 0$	$0, \pm 1$	$\pm 1, \pm 3, ...$(odd)	$0, \pm 2, ...$(even)

This implies that rotational spectra in asymmetric top molecules can exhibit changes in both K_a and K_c. However, it is important to note that these quantum numbers are not necessarily conserved simultaneously, which is further clarified in Table 2.3 In rotational spectroscopy, the transitions with $\Delta J = -1$ are referred to as the P-branch, those with $\Delta J = 0$ as the Q-branch, and those with $\Delta J = +1$ as the R-branch. These branches correspond to different types of rotational transitions and have important features in the analysis of molecular spectra.

2.2 Non-rigid approximation

In the rigid rotor model approximation, molecules are treated as perfectly rigid bodies with fixed bond lengths and bond angles. However, in reality, most molecules are not perfectly rigid. They can undergo small deformations or vibrational motions while they rotate. The non-rigid approximation accounts for these vibrational motions during molecular rotation. The coupling between the rotational and vibrational states of the molecule leads the rotational energy levels to become slightly perturbed by the vibrational motions. This perturbation is known as centrifugal distortion.

In particular, the rotational energy levels deviate from the rigid rotor spacing as the rotational quantum number J increases. The effect of centrifugal distortion becomes more pronounced for molecules with larger rotational constants (i.e., lower moments of inertia) and at higher rotational energies [27, 28, 30]. Therefore with the help of the appropriate model, distortion effects retrieved by analyzing the spectrum, can be used to determine the potential energy surface.

Correction of centrifugal distortion can be performed by introducing higher-order cor-

rection components in the rotation Hamiltonian. Watson addresses centrifugal distortion by including these correction terms in the rotational Hamiltonian expressed as follows [26]:

$$H = H_{rot} + H_d \tag{2.9}$$

where H_{rot} is the rigid rotor Hamiltonian constant described by equation (2.4) and H_d is the centrifugal distortion Hamiltonian. The distortion Hamiltonian with higher order terms (4, 6, 8,...) is written as;

$$H_d = H_4 + H_6 + H_8 + ... \tag{2.10}$$

By considering fourth and sixth-order terms, equation (2.9) becomes:

$$H = H_{rot} + \frac{\hbar^4}{4} \sum_{\alpha\beta\gamma\delta} \tau_{\alpha\beta\gamma\delta} \hat{J}_\alpha \hat{J}_\beta \hat{J}_\gamma \hat{J}_\delta + \hbar^6 \sum_{\alpha\beta\gamma\delta\epsilon,\eta} \tau_{\alpha\beta\gamma\delta,\epsilon,\eta} \hat{J}_\alpha \hat{J}_\beta \hat{J}_\gamma \hat{J}_\delta \hat{J}_\epsilon \hat{J}_\eta \tag{2.11}$$

where $\tau_{\alpha\beta\gamma\delta}$ are the fourth-order centrifugal distortion constants and $\tau_{\alpha\beta\gamma\delta,\epsilon,\eta}$ are the sixth-order centrifugal distortion constants. $\alpha\beta\gamma\delta, \epsilon, \eta$ can have any of the values x, y, and z of the molecule-fixed coordinates. Watson demonstrated that the number of components of the correction term can be reduced to a linear combination of 5 constants for the fourth order and 7 constants for the sixth order to adjust experimental values [31, 32, 33].

Watson developed two reduction techniques that are employed in rotational spectroscopy: the (Asymmetric) A- and (Symmetric) S-reductions, which are most appropriate for asymmetric and symmetric (or slightly asymmetric) molecules, respectively. The rotation Hamiltonian in the A-reduction can be represented as [26]:

$$\begin{aligned}\hat{H} = {} & \frac{1}{2}(B^{(A)} + C^{(A)})\hat{J} + [A^{(A)} - \frac{1}{2}(B^{(A)} + C^{(A)})]\hat{J}_z^2 + \frac{1}{2}(B^{(A)} - C^{(A)})(\hat{J}_x^2 - \hat{J}_y^2) \\ & - \Delta_J \hat{J}^4 - \Delta_{JK} \hat{J}^2 \hat{J}_z^2 - \Delta_K \hat{J}_z^4 - 2\delta_J \hat{J}^2(\hat{J}_x^2 - \hat{J}_y^2) - \delta_K[\hat{J}_z^2(\hat{J}_x^2 - \hat{J}_y^2) - (\hat{J}_x^2 - \hat{J}_y^2)\hat{J}_z^2] \\ & + O(6) + ...\end{aligned} \tag{2.12}$$

where $A^{(A)}, B^{(A)}, C^{(A)}$ are the rotational constants. $\Delta_J, \Delta_{JK}, \Delta_K, \delta_J$ and δ_K are the fourth-order centrifugal distortion constants. In the current work, only the A-reduced Hamiltonian is applied to compute the rotational energy of asymmetric top molecules. Along with vibration motions, molecules may also have internal rotations with respect

to the overall rotation of molecules, which can distort the geometry of a molecule from its equilibrium.

2.3 Nuclear Quadrupole Coupling

In high-resolution spectroscopy, when dealing with molecules containing nuclei with a nonzero electric quadrupole moment possessing a nuclear spin quantum number $I \geq 1$, it becomes pertinent to introduce an additional significant term into the rotational Hamiltonian, known as "nuclear quadrupole coupling (NQC)" [26, 34]. NQC results from the interaction of the nuclear quadrupole moments of quadrupolar nuclei with the electric field gradients within the molecule. This interaction causes perturbations in the energy levels within the rotational Hamiltonian [35, 36, 37]. The NQC-induced perturbation leads to small energy splittings in the rotational energy levels, resulting in hyperfine structure in the rotational spectrum.

The analysis of hyperfine structure in rotational spectra gives us important information about nuclear properties, such as the nuclear spin quantum number (I) and the electric quadrupole moment (Q). It also helps us figure out the molecular structure and the environment around the quadrupolar nuclei inside the molecule. The interaction between the electric quadrupole moment and the electric field gradient leads to a coupling between the nuclear spin angular momentum and the rotational angular momentum (J). The quadrupole coupling energies can be conveniently computed using the sum vector $\vec{F} = \vec{I} + \vec{J}$. The total angular momentum introduces a new quantum number that describes the energy levels of the hyperfine structure in a particular rotational transition. The total quantum number can have the following values:

$$F = J + I, J + I - 1, ..., |J - I| \tag{2.13}$$

The selection rule between hyperfine levels is $\Delta F = 0, \pm 1$. Usually, the transitions with the selection rule $\Delta F = \Delta J$ are significantly more intense than other lines. The quadrupole energy of molecules in the general form is written as [26]:

$$E_Q = eQq_j \frac{(2J+3)}{J} Y(J, I, F) \tag{2.14}$$

The function $Y(J, I, F)$ is called the Casimir function, and it is defined as:

$$Y(J, I, F) = \frac{\frac{3}{4}C(C+1) - I(I+1)J(J+1)}{2(2J-1)(2J+3)I(2I-1)} \tag{2.15}$$

where $C = F(F+1) - J(J+1) - I(I+1)$

The quantity q_j depends on the type of molecule, whether linear, symmetric, or asymmetric. For an asymmetric rotor, it can be expressed as:

$$q_j = \frac{2}{(J+1)(2J+3)} \sum_{g=a,b,c} q_{gg} \langle J_g^2 \rangle \tag{2.16}$$

where q_{aa}, q_{bb}, and q_{cc} are the molecular field gradients at the coupling nucleus with respect to the inertial axes, which are related to the quadrupole coefficient as:

$$\chi_{aa} = eQq_{aa} \qquad \chi_{bb} = eQq_{bb} \qquad \chi_{cc} = eQq_{cc} \tag{2.17}$$

It leads to an equation for quadrupole energy in the form

$$E_Q = \frac{1}{J(J+1)} \left\{ \chi_{aa} \langle J_a^2 \rangle + \chi_{bb} \langle J_b^2 \rangle + \chi_{cc} \langle J_c^2 \rangle \right\} Y(J, I, F) \tag{2.18}$$

Since the total sum of the diagonal term of the quadrupole tensor is zero, $\chi_{aa} + \chi_{bb} + \chi_{cc} = 0$ [26], there are typically just two independent coupling constants. This implies that once we know two of these constants, the third one can be determined from the equation, reducing the complexity of the analysis. Furthermore, the expectation values of the angular momentum operators $\langle J_a^2 \rangle$, $\langle J_b^2 \rangle$, and $\langle J_c^2 \rangle$ can be computed from the rotational eigenfunctions.

The equation (2.18) can be expressed differently by introducing two distinct coupling constants, denoted as χ_+ and χ_-, in the following form [38]:

$$E_Q(I, J, F) = \left[\frac{1}{2}\chi_+ \left\langle J_b^2 + J_c^2 - 2J_a^2 \right\rangle - \frac{1}{2}\chi_- \left\langle J_b^2 - J_c^2 \right\rangle \right] \frac{2Y(J, I, F)}{J(J+1)} \tag{2.19}$$

where $\chi_+ = -\chi_{aa}$, $\chi_- = \chi_{cc} - \chi_{bb}$ [38].

The quadrupolar energy calculated in equation (2.19) is initially determined using a first-order perturbation approach. This approach considers only the diagonal elements of the quadrupolar Hamiltonian. It assumes that the influence of the off-diagonal terms on quadrupolar energy is generally insignificant or negligible. However, the quadrupolar tensor is not perfectly diagonal. These off-diagonal elements represent interactions between

different states of the system and can potentially have some impact on the overall energy and properties being calculated. This can be achieved by introducing a second-order term into the perturbation theory, which takes into account these previously neglected interactions and leads to a more precise evaluation of the quadrupolar energy and associated properties of the molecules.

Hence, the quadrupole energy in (2.19) is computed more accurately by taking into account the off-diagonal term of the quadrupole tensor as [38]:

$$E_Q(I,J,F) = \left[\frac{1}{2}\chi_+\left\langle J_b^2 + J_c^2 - 2J_a^2\right\rangle - \frac{1}{2}\chi_-\left\langle J_b^2 - J_c^2\right\rangle + \chi_{ab}\left\langle J_bJ_a + J_aJ_b\right\rangle\right]\frac{2Y(J,I,F)}{J(J+1)} \tag{2.20}$$

The difference in quadrupole energy between two corresponding levels indicates the precise shift of hyperfine components from their hyperfine-free, pure rotational positions. Consequently, the frequency of each hyperfine component as a function of χ can be calculated as:

$$f_{hf}(\chi) = f_{rot} + \frac{E_Q(I,J',F') - E_Q(I,J'',F'')}{h} \tag{2.21}$$

where f_{rot} is the hyperfine free central transition frequency.

Usually, the spacing between the hyperfine components diminishes as the rotational quantum number J increases. At lower values of J, the hyperfine components are distinctly separated, while at higher J, the spectra often become indistinct. The number of hyperfine components depends on three factors: the count of nuclei with nuclear spins $I \geq 1$, the magnitude of the nuclear spin-angular momentum (I), and the absolute value of the nuclear quadrupole moment (Q). Generally, when the spin quantum number is higher, the observed hyperfine pattern tends to be more complicated.

2.4 Internal rotation

The internal rotation of a C_{3v} symmetric top is an important phenomenon in rotational spectroscopy. The internal rotation occurs when a C_{3v} symmetric top rotates with respect to the rest of the molecule which is called frame. CH_3, CB_3, and CF_3 tops are examples

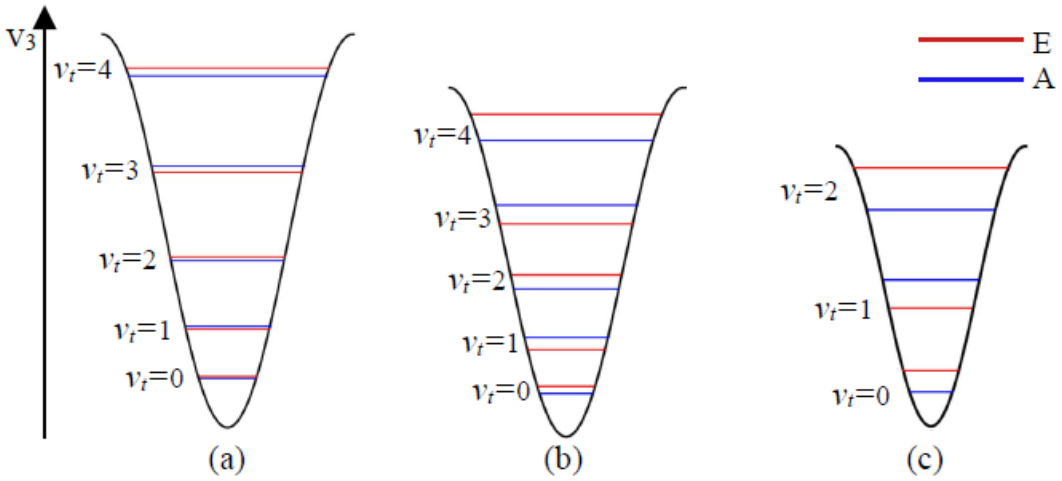

Figure 2.2: The relationship between the barrier height of the internal rotor and torsional splitting in three distinct scenarios (a) high barrier, (b) intermediate barrier, and (c) low barrier.

of such rotations. Internal rotation can lead to the splitting of the rotational energy levels into two torsional components. The energy difference between two torsional components depends on the barrier to internal rotation, which is illustrated in Figure 2.2.

Internal rotor barrier heights determine the degeneracy of the torsional levels for C_{3v} symmetry top. In the case of the finite torsional barrier height, the tunneling results in the division of each torsional level into two sub-levels: doubly degenerate (E symmetry species of the C_{3v} group) and non-degenerate (A symmetry species of the C_{3v} group). For the infinite torsional barrier height, each torsional level is triply degenerate. In some cases, the C_{3v} top can be hindered by a very small, negligible barrier and thus be treated as a free rotor. The magnitude of the spectral splitting increases with decreasing internal rotational barrier.

Even though internal rotation complicates spectrum analysis, chemists and physicists are interested in it because it provides crucial insights into the geometry and behavior of molecules. By analysing the rotational spectra of such molecules, the barrier to internal rotation can be precisely determined.

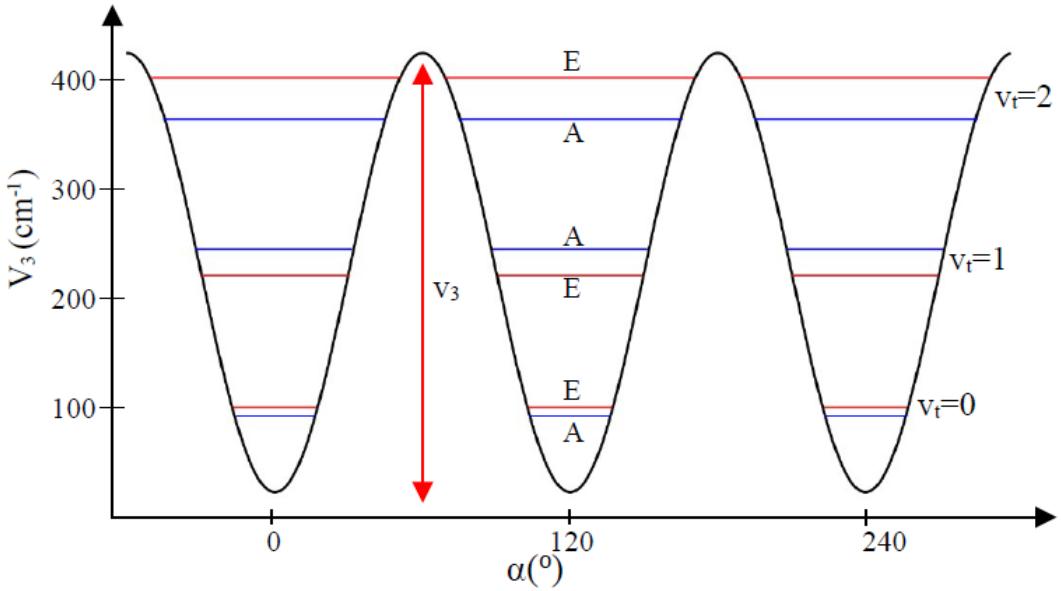

Figure 2.3: Schematic representation of the potential function and torsional energy levels.

2.4.1 Potential function for internal rotation

The internal rotation of molecules is described by a torsional angle α. The term "torsional angle" refers to the angle formed between two planes when the top rotates relative to the molecular frame. Therefore, the potential function is a periodic function in α, with a period of $2\pi/N$ between the interval of $\alpha = 0$ and $\alpha = 2\pi$. Figure 2.3 shows the potential function and torsional energy levels for a system with an intermediate barrier to internal rotation. The potential function for an N-fold symmetric barrier can be represented as [26]:

$$V(\alpha) = \frac{V_N}{2}(1 - \cos N\alpha) + \frac{V_{2N}}{2}(1 - \cos 2N\alpha) + ... \tag{2.22}$$

There are three equivalent minima for the complete rotation of the C_{3v} symmetry top.

V(α) is zero at $\alpha = 0, \pm 2\pi/3, \pm 4\pi/3$, and so on. Hence, the potential function for a barrier with $2\pi/3$ fold of symmetry may be written as:

$$V(\alpha) = \frac{V_3}{2}(1 - \cos 3\alpha) + \frac{V_6}{2}(1 - \cos 6\alpha) + ... \tag{2.23}$$

2.4.2 Torsional energy levels

The Schrödinger equation for an isolated internal rotor with torsional angle α in a threefold hindering potential is written as [26]:

$$-\frac{\hbar^2}{2I_r}\frac{d^2\Psi(\alpha)}{d\alpha^2} + V(\alpha)\Psi(\alpha) = E\Psi(\alpha) \tag{2.24}$$

where E is the total energy, Ψ is the wave function associated with methyl rotor, V(α) is the potential function for internal methyl rotor and I_r is the reduced moment of inertia for the relative motion of methyl rotor with respect to its frame molecules. The reduced moment of inertia for the methyl rotor is expressed as:

$$I_r = \frac{I_\alpha I_\beta}{I_\alpha + I_\beta} \tag{2.25}$$

where I_α is the moment of inertia of the internal rotator and I_β is the moment of inertia of the molecular frame. The reduced moment of inertia has a proportional relation with the internal force constant of the rotor,

$$F = \frac{\hbar^2}{2I_r} \tag{2.26}$$

From (2.24) and (2.26)

$$-F\frac{d^2\Psi(\alpha)}{d\alpha^2} + V(\alpha)\Psi(\alpha) = E\Psi(\alpha) \tag{2.27}$$

It is sufficient to take into consideration the first term of potential from equation (2.23) while examining the torsional energy levels. We consider two extreme cases of barrier height:

1) For extremely high barrier ($V_3 \approx \infty$): equation (2.27) takes the simple expression

$$\frac{d^2\Psi(\alpha)}{d\alpha^2} + \frac{1}{F}[E - \frac{V_3}{2}(1 - \cos 3\alpha)]\Psi(\alpha) = 0 \tag{2.28}$$

For small α values, the Taylor series expansion of cosα becomes

$$\cos 3\alpha = 1 - \frac{9}{2}\alpha^2 + \frac{27}{8}\alpha^4 + ... \tag{2.29}$$

Only considering the first term of (2.29) equation (2.28) reduces to

$$\frac{d^2\Psi(\alpha)}{d\alpha^2} + \frac{1}{F}[E - \frac{9}{4}V_3\alpha^2]\Psi(\alpha) = 0 \tag{2.30}$$

which is same as the wave equation of a simple harmonic oscillator. Therefore, the solution of the equation (2.30) can be written as follows;

$$E = 3(V_3F)^{1/2}(v + \frac{1}{2}) \quad \text{with torsional quantum number } v = 0, 1, 2, 3, \ldots \tag{2.31}$$

And the frequency of torsional oscillation is

$$\nu = \frac{3}{2\pi}\left(\frac{V_3}{2I_r}\right)^{1/2} \tag{2.32}$$

The relationship between the frequency of torsional oscillation and the barrier height allows one to determine the height of the barrier from rotational spectra analysis.

2) For extremely low barrier ($V_3 \approx 0$): equation (2.27) takes the simple expression

$$\frac{d^2\Psi(\alpha)}{d\alpha^2} + \frac{1}{F}E\Psi(\alpha) = 0 \tag{2.33}$$

The quantum particle is at a potential barrier with $V_{(3)}$=0, and the solution is a periodic free internal rotation function:

$$\Psi(\alpha) = Ae^{im\alpha} = A(\cos m\alpha + i \sin m\alpha) \tag{2.34}$$

where A is the normalization factor and m is the free internal rotation quantum number with values m=0,$\pm$ 1,$\pm$ 2,$\pm$ 3,...

Hence, equation (2.33) simplifies to:

$$E = Fm^2 \tag{2.35}$$

Therefore, all free rotor states are doubly degenerate except for the state where m = 0. The equation (2.34) to be well-behaved must satisfy the appropriate boundary condition. Using the boundary condition $\Psi(\alpha) = \Psi(\alpha + 2\pi)$ the normalization condition can be used to calculate the constant A, which gives $A = \frac{1}{\sqrt{2\pi}}$.

2.5 Hamiltonians for internal and overall rotation

In the systematization of different methods used in spectral analysis, it is convenient to separate them into so-called "local" and "global" approaches. Most conventional tools classify rotational energy levels into different groups based on symmetry or vibrational energy

states, especially when dealing with LAM. Each group is then addressed independently using its own Hamiltonian, obtaining a unique set of parameters for each category. These techniques are referred to as "local" methods. For example, Watson's A-reduction Hamiltonian (2.12) is a typical example of "local" method applicable only for rotational transition in a given vibrational state. In the case of LAMs, both "local" and "global" methods exist. In the context of internal rotation of C_{3v} top, the major difference between them is that the "global" approach includes the torsional potential function (2.23).

To accurately analyze a spectrum of molecule with internal rotation, it is essential to apply the appropriate molecular model and quantum mechanical Hamiltonian. In tackling the internal rotation issue, different methods can be employed. A review paper by I. Kleiner [39] represents a comprehensive assessment of different modern method. We will present below only the methods used in the frame of this dissertation.

The principal axis method (PAM) and the rho axis method (RAM) are the two commonly used Hamiltonian methods. Each of these methods follows a unique mathematical framework and uses a different coordinate system.

2.5.1 Principal Axis Methods (PAM)

In the principal axis system, the torsion-rotation Hamiltonian for an asymmetric-top molecule is [39]:

$$H = F(P_\alpha - \rho_a J_a - \rho_b J_b - \rho_c J_c)^2 + V(\alpha) + AJ_a^2 + BJ_b^2 + CJ_c^2 \tag{2.36}$$

where P_α represents the internal rotation angular momentum associated with the torsion angle α and J_g ($g = a, b, c$) signifies the components of the total rotational angular momentum within the principal axis system. The relationships between the rotational constants (A, B, C), the internal rotation constant (F), and the coupling constant vector (ρ) to the principal moments of inertia ($I_g = I_a, I_b, I_c$) and the moment of inertia of the top (I_α) can be expressed in the following manner:

$$\begin{aligned} A &= \frac{\hbar^2}{2I_a}, & B &= \frac{\hbar^2}{2I_b}, & C &= \frac{\hbar^2}{2I_c}, \\ \rho_g &= \frac{\lambda_g I_\alpha}{I_g}, & F &= \frac{\hbar^2}{2rI_\alpha}, & r &= 1 - \sum_g \lambda_g^2 \frac{I_\alpha}{I_g}, \end{aligned} \tag{2.37}$$

In equation (2.37), λ_a, λ_b, and λ_c are the direction cosines of the internal rotation. axis i of the top in the principal axis system, i.e., $\lambda_g = \cos(\theta(i,g))$. In the principal axis system, the Hamiltonian (2.36) contains three quadratic terms ($J_iJ_j + J_jJ_i$) and also three quadratic cross terms in $P_\alpha J_i$ that describe the Coriolis type interaction between the internal rotation of the top and the molecular frame. In the PAM approximation, higher-order cross terms can be eliminated from the matrix, which simplifies and reduces the above Hamiltonian in (2.36). The transformed Hamiltonian matrix can then be factored into smaller effective rotational matrices, one for each torsional state v_t and one for each internal rotation state $\sigma = 0$ (A-state) and $\sigma = \pm 1$ (E-state) [39]:

$$\begin{aligned} H_{v\sigma}^{PAM} &= H_R + F\sum_n W_{v\sigma}^{(n)} \sum_g (\rho_g J_g)^n, \\ \text{and} \qquad H_R &= AJ_a^2 + BJ_b^2 + CJ_c^2 \end{aligned} \tag{2.38}$$

The $W_{v\sigma}^{(n)}$ coefficients of (2.38) result from a van Vleck perturbational treatment. Their values depend on the so-called reduced barrier parameter $s = 4V_3/9F$.

The convergence of the Hamiltonian in this method is influenced by various parameter values, such as the barrier height and internal force constant. This method is especially useful when dealing with high and intermediate energy barriers. However, the Hamiltonian of this approach converges very slowly, particularly for the small barrier (or large ρ). Furthermore, the presence of Coriolis force cross terms in the Hamiltonian makes it difficult to distinguish between torsional and rotating motions.

2.5.2 Rho Axis Methods (RAM)

The PAM Hamiltonian encounters difficulties in achieving fast convergence in cases of low potential barriers or strong torsion-rotation coupling. The inclusion of the Coriolis-type cross term $-2FP_\alpha \boldsymbol{\rho} \cdot \boldsymbol{J}$ in the Hamiltonian adds further complexity. To address these challenges, the rho-axis method has been introduced. This approach allows for the omission of the Coriolis-type cross term, leading to a more streamlined and simplified Hamiltonian. This method is a strong tool for dealing the molecules that have periodic internal rotation. This method has previously been successful in studying a number of molecules that exhibit internal rotation. [40, 41, 42, 43, 44]. The RAM axis system is obtained by rotating the

principal axis system to make the new z axis parallel to the ρ vector. And the angle of rotation can be expressed as [39]:

$$\theta = \arctan\left(\frac{\rho_x}{\rho_z}\right) = \arctan\left(\frac{I_z\lambda_x}{I_x\lambda_z}\right) \tag{2.39}$$

Following the rotation of the axis system, the cross term $-2FP_\alpha \boldsymbol{\rho}\cdot\boldsymbol{J}$ in (2.36) simplifies to $2F\rho_z P_\alpha J_z$. Because the matrix elements of $2F\rho_z P_\alpha J_z$ are diagonal with respect to the symmetric-top quantum number K, this operator can be incorporated into the pure torsional components of the Hamiltonian. As a result, the Hamiltonian becomes dependent on K, and the RAM Hamiltonian can be expressed as follows:

$$H_{\mathrm{RAM}} = H_T + H_R + H_{cd} + H_{int.} \tag{2.40}$$

where H_T represents the torsional Hamiltonian, H_R represents the rotational Hamiltonian in the rho axis system, H_{cd} represents the centrifugal distortion (as explained in Section 2.2), and $H_{int.}$ represents the higher-order torsional-rotational interaction Hamiltonian. After eliminating the cross term, the torsional Hamiltonian within the RAM coordinate system becomes:

$$H_T = F(P_\alpha - \rho J_z)^2 + V(\alpha) \tag{2.41}$$

The rotational Hamiltonian in I^r coordinate representation has the following form:

$$H_R = A_{\mathrm{RAM}}J_z^2 + B_{\mathrm{RAM}}J_x^2 + C_{\mathrm{RAM}}J_y^2 + D_{zx}(J_zJ_x + J_xJ_z) + D_{zy}(J_zJ_y + J_yJ_z) \tag{2.42}$$

Since this new axis system does not coincide with the principal axes in general, the equation (2.42) includes two non-diagonal terms $D_{zx}(J_zJ_x + J_xJ_z)$ and $D_{zx}(J_zJ_y + J_yJ_z)$, one of which is zero for a molecule with a plane of symmetry. The higher-order interaction terms of H_{int} can be obtained by multiplying the powers of the rotation angular momentum components J_i^n with the powers of the torsion operators $P_\alpha^m, (1-\cos 3\alpha), (1-\cos 6\alpha)$, etc. [39].

The constants $\mathrm{A_{RAM}}$, $\mathrm{B_{RAM}}$, and $\mathrm{C_{RAM}}$ in (2.42) are the rotational constants in the RAM axis system. The transformation of the rotational constants from the PAM axis system to

the RAM axis system can be expressed as follows:

$$\begin{aligned} A_{\mathrm{RAM}} &= A_{\mathrm{PAM}}\ \cos^2\theta + B_{\mathrm{PAM}}\ \sin^2\theta \\ B_{\mathrm{RAM}} &= A_{\mathrm{PAM}}\ \sin^2\theta + B_{\mathrm{PAM}}\ \cos^2\theta \\ C_{\mathrm{RAM}} &= C_{\mathrm{PAM}} \end{aligned} \tag{2.43}$$

And the term D_{zx} is written as,

$$D_{zx} = (A_{\mathrm{PAM}} - B_{\mathrm{PAM}})\sin\theta\cos\theta \tag{2.44}$$

Likewise, the conversion of the quadrupole coefficient and dipole moment from the PAM coordinate system to the RAM coordinate system, achieved by employing the rotation angle θ, can be expressed as follows:

$$\begin{aligned} (\chi_{zz})_{\mathrm{RAM}} &= (\chi_{zz})_{\mathrm{PAM}}\ \cos^2\theta + (\chi_{xx})_{\mathrm{PAM}}\ \sin^2\theta - 2(\chi_{zx})_{\mathrm{PAM}}\ \cos\theta\sin\theta \\ (\chi_{xx})_{\mathrm{RAM}} &= (\chi_{zz})_{\mathrm{PAM}}\ \sin^2\theta + (\chi_{xx})_{\mathrm{PAM}}\ \cos^2\theta + 2(\chi_{zx})_{\mathrm{PAM}}\ \cos\theta\sin\theta \\ (\chi_{yy})_{\mathrm{RAM}} &= (\chi_{yy})_{\mathrm{PAM}} \\ (\mu_x)_{\mathrm{RAM}} &= \cos\theta(\mu_x)_{\mathrm{PAM}} - \sin\theta(\mu_z)_{\mathrm{PAM}} \\ (\mu_z)_{\mathrm{RAM}} &= \sin\theta(\mu_x)_{\mathrm{PAM}} + \cos\theta(\mu_z)_{\mathrm{PAM}} \end{aligned} \tag{2.45}$$

RAM does not have the same limitations as PAM at the V_3 and ρ parameter values, and it can be applied to molecules with extremely low barriers and high values. Furthermore, this method is a "global" method that performs all torsional states with a single set of parameters.

2.6 Hamiltonian for the molecules exhibiting two large-amplitude motions

In Section 2.4, I addressed molecules exhibiting one periodic large amplitude motion (C_{3v} internal rotation). Now, in this section, I will delve into molecules exhibiting two LAMs: torsional and wagging motions.

Wagging motion, also known as the back-and-forth motion, in molecules like H_2O (water) and NH_2 (an amino group), when attached to another chemical group, plays an important part in their rotational spectroscopy. This motion involves the oscillation or rocking

motion of certain atomic groups within the molecule, and it has several impacts on the rotational energy levels, and resulting rotational spectra. While wagging motion occurs concurrently with the overall rotation of molecules, leading to complex patterns in energy levels.

When it comes to rotational spectroscopy, these LAMs add more vibrational degrees of freedom, which leads to more complicated energy-level configurations and molecular structures. Such LAMs lead to the splitting of energy levels into sub-levels due to the tunneling effect. Consequently, this increases the possibility of rotational transitions, adding complexity to the interpretation and analysis of these spectra. The spectral lines are no longer solely determined by rotational quantum numbers; they also involve contributions from both torsional and wagging vibrational quantum numbers. Advanced computational techniques, such as simulation and fitting procedures, are often required to extract meaningful information from complex spectra.

2.6.1 High-barrier tunneling formalism

High-barrier tunneling formalism developed by Jon Hougen and his collaborators in the 1980s [45, 46, 47]. The main idea of this formalism is to consider the molecular system as a set of equivalent configurations, each accessible through the tunneling. For each tunneling pathway one can establish its own local system of internal axes in order to cancel the angular momentum resulting from the LAM and tunneling. Each configuration has a vibrational wave function which analytical form remains generally unknown. The latter obviously poses a problem for the treatment with numerical methods. The formalism developed by Hougen and collaborators allows one to bypass this problem. The formalism is based on the fact that the probabilities of the tunneling between the different configurations are proportional to the overlap integrals between the individual wave functions. At the same time, the probabilities of the tunneling are directly related to the splittings of the energy levels. Finally, in the frame of the formalism, the energy levels are presented as a series expansion of the splittings which play the role of parameters to be adjusted.

An example of parametrization of energy levels is presented in the paper [45] for a

molecule having 9 equivalent minima. First, we define : ψ_0, ψ_1,...ψ_8 the individual wave functions associated with 9 minima. The next step is to introduce overlap integrals as parameters $X_1 = \langle\psi_i|H|\psi_{i+1}\rangle$, $X_2 = \langle\psi_i|H|\psi_{i+2}\rangle$ etc. (following the cyclic character : $H_{i,i\pm j} = H_{i,i\pm(n-j)} = X_j$ et $0 \leq j \leq n/2$) which express the interaction between different minimas. In the article [45] it is shown that one can express the eigenvalues (the energy levels) of the Hamiltonian via the parameters X_j :

$$E_r = X_0 + 2\sum_{j=1}^{4} X_j \cos\left(\frac{2\pi jr}{9}\right) + (-1)^r X_{n/2} \tag{2.46}$$

Where the integer r satisfies $0 \leq r \leq n/2$. In general, we sum for all $0 \leq j < n/2$ and the term $X_{n/2}$ is allowed when the number of minima n is even. This is how the matrix elements $X_j = \langle\psi_i|H|\psi_{i+j}\rangle$ become the parameters to be adjusted from the experimental data. In the case of a high barrier tunneling, the main contribution in E_r comes from a few first terms X_j with $j = 0, 1, 2...$ and the series expansion in the (2.46) converges fairly quickly.

On the one hand, this approach allows one to analyze the rotational spectrum with very good accuracy. On the other hand, the parameters resulting from spectral analysis have no direct physical meaning. In particular, the formalism does not provide explicitly the parameters of the potential energy function. However, the potential energy function can be retrieved indirectly by using the value of splittings between substates, as well as the information on the lowest vibration levels that can be obtained by quantum chemistry calculations or by studying vibrational spectra. The formalism has been applied successfully in the analysis of the rotational and vibrational spectra of several molecules exhibiting one or two LAMs, including the internal rotation of a C_{3v} top. The latter is treated using the formalism described above in the ERHAM code, which makes it possible to analyze the spectra of the molecules with one or two C_{3v} rotors [48, 49]. Concerning the inversion-type vibrational motion, the realization of the high-barrier tunneling formalism that can treat this case is often called the « water dimer formalism » [50], because initially it was applied to analyze the two LAMs of the water dimer.

Another limitation of the formalism is its applicability to the case of high tunneling barriers. The high barrier condition suggests that most of the time the system is subject to

rapid oscillations around the equilibrium configuration of the molecule and from time to time the system undergoes a tunneling to move from one configuration to another. From the point of view of quantum mechanics, this means that the wave functions are well localized and that the energy levels splittings due to the tunneling is small compared to the characteristic difference between vibrational levels of the molecule. The situation becomes more complicated for molecules with low barriers. In this case, the wave functions can no longer be well located in the potential energy minima and because of the high tunneling probabilities even between the distant configurations, the convergence of the method decreases significantly. The high-barrier tunneling formalism is a "local" method and for this reason it is difficult to apply it in the case of vibrational interactions even if they involve the vibrations of the same type.

2.6.2 Hybrid formalism

The emergence of the hybrid formalism is related to several cases of molecules exhibiting two LAMs for which tunneling approach has produced unsatisfactory results [51]. The hybridizartion of the method means that it basically combines both "global" and "local" approaches.

The basic of the hybrid formalism is to couple a tunneling formalism for the large-amplitude back-and-forth motion with a standard internal rotation formalism for the large-amplitude rotatory motion of the methyl top. The principal conceptual difficulty in the hybrid formalism is caused by the loss of the concept of basis functions localized in the potential well of a given equilibrium framework.

For example, in the case of methylamine, there are six equivalent minima on the potential energy surface that represent six equivalent configurations connected with each other by tunneling motions (both torsional and inversion), see Figure 2.4. The horizontal minima in Figure 2.4 are connected by torsional motion, whereas the two rows at $+\gamma$ and $-\gamma$ are connected by inversion (wagging) motion. Since in the frame of the hybrid formalism, the internal rotation of the methyl top is treated globally, pictorially, this corresponds to not being able to draw arrows along a horizontal tunneling path from one minimum to another in

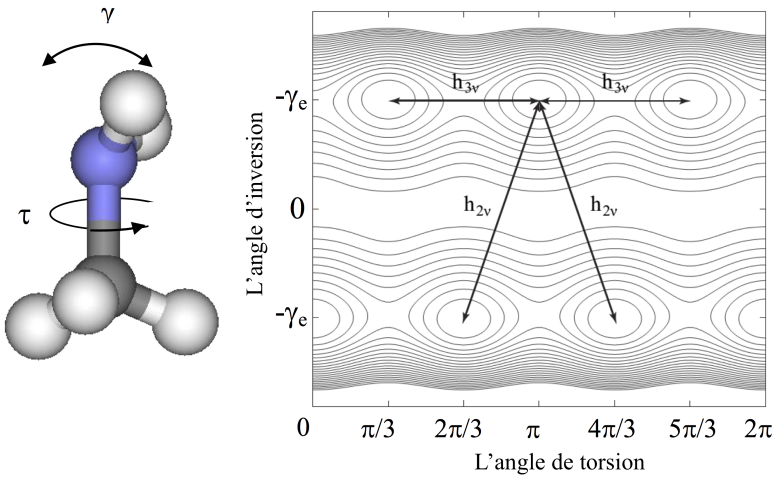

Figure 2.4: The structure of methylamine and the potential energy surface as a function of the torsional angle τ and inversion angle γ. The torsion of the methyl group (h_3v) and the inversion motion of the amino group (h_{2v}) are indicated by the arrows. The inversion of NH_2 must be followed by the rotation of CH_3 by $\pi/3$ thus coupling the two LAMs.

Figure 2.4. Because the concept of localized basis functions is not present in the traditional (i.e., nontunneling) internal-rotation formalism, a given internal-rotation function in the $+\gamma$ and $-\gamma$ parts of Figure 2.4 must be thought of as spread out over all three wells. Thus, the quantum mechanics of the hybrid formalism deals with tunneling from a "delocalized wavefunction".

The torsion-wagging-rotational hybrid Hamiltonian matrix H_{twr} is partitioned into four square submatrices, as shown in Eq. (1) of [52], with blocks noted by L(eft)L(eft), L(eft)R(ight), RL and RR:

$$[H] = \begin{bmatrix} LL & LR \\ RL & RR \end{bmatrix} \equiv \begin{bmatrix} B(+\gamma) & T \\ T^{+} & B(-\gamma) \end{bmatrix} \tag{2.47}$$

The terms "Right" and "Left" originate from the the right and left frameworks as a result of the OH hydrogen tunneling in methyl-malonaldehyde, the first molecule to which the hybrid method was applied [51]. In this case, the tunneling inversion motion is not associated with any physical motion of geometrical coordinate.

The diagonal blocks represents a torsion-rotation Hamiltonian matrix appropriate for a one-top molecule, essentially identical to the RAM Hamiltonian 2.40. Because of symmetry considerations, however, the internal rotation terms such as P_α and $\cos 3\alpha$ are only allowed

in the Hamiltonian when they are multiplied by the wagging coordinate γ. Whereas it may look as a pure mathematical trick, its physical meaning is to show the coupling between torsion and inversion motions. As it can be seen from Figure 2.4, to reach a minimum on the potential energy surface, the inversion of NH_2 must be followed by the rotation of CH_3 by $\pi/3$.

As explained in more detail in [51, 52], the dimension of the $B(+\gamma)$ submatrix is $n \times n$, with n given by the product $(2J+1)(nvt)$, where J is the quantum number of the rotational manifold being considered and nvt is the number of torsional functions retained in the second diagonalization step. The submatrix $B(+\gamma)$ again of dimension $n \times n$, represents the RAM matrix appropriate for a methylamine molecule with the amino group locked in the other of its two symmetrically equivalent equilibrium inversion positions. Matrix elements of the same magnitude are present in $B(+\gamma)$ and $B(-\gamma)$, but symmetry arguments require that the signs of certain terms be opposite in these two submatrices [51]. The $n \times n$ submatrix T and its transpose contain matrix elements associated with tunneling between the two positions of the amino group, as schematically illustrated by vertical arrowas in Figure 2.4. The operators giving rise to these tunneling matrix elements are similar to those that occur on the diagonal blocks, but symmetry arguments require certain differences [51].

2.7 Spectral assignment and fit

The spectral line assignment of rotational transitions indicates the technique for identifying specific energy levels involved in experimentally observed rotational transitions by comparing observed line frequencies to theoretical predictions. This process is made possible by quantum mechanical chemical calculations that provide a theoretical basis for energy levels and transitions in rotating molecules. The purpose of spectral assignment and analysis is to the study molecular structure and dynamics of molecules, which provide a summary of the physicochemical properties of molecules such as moment of inertia, bond lengths, bond angles, dihedral angles, quadrupole constants, etc. To visualize and assign the observed spectra, I used the “Java Spectrum Explorer" software developed by my scientific supervisor.

Various software (computer code) has been developed to fit the observed spectral transitions and estimate the spectroscopic parameters such as SPFIT, XIAM, Ram36_hf, etc. Such types of computer codes are based on the least-squares method. The least-squares method employs statistics to reduce the sum of the squares of the residuals in order to calculate the value of unknown parameters. The least squares approach is applicable to a wide range of functions, including linear, nonlinear, and complex functions. An appropriate technique is chosen on the basis of its efficiency, numerical stability, and ability to handle specific characteristics of the function or data.

2.7.1 The adjustment criteria for least-square method

A least-squares fit is an important tool for analyzing and modeling data. However, it is important to specify the adjustment criteria while using the least-squares approach in order to ensure that the line of best fit accurately represents the data. The adjustment criteria for the least square approach must satisfy the following standards:

- Residuals should be as small as possible. This indicates that the fitted line accurately represents the given data.
- Higher values of the coefficient of determination (R^2), which ranges from 0 to 1 represent a better fit. The coefficient of determination can be calculated as follows:

$$\begin{aligned} R^2 &= 1 - \frac{\text{Sum of squares of residuals}}{\text{Total sum of squares}} \\ &= \frac{\sum_i (y_i - f_i)^2}{\sum_i (y_i - \bar{y})^2} \end{aligned} \tag{2.48}$$

  where y_1,y_2,...,y_n) is the observed data, and f_1,f_2...,f_n) is the calculated data and $\bar{y}$ is the mean of the observed data. In a perfect scenario, the predicted and observed values are identical, resulting in $R^2 = 1$.
- The root mean square (rms) deviation is a measure of the average deviation between a set of observed values and calculated values. The standard error of the estimated parameters should be as small as possible. Mathematically, rms deviation can be expressed as:

$$rms = \sqrt{\frac{\sum_i (y_i^{obs} - y_i^{cal})^2}{N}} \tag{2.49}$$

where y_i^{obs} is the set of observed data, y_i^{cal} is the set of calculated data, and N is the total number of data points.

- The weighted root mean square (wrms) deviation is the unitless standard deviation that evaluates the goodness of fit for the given data. The wrms of the fit should be as small as possible ($\leq$ 1 usually suggests a fit within experimental accuracy). Mathematically, it can be expressed as:

$$wrms = \sqrt{\frac{1}{N}\frac{\sum_i (y_i^{obs} - y_i^{cal})^2}{\Delta_i}} \tag{2.50}$$

  where Δ_i is the experimental error.
- The estimated parameters should be statistically determined: p/Δp >10 where p is the value of an estimated parameter and Δp is the corresponding uncertainty.

A correlation matrix is an important tool for analyzing data and understanding the relationships between different parameters. A positive correlation coefficient indicates a positive relationship, a negative correlation coefficient indicates a negative relationship and a zero correlation coefficient indicates no relationship between the estimated parameters. A set of parameters with a high correlation coefficient may present duplicate information, and selecting one of them may be enough for the study. A correlation matrix can help to select the set of the most relevant parameters for a given set of data.

Usually, a larger number of rotational transitions between various energy levels and sub-levels is essential for determining the precise value of the Hamiltonian parameters (rotational and centrifugal distortion constants). The range of quantum numbers J and K_a also influences the number of Hamiltonian parameters. When a rotational transition with a bigger J and K_a quantum number is included in the fit, a larger number of higher-order parameters is found.

2.7.2 Linear least-squares method

The linear least-squares model estimates the relationship between dependent and independent variables by fitting linear function. It is one of the most widely used models. The increasing or decreasing trends of scatter-plot can be easily analysed with a straight line function.

For example, the linear equation having p parameters $\beta_j(j = 1, 2....p)$ and reference points $x_i(i = 1, 2....n, n \geq p)$. The n experimental data $y_i(i = 1, 2....n, n \geq p)$ can be expressed as:

$$y_i = f(\beta_j, x_i) \tag{2.51}$$

To determine the p unknown parameters, the linear least squares equation becomes [53]:

$$\boldsymbol{y} = \boldsymbol{X} \cdot \boldsymbol{\beta} + \boldsymbol{\epsilon} \tag{2.52}$$

where $\mathbf{X}$ is an $n \times p$ matrix called design matrix with known cofficient, $\boldsymbol{\beta}$ is unknown vector and $\boldsymbol{\epsilon}$ is unknown error. Then the residual $\boldsymbol{r}$ and the sum of the square of residuals S is

$$\begin{aligned} \boldsymbol{r} &= \boldsymbol{y} - \boldsymbol{X} \cdot \hat{\boldsymbol{\beta}} \\ S &= \boldsymbol{r}^{\intercal} \cdot \boldsymbol{r} = \sum_{i=1}^{n} (r_i)^2 = min \end{aligned} \tag{2.53}$$

where $\hat{\boldsymbol{\beta}}$ is the least-squares estimator of unknown vector $\boldsymbol{\beta}$. After minimizing the sum of the squares of residuals, the best-estimated values for the unknown parameters emerge as:

$$\boldsymbol{\beta} = (\boldsymbol{X}^{\intercal} \cdot \boldsymbol{X})^{-1} \boldsymbol{X}^{\intercal} \cdot y \tag{2.54}$$

The standard deviation σ can be expressed as:

$$\sigma = \sqrt{\frac{\sum_{i=1}^{n} (r_i)^2}{n - p}} \tag{2.55}$$

2.7.3 Non-linear least squares method

Nonlinear least squares fitting becomes necessary when there is a non-linear relationship between variables or when the function to be fitted is non-linear. In such a case, the trend of the data cannot be easily defined in terms of a linear straight-line function; instead, it may follow a range of non-linear functions such as exponential functions, logarithmic functions, trigonometric functions, power functions, Gaussian functions, and so on. However, optimizing a non-linear function through least squares is not a straightforward process. In the first step, non-linear functions are transformed into the linear form using techniques like series expansion, and then they are optimized using the least-squares method. The

values of unknown parameters are adjusted through repeated iterations until they reach convergence.

For example, if the relation between p parameters $\beta_j(j = 1, 2....p)$ and n experimental data $y_i(i = 1, 2....n, n \geq p)$ is not linear and cannot be made linear through coordinate transformations, the unknown parameters must be computed using an iterative approach:

$$\beta_j{}^{k+1} = \beta_j{}^{k} + \Delta\beta_j \tag{2.56}$$

Where k represents the iteration number, and $\Delta\beta$ is referred to as the shift vector. In each iteration, the model is made linear by approximating it with a first-order Taylor polynomial expansion centered around β^k.

When dealing with a highly nonlinear problem and the initial estimates are significantly distant from the actual values, the solution may diverge. In such a case, various techniques like the Gauss-Newton algorithm, the Levenberg-Marquardt algorithm, and trust-region approaches can be used, depending on the specific problem. Unlike the linear least squares method, the nonlinear least squares approach demands extensive computational effort.

In the following section, I will provide an overview of all the programs that I used to fit the experimental data during the present research.

2.8 Codes

2.8.1 SPFIT and SPCAT

The SPFIT and SPCAT programs were developed by H. Pickett [54, 55, 56] for fitting and analyzing rotational spectra of linear, symmetric top, and asymmetric top molecules. These programs are based on the Principal Axis Method (PAM). These days, this program is the most common tool for analysing high-resolution spectra and making spectral predictions from spectroscopic datasets for atmospheric and astronomical applications. These programs are capable of determining essential molecular constants such as rotational and centrifugal distortion constants, and they offer insights into the structural and dynamic properties of molecules. SPFIT is a program used to fit experimental spectral lines with a theoretical model, allowing for the determination of molecular or atomic parameters. The

SPCAT program is specialised software used in spectroscopy to predict the frequencies and strengths of spectral lines. The SPFIT/SPCAT program has specific input and output files, as described below:

SPFIT Input

- **.par:** It includes parameter values such as rotational constants and distortion constants with parameter uncertainty. Each parameter is indicated with a unique code. It also contains the maximum number of parameters and the maximum number of iterations.
- **.lin:** This input file likely contains a listing of transitions. These transitions are typically the observed or experimental spectroscopic data, which provide the basis for the analysis conducted by the program.

SPFIT Output

- **.bak:** This is a backup file. It is created at the start of each fitting run and serves as a copy of the original.par file. This backup preserves the initial state and settings of the program before any modifications are made during the fitting process.
- **.par:** The modified .par file is an output that contains the updated or modified constants resulting from the fitting run. These constants have been adjusted or refined based on the program's analysis of the experimental data.
- **.var:** Similar to the .par file, the .var file also contains constants, but it includes information about errors and variance-covariance. This additional information is often necessary for further analysis and may be intended for use in the SPCAT program.
- **.fit:** This file is the main output file. It typically contains the primary results of the fitting run, such as the refined parameters, transition line positions, and intensities that best fit the experimental data.
- **.bin:** This is a binary output file. It contains parameters and variances, which can be used by a predictive program. However, it is noted as "obsolete," suggesting that it may not be the preferred or actively used output format.

SPCAT Input

- **.var:** Similar to the .par file, this file also contains constants, but it includes information about errors and the correlation matrix. which describes the relationships between different constants and their uncertainties, helping to understand how changes

in one constant might affect others.

- **.int:** This file is used to specify the value of the dipole moment components and partition function. The dipole moment information is crucial for the calculation of line intensities, as it determines how strongly a given transition (e.g., rotational or vibrational) will absorb or emit electromagnetic radiation.
- **.bin:** This file represents the binary version of parameters and variances generated by a previous run of the program. It can be used to store and reuse results from previous calculations, which can save time and resources when rerunning SPCAT for the same or similar systems.

SPCAT Output

- **.out:** This is the main output file that SPCAT produces, and it typically includes a block-by-block listing of various pieces of information, such as energy levels correspond to different quantum states, such as rotational, vibrational, or electronic states; lists of the predicted frequencies of spectral transitions between different energy levels.
- **.cat:** This file is a catalog file that typically contains information about the calculated transitions only, which includes the frequency of the line, the $\log_{10}$ of the integrated cross-section in the units of nm^2MHz/molecule sorted by frequency, lower state energy in wavenumbers, upper state degeneracy, etc.
- **.str:** This file provides details about the transition dipole moments, which are essential for understanding the intensity or strength of the spectral lines. It can also include information about the direction of the dipole moment.
- **.egy:** This file contains information about energy levels, derivatives, and eigenvectors. This information is critical for understanding the quantum mechanical properties of the system.

In the input `.par` file for the SPFIT, and `.var` file for the SPCAT program, each model parameter is determined by a sequence of integer numbers that is composed from right to left. Specifically, for rotational Hamiltonian parameters, one can represent a sequence (from right to left) in the following order:

- `v1`: lower energy state identifier
- `v2`: upper energy state identifier

- NSQ: power of $\hat{J}^2$.
- KSQ: power of $\hat{J}_z^2$.
- TYP: projection type, where 0 stands for a scalar, 1 corresponds to J_x^2, 2 is forJ_y^2, and 3 represents J_z^2. Additionally, for values 3 and above, it signifies a combination of J_x^2 and J_y^2 with a factor of $2n$, where n can be any integer from 1 to 9.

Using the rules presented above, we can easily code the parameters of the Watson's A-reduction Hamiltonian (2.12) which are summarized in Table 2.4 (along with the codes for quadrupole coupling Hamiltonian).

Table 2.4: List of main parameters and their codes in .par and .var files of the SPFIT/SPCAT programs

Code	Parameter	Code	Quadrupole constants
10000	A	110010000	$3/2\chi_{aa}$
20000	B	110020000	$3/2\chi_{bb}$
30000	C	110030000	$3/2\chi_{cc}$
200	$-\Delta_J$	110040000	$(\chi_b - \chi_c)/4$
1100	$-\Delta_{JK}$	110610000	χ_{ab}
2000	$-\Delta_K$	110210000	χ_{bc}
40100	$-\delta_J$	110410000	χ_{ac}
41000	$-\delta_K$		

2.8.2 XIAM

XIAM code based on the extended Internal Axis Method (or Combined Axis Method: CAM) [57]. It can predict and fit the rotational spectra of an asymmetrical top molecule with up to three symmetrical internal rotors and one quadrupolar nucleus. The program also allows us to analyze the pure rotational spectra of centrifugal distortions up to the sixth order. The main disadvantage of XIAM is its failure to deal with low-barrier cases [58]. In addition, because this code is based on a so-called local approach, the interactions between each of the torsional states are not well addressed. Despite these limitations, the program was employed in the initial stages of the CH_3COCl analysis to fit existing data and generate initial predictions.

Table 2.5: List of important parameter indices and names used in the XIAM program

Key code	Constants[a]	comments
BJ	0.5 (B_x + B_y)	B_x,B_y,B_z are the rotational constants
BK	B_z - 0.5 (B_x + B_y)	
B-	0.5 (B_x - B_y)	
DJ	Δ_J	4th order centrifugal distortion
DJK	Δ_{JK}	
DK	Δ_K	
dj	δ_J	
dk	δ_K	
chizz	χ_{zz}	Quadrupole coupling constants
chixy	χ_{xy}	
chixz	χ_{xz}	
chiyz	χ_{yz}	

[a]Rotational and quadrupole coupling constants

The XIAM input file is divided into seven blocks. Each block is separated from another by an empty line, and each block has a unique meaning. In particular, the parameters to fit are given in block n°3. Contrary to SPFIT/SPCAT these parameters are "hard coded" by names, so their choice is rather limited. The main parameters are summarized in Table 2.5.

2.8.3 RAM36 and RA36hf

The programs are developed by Vadim Ilyushin [40, 59, 60]. They are based on the Rho Axis Method (RAM) Hamiltonian. These codes aim to deal with two common internal rotation cases [61]:

- Sixfold rotation case with a C_{3v} internal rotor and a C_{2v} frame (such as toluene and nitromethane)
- Threefold rotation case with a C_{3v} internal rotor and a C_s frame (such as acetic acid, acetamide, or methyl formate)

Compared to RAM36, RAM36hf code includes also the terms of nuclear quadrupole cou-

pling Hamiltonian for a single quadrupolar atom. The advantage of the RAM Hamiltonian is that it allows for simultaneous fits over the internal rotation species (A and E) and also the transition from different torsional states. Since it relies on a global approach, it provides a single set of parameters by fitting the rotation spectra from the ground state as well as from the different excited torsional states.

This tool has been used for analyzing the spectra of different molecules including an internal rotor for both high barrier [44] and low barrier cases.

In the input file for both codes, each torsional-rotational energy level is labeled with the quantum numbers m, J, K_a, and K_c. The free-rotor quantum number m is used to label the torsional energy levels for each symmetry species (A and E) from the ground state ($v_t = 0$) to the second excited state (vt = 2) as follows:

- A species: $v_t = 0 \rightarrow m = 0$; $v_t = 1 \rightarrow m = -3$; $v_t = 2 \rightarrow m = 3$
- E species: $v_t = 0 \rightarrow m = 1$; $v_t = 1 \rightarrow m = -2$; $v_t = 2 \rightarrow m = 4$

As for SPFIT/SPCAT programs, the model parameters in RAM36/RAM36hf are coded using a set of seven integer numbers. The Hamiltonian used in this program is written in the following form:

$$\begin{aligned} H = & \frac{1}{2} \sum_{knpqrs} B_{knpqrs0}[J^{2k} J_z^n J_x^p J_y^q p_\alpha^r \cos(3s\alpha) + \cos(3s\alpha) p_\alpha^r J_y^q J_x^p J_z^n J^{2k}] \\ & + \frac{1}{2} \sum_{knpqrt} B_{knpqr0t}[J^{2k} J_z^n J_x^p J_y^q p_\alpha^r \sin(3t\alpha) + \sin(3t\alpha) p_\alpha^r J_y^q J_x^p J_z^n J^{2k}] \end{aligned} \tag{2.57}$$

where

- $B_{knpqrst}$: fit parameters
- J_z, J_y, J_x: components of total angular momentum $\hat{J}$
- p_α: the angular momentum conjugate to the internal rotation angle α

This Hamiltonian allows parameters up to order 12 to be included. The parameters are encoded by a set of integers numbers, which are the powers of the operators of the the above Hamiltonian such as:

- k (the first integer) corresponds to the power of J^2
- n (the second integer) corresponds to the power of J_z
- p and q are the powers of J_x and J_y, respectively
- r is the power of p_α

- s defines the argument of $\cos(3s\alpha)$
- t defines the argument $\sin(3t\alpha)$

By comparing the Hamiltonian in the (2.57) with the explicit expressions for RAM Hamiltonian terms in (2.23), (2.41), and (2.42), one can rather easily deduce the codes for parameters like: $A_{RAM} = B_{0200000}$, $B_{RAM} = B_{0020000}$, $D_{ab} = B_{0110000}$, $V_3/2 = B_{0000000} + B_{0000010}$, $V_6/2 = B_{0000000} + B_{0000020}$ etc.

The only difference is the coding of F and ρ parameters. These second order parameters occur in the RAM Hamiltonian in the form $F(p_\alpha - \rho J_z)^2 + A_{RAM} J_z^2$. The $F(p_\alpha - \rho J_z)^2 + A_{RAM} J_z^2$ part of the Hamiltonian may be regrouped (as it was done for example in [40] to reduce a correlation between main parameters) as :

$$H_T = F p_\alpha^2 - 2F\rho p_\alpha J_z + A_{eff} J_z^2, \tag{2.58}$$

where $A_{eff} = A_{RAM} + F\rho^2$ and $F\rho^2$ is a modification of the rotational constant A due to internal rotation. The $F\rho^2$ modification is negligible when ρ value is small, as it is the case of the acetyl halides studied in the frame of this thesis. In the RAM36/RAM36hf codes, the mixed internal angular momentum expression $p_\alpha - \rho J_z$ which overtly resembles coupling between internal and overall rotation is used only in the second order of the RAM Hamiltonian. This give us unbiased A rotational constant which can be compared to some theoretical value after transforming from RAM to PAM axis system. In the higher orders of RAM Hamiltonian (fourth, six etc.), RAM36 does not allow at the moment mixed angular momentum expression $p_\alpha - \rho J_z$ and all corresponding terms contain just powers of internal rotation angular momentum p_α [62]. As such, F and ρ parameters are coded using regrouped expression (2.58) as: $F = B_{0000200}$, and $\rho = B_{0100100}$. In this case, ρ is unitless.

An example of list main parameters with the encoding of the set of 7 integers (k, n, p, q, r, s, and t) in the input file of *RAM36hf* code is shown in Table 2.6:

In addition to the code, each parameter is identified by an integer in the next to last column (`Diag.`) that corresponds to the diagonalization stage where this parameter is introduced. For usual RAM Hamiltonian parameters this value is set to 1 for F, ρ, and V_3 or 2 for the others. The quadrupole coupling parameters are identified with -1, and molecular dipole moment components with 0.

Table 2.6: List of important parameter used in the *RAM36hf* program for CH_3COCl molecules

Name	k	n	p	q	r	s	t	Values (cm^{-1})	Diag.	ifit
muz ,	0,	1,	0,	0,	0,	0,	0,	0.12080789999999999E+01 ,	0,	0,
mux ,	0,	0,	1,	0,	0,	0,	0,	0.25343306000000001E+01 ,	0,	0,
chi_aa ,	0,	2,	0,	0,	0,	0,	0,	0.11116488470502660E-01 ,	-1,	0,
chi_aa ,	0,	0,	0,	2,	0,	0,	0,	-0.10000000000000000E+01 ,	-1,	-1,
chi_cc ,	0,	0,	2,	0,	0,	0,	0,	-0.61102298781060636E-02 ,	-1,	0,
chi_cc ,	0,	0,	0,	2,	0,	0,	0,	-0.10000000000000000E+01 ,	-1,	-1,
chi_ab ,	0,	1,	1,	0,	0,	0,	0,	-0.13556867568840798E-01 ,	-1,	0,
F ,	0,	0,	0,	0,	2,	0,	0,	0.50891436839940134E+01 ,	1,	0,
RHO ,	0,	1,	0,	0,	1,	0,	0,	0.34504412456834256E-01 ,	1,	0,
0.5V3 ,	0,	0,	0,	0,	0,	0,	0,	0.20914700134381650E+03 ,	1,	0,
0.5V3 ,	0,	0,	0,	0,	0,	1,	0,	-0.10000000000000000E+01 ,	1,	-1,
A ,	0,	2,	0,	0,	0,	0,	0,	0.27931686968921465E+00 ,	2,	1,
B ,	0,	0,	2,	0,	0,	0,	0,	0.16053757989824363E+00 ,	2,	1,
C ,	0,	0,	0,	2,	0,	0,	0,	0.78548991331128054E-01 ,	2,	1,
DAB ,	0,	1,	1,	0,	0,	0,	0,	-0.20545916335568623E+00 ,	2,	0,
-DJ ,	2,	0,	0,	0,	0,	0,	0,	-0.22577700181554139E-07 ,	2,	1,
-DJK ,	1,	2,	0,	0,	0,	0,	0,	0.00000000000000000E+00 ,	2,	0,
-DK ,	0,	4,	0,	0,	0,	0,	0,	-0.37147828706945773E-06 ,	2,	1,
-2*dj ,	1,	0,	2,	0,	0,	0,	0,	-0.99865201688915003E-08 ,	2,	1,
-2*dj ,	1,	0,	0,	2,	0,	0,	0,	-0.10000000000000000E+01 ,	2,	-1,
-2*dk ,	0,	2,	2,	0,	0,	0,	0,	-0.11772296876184008E-07 ,	2,	1,
-2*dk ,	0,	2,	0,	2,	0,	0,	0,	-0.10000000000000000E+01 ,	2,	-1,

The integer value in the last column (`ifit`) sets the corresponding parameter to vary `ifit=1`, or fixes it to the given value, `ifit=0`. It also allows one to group Hamiltonian terms and fit a coefficient in front of a group of terms connected by a fixed linear relationship. As an example, we may consider the $-2\delta_J$ term in Table 2.6. It is coded in two lines that encode $J^2\left[J_x^2, J_y^2\right]$ term. The first line encodes J_x^2, the second line encodes J_y^2. The parameter value in the second line fixes the relationship between J_x^2 and J_y^2 (in our case the second line is subtracted from the first line i.e. the value is -1.0). The parameter value in the first line is the actual value of the composite parameter which is fit. The last column in the second line contains the integer -1, which says that the parameter value by which the J_y^2 term should be multiplied is taken from previous line (so we take the parameter value from the previous line and multiply it by the "parameter value" from current line (in our case this is -1.0) and we get the parameter which will go with J_y^2 in the Hamiltonian matrix). In general a group is not limited to two terms and in this case, the `ifit` decreases each time by 1 with each

new line, so that the parameter value (before modification) is always taken from the first line of the groupe.

The RAM36/RAM36hf programs are versatile in handling data in both MHz and cm^{-1} and offer a standard least squares fit, weighting data by the inverse of the squared measurement uncertainties. The programs have a unique feature for handling blended transitions, treating transitions with the same frequency by averaging their calculated intensities to match observed values. The RAM36hf has also an option to deal with hyperfine-free rotational transitions together with hyperfine components. For hyperfine-free transitions, in the input file, the F quantum number value is set to -1. It is a very convenient feature, as in this case, the input file is greatly simplified. For example, in the case of $I = 3/2$ for acetyl chloride and acetyl bromide, there are at least 4 strong hyperfine components that have to be given in the input file for each rotational transition. Instead, for hyperfine-free transition one can set $F = -1$ in a single line.

Additionally, the program provides two extra fitting options: robust fitting, based on a specific weighting scheme, and the ability to set a cut-off for the difference between observed and calculated values, excluding data points beyond the cut-off during fitting. Moreover, the program offers a prediction option for calculating spectra within specified quantum numbers and frequency ranges. It is particularly useful for low-barrier cases, where standard asymmetric-rotor selection rules may not apply effectively. In these cases, the program calculates all possible $\Delta K_a, \Delta K_c$ transition frequencies and intensities permitted by symmetry for a given pair of upper and lower-state J values, displaying transitions with intensities above a user-defined threshold. This approach provides a more accurate guide for determining line strengths. The program was used in the final fitting process for the molecules CH_3COCl and CH_3COBr. It was applied to fit experimental data and generate precise predictions.

Chapter 3

Spectroscopy of molecules with one periodic large amplitude motion

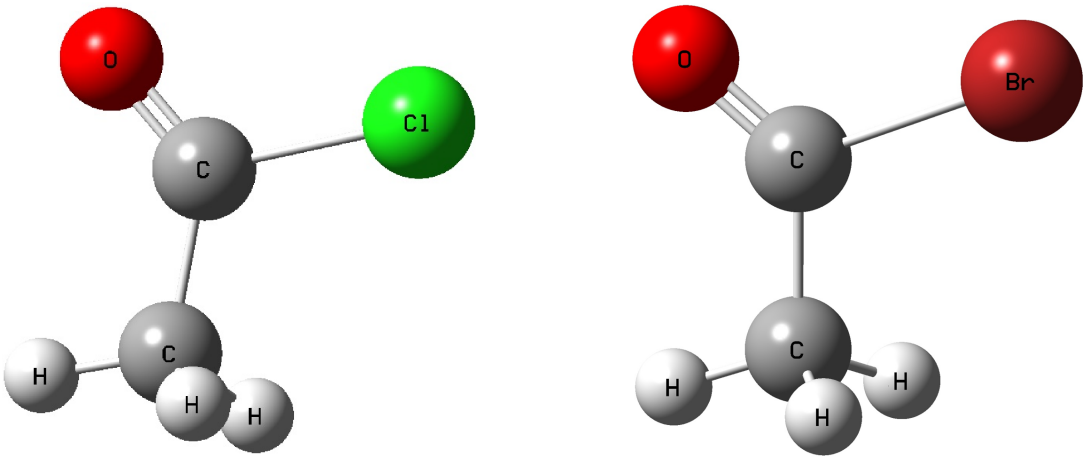

(a) (b)

Figure 3.1: Structure of (a) acetyl chloride (b) acetyl bromide

3.1 Acetyl halides

3.1.1 Introduction

The atmosphere is a complex system that interacts with numerous chemical compounds, including volatile organic compounds (VOCs) [63] and halogenated species [64]. Among these, acetyl halides, comprising acetyl chloride (CH_3COCl) and acetyl bromide (CH_3COBr), have garnered increasing attention in recent years due to their significant implications for atmospheric chemistry. Acetyl halides, such as CH_3COCl and CH_3COBr, can be emitted into the environment from a variety of sources. These sources include biological processes (marine microorganisms and algae), volcanic activity, industrial operations and chemical synthesis, biomass burning, fossil fuel combustion, waste disposal, landfills, and so on. Such halides are versatile compounds that are used in a variety of industrial processes. They possess unique chemical reactivity and can undergo a range of transformations in the atmosphere, ultimately influencing air quality, climate, and the delicate balance of Earth's ecosystems.

One key aspect of acetyl halides lies in their propensity for hydrolysis, reacting readily with water to form acetic acid and the corresponding hydrogen halide [65]. This hydrolytic process releases strong acids into the atmosphere, which can significantly impact the acidity of rainwater, leading to acid deposition and adverse effects on terrestrial and aquatic

ecosystems [66, 67, 68]. Additionally, HCl takes part in several hazardous atmospheric processes [69]. The photolysis of acetyl halides induced by solar radiation represents a crucial mechanism for the release of halogen radicals into the atmosphere [70, 71, 72].

$$\begin{aligned} \mathrm{CH_3COCl} + h\nu - UV\ light &\rightarrow \mathrm{CH_3CO^{\bullet}} + Cl^{\bullet} \\ \mathrm{CH_3COBr} + h\nu - UV\ light &\rightarrow \mathrm{CH_3CO^{\bullet}} + Br^{\bullet} \end{aligned} \tag{3.1}$$

These radicals, in turn, contribute to the depletion of stratospheric ozone, leading to the formation of the notorious "ozone hole" and the subsequent increase in harmful ultraviolet radiation reaching the Earth's surface [67].

Furthermore, acetyl halides can engage in reactions with atmospheric radicals such as hydroxyl radicals (OH), predominantly in the troposphere [70, 71, 73]. These reactions contribute to the formation of secondary organic aerosols (SOAs), which are key components of atmospheric particulate matter and have implications for air quality, visibility, and human health. Additionally, the interaction of acetyl halides with nitrogen oxides (NOx) yields organic nitrates, which act as reservoirs for reactive nitrogen species in the atmosphere, further influencing air quality and participating in the complex photochemical processes that lead to the formation of photochemical smog [70, 74]. The reaction with photochemically produced hydroxyl radicals can destroy vapor-phase acetyl chloride in the environment; the half-life for this reaction in air is estimated to be 5 years. [75, 76].

3.1.2 Motivation

The spectroscopic analysis of acetyl chloride mm-wave and sub-mm-wave plays an essential role in providing detailed information about the rotational behaviour of molecules. This information aids in the understanding of the molecular structure, conformational dynamics, and intermolecular interactions, contributing to a broader understanding of its properties and behaviour in various chemical and atmospheric processes. There have been microwave studies conducted on acetyl chloride [77, 78] and acetyl bromide [79], focusing primarily on the molecular structure. However, these studies have not provided sufficient insight into the internal rotation of the methyl groups, and they are also limited in terms of quantum numbers range. A substantial portion of the rotational spectra of these molecules fall within the millimeter or sub-millimeter wavelength range, but as of the latest available in-

formation, there are no experimental measurements conducted in this specific wavelength range.

The main objective of this study is to perform a spectroscopic study of acetyl chloride in the mm/sub-mm-wave range. Our primary interest is the accurate determination of the barrier to internal rotation of the methyl top and the accurate description of torsional potential energy.

3.2 Spectroscopy of acetyl chloride

3.2.1 Experimental details

In the present study, we performed a new series of measurements of the rotational spectrum of acetyl chloride. All the spectra were recorded in absorption mode using the FLASH spectrometer [23, 24].

The measurements included two frequency ranges: one spanning from 50-110 GHz and another from 150-330 GHz. We utilized a commercial sample of acetyl chloride with a purity level of 99 %. All measurements were consistently conducted under room-temperature conditions. To achieve the best signal-to-noise ratio (S/N) in the recorded spectra, we maintained an optimal gas pressure inside the absorption cell, typically ranging between 10 and 20 µbar, with higher pressures favored at higher frequencies. The stability of acetyl chloride molecules allowed us to easily sustain a constant pressure for several hours. Consequently, our experiments were conducted within a closed-cell configuration, ensuring a controlled environment that maintained stable pressure and consistent conditions throughout the experiment. This meticulous approach contributed to the reliability of our results. The absorption spectra are recorded using zero-bias Schottky diode detectors from VDI. Due to the partially resolved or unresolved nuclear quadrupole hyperfine structure, the measurement uncertainty is estimated to be around 50 kHz for relatively strong isolated lines and 100 kHz for weak or slightly distorted line shapes.

All spectra are assigned using the programming package Java Spectrum Explorer (JSE) created by my scientific supervisor. The spectral line fitting and generation of spectral

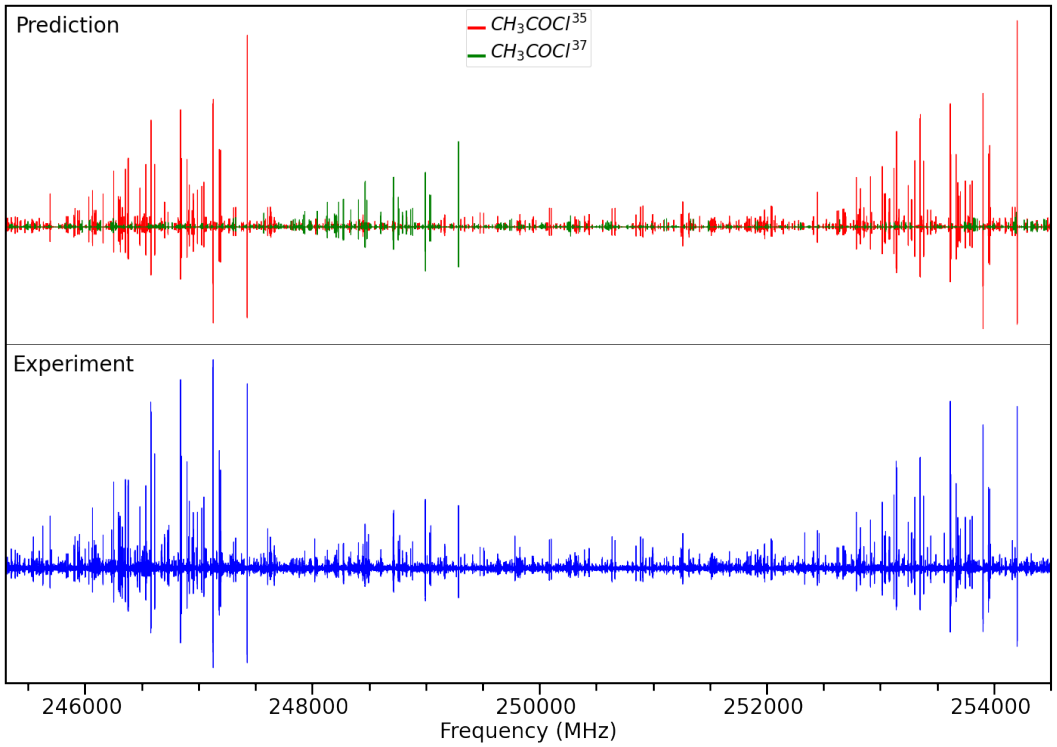

Figure 3.2: A portion of the rotational spectra of CH_3COCl measured between 245 and 255 GHz.

prediction were performed using the *RAM36hf* software package, as described in Section 2.8.3.

3.2.2 Spectral analysis

The rotational spectra of CH_3COCl in the mm/sub-mm wave regions are dominated by R-type transitions. Since $\mu_b > \mu_a$ (ab initio value of $\mu_a = 1.21$ and $\mu_b = 2.59$), b-type transitions are significantly more intense than a-type transitions. The natural abundance of ^{35}Cl is about 75 % and that of ^{37}Cl is about 25 % [80]. Hence, the rotational spectra for CH_3COCl^{35} are roughly 3 times more intense than those for CH_3COCl^{37} and the contribution of each isotopologue. Figure 3.2 shows a portion of the rotational spectra of CH_3COCl.

The initial analysis began with the SPCAT and SPFIT programs [54]. The rotational parameters for this analysis were obtained from previous studies [77, 78], and rotational distortion parameter were obtained from ab initio calculations. At this time, I focused only on the A symmetry species using the semi-rigid rotor approximation. This approach allowed for the successful assignment of a few experimental spectra, particularly those with low K_a transitions. However, I had difficulties generating reliable predictions for higher K_a lines. At this point, it becomes obvious that the internal rotation of CH_3 should be taken into account to continue the analysis.

Consequently, in the second step of the analysis, the *XIAM* program (described in Section 2.8.2) was used. We focused on assigning and fitting A and E symmetry species as well as hyperfine components. The results of this analysis were satisfactory for lower K_a values. However, using this program, I was unable to generate reliable spectral predictions at higher K_a values, especially for hyperfine components. Since *XIAM* is limited by the number of torsion-rotation parameters; it can only fit three torsion-rotation parameters, which is not sufficient for this molecule. Finally, we switched to the *RAM36hf* program, based on the RAM framework (described in Section 2.8.3). The *RAM36hf* program possesses the capability to account for both internal rotation splitting and hyperfine splitting effects. The experimental parameters obtained from *XIAM* were used as an initial parameter for the *RAM36hf* after the rotation to the rho-axis system in an anti-clockwise direction. From the result of *XIAM* fits, the angle of rotation in ab plane θ_{RAM} is 38.9° for ^{35}Cl and 38.6° for ^{37}Cl. The fitting begins with low K_a transitions and a small set of parameters,

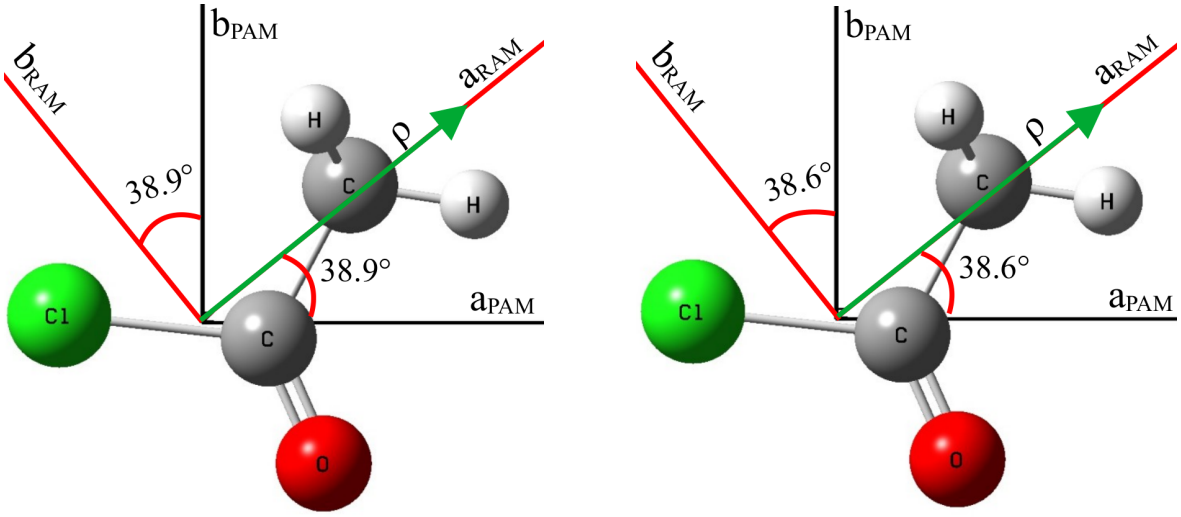

Figure 3.3: A comparison of the principal axes and the rho-axis systems, along with the ρ vector and rotation angles (a) CH_3COCl^{35} molecule (b) CH_3COCl^{37} molecule

which generate a new spectral prediction and allow for the assignment of new lines. This process is repeated several times by adding new lines and releasing new parameters. The fit includes both the mm sub-mm wave spectra from the present work as well as previous microwave spectra by Sinnott and by Hayashi et al. [77, 78].

The barrier to internal rotation in CH_3COCl is of intermediate height: 421.0 cm^{-1} for CH_3COCl^{35} and 419.4 cm^{-1} for CH_3COCl^{37}. Because the rotation of the methyl group is coupled to the rotation of the entire molecule, the energy levels of a molecule are split into two sub-levels of A and E symmetry species of the C_{3v} symmetry point group. For a given torsional state, the separation between A and E sub-levels depends primarily on barrier height, ρ parameter value, and K_a quantum number (see (2.41)). For acetyl chloride, at low K_a values the separation between the A and E components is small, typically on the order of kHz, so individual A and E components can be unresolvable in Doppler-limited resolution of conventional absorption spectra. However, as the quantum number K_a increases, the separation between the A and E components becomes more distinct. At high K_a, the energy difference between these components can be several megahertz (MHz) or even more, leading to well-separated lines in observed spectra.

Figure 3.4 demonstrates the dependence of the energy spacing between the A and E components on the quantum number K_a showing how the separation increases as K_a be-

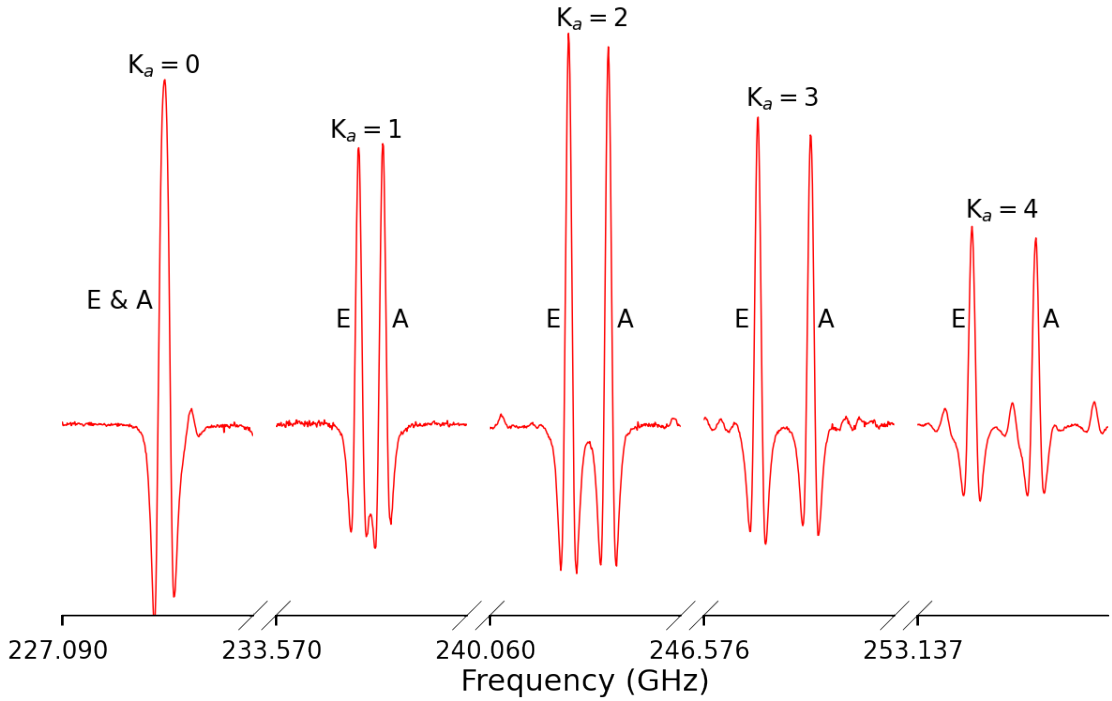

Figure 3.4: The relationship between torsional $A - E$ splittings A (spacing between A and E symmetry species components) and the quantum number K_a for the transition $33_{Ka,33-Ka} = 32_{Ka,32-Ka}$ of CH_3COCl^{35} molecule. The frequency axis is divided into five segments that begin at different frequencies but have an identical frequency span of 10 MHz.

comes larger. This behaviour is a fundamental aspect of the spectroscopy of molecules with methyl rotors and is valuable in understanding their rotational energy levels and transitions.

Upon torsional excitation, the tunneling splitting increases so the A and E components become further separated. In the present work, we observe splitting due to internal rotation in both the ground and lowest excited torsional states. $A - E$ splitting of rotational transition is in the order of 1 MHz in the ground state and increases exponentially to the order of 50 MHz in the first excited torsional state and 500 MHz in the case of the second excited torsional state. The comparison of the torsional splittings of ^{35}Cl and ^{37}Cl on the $v_t = 0, 1, 2$ states for a particular transition ($23_{1\,22} \leftarrow 22_{2\,21}$) is shown in Figure 3.5.

Due to the nuclear spin $I = 3/2$ and the non-spherical distribution of electric charge in Cl atom, we observe the nuclear quadrupole hyperfine structure. Each J level is split into four sublevels with a total quantum number of $F = |J - I|$ to $J + I$. In accordance with the selection rule only the transition with $\Delta J = 0, 1$ and $\Delta F = -1, 0, 1$ are allowed.

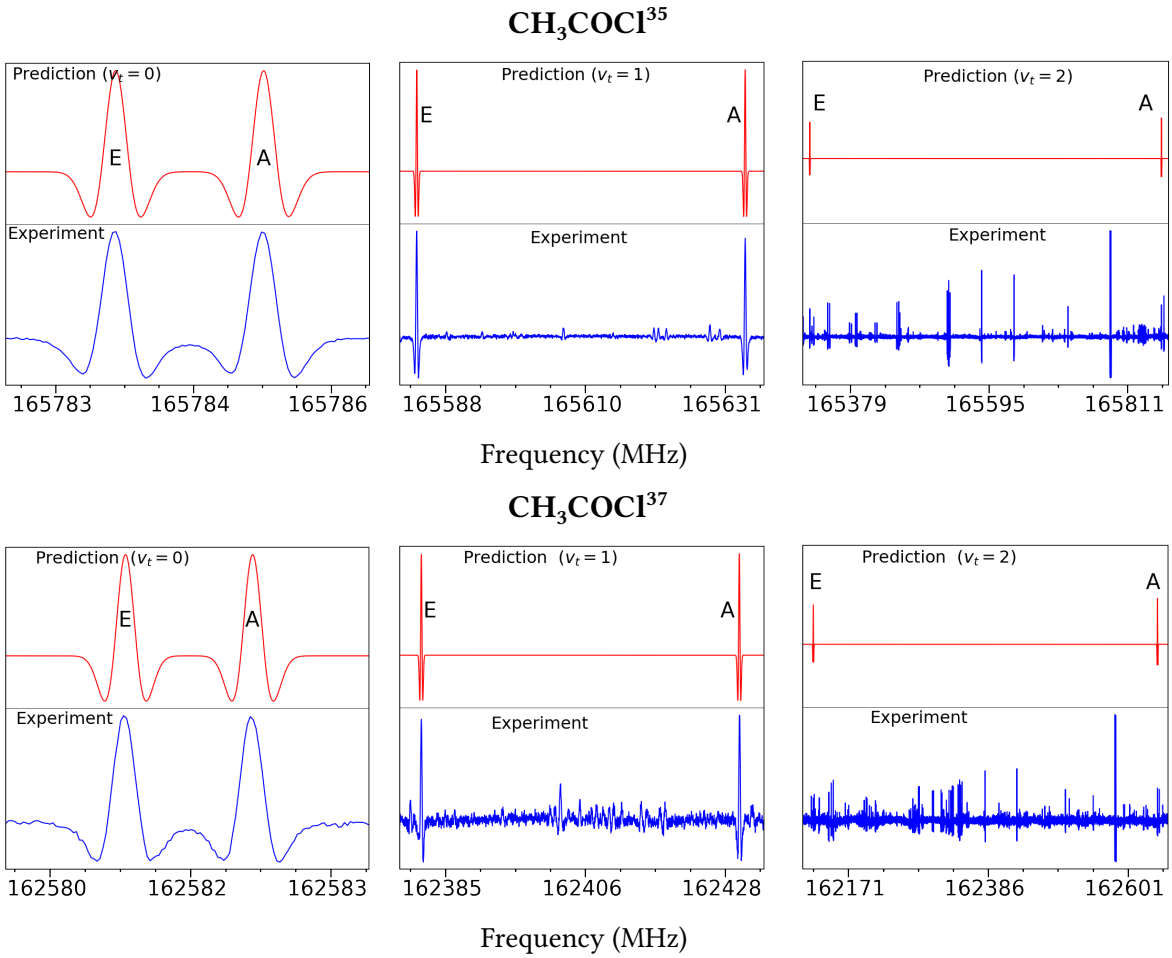

Figure 3.5: Comparing the torsional $A - E$ splitting in the ground state, the first excited state, and the second excited state for the identical transitions ($23_{1\,22} \leftarrow 22_{2\,21}$) in CH_3COCl^{37} and CH_3COCl^{37}

Only strong components with the selection rules $\Delta J = \Delta F$ are observed among all possible transitions. For the ground state spectra of CH_3COCl^{35}, we are able to resolve all four components distributed among two distinct frequency lines, as shown in Figure 3.6a. Out of the four hyperfine components, we observed only two distinct frequencies. The transitions represented by $J' + I - 1 \leftarrow J'' + I - 1$ and $J' - I + 1 \leftarrow J'' - I + 1$ are observed within one observed frequency component, while transitions $J' + I \leftarrow J'' + I$ and $J' - I \leftarrow J'' - I$ are observed within another observed frequency, as shown in Figure 3.6b. In the first case, one may also note relative intensities distribution among hyperfine components that allow their unambiguous assignment.

In this study, the hyperfine structure of both isotopologues was analysed, which involved a total of 5390 hyperfine components for the CH_3COCl^{35} and 178 components for

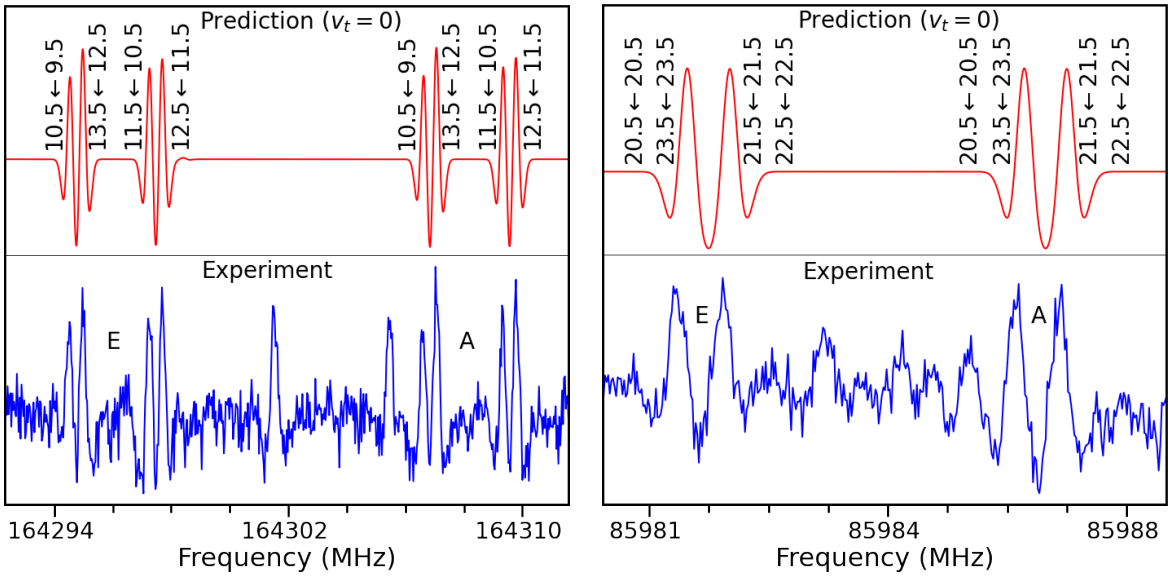

(a) (b)

Figure 3.6: Hyperfine components resulting from nuclear quadrupole interactions that have been observed in the ground state for (a) the $12_{6\,7} \leftarrow 11_{5\,6}$ transition in CH_3COCl^{35} and (b) the $22_{8\,15} \leftarrow 22_{7\,16}$ transition in CH_3COCl^{37}.

CH_3COCl^{37}. Most of the observed hyperfine components are separated by around 1 MHz in frequency. Hyperfine splitting was observed in the ground and in the first excited torsional states. In the $v_t = 2$, state due to decreased intensity of transitions we could assign only the strongest ones with unresolved hyperfine splittings. To correctly assign hyperfine transitions, we used relative intensities considerations. Whereas the difference in the relative intensities of individual hyperfine components is rather limited, we were able to distinguish between different pairs of closely lying components as it is demonstrated in Figure 3.6a.

The assignments performed in this study include R- and Q-branch transitions for both the ground state and the first torsionally excited state, and only the R-branch transitions for the second torsionally excited state. To provide a comprehensive analysis, a global fit was conducted, which integrated transitions from $v_t = 0$, $v_t = 1$, and $v_t = 2$. The particularity of the RAM Hamiltonian applied to acetyl chloride is that due to a large θ_{RAM} value, upon the rotation to the rho-axis system, the off-diagonal χ_{ab} parameter of the quadrupole coupling tensor becomes larger than diagonal elements χ_{aa} and χ_{bb}. Since we did not assign any $\Delta F \neq \Delta J$ hyperfine components due to their weak intensities, we kept χ_{ab} fixed in the fit. It should be also noticed that the values of the quadrupole coupling tensor ele-

Table 3.1: The results of a fit of 11326 transitions, including the rms value for A and E symmetry species for each torsional state for both isotopologues CH_3COCl^{35} and CH_3COCl^{37}.

Transitions	CH_3COCl^{35}				CH_3COCl^{37}			
	Lines[a]	RMS[b]	WRMS[c]	n[d]	Lines[a]	RMS[b]	WRMS[c]	n[d]
$v_t = 0, 1, 2$	9167	0.067 MHz	0.68	37	2159	0.079 MHz	0.76	33
A species[e]	4904	0.090 MHz	-	-	1085	0.083 MHz	-	-
E species[f]	4263	0.073 MHz	-	-	1074	0.085 MHz	-	-
Torsional state								
	qn[g]	Lines[a]	RMS[b]		Lines[a]	RMS[b]		
$v_t = 0$	m=0	3670	0.084 MHz		632	0.096 MHz		
	m=1	3143	0.069 MHz		622	0.096 MHz		
$v_t = 1$	m=-3	1048	0.111 MHz		288	0.065 MHz		
	m=-2	935	0.078 MHz		295	0.065 MHz		
$v_t = 1$	m=3	186	0.072 MHz		165	0.044 MHz		
	m=4	185	0.099 MHz		157	0.072 MHz		

[a]Number of transitions included in the fit.
[b]Root-mean-square residual for the lines in this row.
[c]Weighted root-mean-square residual for the lines in this row.
[d]Number of parameters included in the fit.
[e]A symmetry species.
[f]E symmetry species.
[g]New quantum number defined in *RAM36hf* code to define A and E symmetry species for each torsional state.

ments presented in Table 3.2 were determined in the framework of the RAM Hamiltonian and then were rotated back to the principal axes system. This is done for a straightforward comparison with the values of Hayashi et al. [78]

The results of the final fit with their RMS for each torsional state for both isotopes are shown in Table 3.1. For CH_3COCl^{35}, a total of 9167 transitions with 4751 measured line frequencies were assigned in the mm/sub-mm wave range. This analysis involved the determination of 37 rotation-torsion parameters in the fitting process. The root mean square (rms) deviation of 67 kHz and a unitless weighted root mean square (wrms) of 0.68 are obtained from the fit. The analysis includes 4904 A-symmetry species and 4263 E-symmetry species, with respective rms values of 90 kHz and 72 kHz. Transitions from various torsional states were assigned, including 6813 transitions from the $v_t = 0$ state, 1983 transitions from the $v_t = 1$ state, and 371 transitions from the $v_t = 2$ state, providing a comprehensive understanding of the behaviour of molecule across different torsional states.

Similarly, for the isotopologue CH_3COCl^{37}, a detailed analysis of its rotational transitions in the millimeter and sub-millimeter wave range includes 2159 rotational transitions with 1230 measured line frequencies. The final fit, which includes 33 rotation-torsion parameters, is accurate enough to accord with experimental results. The root mean square (rms) deviation of 79 kHz and a unitless weighted root mean square (wrms) of 0.76 are obtained from the fit. The analysis includes 1085 A-symmetry species and 1074 E-symmetry species, with respective rms values of 82 kHz and 85 kHz. Transitions from various torsional states were assigned, including 1254 transitions from the $v_t = 0$ state, 583 transitions from the $v_t = 1$ state, and 322 transitions from the $v_t = 2$ state.

The larger number of transitions in the ground state than the excited state when subjected to identical selection rules should be attributed to the larger population of the ground torsional state at room temperature due to the Boltzmann factor.

In order to validate the accuracy of the fit in this study, we present a side-by-side comparison in Figure 3.7 of the experimental spectrum (depicted in blue) and the simulated spectrum (depicted in red) for both isotopologues, CH_3COCl^{35} and CH_3COCl^{37}. The simulated spectrum was constructed using the parameters presented in Table 3.2 The agreement in terms of frequency and relative intensity between these spectra is quite satisfactory.

The fitted parameters are also compared with previous results for each isotope. The differences in the rotation-torsion parameters compared to previous research can be attributed to several factors. One significant factor is the choice of the Hamiltonian model. While the previous research relied on the PAM Hamiltonian, this study adopted the RAM Hamiltonian approach. These different models can result in variations in parameter values due to their distinct theoretical foundations and assumptions. Another crucial factor is the large number of transitions with a much wider range of quantum numbers assigned in this work. In the previous studies, the maximum values for rotational quantum numbers (J_{max}) and asymmetry quantum numbers ($K_{a,max}$) were limited to 12 and 4, respectively, for both isotopes of CH_3COCl. In contrast, this experiment extended the range to much higher values, such as J_{max} = 57 and $K_{a,max}$ = 25 for ^{35}Cl and J_{max} = 52 and $K_{a,max}$ = 10 for ^{37}Cl. This broader range of quantum numbers can lead to variations in the derived parameters. Furthermore, the present work encompasses data from not only the ground state but also

Table 3.2: Set of rotational and nuclear quadrupole constants along their experimental values for both CH_3COCl^{35} and CH_3COCl^{37}.

Params.	**CH_3COCl^{35} (MHz)**	**Ref.** [78]	**CH_3COCl^{37} (MHz)**	**Ref.**[78]
A	10194.608(47)	10162.424(20)	10189.544(45)	10160.791(36)
B	4971.451(61)	4946.704(12)	4831.855(59)	4808.782(20)
C	3367.275(78)	3393.064(11)	3306.38(74)	3327.397(17)
$2D_{ab}$	$-5106.759(38)$	-	$-5226.13(34)$	-
F (GHz)	159.836(31)	168.591	158.87(14)	168.477
ρ (Unitless)	0.0426355(39)	-	0.042149(19)	-
V_3 (cm^{-1})	421.031(19)	442.440(10)	419.356(22)	446.987(17)
$-\Delta_J$	$-0.45081(88)\times10^{-2}$	-	$-0.519(12)\times10^{-2}$	-
$-\Delta_{JK}$	$0.2586(28)\times10^{-2}$	-	$0.606(39)\times10^{-2}$	-
$-\Delta_K$	$-0.3043(20)\times10^{-2}$	-	$-0.453(16)\times10^{-2}$	-
$-\delta_j$	$-0.19665(22)\times10^{-2}$	-	$-0.463(12)\times10^{-2}$	-
$-\delta_k$	$-0.19916(9)\times10^{-2}$	-	$-0.32869(28)\times10^{-2}$	-
V_{3J}	$0.27801(76)\times10^{2}$	-	$0.2286(74)\times10^{2}$	-
V_{3K}	$-0.11943(23)\times10^{3}$	-	$-0.1074(20)\times10^{3}$	-
V_{3JJ}	$-0.374(10)\times10^{-5}$	-	$-0.481(18)\times10^{-5}$	-
V_{3KK}	$0.2483(12)\times10^{-2}$	-	$0.316(13)\times10^{-2}$	-
ρ_J	$-0.8305(80)\times10^{-2}$	-	$-0.1052(55)\times10^{-1}$	-
ρ_K	$0.1031(42)\times10^{-1}$	-	-	-
F_J	$-0.3074(40)\times10^{-1}$	-	$-0.2410(36)\times10^{-1}$	-
F_m	$0.3764(60)\times10^{2}$	-	$0.356(11)\times10^{2}$	-
ρ_m	$-0.7282(90)\times10^{1}$	-	$-0.558(23)\times10^{1}$	-
V_{3ab}	$-0.9849(26)\times10^{2}$	-	$-0.1042(10)\times10^{3}$	-
V_{3bc}	$-0.16707(78)\times10^{2}$	-	$-0.1195(74)\times10^{2}$	-
D_{3ac}	$-0.2750(27)\times10^{2}$	-	$-0.380(17)\times10^{2}$	-
D_{3acj}	$0.6282(28)\times10^{-2}$	-	$0.675(35)\times10^{-2}$	-
V_6 (cm^{-1})	$-6.442(12)$	-	$-6.016(20)$	-
D_{ABJ}	$0.84734(70)\times10^{-2}$	-	$0.834(10)\times10^{-2}$	-
V_{6J}	$-0.534(19)\times10^{0}$	-	$-0.2416(35)\times10^{0}$	-
V_{6K}	$0.6055(55)\times10^{1}$	-	$0.836(25)\times10^{1}$	-
V_9 (cm^{-1})	2.394(13)	-	2.631(43)	-
ρ_{mk}	$0.7463(30)\times10^{-3}$	-	$0.928(36)\times10^{-3}$	-
ρ_{mj}	$-0.838(67)\times10^{-5}$	-	-	-
V_{6ab}	$0.909(11)\times10^{1}$	-	$0.1001(19)\times10^{2}$	-
D_{6ac}	$0.370(18)\times10^{1}$	-	-	-
V_{9J}	$0.1321(91)\times10^{0}$	-	-	-
χ_{aa}	$-58.755(34)$	$-58.437(11)$	$-46.264(35)$	$-45.701(16)$
χ_{bb}	36.735(30)	36.493(11)	[28.530]	28.530(16)
χ_{ab}	$[-10.031]^a$	-10.031	$[-7.597]$	-7.597

[a]The parameter value given in square parentheses (such as χ_{ab}) was fixed in our final fit at a value taken from a previous study [78].

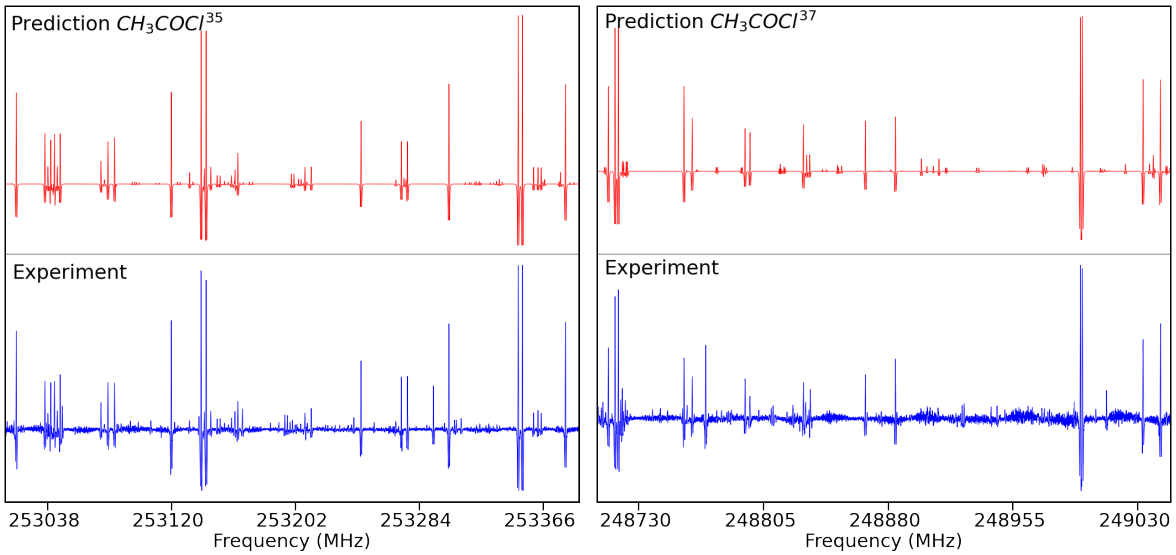

(a) (b)

Figure 3.7: The rotational spectra obtained from experiments (in blue) as well as from calculations (in red) (a) For CH_3COCl^{35} at a frequency of around 253 GHz and (b) For CH_3COCl^{37}at a frequency of around 248 GHz.

the first and second excited torsional states. In this context, particular attention may be drawn to the rotational constant C that normally should not be affected by the rotation of axes in ab plane when switching from PAM to RAM. We can see, however, that the values of C in this work and in previous study differ by about 1%.

3.3 Spectroscopy of acetyl Bromide

3.3.1 Experimental details

Following the study of acetyl chloride, we performed a new series of measurements of the rotational spectrum of acetyl bromide. All the spectra were recorded in absorption mode using the FLASH spectrometer [23, 24].

The measurements encompassed two frequency ranges: one spanning from 50 to 110 GHz and another from 150 to 330 GHz. We utilized a commercial sample of acetyl bromide with a purity level of 99%. All measurements were consistently conducted under room-temperature conditions by employing zero-bias Schottky diode detectors from *VDI* for signal detection. The optimal gas pressure in the absorption cell for the best signal-to-

noise ratio (S/N) of the recorded spectra was between 10 and 20 µbar, with higher pressures preferred at higher frequencies. After completing the measurement of acetyl chloride, we immediately proceeded to record the spectra of acetyl bromide in the same absorption cell. However, unlike acetyl chloride, acetyl bromide exhibited significant instability. Although we attempted to run the experiments within a closed-cell setup, we encountered a challenge: after around 10 to 15 min, the CH_3COBr signal disappeared while the CH_3COCl signal appeared. This was caused by some residual quantities of CH_3COCl or its decomposition product HCl on the absorption cell walls that favoured Cl-Br exchange. Similar behaviour was previosuly observed by Krisher [79]. As a solution, we opted to run the experiment in flow mode. This method allowed us to continuously introduce fresh samples of CH_3COBr, preventing the degradation of signals due to the Cl-Br exchange. Additionally, maintaining consistent pressure throughout the experiment presented a considerable challenge. Hence, we needed to closely monitor the pressure and make necessary adjustments to uphold a stable environment. This careful pressure management was essential to ensuring accurate and reliable experimental results.

3.3.2 Spectral analysis

The analysis began by taking into account the rotational constants and microwave transitions obtained by Krisher [79] as well as the centrifugal distortion constants and quadrupole coefficients obtained from ab initio calculations performed by my scientific supervisor. In the analysis of CH_3COBr, the torsion-rotation RAM Hamiltonian was used; hence, all the parameters obtained from a previous study and ab initio calculations were transformed to a RAM axis system using a rotation matrix. The angle of rotation in the ab plane θ_{RAM} is 28.7° for CH_3COBr^{79} and 29.6° for CH_3COBr^{81} in an anti-clockwise direction.

Since the proportion of natural abundance for ^{79}Br and ^{81}Br is nearly similar (51 % ^{79}Br and 49 % ^{81}Br), the rotational spectra of the two isotopes have the almost same strength. The millimeter-wave spectra of acetyl bromide are comparable to those of the recently studied acetyl chloride molecule. Figure 3.2 shows a portion of the observed rotational spectra of CH_3COBr around 305 GHz.

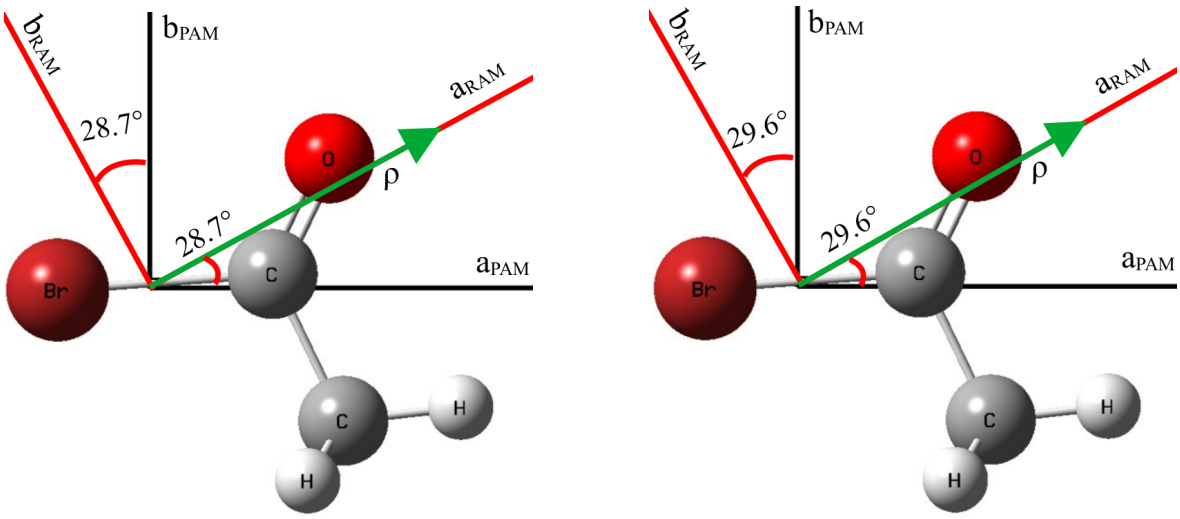

(a) (b)

Figure 3.8: A comparison of the principal axes and the rho-axis systems, along with the ρ vector and rotation angles (a) CH_3COBr^{79} (b) CH_3COBr^{81} molecule

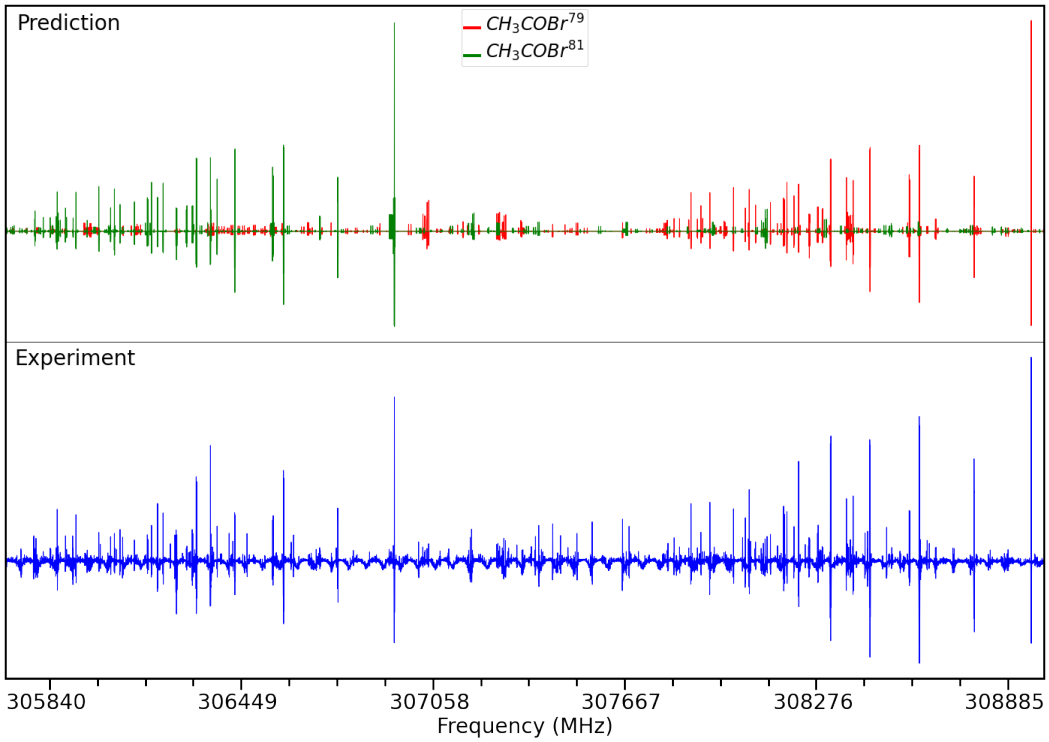

Figure 3.9: A portion of the rotational spectrum of CH_3COBr measured between 305 and 309 GHz.

Acetyl bromide also has spin $I = 3/2$, so the maximum number of possible hyperfine transitions is 9 for the P- and R-branch, and 10 for the Q-branch. However, only the strongest components are observed among all possible transitions. In most cases, we came

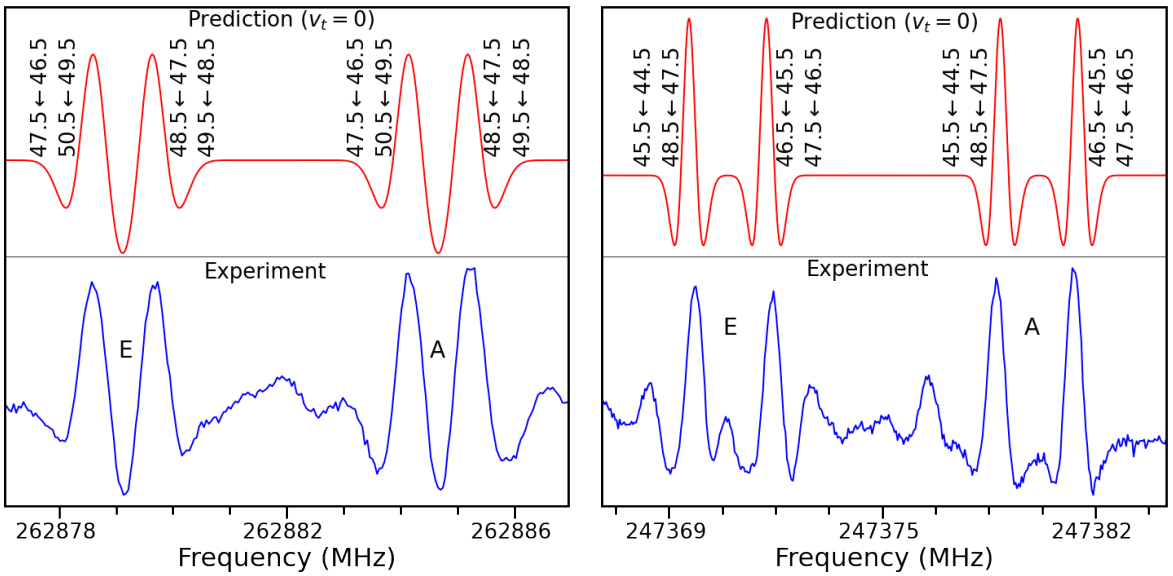

(a) (b)

Figure 3.10: Hyperfine components resulting from nuclear quadrupole interactions that have been observed in the ground state for (a) the $49_{7\,42} \leftarrow 48_{8\,41}$ transition in CH_3COBr^{79} and (b) the $47_{7\,40} \leftarrow 46_{8\,39}$ transition in CH_3COBr^{81}.

across four components with two different frequencies. The transitions with $F = J' + I - 1 \leftarrow J'' + I - 1$ and $J' - I + 1 \leftarrow J'' - I + 1$ observed with one frequency component of hyperfine structure, whereas transitions with $J' + I \leftarrow J'' + I$ and $J' - I \leftarrow J'' - I$ observed with another frequency component of hyperfine structure, as shown in Figure 3.10.

Although the quadrupole coupling parameters of acetyl bromide are almost an order of magnitude higher than those of acetyl chloride, the observed hyperfine splittings in the rotational spectrum of acetyl bromide and acetyl chloride are comparable. This may be explained by the fact that due to increased mass we observed transitions with higher J values for CH_3COBr and hyperfine splittings decrease with increasing J. So in the same frequency range the hyperfina splittings of the two molecules are comparable. Most of the observed hyperfine components are separated by around 1 MHz in frequency. As for the case of acetyl chloride, the hyperfine structure was observed in the ground and in the first excited torsional state. In the second excited state, because of reduced line intensities we were able to observe only the strongest lines with unresolved hyperfine splittings.

In the present work, we successfully assigned 2298 hyperfine components for CH_3COBr^{79} and 2350 for CH_3COBr^{81} and analysed them through effective Hamiltonian in

the RAM axis system. In the RAM method, the off-diagonal terms of the nuclear quadrupole coefficient are significant and comparable to the diagonal ones. Therefore, these off-diagonal terms are included in the fitting method. To find the precise value of the nuclear quadrupole coefficient, χ_{aa} and χ_{bb} are varied, while χ_{ab} is fixed based on ab initio calculations. Table 3.4 shows the experimental values of the nuclear quadrupole coefficients.

Both the R-branch and Q-branch transitions are assigned from the ground state to the first torsionally excited state. Whereas, only R-branch transitions were assigned from the second excited state. To obtain a more comprehensive understanding, a global fit analysis was performed encompassing transitions from several torsional states, including $v_t = 0$, $v_t = 1$ and $v_t = 2$, along with their hyperfine components.

The fitting started with low K_a transitions and a small set of parameters, which generate a new spectral prediction and allow for the assignment of new lines. The fit includes both the mm sub-mm wave spectra from the present work as well as previous microwave spectra by Krisher [79]. The barrier to internal rotation are of intermediate height 428.016 cm^{-1} for CH_3COBr^{79} and 423.56 cm^{-1} for CH_3COBr^{81}. Similar to the acetyl chloride, we observed two components due to torsional splitting, which are denoted by A and E symmetry species. In the case of acetyl bromide, the separation between A and E components also depends primarily on two factors: the quantum number K_a and the vibrational state of molecules. Similar to the pattern demonstrated in Figure 3.4 at low K_a, splitting of $A-E$ components typically occurs in the order of kilohertz; sometimes they may even be unresolvable. However, as the quantum number K_a increases, the separation between the $A-E$ components becomes more distinct. When subjected to torsional excitation, the tunneling probability rises, resulting in increased separation between the A and E components. In our current study, the rotational transition separation ($A-E$) is approximately 1 MHz in the ground state, but it grows exponentially to around 40 MHz in the first excited torsional state and up to 450 MHz in the second excited torsional state. The results of the final fit with RMS for each torsional state for both isotopes are shown in Table 3.3.

For CH_3COBr^{79}, a total of 4768 transitions with 2078 measured line frequencies were assigned, and 31 rotation-torsion parameters were considered in the fitting procedure. The root mean square (rms) deviation of 81 kHz and a unitless weighted root mean square

Table 3.3: The results of a global fit of 9864 transitions, including the rms value for A and E symmetry species for each torsional state for both CH_3COBr^{79} and CH_3COBr^{81}.

Transitions	CH_3COBr^{79}				CH_3COBr^{81}			
	Lines[a]	RMS[b]	WRMS[c]	n[d]	Lines[a]	RMS[b]	WRMS[c]	n[d]
All $v_t = 0, 1, 2$	4768	0.081 MHz	0.89	31	5096	0.084 MHz	0.90	31
A species[e]	2467	0.083 MHz	-	-	2406	0.083 MHz	-	-
E species[f]	2301	0.100 MHz	-	-	2690	0.104 MHz	-	-
Torsional state								
	qn[g]	Lines[a]	RMS[b]		Lines[a]	RMS[b]		
$v_t = 0$	m=0	1649	0.097 MHz		1601	0.093 MHz		
	m=1	1548	0.104 MHz		1875	0.100 MHz		
$v_t = 1$	m=-3	573	0.045 MHz		551	0.053 MHz		
	m=-2	528	0.052 MHz		559	0.070 MHz		
$v_t = 1$	m=3	245	0.045 MHz		254	0.058 MHz		
	m=4	225	0.153 MHz		256	0.175 MHz		

[a]Number of transitions included in the fit.
[b]Root-mean-square residual for the lines in this row.
[c]Weighted root-mean-square residual for the lines in this row.
[d]Number of parameters included in the fit.
[e]A symmetry species.
[f]E symmetry species.
[g]New quantum number defined in *RAM36hf* code to define A and E symmetry species for each torsional state.

(wrms) of 0.8931 are obtained from the fit. The analysis includes 2467 A-symmetry species and 2301 E-symmetry species, with respective rms values of 83 kHz and 100 kHz. The spectroscopic analysis shows that 3197 transitions are from $v_t = 0$, 1101 transitions are from $v_t = 1$, and only 470 transitions are from $v_t = 2$.

Likewise, for CH_3COBr^{81}, a total of 5096 transitions with 2101 measured line frequencies were assigned, and 31 rotation-torsion parameters were considered in the fit. The root mean square (rms) deviation of 84 kHz and a unitless weighted root mean square (wrms) of 0.8985 are obtained from the fit. The analysis includes 2406 A-symmetry species and 2690 E-symmetry species, with respective rms values of 82 kHz and 104 kHz. While comparing the results for different excited states of the molecule, it shows that 3476 assigned transitions originate from $v_t = 0$, 1110 transitions are from $v = 1$, and 510 transitions are from $v_t = 2$. This lower number of transitions at the higher excited state demonstrates a lower

Table 3.4: Set of rotational and quadrupole hyperfine constants along their experimental values for both CH_3COBr^{79} and CH_3COBr^{81}.

Params.	**CH_3COBr^{79} (MHz)**	**Ref.** [79]	**CH_3COBr^{81} (MHz)**	**Ref.** [79]
A	10155.8020(16)	10126.35	10155.8063(59)	10126.11
B	3008.9380(14)	3027.02	3008.9337(67)	3001.64
C	2342.25(31)	2362.52	2335.00(17)	2347.12
$2D_{ab}$	$-6008.0(17)$	-	$-6137.21(93)$	-
F (GHz)	155.53(20)	165.62	153.85(19)	165.60
ρ (Unitless)	0.035494(13)	-	0.034651(12)	-
V_3 (cm^{-1})	428.016(24)	456.7801	423.558(62)	456.0806
$-\Delta_J$	$-0.934(12)\times10^{-3}$	-	$-0.1015(13)\times10^{-2}$	-
$-\Delta_{JK}$	$0.1539(92)\times10^{-2}$	-	$0.1924(94)\times10^{-2}$	-
$-\Delta_K$	$-0.12644(93)\times10^{-1}$	-	$-0.12770(92)\times10^{-1}$	-
$-\delta_j$	$-0.2785(6)\times10^{-3}$	-	$-0.641(13)\times10^{-3}$	-
$-\delta_k$	$-0.314(7)\times10^{-3}$	-	$-0.662(15)\times10^{-3}$	-
V_{3J}	$0.2176(31)\times10^{2}$	-	$0.1352(17)\times10^{2}$	-
V_{3K}	$-0.9839(94)\times10^{2}$	-	$-0.7278(50)\times10^{2}$	-
V_{3JJ}	$-0.4372(46)\times10^{-5}$	-	$-0.4562(44)\times10^{-5}$	-
V_{3KK}	$-0.1959(83)\times10^{-3}$	-	$-0.2335(81)\times10^{-3}$	-
V_{3ab}	$-0.2494(78)\times10^{2}$	-	$-0.4581(38)\times10^{2}$	-
V_{3bc}	$-0.1247(31)\times10^{2}$	-	$-0.428(17)\times10^{1}$	-
D_{3ac}	$-0.518(13)\times10^{2}$	-	$-0.543(14)\times10^{2}$	-
$0.5D_{3acm}$	$-0.1120(14)\times10^{1}$	-	$-0.1154(13)\times10^{1}$	-
D_{3bc}	$0.2223(43)\times10^{2}$	-	$0.2467(45)\times10^{2}$	-
ρ_{bc}	$0.2816(72)\times10^{-2}$	-	$0.2196(72)\times10^{-2}$	-
V_6 (cm^{-1})	$-6.0781(11)$	-	$-6.0622(12)$	-
D_{ABK}	$0.7140(17)\times10^{-2}$	-	$0.8001(19)\times10^{-2}$	-
V_{6J}	$-0.1262(20)\times10^{0}$	-	$-0.1345(19)\times10^{0}$	-
V_{6K}	$0.5103(19)\times10^{1}$	-	$0.4982(21)\times10^{1}$	-
V_9 (cm^{-1})	7.0054(14)	-	7.7133(23)	-
D_{6ac}	$-0.977(30)\times10^{1}$	-	$-0.1027(32)\times10^{2}$	-
Φ_j	$0.930(49)\times10^{-10}$	-	$0.929(49)\times10^{-10}$	-
χ_{aa}	456.1373(27)	460(3)	380.4333(26)	385(3)
χ_{bb}	$-276.0373(51)$	$-277(1)$	$-230.2933(52)$	$-232(1)$
χ_{ab}	[41.6567]	-	[32.6036]	-

[a]The parameter value given in square parentheses (such as χ_{ab}) was fixed in our final fit at a value taken from an ab initio calculation.

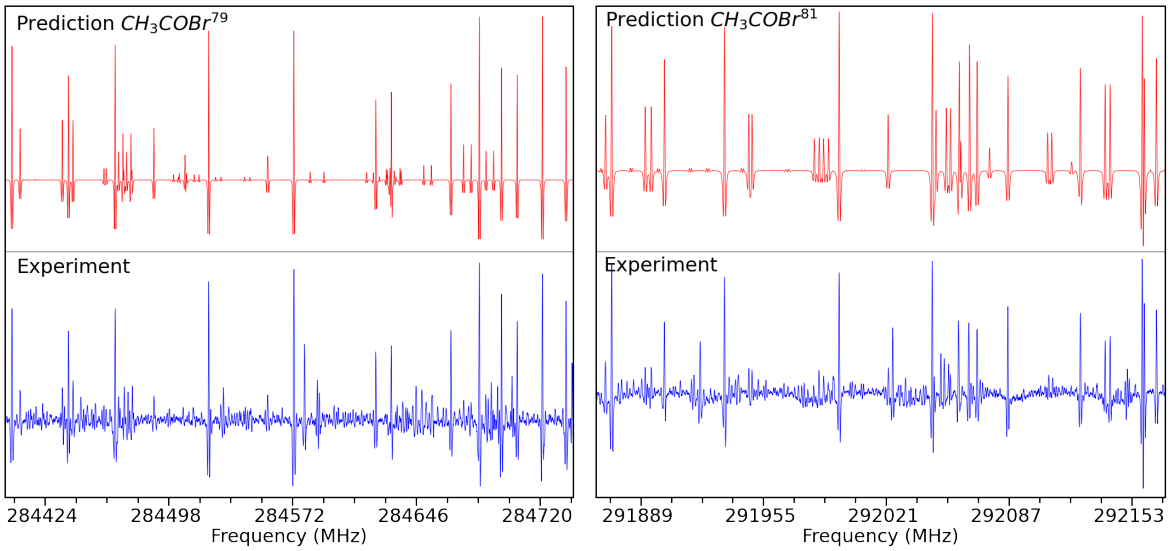

(a) (b)

Figure 3.11: The rotational spectra obtained from experiments (in blue) as well as from calculations (in red) (a) For CH_3COBr^{79} at a frequency of around 284 GHz and (b) For CH_3COBr^{81} at a frequency of around 291 GHz.

population in the excited state compared to the ground state under the given experimental condition. This is consistent with the expected Boltzmann distribution of vibrational energy levels in molecules, which shows a smaller population at higher vibrational states.

From the result, another point to think about is the convergence of the torsional potential function, where V_9 is slightly larger than V_6. Since Fermi-type couplings result from interactions between different vibrational states or low-amplitude vibrations, they influence the potential function [81]. The experimental value observed in the present study could result from interactions between different vibrational modes within acetyl bromide.

In Figure 3.11, we compare experimental spectrum (shown in blue) to a calculated spectrum (shown in red) in this study to illustrate the accuracy of the fit for each isotopologue, CH_3COBr^{79} and CH_3COBr^{81}. The agreement between these spectra in terms of frequency and relative intensity is satisfactory.

Likewise in CH_3COCl, the previous research relied on the PAM Hamiltonian model, while we adopted the RAM Hamiltonian approach. Notably, we achieved a wider span of J and K_a values in our observation. In the previous studies, J_{max} and $K_{a\,max}$ were limited to 12 and 3, respectively. In contrast, our experiment led to significantly higher values of J_{max}

= 71, $K_{a\,max}$ = 15, for both isotopes of CH_3COBr. Furthermore, earlier research concentrated solely on ground state spectra, whereas we encompassed data from the ground state, the first excited torsional state, and the second excited torsional state. As for acetyl chloride we may also notice quite significant discrepancy in the rotational constants of PAM and RAM Hamiltonians, and in particular in the values of C rotational constant.

3.4 Discussion

Upon comparing the rotational spectra of acetyl chloride and acetyl bromide within the 50–330 MHz frequency range, it becomes evident that these two molecules exhibit noteworthy similarities. Internal rotation splittings, hyperfine patterns, and the dominance of b-type transitions over a-type transitions are the same characteristics shared by both molecules. Furthermore, the Q- and R-branches are observable, whereas the P-branch is not in either case.

When isotopologues of these molecules are studied, a remarkable difference arises. In the case of CH_3COCl, the isotopic species CH_3COCl^{37} has a significantly weaker spectral pattern than CH_3COCl^{35}. However, in CH_3COBr, the two naturally occurring isotopic species CH_3COBr^{79} and CH_3COBr^{81} have identical spectral patterns.

For each molecule, roughly 10,000 lines from $v_t = 0, v_t = 1$, and $v_t = 2$ states are assigned and included in the fit. Specifically, for CH_3COCl, approximately 80 % of the assigned lines come from the CH_3COCl^{35} isotope, while the remaining 20 % come from the CH_3COCl^{37} isotope. For CH_3COBr, the lines are evenly distributed in a 50:50 ratio between the CH_3COBr^{79} and CH_3COBr^{81} isotopes. This distribution is consistent with the natural abundance of these isotopes.

The provided information helps ensure that the analysis of these molecules takes into account the most abundant isotopes, which is important for accurate spectroscopic studies and molecular characterization. While examining the result of the fit, the number of fitted parameters for CH_3COCl is quite higher than CH_3COBr. The internal rotation splitting is comparable between CH_3COCl and CH_3COBr. Both molecules have a comparable barrier height of $\approx$ (400 cm^{-1}), an almost equal value of the internal rotation constant (F), and

a similar spacing pattern between the A and E symmetry species. However, the coupling constant ρ for CH_3COCl is significantly higher than that for CH_3COBr, which is most likely due to the lighter mass of CH_3COCl. We observe a similar pattern of hyperfine structure in both cases. In CH_3COCl, a maximum of four hyperfine components with distinct frequencies are observed, whereas in CH_3COBr they overlap into two frequencies. In terms of nuclear quadrupole coefficients, the experimental value of the nuclear quadrupole coefficient for CH_3COBr is quite higher than CH_3COCl. The diagonal term of the nuclear quadrupole coefficient for CH_3COBr is approximately ten times higher than that of CH_3COCl. In both cases, the final fits are within experimental accuracy, and the resultant rotational parameters are consistent with previous results.

Comparing the results of our study to previously published data, an important remark should be made. It can be shown, that in the rigid rotor approximation, the constants F and ρ of torsion-rotational RAM Hamiltonian may be both expressed as functions of the internal rotor inertia moment I_α as [82, 83]:

$$F = \frac{\hbar^2}{2}\left[I_\alpha - I_\alpha^2 \frac{B_{RAM}\left(A_{RAM}B_{RAM} - D_{ab}^2\right)}{\frac{\hbar^2}{2}\left(B_{RAM}^2 + D_{ab}^2\right)}\right]^{-1} \tag{3.2}$$

$$\rho = I_\alpha \frac{A_{RAM}B_{RAM} - D_{ab}^2}{\frac{\hbar^2}{2}\sqrt{B_{RAM}^2 + D_{ab}^2}} \tag{3.3}$$

These expressions assume that in the second order of the torsional-rotational RAM Hamiltonian, there are no structural distortions due to torsional-rotational motion. It follows that under this assumption, F and ρ parameters are not independent; so one can replace them by a single I_α parameter in the fit. While fitting the rotational spectra of CH_3COCl and CH_3COBr with RAM36hf code, we also noticed that using only ground state transitions, we were not able to fit simultaneously F and ρ, and one of the two parameters had to be fixed. However, when $v_t = 1$, and $v_t = 2$ lines were added to the fitted dataset, to achieve experimental accuracy we set both parameters to vary. From these observations, we may conclude that for CH_3COCl and CH_3COBr, notable structural distortions due to torsional-rotational motion appear only upon torsional excitation. These distortions, however, should still be small, since the RAM Hamiltonian expressed as a series expansion in terms of powers of P_α, J, and sine and cosine Fourier series converges well, as it can be seen from the results

of the fits. Hence, I_α values determined using (3.2) and (3.3) should not differ too much.

The inertia moment of the methyl top may be also estimated using pseudo-inertial defect $\Delta = I_a + I_b - I_c$ as [84]:

$$I_\alpha = I_a + I_b - I_c + \Delta' \tag{3.4}$$

where Δ' is the inertia defect of the frame. For both molecules, the frame has a planar structure, so Δ' is relatively small. Herschbach and Laurie [85] estimated $\Delta' = 0.255$ amuÅ^2 for CH_3COCl and $\Delta' = 0.316$ amuÅ^2 for CH_3COBr.

In Table 3.5 we compare $I_\alpha(F)$ and $I_\alpha(\rho)$ values calculated using respectively (3.2) and (3.3) with the values $I_\alpha(RAM)$ and $I_\alpha(PAM)$ calculated using (3.4) with $I_g,\ g = a, b, c$ values from the RAM and PAM Hamiltonian models respectively. The I_g values from the RAM Hamiltonian were calculated from the rotational constants in the rho-axis system rotated back to the principal axe system. These rotational constants are given in Tables 3.2 and 3.4. The analysis of the results presented in Table 3.5 leads us to two important conclusions.

First, $I_\alpha(F)$ and $I_\alpha(\rho)$ determined in the least-squares fit by the application of the RAM method have reasonable values within the interval 3.1–3.4 amuÅ^2 of typical values of the methyl top inertia moment. One can also notice that $I_\alpha(\rho)$ is systematically smaller than $I_\alpha(F)$. These values are also in agreement with $I_\alpha(PAM)$ determined from the results of previous studies obtained using standard principal axes Hamiltonian. Therefore one may conclude that upon correct application, the RAM Hamiltonian produces self consistent sets of parameters with real physical meaning at least for the first order terms. The comparison of $I_\alpha(F)$ and $I_\alpha(\rho)$ is also a tool to check the consistency of the fit results, complementary to the criteria presented in 2.7.1.

Second, one cannot ignore that the $I_\alpha(RAM)$ values in Table 3.5 are in disagreement with the others and are out of the range 3.1–3.4 amuÅ^2. As it was explained, in 3.2.2, the rotational constants determined in the global approach are vibrationally averaged, so the inertia defect Δ used in the calculation of $I_\alpha(RAM)$ may be also considered as vibrationally averaged. Since it is known that out-of-plane vibrations make a negative contribution to inertia defect [26], the Δ values calculated from the rotational constants determined by the RAM36hf code are smaller and lead to lower $I_\alpha(RAM)$. However, one can also note

Table 3.5: Inertia moments of the methyl top (in $\mathrm{amuÅ}^2$) for CH_3COCl and CH_3COBr derived using (3.2), (3.3), and (3.4)

Molecules	$I_\alpha(\rho)$,	$I_\alpha(F)$	$I_\alpha(RAM)$	$I_\alpha(PAM)$
CH_3COCl^{35}	3.180	3.297	1.398	3.204
CH_3COCl^{37}	3.198	3.315	1.596	3.203
CH_3COBr^{79}	3.232	3.352	2.271	3.262
CH_3COBr^{81}	3.240	3.387	1.601	3.272

an inconsistency in the $I_\alpha(RAM)$ value for $CH_3CO^{79}Br$. So as additional explanation, we may suppose that in this particular case, or in general, the correlation between principal rotational constants and higher order centrifugal correction terms involving principal axes, like V_{3ab}, F_{bc}, D_{3ac} etc., may also influence the final values of the fit. Therefore, the rotational constants determined in the RAM Hamiltonian framework even after rotation to the principal axes system, may not be used for accurate molecular structure determination [83].

3.5 Conclusions

This chapter shows how important rotational spectroscopy is for understanding the properties of molecules, as well as the challenges and advances in theoretical and experimental methods for studying molecules that exhibit large amplitude motion. The chapter highlights that spectroscopic studies of acetyl halides are crucial for a variety of scientific purposes, ranging from monitoring gas composition and air quality to understanding climate change and molecular properties.

In the experimental context, during the spectral recording process, we were able to record the spectra of CH_3COCl under static pressure conditions within an enclosed cell. However, we faced a challenge when attempting to record spectra of CH_3COBr in static mode, which led us to collect measurements using a flow mode setup.

Spectroscopic studies discussed in the chapter involve a global fit of CH_3COCl and CH_3COBr molecules. This refers to experimental data to theoretical model to accurately describe the rotational spectra of these molecules. The data incorporate ground state as

well as lowest torsionally states. Whereas the applied models are capable of accurately fitting spectral data within experimental accuracy. To my opinion, the most effective method for dealing with the internal rotation of molecules with C_{3v} symmetry rotors is the RAM. It can be applied to all types of problems independently of the values of the torsion-rotation coupling parameters ρ and F, as well as the barrier height V_3. *RAM36hf* is shown to be a good code for analysing internal rotation because it is flexible in the choice of the Hamiltonian terms and includes the nuclear quadrupole hyperfine structure parameters. However, we have also shown that the parameters derived from the RAM Hamiltonian approach are referred to as effective rotational parameters. These parameters are efficient in characterizing the internal rotational behavior of molecules but are not suitable for determining the molecular structure. We have also shown that the inertia moment of the top derived from fitted parameters may be used as additional criteria in the analysis of the results of the fit.

Chapter 4

Spectroscopy of molecules with two large-amplitude motions

4.1 Methylamine

4.1.1 Introduction

Methylamine (CH_3NH_2) is a seven-atom chemical compound that is the primary alkylamine found in trace amounts in the atmosphere of Earth [86]. It can participate in chemical reactions in the atmosphere. As methylamine plays a role in the production of organic aerosols, it has the potential to impact the radiative balance [87]. Methylamine-containing compounds can scatter and absorb sunlight, which influences the atmospheric energy balance and the temperature of the Earth. It can react with hydroxyl radicals (OH) in the atmosphere and influence the overall oxidative capacity of the atmosphere. This reaction affects the lifetimes of various atmospheric species and can indirectly influence air quality and climate [86]. The study of methylamine helps to understand its effects on air quality, climate, and environmental health. The sole process of oxidation, excluding aerosol uptake, methylamine has lifetimes ranging from 5 to 10 hours in the majority of low- and middle-latitude regions[88]. However, when considering the uptake by secondary species, this leads to a reduction in lifetime by approximately 30% [88].

It is primarily produced through both natural and anthropogenic sources and can have several impacts on the atmosphere [87]. It is released into the atmosphere through natural processes such as microbial activity in soils, vegetation, and bodies of water. It can also be emitted from volcanic activity and wildfires. Also, human activities contribute to methylamine emissions. Industrial processes, including the production of certain chemicals and the combustion of fossil fuels, can release methylamine into the air.

The molecular structure of methylamine leads to a complex rotational spectrum due to its two large amplitude motions: the methyl group torsion motion and the amine inversion (wagging) motion. The ground rotational state ($v_t = 0$) of methylamine and ^{13}C methylamine was successfully analysed in a series of papers [38, 89, 90] using the "tunnelling" approach developed by Ohashi and Hougen [91]. This approach involves fitting each torsional state separately with its own set of molecular parameters. This method provides an accurate result for analysing the $v_t = 0$ state, but it has limitations for analysing the $v_t = 1$

state. Later, there was another study for the $v_t = 0$ state of methylamine by Kleiner et al. [52] using the hybrid approach, including infrared transitions. This study showed that the hybrid approach could provide more accurate results in the analysis of excited vibrational states.

In this view, the main goal of this study is to measure and analyse the rotational spectra of methylamine in its first excited torsional state. In this current research, we employ a hybrid model that is capable of addressing both LAMs and performing a global fit. This study includes both microwave and far infrared datasets. Such analysis not only enhances our understanding of methylamine but also lays the groundwork for spectroscopic investigations of similar molecules with methylamine-like structures. To facilitate access, the spectroscopic data of methylamine in the $v_t = 1$ state obtained in the present study is available in the Lille Spectroscopic Database (https://lsd.univ-lille.fr/).

4.1.2 Experimental details

We performed a new series of measurements of the rotational spectrum of methylamine in the framework of the present study. All the spectra were recorded in absorption mode using the Lille fast-scan hybrid spectrometer [23, 24, 92]. The measurements cover the frequency range 150 – 1520 GHz with a few small gaps. We used a 99 % pure commercial sample of methylamine purchased from Sigma-Aldrich. The optimal gas pressure in the absorption cell for the best signal-to-noise ratio (S/N) of the recorded spectra was between 30 µbar and 60 µbar, with higher pressures preferred at higher frequencies. Due to partially resolved or unresolved nuclear quadrupole hyperfine structure, the measurement uncertainty is estimated to be around 60 kHz for relatively strong isolated lines and 100 kHz for weak or slightly distorted line shapes, and for the lines measured above 1 THz due to line broadening effects (both Doppler and pressure).

As the main goal of the study is the assignment of excited vibrational states, the spectra were recorded with an increased amplitude resolution. In standard conditions, the spectral amplitude resolution is limited by the resolution of the analog-to-digital converter. In the present study, we used a SR7270 DSP lock-in amplifier, the ADC of which has a resolution

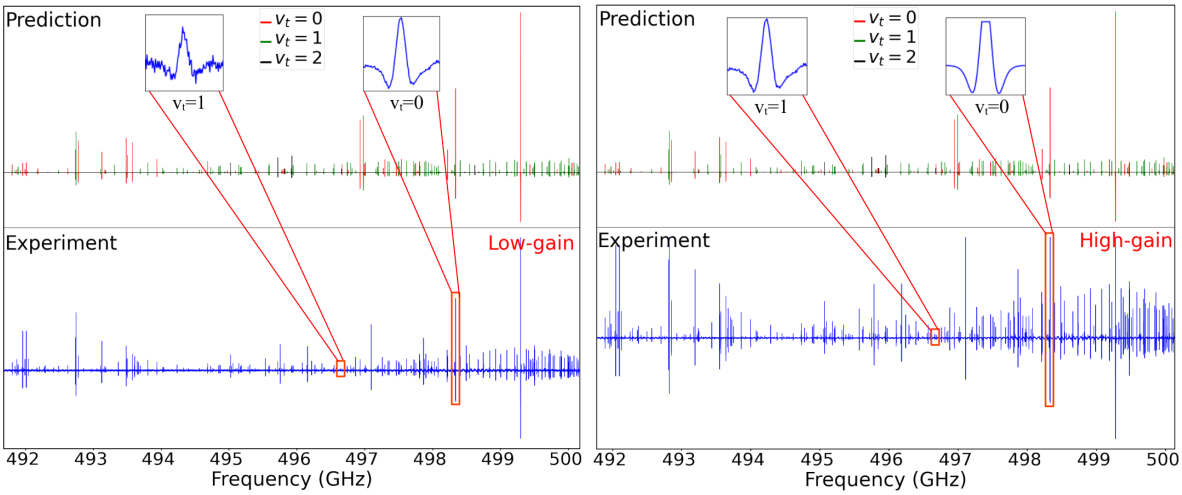

(a) (b)

Figure 4.1: A portion of the rotational spectra of CH_3NH_2 measured between 490 and 500 GHz (a) in low gain mode (b) in high gain mode

of 16 bits. To increase the amplitude resolution, each spectral segment was recorded twice with two gain factors that differed by 20 dB. Lower gain spectra were used to assign the strongest lines, whereas higher gain spectra were particularly useful for the assignment of weak lines in excited torsional states.

As illustrated in Figure Figure 4.1, in low gain mode, low-intensity spectral lines from the excited state are overshadowed by high-intensity spectral lines from the ground state, whereas in high gain mode, spectral lines from the excited state are more apparent, while lines from the ground state are even saturated.

4.1.3 Spectral analysis

In the present work, the analysis focuses on identifying transitions in the $v_t = 1$ vibrational state of the CH_3NH_2 molecule. Our analysis began with a reference to the spectral predictions generated through a hybrid approach. In the initial stages, these predictions were based on the results of the study [52] and were rather shifted significantly from the observed line positions, particularly up to 200 MHz. This discrepancy presented a considerable challenge in assigning the observed lines and obtaining an accurate set of quantum numbers. Additionally, the presence of two large amplitude motions complicated the assignment process by causing energy levels to split into numerous sub-levels. This leads to

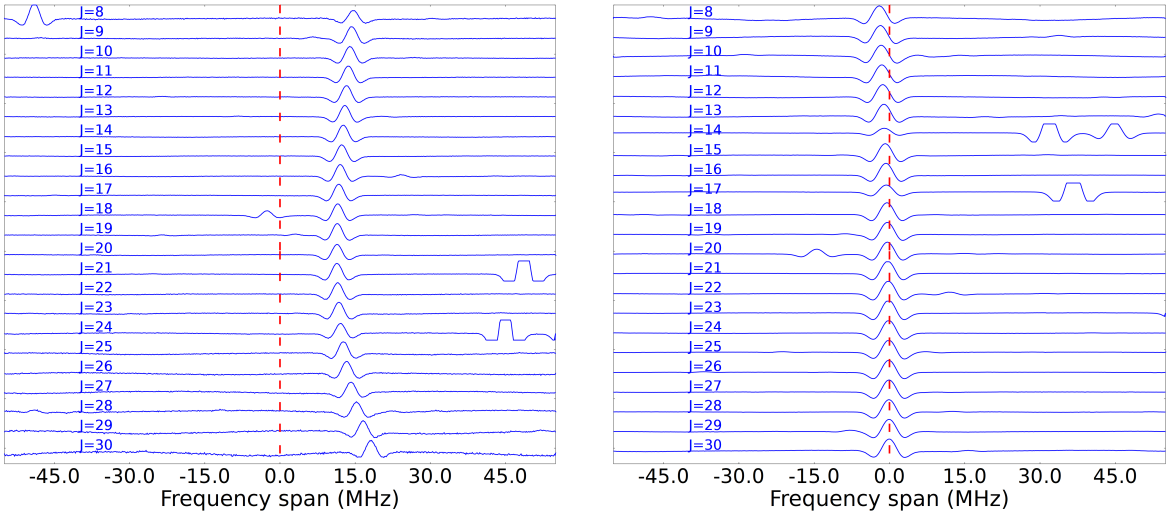

(a) (b)

Figure 4.2: Loomis-Wood diagram centered on predicted frequencies of E_1 ^{c}Q-type series of $v_t = 1$ state of methylamine for transition $K''_a = -8 \leftarrow K'_a = -7$ (a) after several refinements (b) final prediction

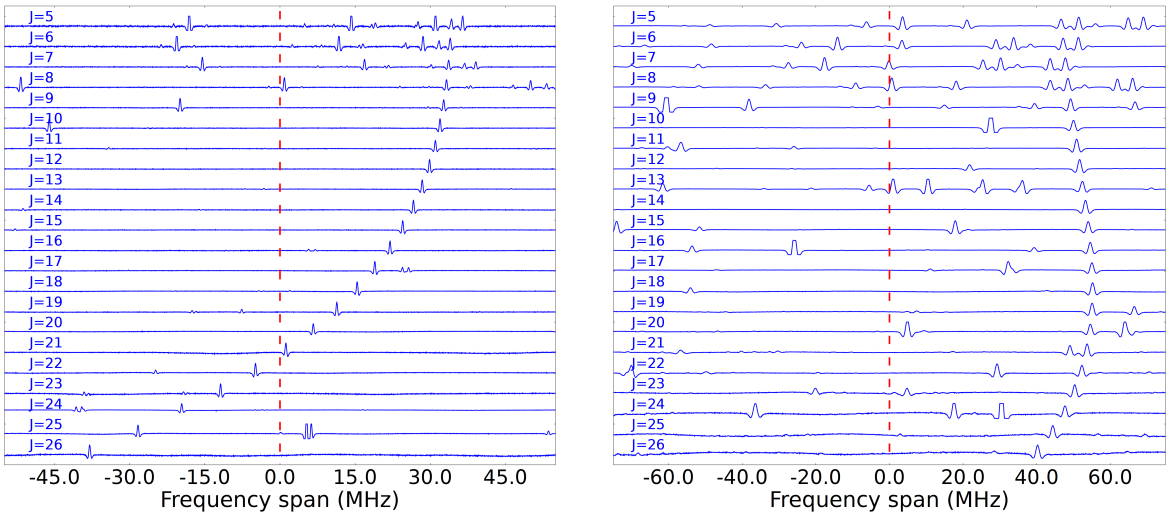

(a) (b)

Figure 4.3: Loomis-Wood diagram centered on predicted frequencies of E_1 ^{c}Q-type series of $v_t = 2$ state of methylamine for transitions (a) $K''_a = 2 \leftarrow K'_a = 1$ (b) $K''_a = -1 \leftarrow K'_a = 0$

a relatively dense spectrum with many overlapped, and mixed spectral features.

To address these challenges, I initiated the plotting of spectral lines using Loomis-Wood diagrams (introduced by Loomis and Wood in 1928 [93]) and tried to get the tendency of spectral lines within a specific series. The technique consists in superposing portions of spectra centered on predicted frequencies of a particular series of transitions where only

one quantum number is varied and the rest are kept constant. In this case, the shifts of the observed lines with respect to the predicted ones exhibit a smooth (typically polynomial) behavior as a function of the varied quantum number and can be easily located on the diagram. For each series, the behaviour of the spectral lines in comparison to their predictions is remarkably smooth. Such diagrams are crucial for accurately identifying transitions within a wide spectrum, particularly during the initial phases of research when predicted transition frequencies significantly diverge from observed frequencies. By integrating the newly assigned spectral series into the least-square fit, it becomes possible to generate more reliable predictions. This iterative approach to the process consistently yields precise spectral predictions that simplify the spectroscopic analysis. An example of a Loomis-Wood plot with respect to the prediction for $v_t = 1$ state and $v_t = 2$ state is shown in Figure 4.2 and Figure 4.3 respectively.

In the present study, a series of rotational transitions for all three branches (R-branches, Q-branches, and P-branches) are assigned. The majority of these transitions belong to the R- and Q-branches, while a smaller portion of them belong to the P-branches. Nuclear spin statistical factors are 3:1 respectively for $E_1, B : E_2, A$ levels. During the series-wise assignment, it was observed that the E_1 series pattern closely resembled that of the E_2 series, while the A_1/A_2 series was identical to the B_1/B_2 series.

Due to the energy level splitting, it became possible to assign more than ten transitions for each combination of the J and K_a quantum numbers. Because of dense spectral patterns, sometimes two or more transitions are exceptionally close. In such scenarios, the stronger lines overshadow the weaker ones, resulting in wider line widths, asymmetric and distorted line shapes, and the need for rigorous interpretation. Due to the influence of these stronger lines, the frequencies of the weaker lines may deviate from their actual positions or, in some cases, become unresolvable. In the $v_t = 1$ state of methylamine, there are numerous transitions, often influenced by the strong lines from the ground state and occasionally influenced by a transition from the same or higher excited states. The comprehensive assignment of rotational transitions conducted in this study encompasses a total of 4386 lines. This assignment comprises 2921 lines for the $v_t = 1 - 1$ state and 1465 lines for the $v_t = 2 - 2$ state. In terms of quantum numbers, we have achieved maximum values of

J up to 40 and maximum values of K_a up to 11.

4.1.4 Analysis of the nuclear quadrupole hyperfine spectra

In methylamine, only the ^{14}N possesses a nuclear spin of $I = 1$, which gives rise to the quadrupole interaction. Consequently, the total angular momentum quantum number F can have only three distinct values, as follows:

$$F = J + 1, \quad F = J \quad \text{and} \quad F = |J - 1| \tag{4.1}$$

As a result, each energy level corresponding to the rotational quantum number J splits into three separate sub-levels, each of which is labeled with a total angular momentum quantum number F. However, only selected transitions between the sub-levels are allowed. Such transitions can be summarised as follows:

$$\Delta J = 0, \pm 1 \quad \text{and} \quad \Delta F = 0, \pm 1 \tag{4.2}$$

For methylamine, there are a total of 7 possible hyperfine transitions allowed in the Q branch and 6 possible transitions permitted in the R and P branches. Since each transition has a different intensity, the relative intensity of each transition can be determined using the formula as follows [27]:

For transition $\Delta J = 1$:

$$I(F' \leftarrow F) = \frac{(J + F' + I + 1)(J + F' + I)(J + F' - I)(J + F' - I - 1)}{F'} \tag{4.3}$$

$$I(F \leftarrow F) = -\frac{(J + F + I + 1)(J + F - I)(J - F + 1)(J - F - I - 1)(2F + 1)}{F(F + 1)} \tag{4.4}$$

$$I(F \leftarrow F') = \frac{(J - F + I)(J - F + I - 1)(J - F - I - 1)(J - F - I - 2)}{(F + 1)} \tag{4.5}$$

For transition $\Delta J = 0$:

$$I(F' \leftarrow F) = -\frac{(J + F' + I + 1)(J + F' - I)(J - F' + I + 1)(J - F' - I)}{F'} \tag{4.6}$$

$$I(F \leftarrow F) = \frac{[J(J + 1) + F(F + 1) - I(I + 1)]^2(2F + 1)}{F(F + 1)} \tag{4.7}$$

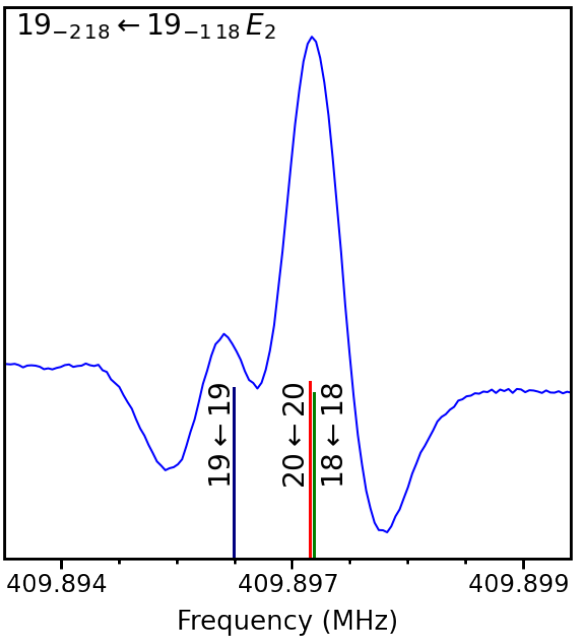

Figure 4.4: Partially resolved hyperfine structure of $19_{-2\,18}E_2 \leftarrow 19_{-12\,18}E_2$ transition of methylamine in $v_t = 1$ state

$$I(F \leftarrow F') = \frac{(J+F+I+2)(J+F-I+1)(J-F+I)(J-F-I-1)}{(F+1)} \tag{4.8}$$

For transition $\Delta J = -1$:

$$I(F' \leftarrow F) = \frac{(J+F+I+1)(J+F+I)(J+F-I)(J+F-I-1)}{F} \tag{4.9}$$

$$I(F \leftarrow F) = -\frac{(J+F+I+1)(J+F-I)(J-F+1)(J-F-I-1)(2F+1)}{F(F+1)} \tag{4.10}$$

$$I(F \leftarrow F') = \frac{(J-F'+I)(J-F'+I-1)(J-F'-I-1)(J-F'-I-2)}{(F'+1)} \tag{4.11}$$

In practice, only the strong hyperfine components with $\Delta F = \Delta J$ selection rule are usually observed, as the relative intensities of the other components decrease very rapidly as J increases. The precise identification of hyperfine components relies on a comprehensive analysis of both the linewidth and line shape in the observed spectrum. Usually, when the hyperfine effect is present, the spectrum can either divide into multiple components or exhibit a broader and asymmetric linewidth. Conversely, a spectrum with a narrower linewidth and a symmetric shape usually indicates the hyperfine-free spectrum.

For example, in Figure 4.4, the hyperfine components in the observed spectrum are clearly separated into two distinct peaks. This enables the assignment of two frequencies to the observed spectrum. In this particular case, the splitting between the frequencies ($f_2 - f_1$ = 0.895 MHz) is notably greater than the Voigt linewidth of each component ($\gamma_v \approx$ 0.366 MHz). In some cases, the spectrum exhibits a single peak with an asymmetric line shape and a broader line width. Under these circumstances, it remains possible to assign two frequencies.

During the process of assigning hyperfine components for the first excited state of methylamine, only two out of three strong components are observable. The intensity ratio between these two components is approximately 1:2, suggesting that the strong component is a combination of two unresolved lines. For all cases (Q, P, and R-branches), the transition $F_2 = J_2 \leftarrow F_1 = J_1$ is well resolved, but $F_2 = J_2 - 1 \leftarrow F_1 = J_1 - 1$ and $F_2 = J_2 + 1 \leftarrow F_1 = J_1 + 1$ remain unresolved. In our experiment, we observed a total of 162 pairs of hyperfine components. The hyperfine spectra of methylamine were observed in a frequency range spanning from 152 GHz to 892 GHz. The difference between the two hyperfine components varied from 0.265 MHz to 2.025 MHz.

Calculation of quadrupole coefficient: The least squares method

The nuclear quadrupole energy can be represented as a function of two independent nuclear quadrupole hyperfine coefficients, denoted as χ_+ and χ_-, as explained in (2.19). By fitting the experimental data, one can determine the experimental values of these coefficients. Throughout this project, the experimental values of χ_+ and χ_- were calculated using the least squares method. The calculation was carried out using self-written Python code. To get these global values, the calculation uses data from the ground state as well as from the first excited torsional state. This computation comprises 1132 hyperfine components from the ground state [90] and 324 hyperfine components from the first excited torsional state. Only strong components with two distinct frequencies have been assigned to the first excited torsional state. In contrast, the ground state assignment involves several hyperfine components, both weak and strong. To streamline the computation process and accurately determine the quantum numbers associated with each transition, a six-digit standardized

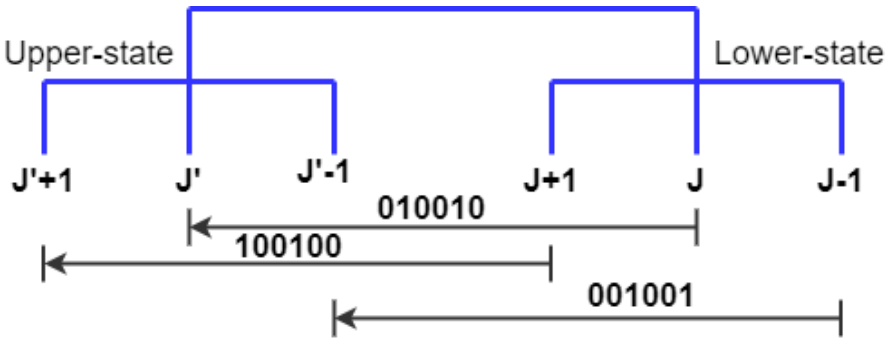

Figure 4.5: Standard identification of each hyperfine component with a six-digit code

code is introduced to each component. The first three digits denote the higher energy state, while the last three digits represent the lower energy state. The unique six-digit code employs the numbers 0 and 1, where 0 indicates an inactive state and 1 indicates an active state, as illustrated in Figure 4.5. For example, standard code `010010` represents the hyperfine transition between two J levels ($J \leftarrow J$), standard code `100100` represents the hyperfine transitions between two $J+1$ levels ($J+1 \leftarrow J+1$), standard code `101101` represents the mixture of two hyperfine transitions between two $J+1$ levels and two $J-1$ levels ($J+1 \leftarrow J+1$ and $J-1 \leftarrow J-1$), etc. The hyperfine component with the code `101101` represents the mixture of two unresolved components; hence, the intensity is almost two times greater than that of another resolved component, `010010`.

Since each observed frequency arises from a combination of the pure rotational frequency and the hyperfine shift, it is possible to express the observed hyperfine components of methylamine as a function of the quadrupole coefficient, as explained in (2.21). Using (2.20) and (2.21), we can determine the pure rotational "de-hyperfine" frequencies and hyperfine parameters χ. The least-squares method is then employed to compute the "de-hyperfine" frequencies and the quadrupole coefficient from the set of observed frequencies $f_{obs}^{(i)}$.

To carry out the computation using the least squares approach, the process involves two main steps. In the first step, the Jacobian matrix of (2.21) is determined, representing the first-order derivative with respect to the constant parameters.

In the subsequent step, the unknown parameters are computed using (2.54) as.

$$\boldsymbol{J}^T \cdot \boldsymbol{J} \cdot P = \boldsymbol{J}^T \cdot f_{obs} \tag{4.12}$$

Table 4.1: ^{14}N nuclear quadrupole coupling parameters for methylamine

Parameter	**Present work**	**Ground state**[90]
χ_+ (MHz)	-2.4139(63)	-2.4129(12)
χ_- (MHz)	6.4058(85)	6.0697(25)
Transitions[a]	1456	1132
rms[b] (MHz)	0.0129	0.0082

[a]The fit includes a total of 324 hyperfine components for $v_t = 1 - 1$ from this study.
[b]Root-mean-square deviation of the hyperfine fit.

Where $\boldsymbol{J}^T$ is the Jacobian matrix, $\boldsymbol{J^T J}$ is called Hessian Matrix (H) and f_{obs} is the observed frequency, and P is a vector of adjusted parameters:

$$P = [f_1, f_2, f_3, ..., \chi_+, \chi_-, \chi_{xz}] \tag{4.13}$$

In this specific scenario, we denote the determined values of hyperfine-free central frequencies as f_1, f_2, f_3,..., while χ_+, χ_-, and χ_{xz} represent the determined quadrupole parameters. The p vector can be therefore expressed as:

$$P = H^{-1} \cdot (\boldsymbol{J^T} \cdot f_{obs}) \tag{4.14}$$

Here, H^{-1} corresponds to the inverse of the Hessian matrix, which is also referred to as the covariance matrix. The diagonal elements of the covariance matrix provide the variance, enabling the calculation of the uncertainty of each parameter.

After examining the uncertainties associated with each parameter, it became clear that the uncertainty of the off-diagonal term of the quadrupole coefficient χ_{xz} is close to its estimated value as -0.820 ± 0.763 MHz . Hence, the impact of the off-diagonal term on the root-mean-square (rms) of the fit is minimal. Therefore, we can confidently exclude it from our fitting procedure. The determined quadrupole parameter values are then compared with the fitted values obtained from the ground state calculation, as outlined in Table 4.1.

While comparing the results in Table 4.1 to those obtained from the ground state calculation, we see that the value of χ_+ is approximately identical. However, the value of χ_- differs significantly. Since quadrupole constants are model-dependent, this variance could be due to the implementation of a different theoretical model to calculate the expectation values of (2.20). In this calculation, we obtain the expectation value from the effective

Hamiltonian of a hybrid model, whereas ground state calculation is based on tunnelling Hamiltonian.

Table 4.2: The results of a global fit of 28802 transitions, including the rms value for A and E symmetry species for each torsional state for CH_3NH_2

	Previous study [52]			Present work		
Transitions[a]	Number[b]	WRMS[c]	RMS[d]	Number[b]	WRMS[c]	RMS[d]
Microwave $v_t = 0$	2288	1.07	0.088 MHz	2790	2.38	0.154 MHz
Microwave $v_t = 1$	137	1.39	0.154 MHz	2921	3.35	0.218 MHz
Microwave $v_t = 2$	–	–	–	40	3.04	0.289 MHz
MW A/B[e] species	1098	1.04		2287	3.03	
MW E[f] species	1327	1.13		3464	2.85	
Infrared v_t = 1 ← 0	11880	1.09	0.00053 cm^{-1}	11643	0.29	0.00015 cm^{-1}
Infrared v_t = 2 ← 1	–		–	6155	1.25	0.00063 cm^{-1}
Infrared v_t = 2 ← 0	–		–	5253	1.27	0.00064 cm^{-1}

	Present work		
Exp. Unc.[g]	Number[b]	WRMS[c]	RMS[d]
0.0008 cm^{-1}	23290	0.59	0.00047 cm^{-1}
0.020 MHz	390	4.45	0.089 MHz
0.045 MHz	210	3.89	0.194 MHz
0.060 MHz	3293	3.05	0.183 MHz
0.100 MHz	1626	2.12	0.212 MHz
0.200 MHz	105	1.33	0.257 MHz
0.500 MHz	127	0.48	0.238 MHz

[a] Transitions in the upper part of this table are grouped by their torsional v_t quantum numbers and/or symmetry species.
[b] Number of lines in the category of this row included in the fit.
[c] Weighted root-mean-square residual for the lines in this row.
[d] Root-mean-square residual in the units of measurement for the lines in this row.
[e] Microwave A_1 A_2 , B_1 and B_2 species.
[f] Transitions in the lower part of this table are grouped by assigned measurement uncertainty.

4.1.5 Fit with the hybrid formalism

During the fitting of the experimental data, an extensive global fit was performed on the 28802 transition of methylamine. Which includes the combination of experimental data for $v_t = 1 - 1$ and $v_t = 2 - 2$ from the current study, ground-state data obtained from a previous study [52, 89, 90], and far-infrared data obtained from our collaborating partner [92]. The global fit includes 2790 transitions from the ground torsional state ($v_t = 0 - 0$), 2921 newly assigned transitions from the first excited torsional state ($v_t = 1 - 1$), and 40 transitions from the second excited torsional state ($v_t = 2 - 2$) in the THz range, along with a far-infrared dataset involving 11643 lines from $v_t = 1 \leftarrow 0$, 6155 lines from $v_t = 2 \leftarrow 1$,

Table 4.3: List of main fitted parameters[a] and their corresponding values (in cm^{-1})[b] for CH_3NH_2.

ntrw[c]	Operator[d] × Params.	Present work	Previous study [52]
2200	$P_\alpha^2 \times F$	[15.1412489]	[15.08857388]
	$\frac{1}{2}(1-\gamma\cos 3\alpha) \times V_3$	695.320556(53)	682.911087(19)
2110	$P_\alpha^2 J_z \times$ RHORHO	0.64935371(10)	0.649355515(26)
2020	$J_z^2 \times$A	3.44098285(66)	3.40280(23)
	$J_x^2 \times$B	0.7256934(20)	0.72874862(31)
	$J_y^2 \times$C	0.75613394(18)	0.756180141(42)

[a]The product of the parameter and operator from a given row yields the term used in the torsion-rotation-tunneling Hamiltonian, except for F, ρ, and A, which occur in the Hamiltonian in the form $F(P_\alpha - \rho P_\alpha)^2 + AP_\alpha^2$, where γ in these operators is shorthand for $\gamma / \langle R|\,\gamma\,|R\rangle$ and so its matrix elements give only a $\pm$ sign to the final matrix element of the full operator expression (see [51]).
[b]All values are provided in cm^{-1}, except for RHORHO, which is unitless. The parameter value given in square parentheses (such as F) was fixed in our final fit at a value taken from an earlier fit where it was floated.
[c]The symbols t and r give the order of the torsional part and the rotational part of the operator, as defined in ([51]); w gives the wagging order, n = t + r + w gives the total order of the operator.
[d]The column contains the operator used in the hybrid Hamiltonian multiplied by the parameter adjusted in the least-square fit.

and lines from 5253 $v_t = 2 \leftarrow 0$.

As can be seen from Table 4.2, we achieve a global weighted standard deviation of 1.53 for 28802 transitions. The quality of the fit is satisfactory, although not completely within experimental uncertainty for the microwave transitions. The upper part of the table presents transitions grouped by their torsional v_t quantum numbers (and spectral range) and/or symmetry species. The rms we obtained for the fit of the ground torsional $v_t = 0-0$ state in the microwave spectral range is higher (154 kHz) than the rms obtained by the tunnelling approach (102 kHz), but we included 236 more lines in our fit (2790 lines instead of 2554 lines) than the previous study by Gulaczyk and Kreglewski (2020) [94]. We obtained an rms of 218 kHz for 2921 lines in the first excited torsional state $v_t = 1 - 1$. Only 214 transitions were accessible in the previous study [94], and these were fitted with an rms of 183 kHz. Finally, our data fit with an rms of 289 kHz for $v_t = 2 - 2$.

The lower part of the table shows root-mean-squared deviations grouped by assigned measurement uncertainty. The 79 floated molecular parameters (plus eight additional parameters, which were fixed at values from previous fits, such as $F, V_9, D_K, WCPG$ (which

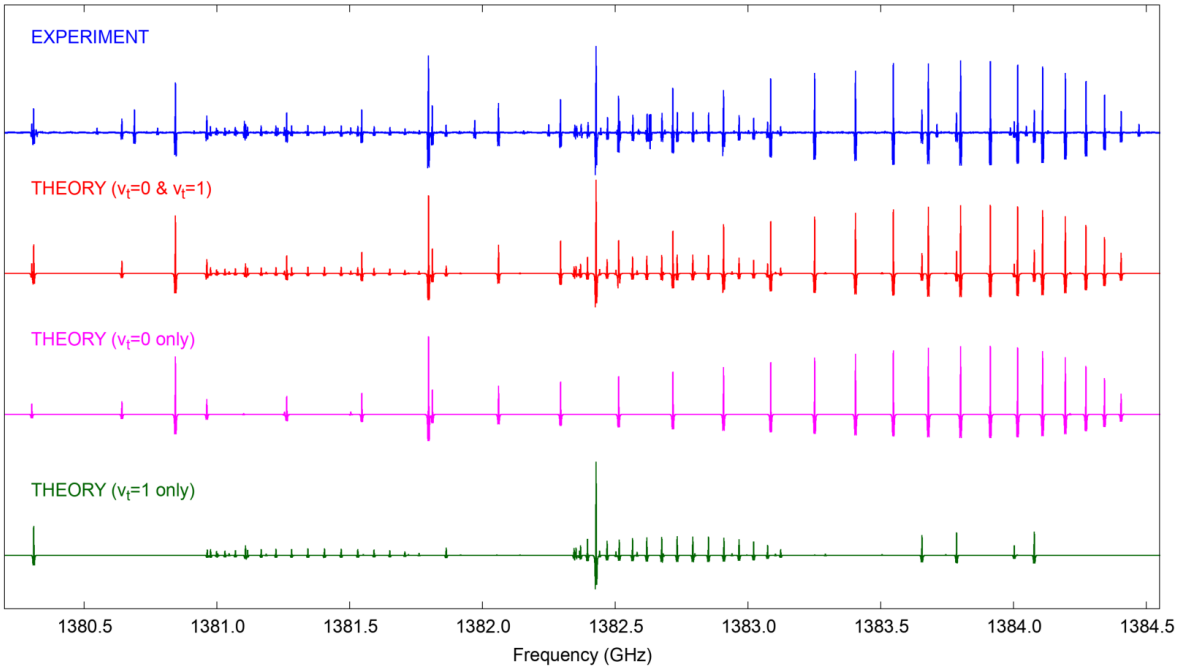

Figure 4.6: Observed (in blue) and predicted (in red) $v_t = 0 - 0$ and $v_t = 1 - 1$ rotational spectrum of methylamine around 1.38 THz. The individual contributions of $v_t = 0 - 0$ and $v_t = 1 - 1$ transitions are shown in magenta and green, respectively. Regular series of lines refer to ^{c}Q-type transitions with $K_a = 9 \leftarrow 8$ and symmetry selection rules: $E_1 \leftarrow E_1$ for $v_t = 0 - 0$, and $E_1 \leftarrow E_1$ (stronger) and $E_2 \leftarrow E_2$ (weaker) for $v_t = 1 - 1$

multiplies the $P_\gamma J_y$ operator), and some higher order K dependent parameters (see Table A.1 Gyawali et al. [92] provided in Appendix A) and compared to the 74 floated and two fixed parameters in the previous work, where a total of 15081 transitions were included [52]. The increase in the number of parameters is very reasonable considering that the number of lines increased by almost a factor of two.

We show a comparison between an experimental spectrum (in blue) and a simulated spectrum (in red) around 1.38 THz in Figure 4.6 to show how accurate the rotational transitions we calculated for methylamine in both its ground and first excited torsional states are in this study. Additionally, we provide individual contributions from the $v_t = 0 - 0$ and $v_t = 1 - 1$ transitions. Overall, the agreement in terms of both frequency and relative intensity is quite satisfactory. Within this frequency range, the majority of strong lines correspond to the $v_t = 0 - 0$ and $v_t = 1 - 1$ transitions.

While the hybrid model is not an ideal one, it still yields fairly precise results for excited states of methylamine. When analysing the first excited state of methylamine with

high precision, the rms is relatively high but remains close to the experimental accuracy. Furthermore, the data obtained from this study are useful for astrophysical applications.

4.1.6 Discussion

By comparing the sets of fitted parameters in table A.1 of Gyawali et al.[92], It is evident that we came up against problems in the current analysis that prevented us from achieving a fit within the experimental error for the available dataset. Indeed, as seen from Table 4.2, even for the torsional ground state, the weighted rms deviation for the microwave data is 2.38. The fact that we get greater rms deviation for the ground state in comparison with the previous fit with the tunneling approach is not surprising. This is because in the present study, we worked with a semi-global approach, which fits the data belonging to a number of torsional states with one set of parameters, and therefore the problems with fitting excited torsional states may also diminish the quality of fitting for the ground state. On the one hand, we are not able to rule out a situation where our current fit corresponds to some local minimum in the vicinity of the global minimum in the functional space of Hamiltonian parameters. Indeed, here we deal with the two large amplitude vibrational motions, which produce a rather complicated landscape in the Hamiltonian parameter space. The fact that a number of low-order parameters (such as V6, AXG, DAB: see e.g., Table A.1 of reference [92]) have changed sign in comparison with our first methylamine study using the hybrid approach [52] shows that, we included a larger number of lines from $v_t = 1$ and some lines from $v_t = 2$ states, but we could still be out of a global minimum with our fit. Further extension of the analysis to the second torsionally excited state may provide necessary information for improving the situation with the global versus local minimum by putting additional constraints on the Hamiltonian parameter set. On the other hand, this problem might be circumvented simply by finding an optimal set of high-order parameters in our Hamiltonian model that allows us to take into account all peculiarities of the energy level structure of the excited torsional states. Here, the fact that poorly fitted lines belong to high J and/or high K transitions —as mentioned above— may be considered as an argument in favor of this explanation. Although our search for the high-order Hamiltonian terms that could help to improve the situation was quite extensive, it was by no means exhaustive,

because this search is very time-consuming in view of the complexity of the Hamiltonian parameter space in the case of two coupled, large-amplitude motions.

A further possible explanation for the remaining problems with fitting the available dataset is the strong influence of intervibrational interactions arising from low-lying non-torsion vibrations in the molecule. In methylamine, the third excited torsional state is already close in energy to the NH_2 wagging mode (see e.g., Fig. 2 of reference [95]) and strong Fermi and Coriolis-type resonances have been reported for this state [96]. Therefore, it is quite probable that these perturbations propagate down through numerous inter-torsional interactions and affect the energy level structure of the lower torsional states. Our current model is not capable of explicitly taking these intervibrational interactions into account since the tunneling part of the hybrid approach represents only a separate wagging state (in our current case, this is the ground wagging state). Therefore, perturbations arising from this intervibrational interaction may only be taken into account indirectly by our current theoretical approach through some additional high-order wagging-torsion-rotation Hamiltonian terms with no guarantee that all the perturbations are accommodated in this way. It may be that it will be impossible to get a fit within experimental error for the current dataset without building a new theoretical approach allowing us to explicitly take into account the intervibrational interactions arising from nontorsion vibrations.

4.2 Weakly bounded water complexes

Water vapour stands as a significant greenhouse gas, and its presence in the atmosphere plays a crucial role in the climate system of the Earth [5, 97]. In our atmosphere, water complexes form as a result of weak bonding between water molecules and other molecules or ions, often involving hydrogen or van der Waals bonding. These complexes possess the capacity to exert various influences on atmospheric chemical reactions, acting as intermediaries, catalysts, or active participants in these processes. They have a substantial impact on the radiative balance, climate change, and the phenomenon of global warming [5]. Furthermore, these water complexes contribute to the generation of aerosols, which are minuscule airborne particles formed through processes such as nucleation. Aerosols exert both direct and indirect effects on the climate by scattering and absorbing sunlight

and serving as nuclei for the formation of clouds. Additionally, these complexes have implications for air quality, with potential consequences for human health. Particulate matter and pollutants influenced by water complexes can lead to respiratory and cardiovascular challenges.

The spectroscopic study of water complexes plays a pivotal role in improving the precision of atmospheric models [5]. This precision is crucial for advancing our comprehension of meteorological patterns, the dynamics of air quality, and the complexities associated with climate change [5, 7]. A thorough understanding of these complexes is essential for making well-informed decisions in shaping environmental policies and addressing the multifaceted issues related to climate and public health.

Due to the weak nature of bonding (usually van der Waals), individual molecules within the complex are able to rotate almost freely during the overall molecular rotation, which is basically the definition of a large amplitude motion. There have been several spectroscopic studies on weakly bounded small water complexes mostly in the microwave frequency range, such as $H_2O{-}CO$ [98], $H_2O{-}CO_2$ [99], $H_2O{-}OH$ [100, 101], $H_2O{-}HO_2$ [102, 103], $H_2O{-}H_2O$ [104, 105, 106, 107], $NH_3{-}H_2O$ [108, 109, 110] and so on. All these studies encountered problems of different difficulty levels due to large amplitude motions. One should also note that most of the studies were performed in the frequency range below 40 GHz as it is a typical limitation for pulsed jet microwave spectrometers. Whereas water complexes with small molecules are characterized by low mass and consequently high rotational constants. In this view, microwave studies do not provide enough information as they give access only to a limiting number of levels and transitions. Consequently, the measurements at millimeter and submillimeter waves are also important as it is shown in the case of $H_2O{-}H_2O$ [105].

As an example, consider the $H_2O{-}CO$ complex [98]. Due to limitations of spectrometer, only the transitions involving $K = 0$, $J \leq 3$ levels were observed. It was thus possible to determine an "averaged" value of B rotational constant and assume, the value of A rotational constant, and no information about C has been provided. The tunneling splittings due to water inversion motion were also observed and used for a rough estimation of the potential barrier height. However, no rigorous treatment of the tunneling problem was

performed due to the limited number of transitions.

Conducting a spectroscopic study of weakly bounded complexes in the mm/sub-mm wave range involves two fundamental challenges. The first challenge is to perform precise theoretical calculations that account for large amplitude motions. The introduction of special Hamiltonians is essential for precise computing of energy levels and for producing reliable spectrum predictions. There are also practical challenges on the experimental side. To achieve a sufficient concentration and to record high-resolution spectra, a supersonic-jet spectrometer with a fast-tunable high-power source is required. As pointed above, the majority of previous studies were concentrated in microwave due to availability of spectrometers. With the advances of relatively high-power agile and fully controllable electronic sources, the design of pulsed millimeter-wave spectrometers is greatly simplified. This is also the case of the Lille spectrometer which design is presented in Chapter 1. We used the Lille spectrometer coupled to a supersonic jet to observe and measure the millimeter-wave spectrum of ammonia-water $NH_3{-}H_2O$ complex as presented below.

4.3 Ammonia-water complex ($NH_3{-}H_2O$)

4.3.1 Introduction

Weakly bounded ammonia-water $NH_3{-}H_2O$ complex is formed through van der Waals interaction, where a nitrogen atom from ammonia forms a bond with a hydrogen atom in water. This specific molecule exhibits two large-amplitude motions: torsion of ammonia and inversion of water moieties. The structure of $NH_3{-}H_2O$ is presented in Figure 4.7 along with two angles that define two LAMs. In 1985, Herbine et al. [108] and in 1992, Fraser et al. [109] conducted microwave studies on $NH_3{-}H_2O$.

Both studies employed a series-wise calculation approach, which yielded distinct sets of rotational constants for each K_a value. Subsequently, in 1992, Stockman et al. [110] performed the measurements of pure rotational spectrum in the range 36–86 GHz and of tunneling ro-vibrational transitions between 520 and 800 GHz. This was the first study in which a systematic and global approach has been used in the analysis of the torsion-inversion-rotational problem. The analysis yielded two sets of parameters for each water

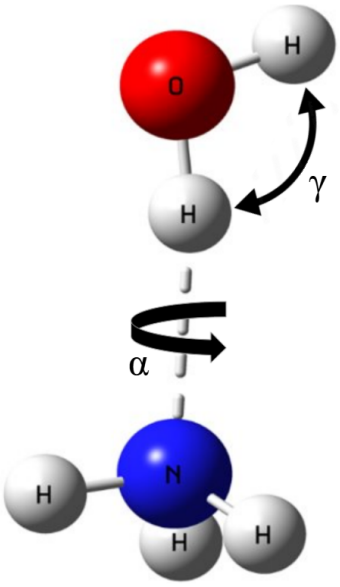

Figure 4.7: Structure of ammonia-water weakly bounded complex

tunneling substate although the residuals of fitted pure rotational and tunneling transitions were too high, above 1 MHz on average. Also, the torsional problem was not really solved, and the torsional barrier value was only assumed.

The spectroscopic study of the ammonia-water complex is crucial for understanding its molecular structure, hydrogen bonding, thermodynamic properties, and reactivity. By analyzing the rotational transitions, one can gain valuable information about the molecular structure, such as bond lengths, bond angles, and the strengths of inter-molecular interactions. The van der Waals bond between ammonia (NH_3) and water (H_2O) leads to a unique interaction, and studying it can provide insights into van der Waals dynamics and how the two molecules interact in a gas-phase environment.

4.3.2 Supersonic jet spectroscopy

Supersonic jet spectroscopy is a widely used technique in scientific research, particularly for studying the behaviour of weakly bound molecular complexes [111, 112]. This method has been employed by various research groups for many years and offers a valuable approach to investigating the structure and dynamics of such complexes. In supersonic jet expansion experiments, high-pressure gas from a reservoir is directed into an experimental chamber

where the pressure is significantly lower. The key feature of this process is that the ratio between the average distance a gas molecule travels between collisions (called the mean free path) and the dimensions of the nozzle is extremely small [113]. Because the mean free path is so much smaller than the nozzle dimensions, there are many collisions among gas molecules as they exit the nozzle. This results in rapid adiabatic cooling, which means that the gas cools down without exchanging heat with its surroundings [114]. This cooling process converts the gas's internal energy into directed kinetic energy, causing the gas to flow at supersonic speeds.

These specific conditions generated through supersonic expansion offer several advantages:

- **Spectral Simplification:** The rapid cooling leads to a significant reduction in the rotational temperature of the molecules. This reduction simplifies the resulting high-resolution spectra, making them easier to analyse.
- **Sub-Doppler Resolution:** The alignment of the Jet nozzle allows researchers to achieve sub-Doppler resolution. Doppler broadening is a phenomenon where spectral lines are broadened due to random thermal motion, but in this case, the motion is highly organised, leading to sharper lines in the spectra.
- **Molecular Complex Formation:** The high collision rate in the expansion zone promotes the formation of molecular complexes and clusters. These are groups of molecules held together by long-range interaction forces.

In the context of gas expansion, gas beams can indeed be categorized into effusive beams and supersonic beams based on their characteristics [115].

Effusive Beam: An effusive beam is formed when the gas expands through a small orifice or nozzle where the diameter of the orifice (D) is much smaller than the mean free path length (λ) of the gas molecules ($D << \lambda$). In this scenario, gas molecules exit the nozzle at relatively low speeds and form a slower-moving, coherent beam. Effusive beams are characterized by a broader velocity distribution and are often used in experiments requiring the controlled and precise delivery of gas molecules to a target or sample.

Supersonic Beam: A supersonic beam is formed when the gas expands through a larger orifice where the diameter of the orifice (D) is much larger than the mean free path length (λ) of the gas molecules ($D >> \lambda$). In this case, gas molecules exit the nozzle at

high speeds due to the significant pressure difference, and the resulting beam exhibits a narrower velocity distribution. Supersonic beams are used in experiments where high velocities and kinetic energies are desired for studying fast reactions, dynamics, and spectroscopic observations.

Indeed, the supersonic expansion process is quite dynamic and involves a multitude of factors that influence the behavior of gas molecules within the expanding jet. Understanding and characterizing this process is crucial for various experimental applications. Analytical and empirical formulas have been developed to estimate key thermodynamic properties like temperature, pressure, and density across the jet's expansion, providing insights into how these properties change as the gas expands. The Mach number (M) is a fundamental parameter in supersonic flow and characterizes the ratio of the velocity of the jet (u) to the local speed of sound (a): $M = \frac{u}{a}$ [116]. It plays a pivotal role in categorizing different regimes within the expanding jet. When $M < 1$, the flow is considered subsonic. Here, the velocity of the gas is lower than the speed of sound, and the flow behavior is relatively predictable. When M ≈ 1, the flow is transonic, where the flow transitions between subsonic and supersonic speeds. This is often a complex regime with shock waves and other flow phenomena. Finally, when $M > 1$, the flow is supersonic. In this regime, the velocity of the gas exceeds the speed of sound, leading to rapid expansion and dynamic behavior.

The key advantage of this technique is that it allows one to probe these cold molecular complexes in a collision-free environment. Furthermore, this technique can be useful in testing and improving interaction potentials for weakly bound molecular species. Such phenomena describe how molecules interact with each other and are essential for understanding and predicting molecular behavior.

4.3.3 Doppler effect

The Doppler effect is a phenomenon observed in waves, such as sound and light waves, when there is relative motion between the source of the wave and an observer. When an

electromagnetic (EM) wave propagates along the z axis, or, equivalently, when the wave vector $\vec{k}$ is parallel to the z axis, the frequency of the wave perceived by a moving molecule is shifted due to the Doppler effect and may express as :

$$f = f_0 \left(1 + \frac{u_z}{c}\right) = f_0 \left(1 + \frac{u}{c}\cos\theta\right) \tag{4.15}$$

where f_0 is the frequency emitted by the source, u_z is the projection of molecular velocity vector $\vec{u}$, c is the speed of sound, and θ is the angle between $\vec{k}$ and $\vec{v}$.

In a typical pulsed jet FTMW experiment [16], molecules are injected into a Fabry-Perot cavity parallel to its optical axis. This results in the well-known phenomenon of Doppler doublets. The EM field created inside the cavity is characterized by two anti-parallel wave vectors $+\vec{k}$ and $-\vec{k}$ producing two distinct Doppler shifted components corresponding to the values of θ in (4.15) of $\theta_+ = 0°$ and $\theta_- = 180°$. The ratio of frequency shift to actual resonance frequency may be thus expressed as :

$$\frac{\delta f^{\pm}}{f_0} = \frac{u}{c}\cos\theta^{\pm} = \pm\frac{u}{c} \tag{4.16}$$

The actual resonance frequency is determined by taking the mean of these two observed frequencies and can be mathematically represented as [117]:

$$f_0 = \frac{\delta f}{2} \tag{4.17}$$

Additionally, the velocity of molecules can be computed from doublet splitting using the formula:

$$u = \frac{c}{2}\frac{\delta f}{f_0} \tag{4.18}$$

Since the splitting between observed doppler doublets ($\delta\nu$) varies with frequency, the $\delta\nu$ value increases at higher frequencies if molecular velocity remains constant.

When molecules are injected perpendicular to the propagation of EM waves, the Doppler shift is suppressed since in this case, $\theta = 90°$. The negative side of perpendicular injection is shorter interaction distance between molecules and the EM field, as well as time-of-flight broadening effect that both result in weaker molecular signals. Perpendicular injection is however much easier in implementation in millimeter and submillimeter waves

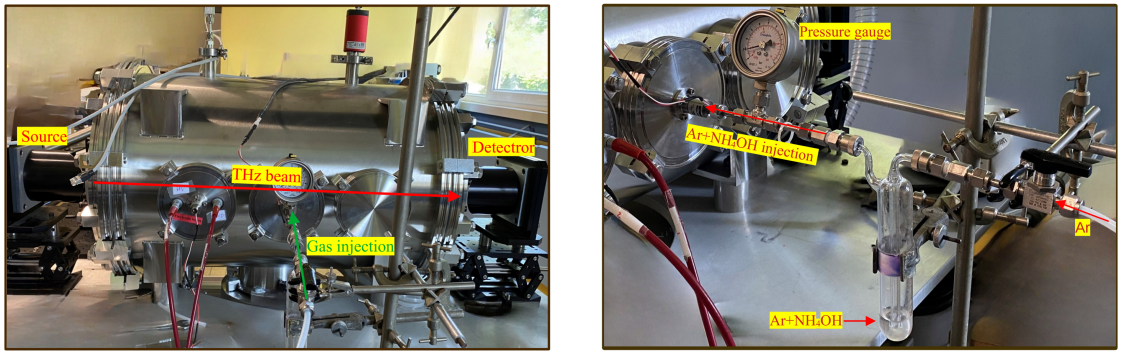

(a) (b)

Figure 4.8: (a) Photo of high-vacuum chamber coupled to chirped-pulse spectrometer (b) Detailed view of the bubbler with NH_4OH solution used to produce $NH_3{-}H_2O$ complex in pulsed supersonic jet

in case of cavity-free propagation of EM waves. In this case, one do not have to optimize the geometries of emitting and detecting horn antennas with the injector to maximize the interaction zone of propagating EM and molecular beams.

4.3.4 Measurement of $NH_3{-}H_2O$ spectra

The rotational spectrum of $NH_3{-}H_2O$ was recorded in millimeter-wave range between 49 and 220 GHz using the Lille hybrid spectrometer coupled to a supersonic jet. The complete design of the spectrometer is described in Chapter 1. Figure 4.8a shows the photo of 60 L high-vacuum chamber in which supersonic expansion takes place. The low pressure in the high-vacuum chamber is maintained by a 700 L/s turbmolecular pump backed by a standard rotary vane pump with a pumping speed of 40 m^3/h. The chamber is equipped with 6 flanges on which a pulsed injector may be installed, but due to current technical limitations, only one injector was used to produce a supersonic expansion. As it can be seen from the photo, we used a perpendicular injection of molecules.

To observe $NH_3{-}H_2O$, we injected a mixture of Ar and NH_4OH (32 %) into a pulsed nozzle at a rate of 2 Hz. The back-in pressure of Ar was maintained at approximately 0.5–1 bar, while the pressure inside the cell was 1–2 µbar taking the injection rate into account.

We performed two series of measurements of $NH_3{-}H_2O$ complex. At first, we used standard conditions, at which the mixture of Ar and NH_4OH was injected directly into the

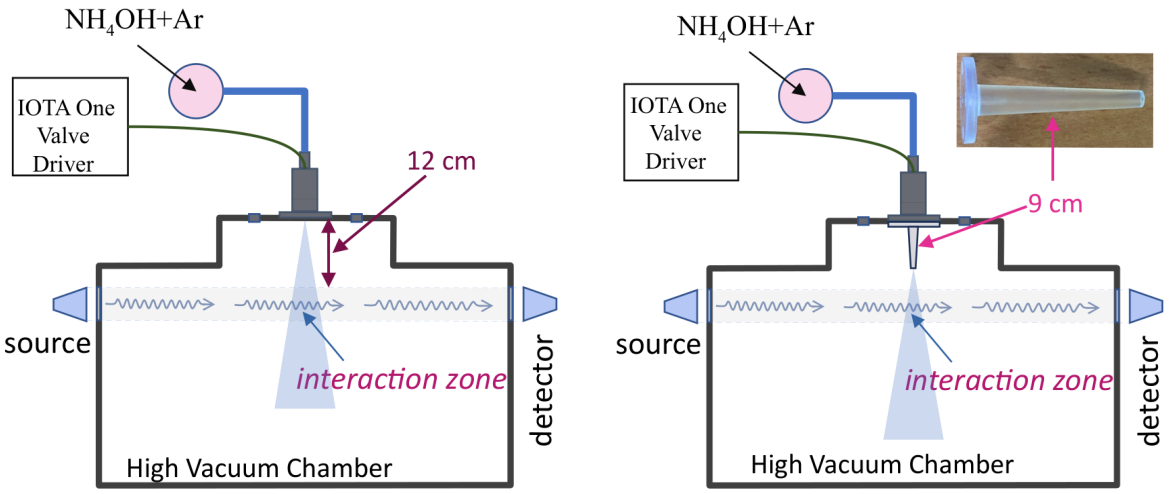

Figure 4.9: Schematic view of the high-vacuum expansion chamber with (a) standard injection; and (b) with installed additional 9 cm nozzle

Table 4.4: Observed Doppler doublets and deduced central frequencies compared with the frequencies of unresolved lines

f^a (MHz)	f_0^b (MHz)	δf^c (MHz)	$f_0'^d$ (MHz)
73877.918 73878.179	73878.049	0.261	73878.050
85907.822 85908.111	85907.967	0.289	85908.000
85963.701 85964.000	85963.850	0.299	85963.800
98208.742 98209.072	97814.887	0.330	98208.850
110352.174 110352.538	110352.356	0.364	110352.300

[a]Frequency of Doppler component.
[b]Mean frequency of Doppler components.
[c]Interval between two Doppler components.
[d]Frequency of a Doppler-free transition observed without a nozzle as illustrated in setup Figure 4.9a.

cell through a pulsed nozzle. For this case, a typically observed spectral line is shown in Figure 4.10a. The main contributions to the line width are: (i) time-of-flight broadening and (ii) the effect of the FFT window function [118]. For example, in the range 75–110 GHz, the observed line width varied from 0.4 to 0.6 MHz.

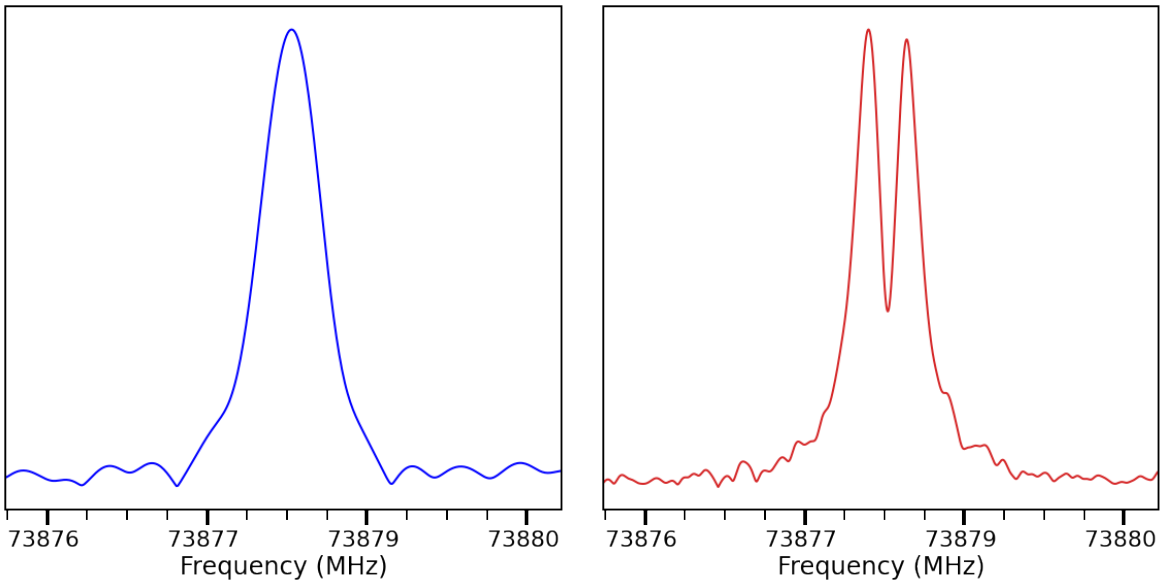

(a) (b)

Figure 4.10: A comparison of the frequency domain signal at the specific frequency of 73 878 MHz (a) previous setup 2022 as shown in Figure 4.9a (b) improved experimental set up as shown in Figure 4.9b

During the analysis of the recorded spectra, we came to the conclusion, that we need to increase the rotational temperature of the jet in order to observe transitions between higher energy levels (with $K_a \geq 3$). For this reason, we performed a second series of experiments in which we tried to probe the initial part of the jet which is characterized by higher molecular density and warmer gas [119]. The difference between two experimental setups is shown in Figure 4.9. In the first experiments, the injector output was placed approximately 12 cm out of the interaction zone which represents a cross-section of molecular and EM radiation beams. For the second series of experiments, at the output of the pulsed valve, we installed a second nozzle which diameter matches the diameter of the pulsed valve orifice. The nozzle was 3D printed using a special polymer material suitable for high-vacuum applications. The length of the nozzle was chosen to be 9 cm in order to probe the initial part of the jet.

The new nozzle was first tested using the rotational lines of CH_3CN and CH_3OH. The tests showed that the rotational temperature of supersonic jet does not change and remained approximately 15 K. However, an important effect of increased spectral resolution was observed. An example is shown in Figure 4.10 where we compare the same spectral line

of NH_3-H_2O recorded in both experiments. Compared to the first experiment, the length of the time-domain FID is almost tripled indicating an increase in spectral resolution by the factor of three. Also, in the new experiment we observe the Doppler doublet effect which is also an indirect indicator of increased spectral resolution. To show, that the observed doublet is caused by the Doppler shift described by (4.16), in Table 4.4 we present selected frequencies of NH_3-H_2O rotational lines with their doublet components. The splittings δf increase almost linearly with the excitation frequency f_0 as predicted by (4.16). The origin of the doublet remains however not completely understood. We suppose that at the output of the additional nozzle, molecular jet is not to strictly normal to EM wave $\vec{k}$ vector, but is rather characterized by two jet velocity components that are symmetrically distributed around normal propagation direction with the angles θ and $\pi - \theta$ relative to $\vec{k}$. Owing to non-perpendicular propagation, the interaction length of the two molecular beams with EM field increases which reduces the time-of-flight-broadening and consequently increases spectral resolution. Therefore, we observe two Doppler components shifted by $\pm f_0 \frac{u}{c} \cos\theta$ with respect to the frequency f_0. The symmetry of the velocity components may be verified by comparing the f_0 frequencies obtained from unresolved single peak analysis in the first stage of our experiment with the f_0 determined as a mean frequency of Doppler doublets (Table 4.4). As one can see, for each rotational transitions, the f_0 obtained by two methods agree within experimental measurement accuracy (0.05 MHz).

Increased spectral resolution had positive effect on spectral analysis as it will be explained below. Nevertheless, the problem of increasing the rotational temperature of the jet is currently remained unsolved and has to be addressed in the nearest future.

4.3.5 Estimation of rotational temperature

The rotational temperature of a molecule can be calculated using the Boltzmann diagram analysis, which is based on the integrated intensities of the observed spectral lines. In this approach, the integrated peak intensity I_p of spectral line may be expressed as [120]:

$$I_p = \int_{-\infty}^{\infty} I d\nu = \frac{hc^3 A g_u}{8\pi k \nu^2} \frac{N_T}{Q(T_{rot})} \exp(-E_u/kT_{rot}) \tag{4.19}$$

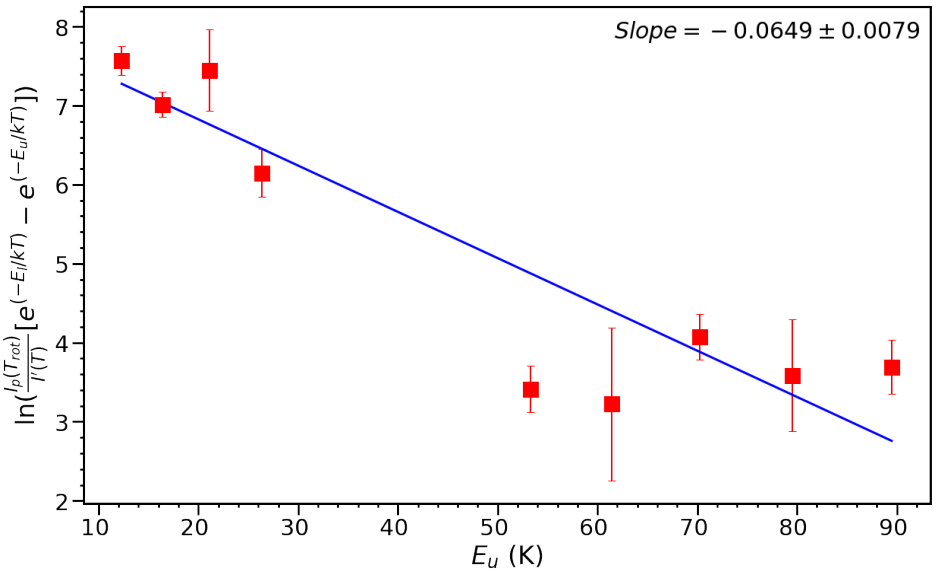

Figure 4.11: Boltzmann diagram for R-type $K_a = 0 \leftarrow 0$, A/B series of transitions of $NH_3{-}H_2O$

where E_u is the upper-state energy, h is the Planck's constant, k is Boltzmann's constant, c is the speed of light, A is the Einstein A-coefficient for the transition, g_u is the upper state degeneracy, ν is the transition frequency, N is the column density, $Q(T_{rot})$ is the rotational partition function for the rotational temperature T_{rot}.

Ignoring constant terms in (4.19) one can write:

$$I_p \propto \frac{Ag_uN}{\nu^2 Q(T_{rot})} \exp(-E_u/kT_{rot}) \tag{4.20}$$

or equivalently:

$$\ln I_p - \ln \frac{Ag_u}{\nu^2} = \ln \frac{N}{Q(T_{rot})} - \frac{E_u}{kT_{rot}} \tag{4.21}$$

The Einstein A-coefficient can be expressed via the integrated absorption cross-section $I'(T)$ at a given temperature T as [121]:

$$A = I'(T)\frac{\nu^2 Q(T)}{g_u}\left[e^{-\frac{E_l}{kT}} - e^{-\frac{E_u}{kT}}\right]^{-1} \times \Lambda \tag{4.22}$$

where Λ is a coefficient allowing the calculation of A in s^{-1}, when I' is expressed in nm^2MHz/molecule and ν in MHz. From (4.22) one can express the logarithm of the product $\frac{Ag_u}{\nu^2}$ as:

$$\ln \frac{Ag_u}{\nu^2} = \ln I'(T) - \ln\left[e^{-\frac{E_l}{kT}} - e^{-\frac{E_u}{kT}}\right] + \ln \Lambda Q(T) \tag{4.23}$$

The combination of (4.23) and (4.21) yields the following equation:

$$\ln\left(\frac{I_p(T_{rot})}{I'(T)}\left[e^{-\frac{E_l}{kT}}-e^{-\frac{E_u}{kT}}\right]\right)=-\frac{E_u}{kT_{rot}}+\text{intercept} \tag{4.24}$$

that gives a linear relationship between $\ln I_p(T_{rot})$ and upper state energy E_u and which slope is inversely proportional to T_{rot}.

To estimate T_{rot}, we used measured integrated intensities of the ${}^aR$-type $K_a = 0$ series of transitions of A and B symmetry covering the range of J values from 6 to 17, excluding J values of 10, 11, and 12. The same series of transitions were also fitted in a linear rotor approximation using SPFIT code to yield pseudo-rotational and centrifugal distortion constants B and D. These constants, together with μ_a dipole moment component were used to calculate corresponding absorption cross-sections $I'(T)$ at $T = 300$ K using SPCAT code, as well as the Boltzmann coefficients. We then plotted the calculated values of $\ln\left(\frac{I_p(T_{rot})}{I'(T)}\left[e^{-\frac{E_l}{kT}}-e^{-\frac{E_u}{kT}}\right]\right)$ as a function of E_u. The plot as well as its linear approximation is shown in Figure 4.11. From the slope of the linear function, the determined rotational temperature is 15.4(18) K. It is in agreement with rotational temperatures determined in previous experiments with pulsed supersonic jet on the molecules like CH_3NH_2 and CH_2NH.

One can note that the alignment of plotted points is rather poor which is also the origin of relatively high uncertainty of the determined T_{rot}. There may be several sources of errors that are not easy to take into account. They include: source power and back-in gas pressure variations, as well as pulsed valve instabilities. The latter may result in significant amplitude variations and are very difficult to control. Nevertheless, the tendency of the intensity decrease with increasing E_u was observed and thus could be exploited.

4.3.6 Spectral analysis

NH_3−H_2O is a near-prolate asymmetric rotor with a Ray asymmetry parameter of κ = 0.99. Due to almost symmetric configuration, it has only one large non-zero component $\mu_a = 2.98$ D, whereas $\sqrt{\mu_b^2+\mu_c^2} = 0.52$ D [108]. The structure and dipole moments imposes tight clustering of a-type $\Delta J = 1$ rotational transitions within a narrow frequency range. The frequency range of each a-type $\Delta J = 1$ series is further reduced due to low rotational tem-

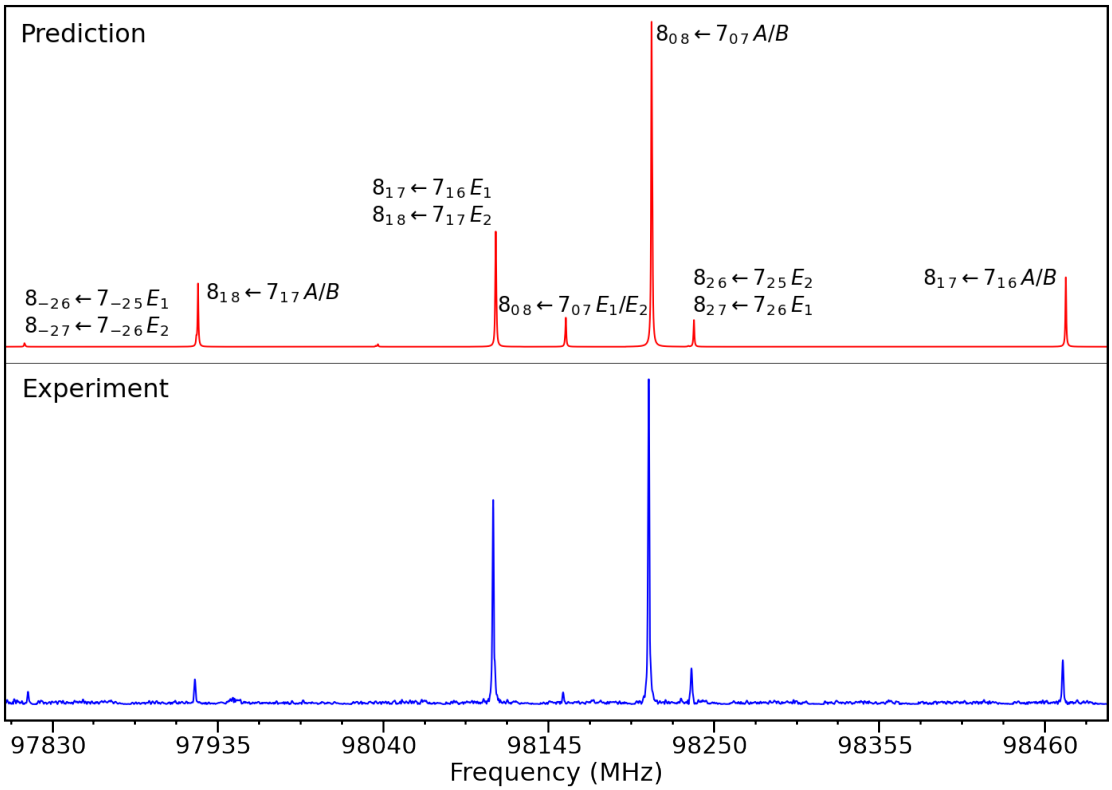

Figure 4.12: Portion of the predicted at $T_{rot} = 15$ K, and observed rotational spectrum of ammonia-water showing a cluster of $J = 8 \leftarrow 7$ transitions. All observed transitions are assigned

perature that allows only the levels with $K_a \leq 2$ to be significantly populated. Figure 4.12 demonstrates predicted and observed $J = 9 \leftarrow 8$ rotational transitions of NH_3—H_2O congested roughly in the bandwidth of 750 MHz with the center around 110.4 GHz.

For the analysis of the rotational spectrum of ammonia-water complex we used the same hybrid formalism as for methylamine. The principal difference between two molecules is that in the case of ammonia-water we have to deal with a very low torsional motion barrier, $\approx$20 cm^{-1}, and relatively high inversion barrier of 700 cm^{-1}, whereas both barriers in methylamine may be considered as relatively high. Due to relatively high inversion barrier, the inversion splittings in the pure rotational spectrum are small and were not resolved in the first series of measurements as it can be seen in Figure 4.12 where the transitions of symmetries A/B and E_1/E_2 are grouped under the same spectral line. One can also notice large torsional splittings even for low-K_a values caused by very low barrier and strong torsion-rotational coupling ($\rho = 0.7$). As such, this rotational spectrum could be analysed

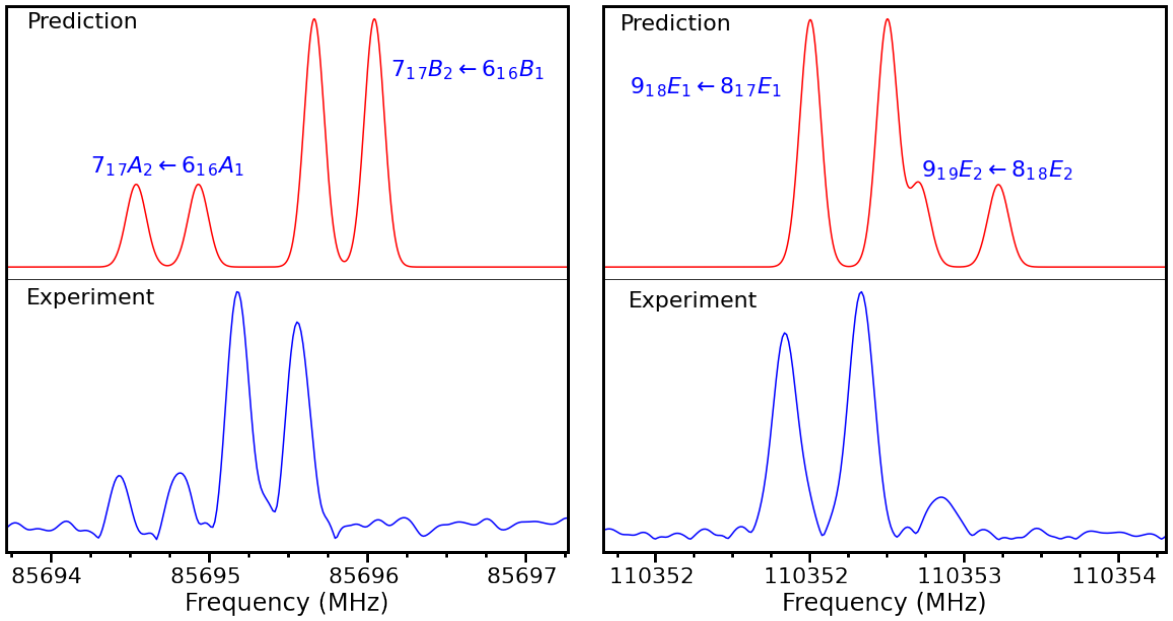

Figure 4.13: Examples of resolved inversion splitting in the pure rotational spectrum of ammonia-water complex

using a simplified approach in which only the torsional motion was considered. We used RAM36 program to fit the assigned transitions with unresolved inversion splittings. The weighted rms obtained in the fit was relatively high, 8.3. Nevertheless, the results of the fit permitted to predict and assign new transitions. We therefore suppose that the major error in the fit was induced by ignoring the inversion problem which not only causes relatively small splittings of rotational transitions, but also shifts their frequencies. We thus showed that the analysis using torsion-rotational Hamiltonian is not sufficient for precise description of spectrum. Whereas the results of the fit were not really satisfactory, they provided us with the guidelines on the values of main torsional Hamiltonian parameters such as ρ, V_3 and F.

The second series of experiments with improved spectral resolution allowed us to observe inversion splittings as it is illustrated in Figure 4.13. The right figure represents a completely resolved $A : B$ inversion doublet with characteristic distribution of relative intensities 1:3 owing to spin statistics. In the left figure the Doppler doublets of $E_1 : E_2$ transitions are overlapped forming a slightly more intense central peak, but overall agreement between theory and experiment is achieved.

In total, in the present study, we assigned 106 a-type transitions of ammonia-water complex, covering rotational quantum numbers up to $J = 15$ and $K_a \leq 2$. Together with 53 transition from previous studies, the newly assigned lines were fitted to a hybrid model containing 19 parameters. The weighted standard deviation of the fit is 1.62, with 106 lines from the present work fitted with an rms of 0.088 MHz and the remaining 53 lines fitted with an rms of 0.439 MHz. The determined values of the rotational constants are provided in Table 4.5. Despite relatively high weighted rms deviation the current fit represents significant progress in the analysis of ammonia-water rotational and inversion-rotational spectrum. Compared to the study of Stockman et al. [110], we reduced the number of fitted parameters by the factor of two. It should be also noted that most of the data used by Stockman et al. contains torsional-rotational transitions, and only 7 pure rotational transitions were included.

Overall, the current situation with the fitting of ammonia-water spectrum is the following. We have two rather distinct sets of data: pure rotational spectral assignments obtained in the present study from millimeter-wave measurements, and torsional bands assignments of Stockman et al. [110] in submillimeter-wave range. Using the hybrid approach we are not able yet to combine the two datasets in a single fit. As it is mentioned above, the combined fit includes only 56 transition from [110] whereas the full dataset of that publication contains 260 lines. Also the measurement accuracy of the submillimeter-wave measurements is 10 to 20 time lower compared to out study. To our opinion, to correctly solve torsion-rotational problem one first has to solve torsional problem which in the case of ammonia-water should also include the solution of inversion tunneling problem. In these terms, the increased spectral resolution achieved using the additional 9 cm nozzle had a significant positive effect on the analysis as it allowed us to apply the hybrid model and to define the inversion term in the Hamilatonian. Nevertheless, some problems remain unsolved. From a detailed comparison of simulated and observed transitions in Figure 4.13 one can see that our current hybrid model overestimates the inversion splitting between A and B or E_1 and E_2. At the same time, current fit contains only one inversion (wagging) parameter: WAG2 in Table 4.5.

Therefore, we need more pure rotational data for better determination of torsional and

Table 4.5: Molecular parameters[a] (in cm^{-1})[b] determined from the dataset for NH_3-H_2O and also compared to the previous results.

ntrw[c]	Operator[d]× Params.	Present work	Previous study [110]
2200	$P_\alpha^2 \times F$	32.978(39)	-
	$\frac{1}{2}(1-\gamma\cos 3\alpha)\times V_3$	23.8(1)	[10.5 Fixed]
2110	$P_\alpha^2 J_z\times$ RHORHO	0.64842(65)	-
2020	$J_z^2\times$A (MHz)	235403.8161(17)	147608.29(30)
	$J_x^2\times$B (MHz)	6067.4995(21)	6168.860(75)
	$J_y^2\times$C (MHz)	6042.7338(13)	6110.556(49)
	$\gamma\{J_x, J_z\}\times$DAB	-0.04159(12)	-
2002	1 ×WAG2	-0.000954(21)	-
4220	$(1-\gamma\cos 3\alpha)J^2\times$FV	0.00296(18)	-
	$(1-\gamma\cos 3\alpha)(J_x^2-J_y^2)\times$C2	0.001571(75)	-
	$\gamma P_\alpha^2\{J_x, J_z\}\times$DELTA	0.02349(88)	-
4130	$P_\alpha^2 J^2 J_z\times$ ALV	0.0000943(64)	-
	$P_\alpha\{J_z, (J_x^2-J_y^2)\}\times$C4	-0.00000496(38)	-
	$P_\alpha(J_z^2, J_x)\times$ODELTA	-0.02243(81)	-
4040	$-J^4\times$DJ	$1.070(59)\times10^{-6}$	-
	$-2J^2(J_x^2-J_y^2)\times$ODELN	$4.019(79)\times10^{-9}$	-
6240	$(1-\gamma\cos 3\alpha)J^4\times$OFV	$-1.031(60)\times10^{-7}$	-
6042	$P_\alpha J^4 J_z\times$OLV	$5.670(27)\times10^{-9}$	-
6060	$J^6\times$HJ	$-1.418(15)\times10^{-11}$	-

[a]The product of the parameter and operator from a given row yields the term used in the torsion-rotation-tunneling Hamiltonian, except for F, ρ, and A, which occur in the Hamiltonian in the form $F(P_\alpha-\rho P_\alpha)^2 + AP_\alpha^2$, where γ in these operators is shorthand for $\gamma/\langle R|\gamma|R\rangle$ and so its matrix elements give only a $\pm$ sign to the final matrix element of the full operator expression (see [51]).
[b]All values are provided in cm^{-1}, except for A, B, C, which are expressed in MHz, and RHORHO is unitless.
[c]The symbols t and r give the order of the torsional part and the rotational part of the operator, as defined in ([51]); w gives the wagging order, n = t + r + w gives the total order of the operator.
[d]The column contains the operator used in the hybrid Hamiltonian multiplied by the parameter adjusted in the least-square fit.

inversion parameters but also to remove correlations between them. For the measurements of pure rotational transitions in millimeter-wave range, we currently achieved our sensitivity limit.

From Figure 4.12, one can see that we assigned all observed transitions in the spectrum. The intensity of $K_a = 3$ transitions compared to $K_a = 2$ drops by almost two orders of magnitude. To observe them, we thus have to increase the observation time by the

factor of 4 which is quite hard to achieve assuming that one also has to maintain constant all experimental parameters during integration of spectral records. That is why we were looking for a solution to increase the rotational temperature of the jet that will increase the population and hence the intensity of transitions involving higher values of K_a. And this experimental problem still has to be solved in the nearest future.

4.4 Conclusions

This chapter provides a concise overview of our research, which focuses on the analysis of the rotational spectra of molecules exhibiting two large amplitude motions (LAMs): torsion and inversion and, in particular, on the application of the hybrid approach for fitting and predicting rotational spectra. The two molecules considered here: methylamine and ammonia-water represent good benchmark cases. For methylamine which may be characterized as "medium torsion - high inversion barrier" case, we were able to characterize for the first time its first excited torsional state $v_t = 1$ with almost experimental accuracy. Using Loomis-Wood plot and based on the hybrid model predictions, we were also able to accurately assign $v_t = 2$ state. We have shown that the hybrid approach may be also applied in the case of “low torsion - medium inversion barrier” for ammonia-water complex. In this case, we have also presented the current experimental limitations that hamper the application of highly non-linear models for spectral analysis. In particular, the quest has to be solved for obtaining a large dataset of molecular transitions involving many different energy levels, as it is the only solution to accurately determine the key model parameters and to remove or reduce the correlations between them.

Summary

The dissertation is primarily structured into two sections: the first part focuses on experimental instrumentation, while the second part delves into laboratory spectroscopy, although some additional experimental details are also given in Chapter 4 of the second part.

In the main instrumentation part of my thesis, the primary achievement is the successful development of a new DDS-based up-converter suitable for broadband chirped-pulse rotational spectroscopy in millimeter-wave range. The custom-built DDS-based up-converter offers a significant advantage in high-resolution spectroscopy, serving as a more efficient alternative to standard arbitrary waveform generators for producing chirped pulses. This DDS-based source is capable of generating both single-frequency and chirped pulses, with a maximum achievable bandwidth of chirped pulses beyond 500 MHz which is the limiting bandwidth of the ADC card used in the spectrometer. As a next step we can therefore consider the acquisition of a new ADC card with a larger bandwidth. We presented the design of the up-converter and the parameters of its key elements. In addition, we developed new 2.5 GHz reference synthesizer for the DDS and showed how it improves the spectral purity of the output signal. We can expect the enhancement of sensitivity of the spectrometer; new measurements have to be performed for confirmation. Finally, we also developed a new method for optimal digital band-stop filtering of the FID signal. The new method permitted more efficient use of the lower frequency part of chirped pulse spectrum. We thus increase the effective frequency range of the chirped-pulse excitation which is especially useful in the case dual-direction mode excitation. Ultimately, the new spectrometer that includes all the developments in the frame of the thesis presented above was applied in coupling with pulsed molecular jet system to measure the rotational spectrum of ammonia-water complex in the range 49–220 GHz using segmented method.

In the second part of this dissertation, the focus shifts towards the analysis of the rotational spectra of molecules exhibiting LAMs. During these investigations, we analysed the rotational spectra of several species of atmospheric interest in the THz range. Our primary focus in this study was to gain a deep understanding of periodic large-amplitude motion and its influence on pure rotational spectra. We separated the molecules according to the

level of complexity. First, we provided the analysis of molecules characterized by a single internal rotor of C_{3v} symmetry.

Acetyl chloride and acetyl bromide (CH_3COCl and CH_3COBr): We were able to assign and analyse more than 20000 rotational transitions of the two species in the ground and two lowest excited vibrational states. It represents a huge increase in the number of measured transitions and in the range of quantum numbers such J and K_a. We are able to determine the relationship between the splitting of the A and E symmetry transitions with the K_a quantum number and vibrational state. Another crucial outcome of our research is the analysis of the nuclear quadrupole hyperfine structure of both species. We produced the sets of rotational and torsion-rotational parameters that permit the description of the rotational spectra of acetyl chloride and acetyl bromide with experimental accuracy. We also provided accurate description of the potential function for the methyl group torsional motion. We demonstrated how to use the inertia moment of the internal rotor in the evaluation of the overall quality of the least-squares fit in addition to standard criteria like rms deviation. Overall, we showed that RAM Hamiltonian is the most suitable model for the analysis of a single internal rotor of C_{3v} symmetry. Despite its efficacy, we also demonstrate that the RAM Hamiltonian has a drawback which consists in the effective nature of rotational constants A, B, and C. It is thus impossible to use these parameters for accurate molecular structure determination, since the rotational constants are averaged over all vibrational states in the global analysis. They may be also affected by the correlation with higher order centrifugal distortion terms. The results of the two studies may be used to model the rotational spectra of CH_3COCl and CH_3COBr in the THz range for further application for in- or ex-situ observations. The results are also an important contribution for the analysis of the ro-vibrational spectra for which the accurate knowledge on the ground state energy levels is required. In perspective, the studies of acetyl halides could be extended to CH_3COI and CH_3COF. The former would give even more complex hyperfine patterns because of its spin $I = 5/2$, whereas the latter, in the absence of quadrupole splitting would nevertheless present more complications due to reduced mass and consequently increased torsional-rotational coupling (compared to CH_3COCl and CH_3COBr).

By increasing the level of complexity we turned to the molecules that exhibit two LAMs.

In this context, our primary goal was to benchmark the recently developed "hybrid" approach to the analysis of torsional and inversion motions. The approach combines the global description containing explicit expressions for the kinetic energy operator and the three-well potential energy operator, and effective modelling of inversion motion in a tunneling formalism. It is thus suited for the cases where tunneling formalism has previously produced unsatisfactory results: medium to low torsional barriers, or excited torsional states.

Methylamine CH_3NH_2: We remeasured the rotational spectrum of methylamine in the range 0.15–1.52 THz with a special focus on high amplitude resolution for the lines of excited vibrational states. Owing, in particular, to the high amplitude resolution of recorded spectra we assigned about 4400 lines of the rotational transitions of methylamine in the first and second excited torsional states. The assignment was greatly facilitated by the Loomis-Wood plots. We analyzed nuclear quadrupole hyperfine structure of $v_t = 1$ rotational lines of methylamine and produced "dehyperfined" frequencies. The global analysis of methylamine performed in collaboration with I. Kleiner includes all the $v_t = 1$ transitions from this study as well as the data from previous studies on the ground state pure rotational spectra and on the FIR ro-vibrational spectra. Although, the global analysis using the "hybrid" model did not attain experimental accuracy, we obtained the most accurate description of the rotational spectrum of methylamine in the ground and lowest excited torsional states. The data on $v_t = 1$ spectrum from our study enable the detection of $v_t = 1$ rotational lines of methylamine in the interstellar medium [92]. In perspective, owing to high amplitude resolution and SNR of the recorded spectra, the assignment of $v_t = 3$ rotational transitions is also realizable.

Ammonia-water complex NH_3–H_2O: Millimeter-wave spectra of ammonia-water complex were measured in the frequency range 49–220 GHz. As methylamine, ammonia-water exhibit torsional and inversion LAMs although characterized by much lower barriers. We assigned all 106 observed rotational transitions within experimental frequency range. On the experimental side, we developed a new nozzle that allowed us to increase spectral resolution in perpendicular injection of molecular jet and to resolve for the first time inversion doublets in pure rotational transitions. By the application of the "hybrid" model we

were able to fit the observed rotational transitions with the accuracy close to experimental one. However, in the fit, the majority of torsion-rotational transitions assigned in the previous study was omitted and the problem of combination of pure rotational data with rovibrational torsional bands remain unsolved for the moment. To our opinion, to solve the problem one has to improve the accuracy of torsional parameters and remove correlations between them and between torsional and inversion parameters. For this purpose, a solution has to be found to increase the temperature of the molecular jet in which ammonia-water complex is produced.

Bibliography

[1] U. Pöschl. "Atmospheric aerosols: Composition, transformation, climate and health effects". *Angew. Chem. Int. Ed.* 44 (2005), pp. 7520–7540. DOI: 10.1002/anie.200501122.

[2] D. Fowler, K. Pilegaard, M. A. Sutton, P. Ambus, M. Raivonen, J. Duyzer, D. Simpson, H. Fagerli, S. Fuzzi, J. K. Schjoerring, C. Granier, A. Neftel, I. S.A. Isaksen, P. Laj, M. Maione, P. S. Monks, J. Burkhardt, U. Daemmgen, J. Neirynck, E. Personne, R. Wichink-Kruit, K. Butterbach-Bahl, C. Flechard, J. P. Tuovinen, M. Coyle, G. Gerosa, B. Loubet, N. Altimir, L. Gruenhage, C. Ammann, S. Cieslik, E. Paoletti, T. N. Mikkelsen, H. Ro-Poulsen, P. Cellier, J. N. Cape, L. Horváth, F. Loreto, Ü Niinemets, P. I. Palmer, J. Rinne, P. Misztal, E. Nemitz, D. Nilsson, S. Pryor, M. W. Gallagher, T. Vesala, U. Skiba, N. Brüggemann, S. Zechmeister-Boltenstern, J. Williams, C. O'Dowd, M. C. Facchini, G. de Leeuw, A. Flossman, N. Chaumerliac, and J. W. Erisman. "Atmospheric composition change: Ecosystems-Atmosphere interactions". *Atmos. Environ.* 43 (2009), pp. 5193–5267. DOI: 10.1016/j.atmosenv.2009.07.068.

[3] U. Pöschl and M. Shiraiwa. "Multiphase Chemistry at the Atmosphere-Biosphere Interface Influencing Climate and Public Health in the Anthropocene". *Chem. Rev.* 115 (2015), pp. 4440–4475. DOI: 10.1021/cr500487s.

[4] K. Welbourn, G. Will, J. Sutton, S. Newton, S. Ryan, D. Ferguson, N. Catto, and R. Schmiendendorf. "Towards a sustainable future". *Newfoundland and Labrador* (2009). URL: https://www.gov.nl.ca/education/files/ENVIR001_Unit_1_lorez.pdf.

[5] J. E. Headrick and V. Vaida. "Significance of water complexes in the atmosphere". *Phys. Chem. Earth, Part C* 26 (2001), pp. 479–486. DOI: 10.1016/S1464-1917(01)00035-6.

[6] S. H. Lee, H. Gordon, H. Yu, K. Lehtipalo, R.n Haley, Y. Li, and R. Zhang. "New Particle Formation in the Atmosphere: From Molecular Clusters to Global Climate". *J GEOPHYS RES-ATMOS* 124 (2019), pp. 7098–7146. DOI: 10.1029/2018JD029356.

[7] N. C. Frederiks, A. Hariharan, and C. J. Johnson. "Spectroscopic Studies of Clusters of Atmospheric Relevance". *Annu. Rev. Phys. Chem. 2023* 74 (2023), pp. 99–121. URL: https://www.annualreviews.org/doi/pdf/10.1146/annurev-physchem-062322-041503.

[8] T. S. Hearne, O. A. Khedaoui, B. M. Hays, T. Guillaume, and I. R. Sims. "A novel Ka-band chirped-pulse spectrometer used in the determination of pressure broadening coefficients of astrochemical molecules". *J. Chem. Phys.* 153 (2020), p. 084201. DOI: 10.1063/5.0017978.

[9] D. P. Zaleski, L. B. Harding, S. J. Klippenstein, B. Ruscic, and K. Prozument. "Time-Resolved Kinetic Chirped-Pulse Rotational Spectroscopy in a Room-Temperature Flow Reactor". *J. Phys. Chem. Lett.* 8 (2017), pp. 6180–6188. URL: https://doi.org/10.1021/acs.jpclett.7b02864.

[10] K. M. Yocum, H. H. Smith, E. W. Todd, L. Mora, Pe. A. Gerakines, S. N. Milam, and S. L. Widicus Weaver. "Millimeter/Submillimeter Spectroscopic Detection of Desorbed Ices: A New Technique in Laboratory Astrochemistry". *J. Phys. Chem. A* 123 (2019), pp. 8702–8708. DOI: 10.1021/acs.jpca.9b04587.

[11] O. Auriacombe, S. Rea, S. Ioppolo, M. Oldfield, S. Parkes, B. Ellison, and H. J. Fraser. "TeraHertz Desorption Emission Spectroscopy (THz DES) of space relevant ices". *MNRAS* 515 (2022), pp. 2698–2709. DOI: 10.1093/mnras/stac1903.

[12] J. C. McGurk, T. G. Schmalz, and W. H. Flygare. "Fast passage in rotational spectroscopy: Theory and experiment". *J. Chem. Phys.* 60 (1974), pp. 4181–4188. DOI: 10.1063/1.1680886.

[13] G. B. Park, A. H. Steeves, K. Kuyanov-Prozument, J. L. Neill, and R. W. Field. "Design and evaluation of a pulsed-jet chirped-pulse millimeter-wave spectrometer for the 70-102 GHz region". *J. Chem. Phys.* 135 (2011), p. 024202. DOI: 10.1063/1.3597774.

[14] G. G. Brown, B. C. Dian, K. O. Douglass, S. M. Geyer, S. T. Shipman, and B. H. Pate. "A broadband Fourier transform microwave spectrometer based on chirped pulse excitation". *Rev. Sci. Instrum.* 79 (2008), p. 053103.

[15] G. G. Brown, B. C. Dian, K. O. Douglass, S. M. Geyer, and B. H. Pate. "The rotational spectrum of epifluorohydrin measured by chirped-pulse Fourier transform microwave spectroscopy". *J. Mol. Spectrosc.* 238 (2006), pp. 200–212. DOI: 10.1016/J.JMS.2006.05.003.

[16] S. Kassi, D. Petitprez, and G. Wlodarczak. "Microwave Fourier transform spectroscopy of t-butylchloride and t-butylbromide isotopic species". *J. Mol. Struct.* 517–518 (2000), pp. 375–386. URL: https://doi.org/10.1016/S0022-2860(99)00296-3.

[17] I. A. Finneran, D. B. Holland, P. B. Carroll, and G. A. Blake. "A direct digital synthesis chirped pulse Fourier transform microwave spectrometer". *Rev. Sci. Instrum.* 84 (2013), p. 083104. URL: https://doi.org/10.1063/1.4818137.

[18] E. Murphy and C. Slattery. "All About Direct Digital Synthesis". *Analog Devices* (2004). URL: https://www.analog.com/en/analog-dialogue/articles/all-about-direct-digital-synthesis.html.

[19] Analog Devices. "A Technical Tutorial on Digital Signal Synthesis" (1999). URL: https://www.ieee.li/pdf/essay/dds.pdf.

[20] C. N. Banwell and E.M. McCash. "Fundamentals of Molecular Spectroscopy". *McGraw-Hill* (1994).

[21] L. Zou, R. A. Motiyenko, L. Margulès, and E.A. Alekseev. "Millimeter-wave emission spectrometer based on direct digital synthesis". *Rev. Sci. Instrum.* 91 (2020), p. 063104. URL: https://doi.org/10.1063/5.0004461.

[22] D. A. Skoog, F.J. Holler, and S.R. Crouch. "Principles of Instrumental Analysis". *Cengage Learning* (2007).

[23] O. Zakharenko, R. A. Motiyenko, L. Margulès, and T. R. Huet. "Terahertz spectroscopy of deuterated formaldehyde using a frequency multiplication chain". *J. Mol. Spectrosc.* 317 (2015), pp. 41–46. DOI: 10.1016/J.JMS.2015.09.005.

[24] R. A. Motiyenko, I. A. Armieieva, L. Margulès, E. A. Alekseev, and J. C. Guillemin. "Rotational spectroscopy of malononitrile and its corresponding monoisocyanide isomer, isocyanoacetonitrile". *A&A* 623 (2019), A162. DOI: 10.1051/0004-6361/201834587.

[25] E. Alekseev, V. V. Ilyushin, R. Motiyenko, and V. Budnikov. "The DDS-based Multifunctional Spectrometer". *2022 IEEE 2nd Ukrainian Microwave Week* (2022), pp. 109–112. DOI: 10.1109/UKRMW58013.2022.10037137.

[26] W. Gordy and R.L. Cook. "Microwave Molecular Spectra". *Wiley* (1984).

[27] C. H. Townes and A.L. Schawlow. "Microwave Spectroscopy". *Dover Publications* (2013).

[28] H. W. Kroto. "Molecular Rotation Spectra". *Dover Publications* (1992).

[29] A. Kraśnicki. "Rotational spectroscopy of selected molecules of astrophysical importance". *Pd.D dissertation* (2011).

[30] P. R. Bunker and P. Jensen. "Fundamentals of Molecular Symmetry". *CRC Press.* Series in Chemical Physics (2018).

[31] J. K. G. Watson. "Determination of centrifugal distortion coefficients of asymmetric-top molecules". *J. Chem. Phys.* 46 (1967), pp. 1935–1949. DOI: 10.1063/1.1840957.

[32] J. K. G. Watson. "Determination of Centrifugal Distortion Coefficients of Asymmetric-Top Molecules. III. Sextic Coefficients". *J. Chem. Phys.* 48 (1968), pp. 4517–4524. DOI: 10.1063/1.1668020.

[33] M. Quack and F. Merkt. "Handbook of High-resolution Spectroscopy". *John Wiley and Sons* (2011). DOI: 10.1002/9780470749593.HRS017.

[34] C. Puzzarini. "Rotational spectroscopy meets theory". *PCCP* 15 (2013), pp. 6595–6607. DOI: 10.1039/C3CP44301A.

[35] H. P. Benz, A. Bauder, and Hs. H. Gunthard. "Exact Quadrupole Interaction Energies in Rotational Spectra". *J. Mol. Spectrosc.* 23 (1966), pp. 156–164. URL: https://doi.org/10.1016/0022-2852(66)90134-2.

[36] H. O. Leung, D. Gangwani, and J. U. Grabow. "Nuclear Quadrupole Hyperfine Structure in the Microwave Spectrum of Ar–N_2O". *J. Mol. Spectrosc.* 184 (1997), pp. 106–112. DOI: 10.1006/JMSP.1997.7293.

[37] M. R. Aliev and J. T. Hougen. "The effects of vibration-rotation interaction on the quadrupole hyperfine structure of molecular rotational levels". *J. Mol. Spectrosc.* 106 (1984), pp. 110–123. DOI: 10.1016/0022-2852(84)90086-9.

[38] R. A. Motiyenko, L. Margulès, V. V. Ilyushin, I. A. Smirnov, E. A. Alekseev, D. T. Halfen, and L. M. Ziurys. "Millimeter and submillimeter wave spectra of 13C methylamine". *A&A* 587 (2016), A152. DOI: 10.1051/0004-6361/201526924.

[39] I. Kleiner. "Asymmetric-top molecules containing one methyl-like internal rotor: Methods and codes for fitting and predicting spectra". *J. Mol. Spectrosc.* 260 (2010), pp. 1–18. DOI: 10.1016/j.jms.2009.12.011.

[40] V. V. Ilyushin, Z. Kisiel, L. Pszczolkówski, H. Mäder, and J. T. Hougen. "A new torsion–rotation fitting program for molecules with a sixfold barrier: Application to the microwave spectrum of toluene". *J. Mol. Spectrosc.* 259 (2010), pp. 26–38. DOI: 10.1016/J.JMS.2009.10.005.

[41] V. V. Ilyushin, C. P. Endres, F. Lewen, S. Schlemmer, and B. J. Drouin. "Submillimeter wave spectrum of acetic acid". *J. Mol. Spectrosc.* 290 (2013), pp. 31–41. DOI: 10.1016/J.JMS.2013.06.005.

[42] I. A. Smirnov, E. A. Alekseev, V. V. Ilyushin, L. Margulès, R. A. Motiyenko, and B. J. Drouin. "Spectroscopy of the ground, first and second excited torsional states of acetaldehyde from 0.05 to 1.6 THz". *J. Mol. Spectrosc.* 295 (2013), pp. 44–50. DOI: 10.1016/j.jms.2013.11.006.

[43] A. Belloche, A. A. Meshcheryakov, R. T. Garrod, V. V. Ilyushin, E. A. Alekseev, R. A. Motiyenko, L. Margulès, H. S. P. Muller, and K. M. Menten. "Astrophysics Rotational spectroscopy, tentative interstellar detection, and chemical modeling of N-methylformamide". *A&A* 601 (2017), A49. DOI: 10.1051/0004-6361/201629724.

[44] C. Bermudez, R. A. Motiyenko, C. Cabezas, V. V. Ilyushin, L. Margulès, Y. Endo, and J. C. Guillemin. "Internal rotation analysis of the microwave and millimeter wave spectra of fluoral (CF_3CHO)". *Spectrochimica Acta Part A* 274 (2022), p. 121071. DOI: 10.1016/j.saa.2022.121071.

[45] J. T. Hougen and B. M. DeKoven. "The application of extended permutation-inversion groups to internal rotation of a symmetric rotor top in a symmetric or asymmetric rotor molecule". *J. Mol. Spectrosc.* 98 (1983), pp. 375–391. DOI: 10.1016/0022-2852(83)90249-7.

[46] J. T. Hougen. "A generalized internal axis method for high barrier tunneling problems, as applied to the water dimer". *J. Mol. Spectrosc.* 114 (1985), pp. 395–426. DOI: 10.1016/0022-2852(85)90234-6.

[47] N. Ohashi and J. T. Hougen. "The torsional-wagging tunneling problem and the torsional-wagging-rotational problem in hydrazine". *J. Mol. Spectrosc.* 112 (1985), pp. 384–400. DOI: 10.1016/0022-2852(85)90170-5.

[48] P. Groner. "Large-amplitude motion tunneling parameters in effective rotational Hamiltonians from rotation-internal rotation theory". *J. Mol. Spectrosc.* 156 (1992), pp. 164–189. DOI: 10.1016/0022-2852(92)90101-S.

[49] P. Groner. “Effective rotational Hamiltonian for molecules with two periodic large-amplitude motions”. *J. Chem. Phys* 107 (1997), pp. 4483–4498. DOI: 10.1063/1.474810.

[50] L. H. Coudert and J. T. Hougen. “Tunneling splittings in the water dimer: Further development of the theory”. *J. Mol. Spectrosc.* 130 (1988), pp. 86–119. DOI: 10.1016/0022-2852(88)90286-X.

[51] I. Kleiner and J. T. Hougen. “A Hybrid Program for Fitting Rotationally Resolved Spectra of Floppy Molecules with One Large-Amplitude Rotatory Motion and One Large-Amplitude Oscillatory Motion”. *J. Phys. Chem. A* 119 (2015), pp. 10664–10676. DOI: 10.1021/acs.jpca.5b08437.

[52] I. Kleiner and J. T. Hougen. “A simultaneous fit of v t = 0 and 1 torsion-wagging-rotational levels of CH_3NH_2 using a hybrid ”tunneling and non-tunneling" Hamiltonian formalism”. *J. Mol. Spectrosc.* 368 (2020), p. 111255. DOI: 10.1016/j.jms.2020.111255.

[53] J. Demaison, J .E. Boggs, and A.G. Csaszar. “Equilibrium Molecular Structures: From Spectroscopy to Quantum Chemistry”. *CRC Press* (2016).

[54] H. M. Pickett. “The fitting and prediction of vibration-rotation spectra with spin interactions”. *J. Mol. Spectrosc.* 148 (1991), pp. 371–377. DOI: 10.1016/0022-2852(91)90393-O.

[55] H. Dreizler, U. Andresen, J. Gripp, I. Merke, M. Meyer, W. Stahl, R. Schwarz, and K. Vormann. “A Microwave Fourier Transform Spectrometer in the Region between 26 and 36 GHz”. *Z. fur Naturforsch. - J. Phys. Sci.* 42 (1987), pp. 1279–1282. URL: https://www.degruyter.com/document/doi/10.1515/zna-1987-1109/html.

[56] J. U. Grabow, W. Stahl, and H. Dreizler. “A multioctave coaxially oriented beam-resonator arrangement Fourier-transform microwave spectrometer”. *Rev. Sci. Instrum.* 67 (1998), p. 4072. DOI: 10.1063/1.1147553.

[57] H. Hartwig and H. Dreizler. “The Microwave Spectrum of trans-2,3-E-imethyloxirane in Torsional Excited States”. *Z. Naturforsch. A* 51 (1996), pp. 923–932. URL: https://doi.org/10.1515/zna-1996-0807.

[58] S. Herbers, O. Zingsheim, H. V. L. Nguyen, L. Bonah, B. Heyne, N. Wehres, and S. Schlemmer. “Internal rotation arena: Program performances on the low barrier problem of 4-methylacetophenone”. *J. Chem. Phys.* (2021), p. 224302. URL: https://doi.org/10.1063/5.0070298.

[59] V. V. Ilyushin, L. B. Favero, W. Caminati, and J. U. Grabow. “Intertorsional Interactions Revealing Absolute Configurations: The V6 Internal Rotation Heavy-Top Case of Benzotrifluoride”. *ChemPhysChem* 11 (2010), pp. 2589–2593. DOI: 10.1002/CPHC.201000223.

[60] J. K. G. Watson. “Robust weighting in least-squares fits”. *J. Mol. Spectrosc.* 219 (2003), pp. 326–328. DOI: 10.1016/S0022-2852(03)00100-0.

[61] V. V. Ilyushin. “Millimeter wave spectrum of nitromethane”. *J. Mol. Spectrosc.* (2017), pp. 64–69. DOI: 10.1016/j.jms.2017.12.005.

[62] R. A. Motiyenko, V. V. Ilyushin, J. Demaison, N. Vogt, L. Margulès, H. Mollendal, and J. C. Guillemin. “The rotational spectrum of Methylarsine”. *J. Mol. Struct.* 1213 (2020), p. 128037. DOI: 10.1016/J.MOLSTRUC.2020.128037.

[63] R. Atkinson. “Atmospheric chemistry of VOCs and NOx”. *Atmos. Environ.* 34 (2000), pp. 2063–2101. URL: https://doi.org/10.1016/S1352-2310(99)00460-4.

[64] J. P.D. Abbatt, J. L. Thomas, K. Abrahamsson, C. Boxe, A. Granfors, A. E. Jones, M. D. King, A. Saiz-Lopez, P. B. Shepson, J. Sodeau, D. W. Toohey, C. Toubin, R. Von Glasow, S. N. Wren, and X. Yang. “Halogen activation via interactions with environmental ice and snow in the polar lower troposphere and other regions”. *Atmos. Chem. Phys.* 12 (2012), pp. 6237–6271. DOI: 10.5194/acp-12-6237-2012.

[65] A. R. Katritzky and C. W. Rees. “Comprehensive Organic Functional Group Transformations”. *Elsevier Ltd* (1995).

[66] S. Deshmukh, J. D. Myers, S. S. Xantheas, and W. P. Hess. “Investigation of Acetyl Chloride Photodissociation by Photofragment Imaging”. *J. Phys. Chem* 98 (1994), pp. 12535–12544. URL: https://doi.org/10.1021/j100099a016.

[67] S. Solomon. “The mystery of the Antarctic Ozone “Hole””. *Rev. Geophys.* 26 (1988), pp. 131–148. DOI: 10.1029/RG026I001P00131.

[68] J. Prakash, S. B. Agrawal, and M. Agrawal. “Global Trends of Acidity in Rainfall and Its Impact on Plants and Soil”. *J. Soil Sci. Plant Nutr.* 23 (2022), pp. 398–419. DOI: 10.1007/s42729-022-01051-z.

[69] “National Emission Standards for Hazardous Air Pollutants: Hydrochloric Acid Production”. *Environmental Protection Agency* 66 (2001). URL: https://www.federalregister.gov/d/01-23083.

[70] D. H. Etzler and G. K. Rollefson. “The Photolysis of Acetyl Bromide”. *J. Am. Chem. Soc.* 61 (1939), pp. 800–806. URL: https://pubs.acs.org/doi/abs/10.1021/ja01873a011.

[71] W. D. Capey, J. R. Majer, and J. C. Robb. “Photolysis of Acetyl Chloride”. *J. Phys. Chem. B* 30 (1968), p. 2182.

[72] S. Patai. “The Chemistry of Acyl Halides”. *John Wiley & Sons.* The Chemistry of functional groups The chemistry of acyl halides (1972).

[73] Y. Dong, W. Peng, Y. Liu, and Z. Wang. “Photochemical origin of reactive radicals and halogenated organic substances in natural waters: A review”. *J. Hazard. Mater.* 401 (2021), p. 123884. DOI: 10.1016/j.jhazmat.2020.123884.

[74] C. B. Faxon and D. T. Allen. “Chlorine chemistry in urban atmospheres”. *Environ. Chem.* 10 (2013), pp. 221–233. URL: https://www.publish.csiro.au/en/pdf/EN13026.

[75] “PubChem Compound Summary for CID 6367, Acetyl chloride”. *National Center for Biotechnology Information.* (2005). URL: https://pubchem.ncbi.nlm.nih.gov/compound/Acetyl-chloride.

[76] "PubChem Compound Summary for CID 10482, Acetyl bromide." *National Center for Biotechnology Information.* (2005). URL: https://pubchem.ncbi.nlm.nih.gov/compound/Acetyl-chloride.

[77] K. M. Sinnott. "Microwave spectrum of acetyl chloride". *J. Chem. Phys.* 34 (1961), pp. 851–861. DOI: 10.1063/1.1731685.

[78] A. M. Hayashi, N. Inada, and Y. Niide. "Microwave spectrum, structure, internal rotation, and nuclear quadrupole coupling constant tensor of acetyl chloride". *J. Mol. Struct.* 352 (1995), pp. 325–334. URL: https://doi.org/10.1016/0022-2860(95)08828-J.

[79] L. C. Krisher. "Microwave spectrum, barrier to internal rotation, and quadrupole coupling of acetyl bromide". *J. Chem. Phys.* 33 (1960), pp. 1237–1241. DOI: 10.1063/1.1731363.

[80] J. P. Schiffer, C. R. Gossett, G. C. Phillips, and T. E. Young. "Inelastic Scattering of Protons from Cl^{35} and Cl^{37}". *Phys. Rev.* 103 (1956), pp. 134–135. DOI: 10.1103/PhysRev.103.134.

[81] O. Zakharenko, V. V. Ilyushin, F. Lewen, H. S.P. Müller, S. Schlemmer, E. A. Alekseev, M. L. Pogrebnyak, I. A. Armieieva, O. Dorovskaya, L. H. Xu, and R. M. Lees. "Rotational spectroscopy of methyl mercaptan CH332SH at millimeter and submillimeter wavelengths". *A&A* 629 (2019), A73. DOI: 10.1051/0004-6361/201935759.

[82] V. V. Ilyushin. "Microwave Spectroscopy of Torsion Vibrations in Molecules: Approximation of Rigid Constraint on Structural Torsional Parameters ρ and F in Rho Axis Method". 16 (2011), pp. 414–423. URL: http://rpra-journal.org.ua/index.php/ra/article/view/425.

[83] J. Demaison, L. Margulès, I. Kleiner, and A. G. Császár. "Equilibrium structure in the presence of internal rotation: A case study of cis-methyl formate". *J. Mol. Spectrosc.* 259 (2010), pp. 70–79. DOI: 10.1016/j.jms.2009.11.007.

[84] A. Bauder and Hs. H. Gunthard. "Internal Rotation in Acetaldehyde". *J. Mol. Spectrosc.* 60 (1976), pp. 290–311. URL: https://doi.org/10.1016/0022-2852(76)90133-8.

[85] D. R. Herscheach and V. W. Laurie. "Influence of vibrations on molecular structure determinations. III. Inertial defects". *J. Chem. Phys.* 40 (1964), pp. 3142–3153. DOI: 10.1063/1.1724977. URL: https://doi.org/10.1063/1.1724977.

[86] E. C. Tuazon, R. Atkinson, S. M. Aschmann, and J. Arey. "Kinetics and products of the gas-phase reactions of O3 with amines and related compounds". *Res. Chem. Intermed* 20 (1994), pp. 303–320. URL: https://link.springer.com/article/10.1163/156856794X00351.

[87] S. M. Murphy, A. Sorooshian, J. H. Kroll, N. L. Ng, P. Chhabra, C. Tong, J. D. Surratt, E. Knipping, R. C. Flagan, and J. H. Seinfeld. "Secondary aerosol formation from atmospheric reactions of aliphatic amines". *Atmos. Chem. Phys* 7 (2007), pp. 2313–2337. URL: https://doi.org/10.5194/acp-7-2313-2007.

[88] F. Yu and G. Luo. "Modeling of gaseous methylamines in the global atmosphere: Impacts of oxidation and aerosol uptake". *Atmos. Chem. Phys.* 14 (2014), pp. 12455–12464. DOI: 10.5194/acp-14-12455-2014.

[89] V. V. Ilyushin, E. A. Alekseev, S. F. Dyubko, R. A. Motiyenko, and J. T. Hougen. "The rotational spectrum of the ground state of methylamine". *J. Mol. Spectrosc.* 229 (2005), pp. 170–187. DOI: 10.1016/J.JMS.2004.08.022.

[90] R. A. Motiyenko, V. V. Ilyushin, B. J. Drouin, S. Yu, and L. Margulès. "Rotational spectroscopy of methylamine up to 2.6 THz". *A&A* 563 (2014), A137. DOI: 10.1051/0004-6361/201323190.

[91] N. Ohashi and J. T. Hougen. "The torsional-wagging tunneling problem and the torsional-wagging-rotational problem in methylamine". *J. Mol. Spectrosc.* 121 (1987), pp. 474–501. DOI: 10.1016/0022-2852(87)90064-6.

[92] P. Gyawali, R. A. Motiyenko, A. Belloche, I. Kleiner, V. V. Ilyushin, E. A. Alekseev, I. Gulaczyk, and M. Kreglewski. "Rotational spectrum and interstellar detection of the first torsionally excited state of methylamine". *A&A* 677 (2023), A65. DOI: 10.1051/0004-6361/202346518.

[93] F. W. Loomis and R. W. Wood. "The Rotational Structure of the Blue-Green Bands of Na_2". *Phys. Rev.* 32 (1928), pp. 223–237. URL: https://doi.org/10.1103/PhysRev.32.223.

[94] I. Gulaczyk and M. Kreglewski. "IR rotational spectrum of methylamine". *JQSRT* 252 (2020), p. 107097. DOI: 10.1016/J.JQSRT.2020.107097.

[95] I. Gulaczyk. "Gas-phase high-resolution molecular spectroscopy for LAV molecules". *Phys. Sci. Rev.* 2 (2017), p. 20170139. URL: https://www.degruyter.com/document/doi/10.1515/psr-2017-0139/html.

[96] I. Gulaczyk, W. Lodyga, M. Kreglewski, and V. M. Horneman. "Reinvestigation of the wagging band of methylamine". *Mol. Phys.* 108 (2010), pp. 2389–2394. DOI: 10.1080/00268976.2010.499114.

[97] S. Aloisio and J. S. Francisco. "Radical-water complexes in earth's atmosphere". *Acc. Chem. Res.* 33 (2000), pp. 825–830. DOI: 10.1021/ar000097u.

[98] D. Yaron, K. I. Peterson, D. Zolandz, W. Klemperer, F. J. Lovas, and R. D. Suenram. "Water hydrogen bonding: The structure of the water-carbon monoxide complex". *J. Chem. Phys.* 92 (1990), pp. 7095–7109. DOI: 10.1063/1.458250.

[99] K. I. Peterson and W. Klemperer. "Structure and internal rotation of $H_2O{-}CO_2$, $HDO{-}CO_2$, and $D_2O{-}CO_2$ van der Waals complexes". *J. Chem. Phys.* 80 (1983), pp. 2439–2445. DOI: 10.1063/1.446993.

[100] C. S. Brauer, G. Sedo, E. M. Grumstrup, K. R. Leopold, M. D. Marshall, and H. O. Leung. "Effects of partially quenched orbital angular momentum on the microwave spectrum and magnetic hyperfine splitting in the OH-water complex". *Chem. Phys. Lett.* 401 (2005), pp. 420–425. DOI: 10.1016/j.cplett.2004.11.090.

[101] Y. Ohshima, K. Sato, Y. Sumiyoshi, and Y. Endo. "Rotational spectrum and hydrogen bonding of the H_2O—HO radical complex". *J. Am. Chem. Soc.* 127 (2005), pp. 1108–1109. DOI: 10.1021/ja0442973.

[102] S. Aloisio and J. S. Francisco. "Existence of a Hydroperoxy and Water ($HO_2 \cdot H_2O$) Radical Complex". *J. Phys. Chem.* 102 (1998), pp. 1899–1902. URL: https://pubs-acs-org.ressources-electroniques.univ-lille.fr/doi/epdf/10.1021/jp972173p.

[103] J. C. Crowhurst, A. F. Goncharov, B. Sadigh, C. L. Evans, P. G. Morrall, J. L. Ferreira, and A. J. Nelson. "Synthesis and characterization of the nitrides of platinum and iridium". *Science* 311 (2006), pp. 1275–1278. DOI: 10.1126/science.1121813.

[104] T. R. Dyke and J. S. Muenter. "Microwave spectrum and structure of hydrogen bonded water dimer". *J. Chem. Phys.* 60 (1974), pp. 2930–2931. DOI: 10.1063/1.1681463.

[105] E. Zwart, J. J. ter Meulen, W. L. Meerts, and L. H. Coudert. "The Submillimeter Rotation Tunneling Spectrum of the Water Dimer". *J. Mol. Spectrosc.* 147 (1991), pp. 27–39. URL: https://doi.org/10.1016/0022-2852(91)90165-7.

[106] T. R. Dyke, K. M. Mack, and J. S. Muenter. "The structure of water dimer from molecular beam electric resonance spectroscopy". *J. Chem. Phys.* 66 (1977), pp. 498–510. DOI: 10.1063/1.433969.

[107] E. A. Serov, M. A. Koshelev, T. A. Odintsova, V. V. Parshin, and M. Yu Tretyakov. "Rotationally resolved water dimer spectra in atmospheric air and pure water vapour in the 188-258 GHz range". *PCCP* 16 (2014), pp. 26221–26233. DOI: 10.1039/c4cp03252g.

[108] P. Herbine and T. R. Dyke. "Rotational spectra and structure of the ammonia-water complex". *J. Chem. Phys.* 83 (1985), pp. 3768–3774. DOI: 10.1063/1.449139.

[109] G. T. Fraser and R. D. Suenram. "Perturbations in the infrared spectrum of the NH_3 umbrella mode of HOH—NH_3". *J. Chem. Phys.* 96 (1992), pp. 7287–7297. URL: https://doi.org/10.1063/1.462433.

[110] P. A. Stockman, Ro. E. Bumgarner, S. Suzuki, and G. A. Blake. "Microwave and tunable far-infrared laser spectroscopy of the ammonia-water dimer". *J. Chem. Phys.* 96 (1992), pp. 2496–2510. DOI: 10.1063/1.462054.

[111] T. J. Balle and W. H. Flygare. "Fabry–Perot cavity pulsed Fourier transform microwave spectrometer with a pulsed nozzle particle source". *Rev. Sci. Instrum.* 52 (1981), pp. 33–45. URL: https://doi.org/10.1063/1.1136443.

[112] M. Takami, Y. Ohshima, S. Yamamoto, and Y. Matsumoto. "Free-jet Infrared Absorption Spectroscopy of Stable and Unstable Molecular Species". *Faraday Discuss.* 86 (1988), pp. 1–12. URL: https://doi.org/10.1039/DC9888600001.

[113] A. Potapov and P. Asselin. "High-resolution jet spectroscopy of weakly bound binary complexes involving water". *Int. Rev. Phys. Chem.* 33 (2014), pp. 275–300. DOI: 10.1080/0144235X.2014.932578.

[114] U. Even. “The Even-Lavie valve as a source for high-intensity supersonic beam”. *EPJ tech. instrum.* 2 (2015), pp. 1–22. DOI: 10.1140/epjti/s40485-015-0027-5.

[115] M. D. Morse. “Supersonic Beam Sources”. *Exp. Methods Phys. Sci.* 29 (1996), pp. 21–47. DOI: 10.1016/S0076-695X(08)60784-X.

[116] A. Gutsol. “Microwave discharge in supersonic flows of molecular gases”. *Sov. Phys. Tech. Phys* 35 (1990), pp. 789–794. URL: https://www.researchgate.net/publication/253064185.

[117] M. Guéron. “The Doppler effect in NMR spectroscopy”. *J. Magn. Reson.* 160 (2003), pp. 151–156. DOI: 10.1016/S1090-7807(02)00185-4.

[118] L. Zou and R. Motiyenko. “Window function for chirped pulse spectroscopy with enhanced signal-to-noise ratio and lineshape correction”. *JQSRT* 268 (2021), p. 107608. URL: https://www.sciencedirect.com/science/article/pii/S0022407321001011.

[119] M. Herman, K. Didriche, D. Hurtmans, B. Kizil, P. MacKo, A. Rizopoulos, and P. Van Poucke. “FANTASIO: a versatile experimental set-up to investigate jet-cooled molecules”. *Mol. Phys.* 105 (2007), pp. 815–823. DOI: 10.1080/00268970601063820.

[120] J. C. Laas, B. M. Hays, and S. L. Widicus Weaver. “Multipass millimeter/submillimeter spectrometer to probe dissociative reaction dynamics”. *J. Phys. Chem. A* 117 (2013), pp. 9548–9554. DOI: 10.1021/jp3122402.

[121] H. M. Pickett, R. L. Poynter, E. A. Cohen, M. L. Delitsky, J. C. Pearson, and H. S.P. Muller. “Submillimeter, Millimeter, and Microwave Spectral Line Catalog”. *Journal of Quantitative Spectroscopy and Radiative Transfer* 60 (5 1998), pp. 883–890. DOI: 10.1016/S0022-4073(98)00091-0.

Appendix A

Study of methylamine in the first excited torsional state

A&A, 677, A65 (2023)
https://doi.org/10.1051/0004-6361/202346518

Astronomy & Astrophysics

Rotational spectrum and interstellar detection of the first torsionally excited state of methylamine⋆

P. Gyawali[1], R. A. Motiyenko[1], A. Belloche[2], I. Kleiner[3], V. V. Ilyushin[4], E. A. Alekseev[1,4], I. Gulaczyk[5], and M. Kreglewski[5]

[1] Univ. Lille, CNRS, UMR 8523 – PhLAM – Physique des Lasers Atomes et Molécules, 59000 Lille, France
e-mail: roman.motiyenko@univ-lille.fr
[2] Max-Planck-Institut für Radioastronomie, Auf dem Hügel 69, 53121 Bonn, Germany
[3] Université Paris-Cité and Univ. Paris-Est Creteil, CNRS, LISA, 75013 Paris, France
[4] Radiospectrometry Department, Institute of Radio Astronomy of NASU, Mystetstv 4, 61002 Kharkiv, Ukraine
[5] Faculty of Chemistry, Adam Mickiewicz University in Poznań, ul. Uniwersytetu Poznańskiego 8, 61-614 Poznań, Poland

Received 28 March 2023 / Accepted 14 June 2023

ABSTRACT

Context. Methylamine (CH_3NH_2) was first detected in the interstellar medium (ISM) toward Sgr B2 almost 50 years ago by observation of rotational transitions in its torsional ground state. Methylamine exhibits two large-amplitude motions (LAMs), the methyl torsion and amine wagging, which complicate the spectral analysis, especially in excited vibration states. The lack of an accurate model of the two coupled LAMs has also hampered the identification in the ISM of rotational transitions in excited vibrational states.
Aims. The aim of this work is to study the terahertz and microwave rotational spectra of methylamine experimentally and theoretically in order to provide a reliable basis for the detection of its rotational transitions in the first torsionally excited state, $v_t = 1$, in the ISM.
Methods. The terahertz spectrum of methylamine was measured from 150 to 1520 GHz with the Lille fast scan spectrometer. Using a new "hybrid" Hamiltonian model, we were able to analyze the nuclear quadrupole hyperfine structure and to accurately fit the rotational spectrum of the $v_t = 1$ state of methylamine. We used the imaging spectral line survey ReMoCA performed with the Atacama Large Millimeter/submillimeter Array (ALMA) to search for rotational transitions of methylamine in its first torsionally excited state toward the high-mass star forming region Sgr B2(N). The observed spectra are modeled under the assumption of local thermodynamic equilibrium (LTE).
Results. Accurate spectral predictions were obtained for the ground and first excited states of CH_3NH_2. We report the first interstellar detection of methylamine in the $v_t = 1$ state toward the offset position Sgr B2(N1S) in the hot molecular core Sgr B2(N1). The LTE parameters derived previously from the rotational emission of methylamine in its torsional ground state toward Sgr B2(N1S) yield synthetic spectra of methylamine in the $v_t = 1$ state that are fully consistent with the ALMA spectra and allow us to identify five rotational lines of this state.

Key words. ISM: molecules – methods: laboratory: molecular – submillimeter: ISM – molecular data – line: identification

1. Introduction

Methylamine (CH_3NH_2) is a seven-atom organic molecule and the simplest primary alkylamine. It is considered to be a possible precursor of the simplest amino acid, glycine, NH_2CH_2COOH (Holtom et al. 2005). In particular, the radical–radical reaction of CH_2NH_2 and HOCO in the gas phase, on grain surface, and in bulk ice is considered to be one of the most feasible glycine formation routes (see Joshi & Lee 2022, and references therein). Another recent review (see Aponte et al. 2017, and references therein) provides an analysis of potential synthetic routes of glycine and methylamine from a common set of precursors present in carbonaceous chondrite meteorites, as both molecules have also been detected in multiple extraterrestrial samples (e.g., Pizzarello & Holmes 2009).

Methylamine was first detected in the interstellar medium (ISM) almost 50 years ago by observation of rotational transitions in its torsional ground state toward the high-mass star forming region Sagittarius B2 (Sgr B2) located in the Galactic center region (Kaifu et al. 1974; Fourikis et al. 1974). For a long time, methylamine was only securely detected toward Sgr B2, in particular in its hot molecular cores, Sgr B2(N) and Sgr B2(M) (Belloche et al. 2013; Halfen et al. 2013). With the imaging spectral line survey Re-exploring Molecular Complexity with ALMA (ReMoCA) performed toward Sgr B2(N) with the Atacama Large Millimeter/submillimeter Array (ALMA; Belloche et al. 2019), the abundance of methylamine was found to be 0.07 relative to methanol toward the main hot core of Sgr B2(N) (Kisiel et al. 2022; Motiyenko et al. 2020). Methylamine was also detected in G+0.693–0.27, a shocked region of the Sgr B2 molecular cloud complex not related to the hot cores, with an abundance of 0.2 relative to methanol, which is close to the value derived toward the main hot core of Sgr B2(N) (Zeng et al. 2018; Rodríguez-Almeida et al. 2021)[1]. A tentative detection for the first time outside the Galactic center region was reported with

⋆ Full Tables B.1 and B.2 are only available at the CDS via anonymous ftp to cdsarc.cds.unistra.fr (130.79.128.5) or via https://cdsarc.cds.unistra.fr/viz-bin/cat/J/A+A/677/A65

[1] The column density of methylamine reported in Table 2 of Zeng et al. (2018) is erroneous. The value should be ten times higher. However, the abundance of methylamine relative to H_2 reported in their Table 5 is correct (V. Rivilla, priv. comm.).

ALMA in the nearby star forming region Orion KL by Pagani et al. (2017).

Nondetections of methylamine were reported in a number of hot cores by Ligterink et al. (2015) with upper limits to the abundance ratio of methylamine to methanol of between 0.02 and 2, most of them being at a similar level to the ratio measured toward the main hot core of Sgr B2(N). However, a nondetection was also reported toward the low-mass Class 0 protostar IRAS 16293–2422B, where the abundance of methylamine relative to methanol was determined to be lower than 5.3×10^{-5}, which is nearly three orders of magnitude lower than in Sgr B2(N) (Ligterink et al. 2018). This substantial difference departs from the overall good correlation found by Jørgensen et al. (2020) between the abundances of complex organic molecules, that is, carbon-bearing molecules containing at least six atoms (Herbst & van Dishoeck 2009), in IRAS 16293–2422B and the secondary hot core of Sgr B2(N).

Ohishi et al. (2019) detected methylamine with the Nobeyama radio telescope in another hot core, G10.47+0.03. Bøgelund et al. (2019) also managed to detect CH_3NH_2 with ALMA toward at least one hot core within the molecular cloud complex NGC 6334[2], with an abundance ratio relative to methanol of about one order of magnitude lower than that found for the main hot core of Sgr B2(N). These detections, along with the detection in Orion KL, suggest that methylamine is more widespread – albeit difficult to detect – in our Galaxy than initially thought. Methylamine has even been detected with the Australia Telescope Compact Array (ATCA) in the disk of a spiral galaxy at a redshift of 0.89 (Muller et al. 2011). The detection was made in absorption against the bright background quasar PKS 1830–211. Muller et al. (2011) derived a methylamine abundance on the order of 0.1–0.2 relative to methanol, which is similar to the ratios measured in the main hot core of Sgr B2(N) and G+0.693–0.027.

On the chemical modeling side, the recent models of gas-grain chemistry in hot molecular cores presented by Garrod et al. (2022) predict that methylamine is predominantly formed in the ice mantles of dust grains at low temperature during the prestellar phase. The ratio of peak gas-phase abundances of methylamine to methanol during the warm-up phase predicted by these models is in the range 0.03–0.04 depending on the warm-up timescale, which agrees within a factor of about two with the ratio reported above for the main hot core of Sgr B2(N). This agreement suggests that the formation of methylamine in Sgr B2 is dominated by radical reactions in the solid phase rather than gas-phase chemistry.

Given the intensities of the $v_t = 0$ transitions of methylamine measured toward Sgr B2(N1S) with the ReMoCA survey and their rotational temperature of ~230 K (Kisiel et al. 2022), we expected the strongest $v_t = 1$ transitions of methylamine to be detectable above the 3σ level in this survey. Detecting such rotational transitions within the first torsionally excited state requires laboratory measurements and a good spectroscopic modeling of their frequencies and intensities.

So far, methylamine has only been detected in its ground torsional state, mainly due to the lack of a complete and precise spectroscopic database in the excited states. In this paper, we derive those parameters for the first excited torsional state of methylamine. The methylamine rotational spectrum has a complex structure due to two coupled large-amplitude motions: the methyl torsion and the amine inversion, or wagging. The ground rotational state of methylamine was successfully analyzed using the effective Hamiltonian approach (high-barrier "tunneling" approach) of Ohashi and Hougen (Ohashi & Hougen 1987). In this approach, each v_t torsional state is fitted separately (with its own set of molecular parameters). The analysis yielded an accurate model of the rotational spectrum in the $v_t = 0$ state (Ilyushin et al. 2005; Motiyenko et al. 2014), but showed some limitations with respect to the $v_t = 1$ state. To overcome these limitations, we use a new hybrid model and the BELGI-hybrid code described in Kleiner & Hougen (2015) which takes into account all the torsional states arising from internal rotation of the methyl group of methylamine in a global way (Kleiner & Hougen 2020). The second large-amplitude motion of the NH_2 inversion is taken into account within the tunneling approach.

In our first paper on CH_3NH_2 (Kleiner & Hougen 2020), we used a dataset for $v_t = 0$ and 1 that combines previously published data in the infrared (Ohashi et al. 1987, 1988; Gulaczyk et al. 2017) with data in the microwave spectral range (Motiyenko et al. 2014; Ohashi et al. 1989; Kręglewski & Wlodarczak 1992; Ilyushin et al. 2005; Ilyushin & Lovas 2007), which were fitted using the tunneling formalism from Hougen and Ohashi. We successfully fitted 11880 $v_t = 1 \leftarrow 0$ transitions in the far-infrared spectral range, as well as 2288 rotational transitions belonging to the ground torsional state $v_t = 0$ in the microwave spectral range, but we only fitted a limited number (137) of pure rotational transitions belonging to the first excited state $v_t = 1$–1. The aim of this paper is to extend our analysis of the first torsionally excited state of methylamine using the "hybrid" approach.

The paper is divided into five further sections. Section 2 describes the experimental details. Section 3 presents the spectral data used in the present fit. Section 4 describes the Hamiltonian theoretical model and BELGI-hybrid code that we used, including the nuclear quadrupole hyperfine structure and the intensity calculation. Section 5 presents the results of the search for $v_t = 1$ rotational transitions of methylamine in the ISM, and Sect. 6 gives a discussion of some spectroscopic and observational issues connected to our current results. The conclusions of this work are presented in Sect. 7.

2. Experimental details

We performed a new series of measurements of the rotational spectrum of methylamine in the framework of the present study. All the spectra were recorded in absorption mode using the Lille fast-scan hybrid spectrometer (Zakharenko et al. 2015; Motiyenko et al. 2019). The measurements cover the frequency range 150 – 1520 GHz with a few small gaps. We used a 99% pure commercial sample of methylamine purchased from Sigma-Aldrich. The optimal gas pressure in the absorption cell for the best signal-to-noise ratio (S/N) of the recorded spectra was between 30 μbar and 60 μbar, with higher pressures preferred at higher frequencies. Due to partially resolved or unresolved nuclear quadrupole hyperfine structure, the measurement uncertainty is estimated to be around 60 kHz for relatively strong isolated lines and 100 kHz for weak or slightly distorted line shapes, and for the lines measured above 1 THz due to line broadening effects (both Doppler and pressure).

As the main goal of the study is the assignment of excited vibrational states, the spectra were acquired with an increased amplitude resolution. In standard conditions, the spectral amplitude resolution is limited by the resolution of the analog-to-digital converter. In the present study, we used a SR7270 DSP

[2] The other two detections reported in Fig. 2 of Bøgelund et al. (2019) are debatable.

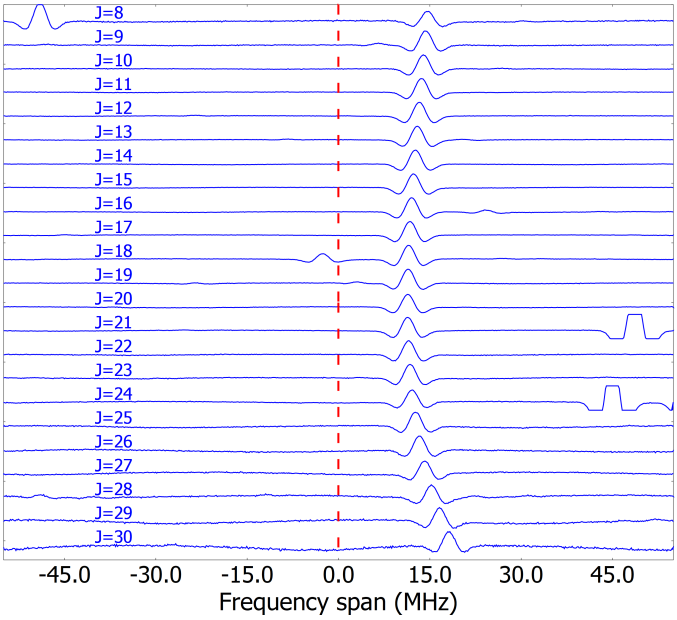

Fig. 1. Loomis-Wood diagram centered on predicted frequencies of E_1 ^cQ-type series of transitions of methylamine with $K_a'' = -8 \leftarrow K_a' = -7$.

lock-in amplifier, the ADC of which has a resolution of 16 bits. To increase the amplitude resolution, each spectral segment was recorded twice with two gain factors that differed by 20 dB. Lower gain spectra were used to assign the strongest lines, whereas higher gain spectra were particularly useful for the assignment of weak lines in excited torsional states.

3. Spectral data

3.1. Microwave, millimeter, and submillimeter data

The assignment of the rotational spectrum of methylamine in excited vibrational states was aided by Loomis-Wood-type diagrams (Loomis & Wood 1928). These diagrams allow the accurate assignment of broadband spectra, especially at the initial stage of analysis when predicted transition frequencies may be significantly different from observed ones. The technique consists in superposing portions of spectra centered on predicted frequencies of a particular series of transitions where only one quantum number is varied and the rest are kept constant. In this case, the shifts of the observed lines with respect to the predicted ones exhibit a smooth (typically polynomial) behavior as a function of the varied quantum number and can be easily located on the diagram. An example of a Loomis-Wood plot for a series of v_t = 1–1 rotational transitions is shown in Fig. 1. This latter was built using the predicted frequencies from our previous study (Kleiner & Hougen 2020). Even if the lines are shifted with respect to predictions by 15 to 20 MHz, the smooth variation allows easy identification. After the series was included in the fit, and after the refinement of the Hamiltonian parameters, the newly predicted frequencies almost coincide with the observed ones. In this case, all experimental lines would be vertically aligned on the new diagram. To build Loomis-Wood plots, we used home-made software for spectral analysis, which is available from the corresponding author upon request.

In the present study, using the new spectra records, the dataset for the ground torsional state v_t = 0–0 was increased to 2790 microwave, millimeter and submillimeter transitions, compared to the published 2400 transitions up to J = 40 from the supplementary material from Motiyenko et al. (2014) and compared to our previous fit of 2288 transitions from Kleiner & Hougen (2020). For the first excited state, about 212 microwave lines existed in the literature (Ohashi et al. 1987, 1988; Gulaczyk et al. 2017) and in our previous paper we only fitted 137 of them (Kleiner & Hougen 2020). In the present work, we were able to assign and fit 2921 new v_t = 1–1 rotational transitions. These were combined with previously assigned v_t = 1–1 lines in the frequency range 49–149 GHz (Motiyenko, priv. comm.). These assignments were done using the spectrum records obtained for methylamine by Ilyushin et al. (2005). In addition, 40 v_t = 2–2 rotational transitions were also newly assigned and fitted. We also replaced 3 lines from Kręglewski & Wlodarczak (1992) and 132 lines from Ohashi et al. (1989) with our more accurate measurements.

As in our previous paper, the frequency measurement uncertainties of microwave transitions ranged between 20 kHz, 50 kHz, 60 kHz, 100 kHz, 200 kHz, and 500 kHz depending on the measurement source. The hyperfine structure was removed for most of those lines in the literature, but for some of them this was done only by visual inspection, and so they were given a weight of 500 kHz, whereas the hyperfine splittings for the lines from Motiyenko et al. (2014) were removed properly, and so they were given weights from 20 to 200 kHz (see Sect. 2 of Kleiner & Hougen 2020).

3.2. Far-infrared data

The number of transitions in the far-infrared fundamental band v_t = 1 ← 0 was kept about the same (11643) as in our previous paper (11880) with J up to 40 and K up to 17. In the present fit, we added 6155 transitions belonging to the hot band v_t = 2 ← 1 and 5253 transitions belonging to the overtone v_t = 2 ← 0 from (Gulaczyk et al. 2018; Gulaczyk & Kręglewski 2020). We decided to include neither the previously published ground state v_t = 0 combination differences (GSCDs) – as their large number tends to decrease the impact of the more accurate microwave transitions, thus causing the parameters to drift – nor the pure rotational transitions v_t = 0–0, v_t = 1–1 or v_t = 2–2, which were initially measured in the far-infrared range, as for a number of them our remeasurements in high-resolution THz spectra obtained in this study showed discrepancies in the measured frequencies of up to 30 MHz, which is much higher than the microwave measurement accuracy.

3.3. Hyperfine structure analysis

In methylamine, the interaction of the ^{14}N electric quadrupolar moment with the molecular field gradient results in the hyperfine structure of the rotational spectrum. The interaction couples the nuclear spin I to the molecular rotational angular momentum J to form a resultant total angular momentum vector F. As the nuclear spin of ^{14}N is I = 1, each rotational level of methylamine is split into three hyperfine sublevels: $F = J + 1$, $F = J$, and $F = J - 1$. The transitions between hyperfine levels obey the selection rules $\Delta F = 0, \pm 1$ and can give rise to a complex hyperfine structure for low-J rotational transitions. With increasing J, only hyperfine transitions with $\Delta F = \Delta J$ selection rule are usually observed, as their sum of relative intensities represents more than 99% of the total intensity of the hyperfine components for a given rotational transition. Therefore, the hyperfine structure for high-J transitions of methylamine is usually represented by three components.

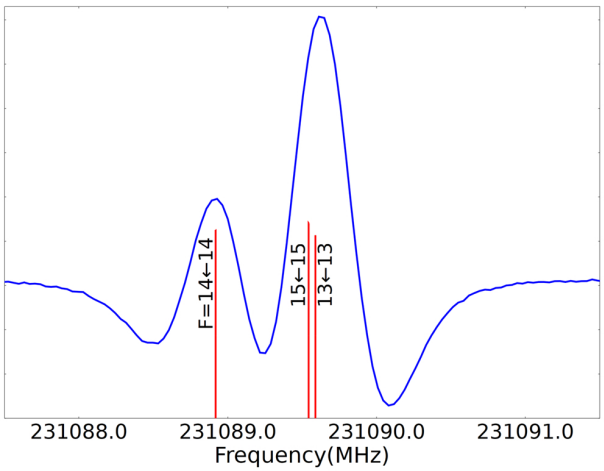

Fig. 2. Partially resolved hyperfine structure of the v_t = 1–1 $14_{1,13}$–$14_{0,14}$ E_1 transition of methylamine. The stick spectrum shows the calculated positions of hyperfine components.

Due to Doppler-limited spectral resolution, the hyperfine structure in the spectrum of methylamine has only been partially resolved for a limited number of rotational transitions. A resolved pattern of the hyperfine structure was observed as a doublet with an intensity ratio of 2:1. The stronger doublet component contains unresolved transitions with $F' = J' + 1 \leftarrow F = J + 1$ and $F' = J' - 1 \leftarrow F = J - 1$ selection rules, whereas the weaker doublet component corresponds to the $F' = J' \leftarrow F = J$ transition. An example of partially resolved hyperfine structure for a v_t = 1–1 rotational transition of methylamine is shown in Fig. 2.

Each hyperfine transition frequency may be expressed as

$$f_{\rm hf} = f_{\rm rot} + \frac{E_{\rm hf}(I, J', F') - E_{\rm hf}(I, J, F)}{h}, \tag{1}$$

where $f_{\rm rot}$ is the hyperfine-free central frequency and $E_{\rm hf}$ denotes the addition to the energy due to hyperfine coupling. $E_{\rm hf}$ may be expressed in terms of rotational angular momentum operators and nuclear quadrupole coupling tensor components χ_{ij}, $i, j = a, b, c$ as (Ilyushin et al. 2005):

$$E_{\rm hf}(I, J, F) = \left[\frac{1}{2}\chi_+ \left\langle J_b^2 + J_c^2 - 2J_a^2 \right\rangle - \frac{1}{2}\chi_- \left\langle J_b^2 - J_c^2 \right\rangle + \chi_{ab} \langle J_a J_b + J_b J_a \rangle \right] 2f(I, J, F)/J(J+1) \tag{2}$$

where $\chi_+ = -\chi_{aa}$, $\chi_- = \chi_{cc} - \chi_{bb}$ and $f(I, J, F)$ is the Casimir function (Gordy & Cook 1984).

Equations (1) and (2) were used to obtain hyperfine-free rotational transition frequencies $f_{\rm rot}$ for the global fit. We used a perturbation approach similar to that used for acetamide, a C_s molecule with one methyl internal rotor large-amplitude motion, and one nitrogen quadrupole nucleus (see Eq. (1) of Suenram et al. 2001). The same approach was also used in the analysis of the ground-state rotational spectrum of ^{12}C–methylamine (Ilyushin et al. 2005; Motiyenko et al. 2014) and ^{13}C–methylamine (Motiyenko et al. 2016). Using the BELGI-hybrid code, we obtained the rotation-torsion eigenvalues and eigenvectors from the usual two-step diagonalization of the Hamiltonian $H_{\rm WTR}$, as described in Sect. 4. The global fitting BELGI-hybrid program was modified to output expectation values of $\langle J_a \rangle^2$, $\langle J_b \rangle^2$, $\langle J_c \rangle^2$, and $\langle J_a J_b + J_b J_a \rangle$ in the rho axis system (a, b, c). To obtain hyperfine-free rotational transition frequencies, each hyperfine component was fitted to Eq. (1). The linear least-squares Gauss-Newton algorithm was applied using a dedicated Python code. In the present study, we assigned 324 partially resolved hyperfine components of v_t = 1–1 rotational transitions. These were fitted together with 1132 v_t = 0–0 components from this and previous studies (Ilyushin et al. 2005; Motiyenko et al. 2014) to yield 653 hyperfine-free rotational transition frequencies and two hyperfine constants χ_+ and χ_-, the values of which are given in Table 1. As a point of comparison, the last column of Table 1 provides the corresponding values obtained using high-barrier tunneling Hamiltonian expectation values. As can be seen from Table 1, the χ_+ values match well, whereas the χ_- values are outside the confidence intervals of both studies. This significant difference in the χ_- parameter probably arises from the different Hamiltonians used for obtaining expectation values of the necessary rotational operators. In this connection, it is interesting to note that our current value for χ_- = 6.4058(85) MHz is in much better agreement with χ_- = 6.3746(81) MHz obtained by Kręglewski et al. (1992), which supports our hypothesis that the difference with our previous result is caused by the difference in the Hamiltonian models used.

Table 1. ^{14}N nuclear quadrupole coupling parameters for methylamine

Parameter	This study	Motiyenko et al. (2014)
χ_+ (MHz)	–2.4139(63)	–2.4129(12)
χ_- (MHz)	6.4058(85)	6.0697(25)
Transitions [a]	1456	1132
rms [b] (MHz)	0.0129	0.0082

Notes. [a]Number of hyperfine transitions used in the fit. In this study, the number of transitions includes 324 v_t = 1–1 hyperfine components [b]Root-mean-square deviation of the hyperfine fit.

4. Theoretical model and analysis

The theoretical Hamiltonian model used in our fit is the so-called hybrid Hamiltonian, which allows us to deal with the two coupled large-amplitude motions present in methylamine, namely the internal rotation of the methyl group CH_3 and the back-and-forth oscillatory inversion motion, or wagging, of the amine group NH_2. This approach has been tested in the ground torsional state of methyl-malonaldehyde (Kleiner & Hougen 2015), and also in our previous study of the ground and first excited state of methylamine (Kleiner & Hougen 2020).

As the hybrid model and the BELGI-hybrid code have been presented in detail elsewhere (Kleiner & Hougen 2015, 2020), here we only give a short summary of the approach. In the hybrid Hamiltonian, we mix two methods to deal with the coupling of two large-amplitude motions. The first method treats the internal rotation of the CH_3 group in a similar way to the method presented in the series of BELGI programs (Kleiner et al. 1992; Kleiner 2010). Those "BELGI"-type terms contain an explicit form for the potential barrier hindering the methyl internal rotation or torsion. For the internal rotation of the CH_3 group, the rotation–torsion Hamiltonian has the form:

$$H_{TR} = F(P_\alpha - \rho J_z)^2 + V(\alpha) + AJ_z^2 + BJ_x^2 + CJ_y^2 + \text{higher order torsion–rotation terms as found in the BELGI code,} \tag{3}$$

Table 2. Overview of a fit of 28 802 transitions of methylamine with $J \leq 40$, $K \leq 17$, using 79 parameters floated to give a weighted standard deviation of 1.53.

	Previous study (Kleiner & Hougen 2020)			Present work		
Transitions [a]	Number [b]	WRMS [c]	RMS [d]	Number [b]	WRMS [c]	RMS [d]
Microwave $v_t = 0$	2288	1.07	0.088 MHz	2790	2.38	0.154 MHz
Microwave $v_t = 1$	137	1.39	0.154 MHz	2921	3.35	0.218 MHz
Microwave $v_t = 2$	–	–	–	40	3.10	0.289 MHz
MW A/B [e] species	1098	1.04		2287	3.03	
MW E [f] species	1327	1.13		3464	2.85	
Infrared $v_t = 1 \leftarrow 0$	11 880	1.09	0.00053 cm^{-1}	11 643	0.29	0.00015 cm^{-1}
Infrared $v_t = 2 \leftarrow 1$	–		–	6155	1.25	0.00063 cm^{-1}
Infrared $v_t = 2 \leftarrow 0$	–		–	5253	1.27	0.00064 cm^{-1}

	Present work		
Exp. Unc. [g]	Number [b]	WRMS [c]	RMS [d]
0.0008 cm^{-1}	23 051	0.59	0.00047 cm^{-1}
0.020 MHz	390	4.45	0.089 MHz
0.045 MHz	210	3.89	0.194 MHz
0.060 MHz	3293	3.05	0.183 MHz
0.100 MHz	1626	2.12	0.212 MHz
0.200 MHz	105	1.33	0.257 MHz
0.500 MHz	127	0.48	0.238 MHz

Notes. [a]Transitions in the upper part of this table are grouped by their torsional v_t quantum numbers and/or symmetry species. [b]Number of lines in the category of this row included in the fit. [c]Weighted root-mean-square residual for the lines in this row. [d]Root-mean-square residual in the units of measurement for the lines in this row. [e]Microwave A_1, A_2 , B_1 and B_2 species. [f]Microwave E_1, E_2 species. [g]Transitions in the lower part of this table are grouped by assigned measurement uncertainty.

where F is the internal rotation constant, P_α is the internal rotation angular momentum, ρ is the coupling constant between internal and global rotation, J_x, J_y, and J_z are angular momentum projections along x, y, and z molecular axes, and $V(\alpha)$ is the potential internal rotation barrier described as a Fourier series:

$$V(\alpha) = \frac{V_3}{2}(1 - \cos 3\alpha) + \frac{V_6}{2}(1 - \cos 6\alpha) + \frac{V_9}{2}(1 - \cos 9\alpha) + \ldots \quad (4)$$

The second method treats the back-and-forth (wagging) motion of the amino group NH_2 using the tunneling approach as described by Ohashi & Hougen (1987). Those tunneling-type terms, which contain matrix elements associated with tunneling between the two positions of the amino group, do not contain any explicit form for the double-well tunneling potential. Instead $H = T + V$ for the wagging motion is replaced with one tunneling splitting parameter plus higher-order torsion–rotation corrections.

Here, we used a two-step diagonalization procedure similar to the one used in the one-top BELGI code (Kleiner et al. 1992; Kleiner 2010). In the first step, we diagonalize the torsion-K-rotation part of the matrix associated with the two first terms of the Hamiltonian given in Eq. (3). We separate the nondegenerate torsional-wagging-rotational (twr) states (of symmetry species ${}^{\rm twr}A_1 \oplus {}^{\rm twr}A_2 \oplus {}^{\rm twr}B_1 \oplus {}^{\rm twr}B_2$) from the set of doubly degenerate states (of species ${}^{\rm twr}E_1 \oplus {}^{\rm twr}E_2$) using the $\sigma = 0$ and $\sigma = \pm 1$ characters associated with irreducible representations of the permutation-inversion G_{12} group. We then separately diagonalize the Hamiltonian matrix for each of those two sets.

This torsion-wagging-rotational hybrid Hamiltonian matrix $H_{\rm twr}$ is partitioned into four square submatrices, as shown in Eq. (1) of Kleiner & Hougen (2020), with blocks noted by L(eft)L(eft), L(eft)R(ight), RL, and RR:

$$[H] = \begin{bmatrix} \mathrm{LL} & \mathrm{LR} \\ \mathrm{RL} & \mathrm{RR} \end{bmatrix}, \quad (5)$$

where $H_{\rm RR}$ corresponds to the torsion-rotation Hamiltonian, which is identical to that used in the BELGI series of codes for the one-top molecules, where the amino group NH_2 of the methylamine molecule is locked in one of its two symmetrically equivalent equilibrium inversion positions and is localized in a well on the positive side of the γ axis, where γ designates the inversion or wagging coordinate. $H_{\rm LL}$ represents the BELGI matrix, which corresponds to a methylamine molecule with the amino group locked in the other of the two symmetrically equivalent equilibrium inversion positions and localized in the negative side of the γ axis. $H_{\rm RL}$ and $H_{\rm LR}$ contain matrix elements that describe the amino group tunneling from the positive region of γ to the negative region, or vice versa; that is, they describe inversion motion.

4.1. Fit with the hybrid formalism

The BELGI-hybrid code globally fits a large microwave, millimeter, and submillimeter dataset for 2790 v_t = 0–0, 2921 v_t = 1–1, and 40 v_t = 2 – 2 pure rotational transitions, as well as the far-infrared dataset involving 11643 $v_t = 1 \leftarrow 0$, 6155 $v_t = 2 \leftarrow 1$, and 5253 $v_t = 2 \leftarrow 0$ transitions up to $J = 40$.

As can be seen from Table 2, we achieve a global unitless standard deviation of 1.53 for 28802 transitions. The quality of the fit is satisfactory, although not completely within experimental uncertainty for the microwave transitions. The upper part

of the table presents transitions grouped by their torsional v_t quantum numbers (and spectral range) and/or symmetry species. The lower part of the table shows root-mean-squared deviations grouped by assigned measurement uncertainty.

The 79 floated molecular parameters (plus eight additional parameters, which were fixed at values from previous fits, such as F, V_9, D_K, WCPG (which multiplies the $P_\gamma J_y$ operator), and some higher order K dependent parameters) are listed in Table A.1 and compared to the 74 floated and two fixed parameters in the previous work, where we fitted a total of 15081 transitions (Kleiner & Hougen 2020). The increase in the number of parameters is very reasonable considering that the number of lines increased by almost a factor of two. As detailed in Kleiner & Hougen (2020), the first column of Table A.1, labeled *ntrw*, contains four indices describing the order of the term with $n = t + r + w$, where t and r are the traditional torsional and rotational orders and w is the amino wagging order (see Kleiner & Hougen 2020 for details). The second column gives the name of the molecular parameter as used in the BELGI-hybrid code and the operator that it multiplies. These operators must all be: (i) Hermitian, (ii) of species A_1 in the permutation-inversion group G_{12} (Kleiner & Hougen 2015), and (iii) invariant to time reversal. The third column gives numerical values for the molecular parameters obtained from the previous fit (Kleiner & Hougen 2020), and the fourth column gives the values of the parameters as obtained from the present fit described in Table 2, together with their standard errors. As already mentioned in Kleiner & Hougen (2020), we note that a factor of γ was omitted in three operators of Table 5 of Kleiner & Hougen (2015), namely those multiplied by the coefficients DAB, ODAB, and ODELTA in that table. The correct operators are those given in Table A.1 here, where we also change the name of the ODELTA parameter to AXGK.

Compared to our previous fit, the variation of the second-order term in the potential (V_6) is relatively large, showing the influence of the $v_t = 1$ and 2 excited states in determining the potential terms in the Fourier expansion. We also noticed that a number of low-order parameters have changed sign (such as V_6, AXG, and DAB which multiply $\frac{1}{2}(1 - \cos 6\alpha)$ term, $\gamma P_\alpha J_x$ term and $\gamma\{J_x, J_z\}$ respectively).

Compared to the previous tunneling fits of the literature, here a large reduction in parameters is obtained in our global fit, because the 55 + 88 = 143 tunneling parameters used in the final fit of Gulaczyk & Kręglewski (2020) are reduced by almost a factor of 1.6 to 79 (+8 fixed parameters) in Table A.1. For the far-infrared data, our rms deviations for the fundamental band $v_t = 1 \leftarrow 0$, the hot band $v_t = 2 \leftarrow 1$, and the overtone $v_t = 2 \leftarrow 0$ are 0.00015 cm^{-1} for 11643 lines, 0.00063 cm^{-1} for 6155 lines, and 0.00064 cm^{-1} for 5253 lines compared to the rms of 0.00058 cm^{-1} for 12237 lines, 0.00209 cm^{-1} for 6609 lines, and 0.00197 cm^{-1} for 7735 lines obtained in Gulaczyk & Kręglewski (2020) for the same bands, respectively. This comparison is not totally fair because the number of transitions fitted in Gulaczyk & Kręglewski (2020) is not the same as ours; in their study they fit up to $J = 50$. In the present work, because of the size of the matrix that we need to take into consideration in our global approach and the computer time required subsequently, we decided to fit only up to $J = 40$.

In the microwave spectral range, the rms we obtained for the fit of the ground torsional $v_t = 0$–0 state is higher (154 kHz) than the rms obtained by the tunneling approach (102 kHz), but we included 236 more lines in our fit (2790 lines instead of 2554 lines) than in Gulaczyk & Kręglewski (2020). For the first excited state $v_t = 1$–1, we obtained a rms of 218 kHz for 2921 lines. In Gulaczyk & Kręglewski (2020), only 214 transitions were available at that time and these authors fitted them with a rms of 183 kHz. Finally, our $v_t = 2$–2 data fit with a rms of 289 kHz.

In a general way, and this was also noticed in our previous paper (Kleiner & Hougen 2020), poorly fitted lines belong to high J and/or high K transitions and this tendency is also visible in the microwave spectral range. A number of transitions $v_t = 1$–1 with $K = 0$ and 1 in the A and B nondegenerate species did not fit either within experimental accuracy, and large observed-calculated values of up to 1 or 2 MHz are observed. The energy levels of those transitions were shown by Ohashi et al. (1989, see their Figs. 1 and 2) to contribute to an avoided crossing in the case of the B species and to an unavoided crossing for the A species series. We used several Hamiltonian terms with matrix elements connecting energy levels differing by $\Delta K = \pm 1$ to take into account this perturbation, such as DAB, AXG, DAC (see Table A.1) and so on, but we did not succeed in decreasing the observed-calculated values for those lines with $K = 0$ and 1 and we finally omitted them in the fit.

The lists of rotational and rovibrational transitions of methylamine are presented in Tables B.1 and B.2 and are available at the CDS[3]. In the first ten columns of both tables, the quantum numbers for each spectral line are given: v_t, J, K_a, K_c, and symmetry label Γ. In the subsequent four columns, we provide the observed transition frequencies, measurement uncertainties, residuals from the fit, and a binary flag indicating whether the transition was included in the final fit. The last column of Table B.1 contains a reference from which the measurements were obtained. The last column of Table B.2 contains an optional flag "L" for $v_t = 2 \leftarrow 1$ and $v_t = 2 \leftarrow 0$ transitions of A_1, A_2, B_1, and B_2 symmetries. The flag indicates that the $K_a = 2$ and $K_a = 4$ labels are reversed compared to the labels from Gulaczyk & Kręglewski (2020). This difference in the labeling occurs during the procedure of assignment of the K_a quantum number after the diagonalization of the Hamiltonian matrix and reveals the mixing of the eigenfunctions.

4.2. Intensity calculation

The BELGI-hybrid code was modified to provide the line strength calculations for methylamine transitions. The line strength (S) of the torsion-rotation transition between the level L' containing all $(2J' + 1)$ M' components and the level L containing all $(2J + 1)$ M components is given by the formula (Ilyushin & Lovas 2007):

$$S(L';L) = \frac{1}{\mu^2}\sum_M 3\left|\sum_g \sum_{\substack{K',K=-J,J \\ v_t''',v_t''=0,N_t-1}} C_{K',v_t'''}^{J',\tau',v_t',\sigma',w'} C_{K,v_t''}^{J,\tau,v_t,\sigma,w} \times \langle K', v_t''', \sigma', w'|\mu_g|K, v_t'', \sigma, w\rangle \times \langle J', K', M|\Phi_{Zg}|J, K, M\rangle\right|^2, \quad (6)$$

where $|K, v_t, \sigma, w\rangle$ and $|J, K, M\rangle$ are the torsion-rotation-inversion and symmetric rotor basis functions used to set up the wagging-torsion-rotation Hamiltonian matrix for the second diagonalization step; the coefficients $C_{K,v_t''}^{J,\tau,v_t,\sigma,w}$ are the eigenvectors coefficients obtained after diagonalization of the wagging-torsion-rotation Hamiltonian matrix; the Φ_{Zg} represents direction cosines, and μ_g is the electric dipole moment along the

[3] http://cdsweb.u-strasbg.fr/

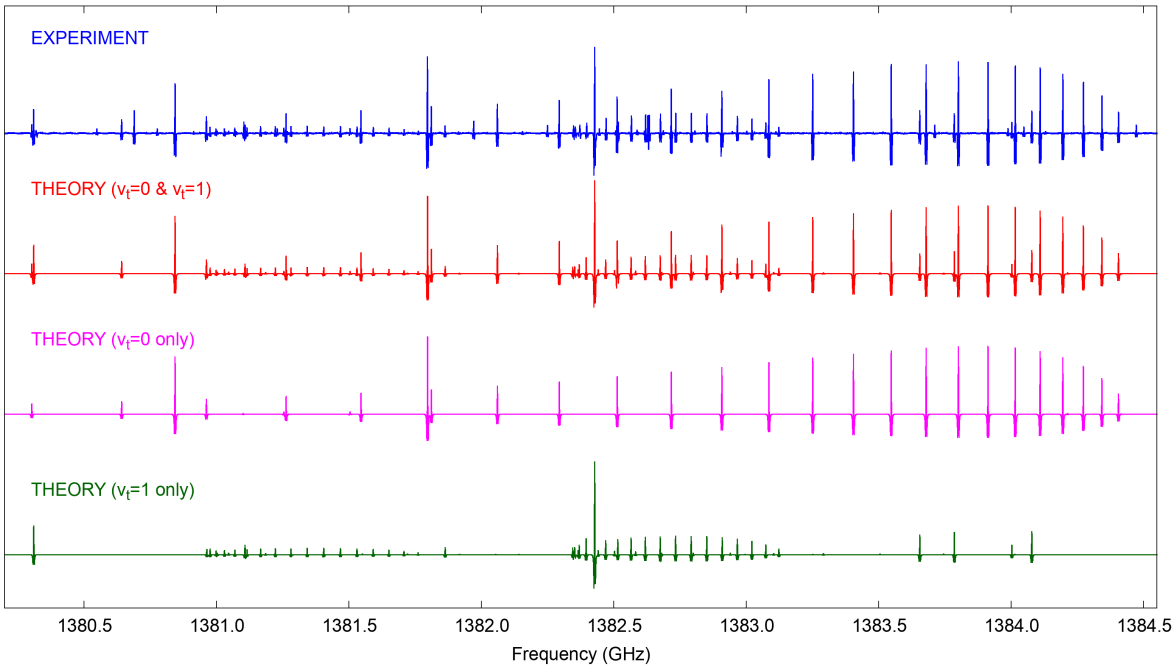

Fig. 3. Observed (in blue) and predicted (in red) v_t = 0–0 and v_t = 1–1 rotational spectrum of methylamine around 1.38 THz. The individual contributions of v_t = 0–0 and v_t = 1–1 transitions are shown in magenta and green, respectively. Regular series of lines refer to ^cQ-type transitions with $K_a = 9 \leftarrow 8$ and symmetry selection rules: $E_1 \leftarrow E_1$ for v_t = 0–0, and $E_1 \leftarrow E_1$ (stronger) and $E_2 \leftarrow E_2$ (weaker) for v_t = 1–1.

molecular-fixed $g = x, y, z$ axis. The electric dipole moment is a function of the methyl torsion angle α and of the amino umbrella γ coordinate (Ilyushin & Lovas 2007). The torsional dependence of μ_g is given as a Fourier expansion in the torsional angle (see Eq. (19) of Hougen et al. 1994). For the present work, we are concerned with the intensities of pure rotational transitions and so we neglect the cosine and sine dependence of the dipole moment components, and keep only the leading (independent of α) terms. We also neglected the tunneling contributions in γ of the dipole moments, as was also done in Ilyushin & Lovas (2007). For methylamine, the nonzero value of the dipole moment components are μ_a (μ_z) and μ_c ($\mu_x \pm i\mu_y$).

In the Principal Axis Method (PAM), the dipole moment components are measured using Stark effect measurements by Lide (1957), and are then corrected by Takagi & Kojima (1973) with $\mu_a = -0.307$ D and $\mu_c = 1.258$ D. In the Rho Axis Method (RAM), those values need to be transformed using Eq. (20) of Kleiner (2010), but since for methylamine the angle between PAM and RAM is very small, the values we used for the dipole moments in this system, namely $\mu_a = -0.226$ D and $\mu_c = 1.275$ D, are very close to the PAM ones.

As the hyperfine splittings for methylamine can reach up to a few MHz and are essential in correctly fitting the astronomical spectra, we also calculate the relative intensities of the quadrupole hyperfine components using the formula given by Townes & Schawlow (1955). We multiply the $\mu^2 S$ of each rotational transition by the relative intensity of the quadrupole component. For the intensity calculation we also had to take into account the nuclear spin statistical weight (W_{st}), which is equal to 1 for A_1, A_2, and E_2 species and to 3 for B_1, B_2, and E_1.

The calculated v_t = 1–1 rotational spectrum of methylamine is available at the Lille Spectroscopic Database[4] (LSD) in two versions: (1) pure rotational transition frequencies, and (2) a rotational spectrum, taking the nuclear hyperfine structure into account. The spectra may be generated with different line "intensity" units: line strength (D^2), Einstein A_{ij} coefficients (s^{-1}), and absorption cross-sections (nm^{2}MHz/molecule). For the latter, the rotational partition function calculated from first principles by Motiyenko et al. (2014) is used. We also note that although the "hybrid" global model used in the present study predicts both v_t = 0–0 and v_t = 1–1 rotational transitions, in the LSD, we decided to keep the spectral predictions calculated by Motiyenko et al. (2014) as the entries for v_t = 0–0 spectra. We did this for two reasons. First, the effective high-barrier tunneling Hamiltonian model from Motiyenko et al. (2014) covers the wider range of rotational quantum numbers up to $J \leq 50$, whereas present hybrid model fits rotational levels only up $J \leq 40$ (this reduction in the upper value of J is caused by the necessity to keep the computation time within reasonable limits in the case of the hybrid approach because it deals with a much larger basis set than high-barrier tunneling Hamiltonian). Second, we believe that for the v_t = 0–0 transitions, high-barrier tunneling formalism provides predictions of slightly better accuracy, as evidenced by the better rms and weighted rms deviations achieved for v_t = 0–0 in Motiyenko et al. (2014) in comparison with our current result with the hybrid approach. This is due to the fact that separate state models of the high-barrier tunneling approach do not need to accommodate torsion–rotation and intervibrational perturbations from higher excited states in methylamine. However, this advantage of the high barrier tunneling formalism becomes a disadvantage when we need to deal with the first excited torsional state, where the hybrid approach indeed shows much better results. Therefore, at present, we believe that it is better to use predictions based on the high-barrier tunneling Hamiltonian of Motiyenko et al. (2014) for v_t = 0–0 transitions and predictions based on the current hybrid approach for v_t = 1–1 transitions.

To illustrate the quality of the rotational transitions of methylamine in the ground and first excited torsional states calculated in this study, we compare an experimental (in blue) and a modeled (in red) spectrum around 1.38 THz in Fig. 3; here, we also

[4] https://lsd.univ-lille.fr/

Table 3. Parameters of our best-fit LTE model of methylamine (with hyperfine structure) toward Sgr B2(N1S).

Molecule	Status [a]	N_{det} [b]	Size [c] ($''$)	T_{rot} [d] (K)	N [e] (cm^{-2})	F_{vib} [f]	ΔV [g] (km s^{-1})	V_{off} [h] (km s^{-1})	$\frac{N_{ref}}{N}$ [i]
CH_3NH_2, $v = 0$ ⋆	d	10	2.0	230	1.4 (18)	1.25	5.0	0.0	1
$v_t = 1$	d	5	2.0	230	1.4 (18)	1.25	5.0	0.0	1

Notes. [a]d: detection. [b]Number of detected lines (conservative estimate, see Sect. 3 of Belloche et al. 2016). One line of a given species may mean a group of transitions of that species that are blended together. [c]Emission size (FWHM). [d]Rotational temperature. [e]Total column density of the molecule. x (y) means $x \times 10^y$. [f]Correction factor that was applied to the column density to account for the contribution of vibrationally excited states in the cases where this contribution was not included in the partition function of the spectroscopic predictions. [g]Line width (FWHM). [h]Velocity offset with respect to the assumed systemic velocity of Sgr B2(N1S), V_{sys} = 62 km s^{-1}. [i]Column density ratio, with N_{ref} the column density of the previous reference species marked with a ⋆.

show individual contributions of v_t = 0–0 and v_t = 1–1 transitions. Overall, the agreement in terms of frequency and relative intensity is good. We also note that, in this frequency region, the great majority of strong lines refer to v_t = 0–0 and v_t = 1–1 transitions.

5. Interstellar detection of methylamine in its first torsionally excited state

5.1. Observations

The imaging spectral line survey Reexploring Molecular Complexity with ALMA (ReMoCA) targeted the high-mass star forming protocluster Sgr B2(N) with ALMA. We used this survey to carry out an interstellar search for methylamine in its first torsionally excited state. The main features of the survey are summarized below. More details about the observations and data reduction can be found in Belloche et al. (2019). The phase center is located at the equatorial position $(\alpha, \delta)_{J2000}$= ($17^h47^m19\overset{s}{.}87$, $-28°22'16\overset{''}{.}0$), which is halfway between the two hot molecular cores Sgr B2(N1) and Sgr B2(N2). The survey covers the frequency range from 84.1 GHz to 114.4 GHz at a spectral resolution of 488 kHz (1.7 to 1.3 km s^{-1}). This coverage was obtained with five different frequency tunings. The observations achieved a sensitivity per spectral channel ranging between 0.35 mJy beam^{-1} and 1.1 mJy beam^{-1} (rms) depending on the setup, with a median value of 0.8 mJy beam^{-1}. The angular resolution (half-power beam width, HPBW) varies between ∼0.3$''$ and ∼0.8$''$ with a median value of 0.6$''$ that corresponds to ∼4900 au at the distance of Sgr B2 (8.2 kpc, Reid et al. 2019). Here, we used the slightly improved version of the data reduction that one of us described in Melosso et al. (2020).

As in Belloche et al. (2019), we analyzed the spectrum obtained toward the position Sgr B2(N1S) at $(\alpha, \delta)_{J2000}$= ($17^h47^m19\overset{s}{.}870$, $-28°22'19\overset{''}{.}48$), which is offset by about 1$''$ to the south of the main hot core Sgr B2(N1). This position was chosen for its lower continuum opacity compared to the peak of the hot core. We compared the observed spectrum to synthetic spectra computed under the assumption of local thermodynamic equilibrium (LTE) with the astronomical software Weeds (Maret et al. 2011). This assumption is justified by the high densities of the regions where hot-core emission is detected in Sgr B2(N) ($> 1 \times 10^7$ cm^{-3}, see Bonfand et al. 2019).

The software takes the angular resolution of the observations and the optical depth of the rotational transitions into account. We derived a best-fit synthetic spectrum for each molecule separately, and then added together the contributions of all identified molecules. Each species was modeled with a set of five parameters: size of the emitting region (θ_s), column density (N), temperature (T_{rot}), line width (ΔV), and velocity offset (V_{off}) with respect to the assumed systemic velocity of the source, V_{sys} = 62 km s^{-1}. The line width and velocity offset are obtained directly from the well-detected and uncontaminated lines. The emission of complex organic molecules is extended over several arcseconds around Sgr B2(N1) (see Busch et al. 2022). For the LTE modeling, we assumed an emission size of 2$''$, as in Belloche et al. (2019), which is much larger than the beam, meaning that the derived column densities do not depend on the exact value of this size parameter.

5.2. Detection of CH_3NH_2 in its first torsionally excited state

One of us reported the detection of methylamine in its torsional ground state toward Sgr B2(N1S) in Kisiel et al. (2022; see their Fig. A.5). The analysis presented in this latter study used the spectroscopic entry 31008 (version 1) available in the Jet Propulsion Laboratory (JPL) spectroscopic database (Pickett et al. 1998), which is based on the combined fit by Ilyushin et al. (2005). This entry does not account for the hyperfine structure of methylamine. However, we found that the spectral broadening due to the hyperfine structure is not negligible for some methylamine lines given the typical line width of 5 km s^{-1} (about 1.7 MHz) toward Sgr B2(N1S). Therefore, here we used the spectroscopic entry 31802 (version 2021.08) of the LSD, which is based on Motiyenko et al. (2014) and accounts for the hyperfine structure.

The LTE synthetic spectrum computed with the LSD entry using the same LTE parameters as those reported in Table 3 of Kisiel et al. (2022) is compared to the ReMoCA spectrum of Sgr B2(N1S) in Fig. C.1. These LTE parameters are listed in Table 3. A detailed comparison of Fig. A.1 to Fig. A.5 of Kisiel et al. (2022) shows that the hyperfine structure does indeed broaden several lines of methylamine and in turn reduces their peak temperature compared to the previous study, where the hyperfine structure was not accounted for (see, e.g., the lines at 84.215, 86.075, or 95.146 GHz). As a result, several lines that were counted as detected in Table 3 of Kisiel et al. (2022) are now below the threshold considered here to count a line as firmly detected. The adopted threshold depends on the degree of contamination of the line, but it roughly corresponds to two-thirds of the peak of the observed line. To count a given line as detected, we also require that there be a clear peak in the observed spectrum at the frequency of this line, and that the peaks of both the synthetic and observed lines be above three times the rms noise level (dotted lines in the figures). With these criteria, we count 10 lines of methylamine in its torsional ground state as detected in Fig. C.1 while 15 were counted in the previous study that

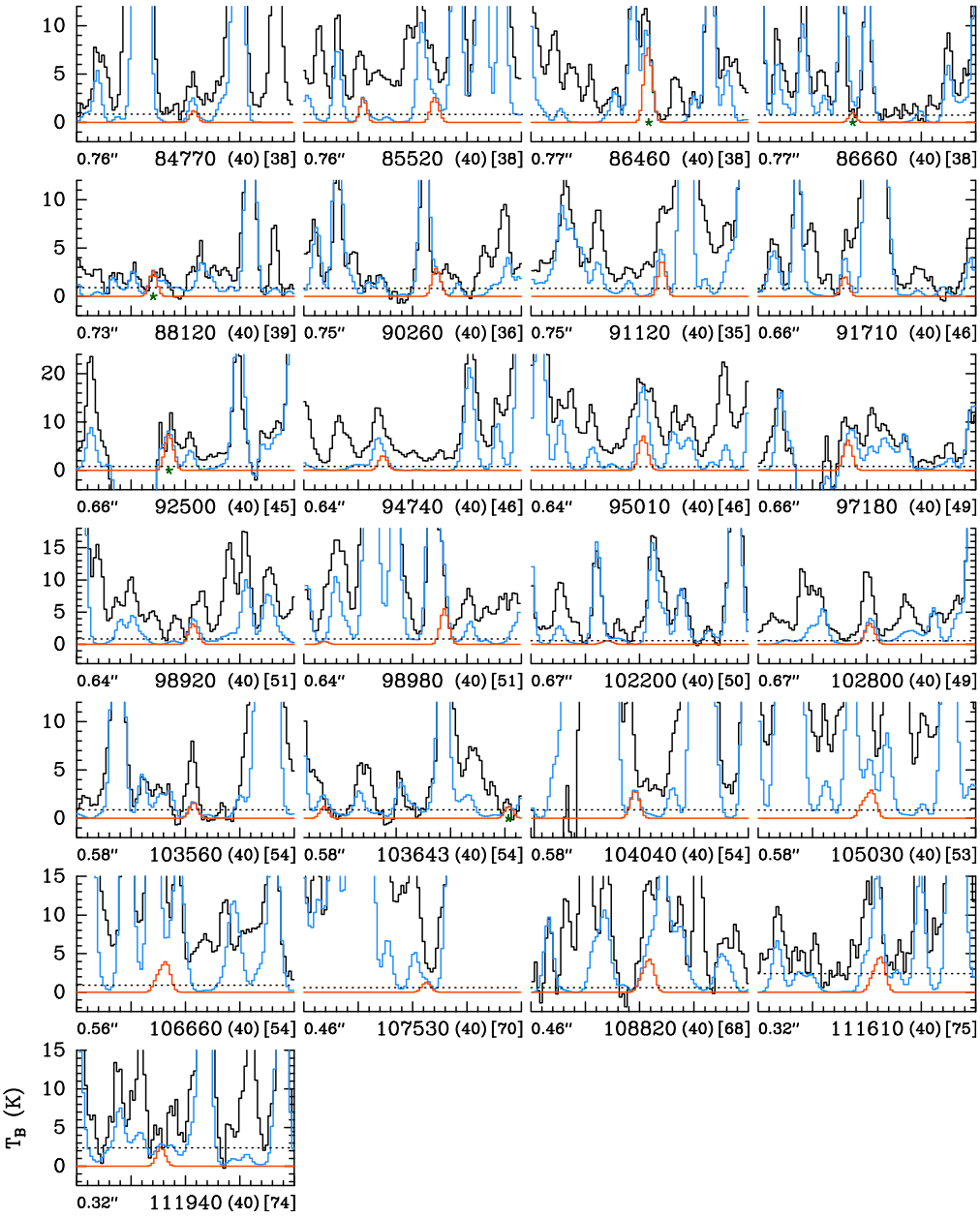

Fig. 4. Selection of rotational transitions of methylamine CH_3NH_2 in its first torsionally excited state covered by the ReMoCA survey. The LTE synthetic spectrum of CH_3NH_2 $v_t = 1$ is displayed in red and overlaid on the observed spectrum of Sgr B2(N1S) shown in black. The blue synthetic spectrum contains the contributions of all molecules identified in our survey so far, including the contribution of the species shown in red. The values written below each panel correspond from left to right to the half-power beam width, the central frequency in MHz, the width in MHz of each panel in parentheses, and the continuum level in K of the baseline-subtracted spectra in brackets. The y-axis is labeled in brightness temperature units (K). The dotted line indicates the 3σ noise level. The green stars highlight the lines of methylamine in its first torsionally excited state that are not excessively contaminated by emission from other species and are counted as detected lines in Table 3.

ignored the hyperfine structure of methylamine. The ten detected ground-state lines of methylamine are marked with a green star in Fig. C.1.

We computed an LTE synthetic spectrum of the rotational transitions of methylamine in its first torsionally excited state using the spectroscopic predictions obtained in Sect. 4 and assuming the same LTE parameters as for the torsional ground state. This synthetic spectrum is a good match to the ReMoCA spectrum of Sgr B2(N1S) (see Fig. 4). Many transitions are contaminated by emission from other molecules, but five lines of CH_3NH_2 $v_t = 1$ are strong enough and sufficiently uncontaminated to be counted as detected. They are highlighted with a green star in Fig. 4. One comment should be made concerning the $v_t = 1$ line of methylamine at 86657 MHz. The two strong transitions on each side of this line are from ethylene glycol $(CH_2OH)_2$. As can be seen in Fig. 4, the LTE model displayed in blue, which includes the contribution of all identified molecules, slightly overestimates the widths of these ethylene glycol lines in this frequency range, which artificially increases the contamination of the methylamine line that lies in between. This is why we still consider this line of methylamine as being sufficiently uncontaminated.

We produced a population diagram that includes transitions from both torsional states (Fig. 5). After correction for the

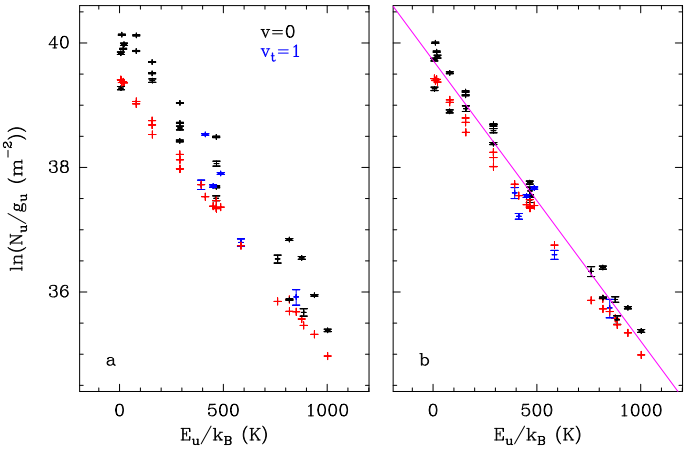

Fig. 5. Population diagram of CH_3NH_2 toward Sgr B2(N1S). The observed data points are shown in black for $v = 0$ and in blue for $v_t = 1$ while the synthetic populations are shown in red. No correction is applied in panel a. In panel b, the optical depth correction has been applied to both the observed and synthetic populations and the contamination by all other species included in the full model has been subtracted from the observed data points. The purple line is a linear fit to the observed populations (in linear-logarithmic space).

Table 4. Rotational temperature of methylamine derived from its population diagram toward Sgr B2(N1S).

Molecule	States [a]	T_{fit} [b] (K)
CH_3NH_2	$v = 0, v_t = 1$	222 (8)

Notes. [a]Vibrational states that were taken into account to fit the population diagram. [b]The standard deviation of the fit is given in parentheses. As explained in Sect. 3 of Belloche et al. (2016) and in Sect. 4.4 of Belloche et al. (2019), this uncertainty is purely statistical and should be viewed with caution. It may be underestimated.

optical depth of the lines and subtraction of the contamination from other molecules included in our full model (i.e., the difference between the blue and red spectra in Figs. C.1 and 4), the observed data points are roughly distributed along a straight line, which indicates that the emission of methylamine in both torsional states can be described by a single temperature component. A fit to the population diagram yields a rotational temperature of 222 ± 8 K, as reported in Table 4. The temperature that we assumed for the LTE synthetic spectra (see Table 3) is consistent with the temperature derived from the population diagram within 1σ. The partition function of both the $v = 0$ and $v_t = 1$ spectroscopic entries includes only the rotational part. The column density derived in Table 3 was corrected to account for the vibrational part of the partition function. This correction was computed in the harmonic approximation using the vibrational energies of methylamine provided by Shimanouchi (1972) and Gulaczyk & Kręglewski (2020).

6. Discussion

It is evident that we came up against problems in current analysis that prevented us from achieving a fit within the experimental error for the available dataset. Indeed, as seen from Table 2, even for the torsional ground state, the weighted rms deviation for the microwave data is 2.38. The fact that we get greater rms deviation for the ground state in comparison with the previous fit with the tunneling approach is not surprising. This is because in the present study, we worked with a semi-global approach, which fits the data belonging to a number of torsional states with one set of parameters, and therefore the problems with fitting excited torsional states may also diminish the quality of fitting for the ground state. On the one hand, we are not able to rule out a situation where our current fit corresponds to some local minimum in vicinity of the global minimum in the functional space of Hamiltonian parameters. Indeed, here we deal with the two large-amplitude vibrational motions, which produce a rather complicated landscape in the Hamiltonian parameter space. The fact that a number of low-order parameters (such as V_6, AXG, DAB) have changed sign in comparison with our first methylamine study using the hybrid approach (Kleiner & Hougen 2020) shows that, at least with respect to our previous study, we changed our position in the Hamiltonian parameter space quite significantly and therefore we could still be out of a global minimum with our fit. Further extension of the analysis to the second torsionally excited state may provide necessary information for improving the situation with the global versus local minimum by putting additional constraints on the Hamiltonian parameter set. On the other hand, this problem might be circumvented simply by finding an optimal set of high-order parameters in our Hamiltonian model that allow us to take into account all peculiarities of the energy level structure of the excited torsional states. Here, the fact that poorly fitted lines belong to high J and/or high K transitions – as mentioned above – may be considered as an argument in favor of this explanation. Although our search for the high-order Hamiltonian terms that could help to improve the situation was quite extensive, it was not exhaustive, because this search is very time consuming in view of the complexity of the Hamiltonian parameter space in the case of two coupled, large-amplitude motions.

A further possible explanation for the remaining problems with fitting the available dataset is the strong influence of intervibrational interactions arising from low-lying nontorsion vibrations in the molecule. In methylamine, the third excited torsional state is already close in energy to the NH_2 wagging mode (see e.g., Fig. 2 of Gulaczyk et al. 2017) and strong Fermi and Coriolis-type resonances have been reported for this state (Gulaczyk et al. 2010). Therefore, it is quite probable that these perturbations propagate down through numerous intertorsional interactions and affect the energy level structure of the lower torsional states. Our current model is not capable of explicitly taking these intervibrational interactions into account since the tunneling part of the hybrid approach represents only a separate wagging state (in our current case, this is the ground wagging state). Therefore, perturbations arising from this intervibrational interaction may only be taken into account indirectly by our current theoretical approach through some additional high-order wagging-torsion-rotation Hamiltonian terms with no guarantee that all the perturbations are accommodated in this way. It may be that it will be impossible to get a fit within experimental error for the current dataset without building a new theoretical approach allowing us to explicitly take into account the intervibrational interactions arising from nontorsion vibrations.

On the observational side, in Sect. 5.2 we claim the detection of methylamine in its first torsionally excited state on the basis of five relatively uncontaminated lines. While this would be insufficient for the secure identification of a new molecule in the ISM, the situation here is different. We already presented a secure detection of methylamine in its torsional ground state

toward Sgr B2(N1S), from which we derived LTE parameters (Kisiel et al. 2022). The synthetic spectrum of methylamine in its v_t=1 state computed with the same set of LTE parameters was found here to be consistent with the observed spectrum of Sgr B2(N1S). Five transitions are even sufficiently free of contamination, which means that this match is unlikely due to chance. Other COMs in Sgr B2(N) were also detected in v = 0 and v>0 states with intensities consistent with a single set of LTE parameters per molecule (see, e.g., the case of aminoacetonitrile in Melosso et al. 2020). Therefore, we believe our claim of a detection of methylamine in its v_t = 1 state to be robust given the combination of the fact that the synthetic spectra computed with the same set of LTE parameters match lines in both the ground and first torsionally excited states of methylamine and the fact that five v_t = 1 lines are relatively uncontaminated.

7. Conclusions

We carried out a new analysis of the rotational spectrum for the first excited torsional state of CH_3NH_2 up to 1.52 THz. Improving upon the results of the tunneling approach used previously for the ground state analysis and having shown limitations for analyzing the microwave and millimeter-wave data of the first excited state v_t = 1, we were able to generate global fits for v_t = 0, 1, and 2 using our new hybrid Hamiltonian model. In addition, a number of far-infrared transitions are fitted alongside microwave data, achieving a weighted standard deviation of 1.53.

We report the first interstellar detection of methylamine in its first torsionally excited state. The detection was obtained with ALMA toward the offset position Sgr B2(N1S) of the hot molecular core Sgr B(N1). Five lines were unambiguously assigned to rotational transitions of this state and their measured intensities are consistent with the emission of methylamine in the torsional ground state at a temperature of about 230 K with a column density of 1.4×10^{18} cm^{-2}.

The identification of a handful of rotational lines from the first torsionally excited state of methylamine contributes to our efforts to reduce the number of unidentified lines in the ReMoCA survey. The identification of new molecules in such a survey – with its high spectral line density— requires us to account for the contribution of all known interstellar species in order to avoid erroneous assignments. Therefore, expanding the spectroscopic predictions of known interstellar molecules to account for rotational transitions in their torsionally and vibrationally excited states is of prime importance for the analysis of astronomical spectral line surveys and should be continued.

Acknowledgements. Part of this work has been funded by French ANR agency under contract No. ANR-11-LABX-0005-01 CaPPA (Chemical and Physical Properties of the Atmosphere) and also supported by the Programme National "Physique et Chimie du Milieu Interstellaire" (PCMI) of CNRS/INSU with INC/INP co-funded by CEA and CNES. This paper makes use of the following ALMA data: ADS/JAO.ALMA#2016.1.00074.S. ALMA is a partnership of ESO (representing its member states), NSF (USA), and NINS (Japan), together with NRC (Canada), NSC and ASIAA (Taiwan), and KASI (Republic of Korea), in cooperation with the Republic of Chile. The Joint ALMA Observatory is operated by ESO, AUI/NRAO, and NAOJ. The interferometric data are available in the ALMA archive at https://almascience.eso.org/aq/. Part of this work has been carried out within the Collaborative Research Centre 956, subproject B3, funded by the Deutsche Forschungsgemeinschaft (DFG) – project ID 184018867.

References

Aponte, J. C., Elsila, J. E., Glavin, D. P., et al. 2017, ACS Earth Space Chem., 1, 3
Belloche, A., Müller, H. S. P., Menten, K. M., Schilke, P., & Comito, C. 2013, A&A, 559, A47
Belloche, A., Müller, H. S. P., Garrod, R. T., & Menten, K. M. 2016, A&A, 587, A91
Belloche, A., Garrod, R. T., Müller, H. S. P., et al. 2019, A&A, 628, A10
Bøgelund, E. G., McGuire, B. A., Hogerheijde, M. R., van Dishoeck, E. F., & Ligterink, N. F. 2019, A&A, 624, A82
Bonfand, M., Belloche, A., Garrod, R. T., et al. 2019, A&A, 628, A27
Busch, L. A., Belloche, A., Garrod, R. T., Müller, H. S. P., & Menten, K. M. 2022, A&A, 665, A96
Fourikis, N., Takagi, K., & Morimoto, M. 1974, ApJ, 191, L139
Garrod, R. T., Jin, M., Matis, K. A., et al. 2022, ApJS, 259, 1
Gordy, W., & Cook, R. L. 1984, Microwave Molecular Spectra, Techniques of Chemistry, XVIII (New York: Wiley)
Gulaczyk, I., & Kręglewski, M. 2020, JQSRT, 252, 107097
Gulaczyk, I., Łodyga, W., Kręglewski, M., & Horneman, V.-M. 2010, Mol. Phys., 108, 2389
Gulaczyk, I., Kręglewski, M., & Horneman, V. 2017, J. Mol. Spectrosc., 342, 25
Gulaczyk, I., Kręglewski, M., & Horneman, V.-M. 2018, JQSRT, 217, 321
Halfen, D. T., Ilyushin, V. V., & Ziurys, L. M. 2013, ApJ, 767, 66
Herbst, E., & van Dishoeck, E. F. 2009, ARA&A, 47, 427
Holtom, P. D., Bennett, C. J., Osamura, Y., Mason, N. J., & Kaiser, R. I. 2005, ApJ, 626, 940
Hougen, J. T., Kleiner, I., & Godefroid, M. 1994, J. Mol. Spectrosc., 163
Ilyushin, V. V., & Lovas, F. J. 2007, J. Phys. Chem. Ref. Data, 36, 1141
Ilyushin, V., Alekseev, E., Dyubko, S., Motiyenko, R., & Hougen, J. T. 2005, J. Mol. Spectrosc., 229, 170
Jørgensen, J. K., Belloche, A., & Garrod, R. T. 2020, ARA&A, 58, 727
Joshi, P. R., & Lee, Y.-P. 2022, Commun. Chem., 5, 62
Kaifu, N., Morimoto, M., Nagane, K., et al. 1974, ApJ, 191, L135
Kisiel, Z., Kolesniková, L., Belloche, A., et al. 2022, A&A, 657, A99
Kleiner, I. 2010, J. Mol. Spectrosc., 260, 1
Kleiner, I., & Hougen, J. T. 2015, J. Phys. Chem. A, 119, 10664
Kleiner, I., & Hougen, J. T. 2020, J. Mol. Spectrosc., 368, 111255
Kleiner, I., Hougen, J. T., Suenram, R. D., Lovas, F. J., & Godefroid, M. 1992, J. Mol. Spectrosc., 153, 578
Kręglewski, M., & Wlodarczak, G. 1992, J. Mol. Spectrosc., 156, 393
Kręglewski, M., Stahl, W., Grabow, J.-U., & Wlodarczak, G. 1992, Chem. Phys. Lett., 196, 155
Lide, D. R., Jr. 1957, J. Chem. Phys., 27, 343
Ligterink, N. F. W., Tenenbaum, E. D., & van Dishoeck, E. F. 2015, A&A, 576, A35
Ligterink, N. F. W., Calcutt, H., Coutens, A., et al. 2018, A&A, 619, A28
Loomis, F., & Wood, R. 1928, Phys. Rev., 32, 223
Maret, S., Hily-Blant, P., Pety, J., Bardeau, S., & Reynier, E. 2011, A&A, 526, A47
Melosso, M., Belloche, A., Martin-Drumel, M. A., et al. 2020, ApJ, 641, A160
Motiyenko, R. A., Ilyushin, V. V., Drouin, B. J., Yu, S., & Margulès, L. 2014, A&A, 563, A137
Motiyenko, R. A., Margulès, L., Ilyushin, V. V., et al. 2016, A&A, 587, A152
Motiyenko, R. A., Armieieva, I., Margulès, L., Alekseev, E., & Guillemin, J.-C. 2019, A&A, 623, A162
Motiyenko, R. A., Belloche, A., Garrod, R. T., et al. 2020, A&A, 642, A29
Muller, S., Beelen, A., Guélin, M., et al. 2011, A&A, 535, A103
Ohashi, N., & Hougen, J. T. 1987, J. Mol. Spectrosc., 121, 474
Ohashi, N., Takagi, K., Hougen, J. T., Olson, W. B., & Lafferty, W. J. 1987, J. Mol. Spectrosc., 126, 443
Ohashi, N., Takagi, K., Hougen, J. T., Olson, W. B., & Lafferty, W. J. 1988, J. Mol. Spectrosc., 132, 242
Ohashi, N., Tsunekawa, S., Takagi, K., & Hougen, J. T. 1989, J. Mol. Spectrosc., 137, 33
Ohishi, M., Suzuki, T., Hirota, T., Saito, M., & Kaifu, N. 2019, PASJ, 71, 86
Pagani, L., Favre, C., Goldsmith, P. F., et al. 2017, A&A, 604, A32
Pickett, H. M., Poynter, R. L., Cohen, E. A., et al. 1998, JQSRT, 60, 883
Pizzarello, S., & Holmes, W. 2009, Geochim. Cosmochim. Acta, 73, 2150
Reid, M. J., Menten, K. M., Brunthaler, A., et al. 2019, ApJ, 885, 131
Rodríguez-Almeida, L. F., Jiménez-Serra, I., Rivilla, V. M., et al. 2021, ApJ, 912, L11
Schimanouchi, T. 1972, Tables of Molecular Vibrational Frequencies, Vol. I: consolidated (Washington, DC: National Bureau of Standards)
Suenram, R. D., Golubiatnikov, G. Y., Leonov, I., et al. 2001, J. Mol. Spectrosc., 208, 188
Takagi, K., & Kojima, T. 1973, ApJ, 181, L91
Townes, C. H., & Schawlow, A. L. 1955, Microwave Spectroscopy (New York, NY: McGrawHill)
Zakharenko, O., Motiyenko, R. A., Margulès, L., & Huet, T. R. 2015, J. Mol. Spectrosc., 317, 41
Zeng, S., Jiménez-Serra, I., Rivilla, V. M., et al. 2018, MNRAS, 478, 2962

Appendix A: Molecular parameters of methylamine

Table A.1: Molecular parameters[a] (in cm^{-1}) [b] determined from the dataset summarized in Table 2.

ntrw[c]	Parameter × Operator[d]	Value(unc) from previous fit[e]	Value(unc) from present fit[e]
2200	$P_\alpha^2 \times F$	[15.1412489][f]	[15.08857388][f]
	$\frac{1}{2}(1-\gamma\cos 3\alpha)\times V_3$	695.320556(53)	682.911087(19)
2110	$P_\alpha J_z\times$ RHORHO[a]	0.64935371(10)[a]	0.649355515(26)[a]
	$\gamma P_\alpha J_x \times$ AXG	0.15595(28)	-0.158311(17)
2020	$J_x^2 \times$ B	0.7256934(20)	0.72874862(31)
	$J_y^2 \times$ C	0.75613394(18)	0.756180141(42)
	$J_z^2 \times$ A	3.44098285(66)	3.40280(23)
	$\gamma\{J_x, J_z\}\times$ DAB	-0. 07373(13)	0.1704383(82)
2002	$1 \times$ WAG2	-0.64470(98)	-0.31490(10)
3012	$P_\gamma J_y \times$ WCPG	-0.000844(13)	[0.001052604][f]
4400	$P_\alpha^4 \times$ AK4	0.00005168(11)	-0.001353681(63)
	$\frac{1}{2}(1-\cos 6\alpha)\times V_6$	-27.594750(75)	0.316699(41)
4310	$P_\alpha^3 J_z \times$ AK3	0.00075529(31)	0.00439259(13)
	$\gamma P_\alpha^3 J_x \times$ AXG3	-0.0000137(20)	0.00040774(39)
	$\gamma\{P_\alpha, \cos 3\alpha\}J_z \times$ AK6	–	0.02926(18)
4220	$(\gamma-\cos 3\alpha)\{J_x, J_z\} \times$ ODAB	0.009123(14)	-0.1053088(21)
	$(1-\gamma\cos 3\alpha)J^2 \times$ FV	-0.00380679(55)	-0.00451830(10)
	$(1-\gamma\cos 3\alpha)J_z^2 \times$ AK5	0.0206331(18)	0.05982(23)
	$(1-\gamma\cos 3\alpha)(J_x^2-J_y^2) \times$ C2	-0.00027295(28)	-0.00107326(18)
	$\sin 3\alpha\{J_y, J_z\} \times$ DAC	-0.00366(11)	-0.003623(16)
	$\gamma\sin 3\alpha\{J_x, J_y\} \times$ DBC	-0.001638(11)	-0.0008978(42)
	$P_\alpha^2 J^2 \times$ GV	0. 000060955(15)	-0.0000636354(17)
	$P_\alpha^2 J_z^2 \times$ AK2	-0. 00243340(42)	-0.00592494(10)
	$2P_\alpha^2(J_x^2-J_y^2) \times$ C1	0.00004680(22)	0.000030801(80)
	$\gamma P_\alpha^2\{J_x, J_z\} \times$ DELTA	-0.0001072(20)	-0.00036012(25)
4202	$P_\alpha^2 \times$ WF	0.006876(39)	0.0062553(23)
4130	$P_\alpha J^2 J_z \times$ ALV	0.000078897(23)	[0.0000813080][f]
	$P_\alpha J_z^3 \times$ AK1	0.00218065 (27)	0.003655932(35)
	$P_\alpha\{J_z, (J_x^2-J_y^2)\} \times$ C4	-0.00006847(24)	-0.000052393(85)
	$\gamma P_\alpha\{J_x, J_z^2\} \times$ AXGK	0.0000976(17)	0.00015818(17)
4112	$P_\alpha J_z \times$ WRHO	-0. 011533(34)	-0.0106006(33)
4040	$-J^4 \times$ DJ	$1.325232(21)\times 10^{-6}$	$1.322019(15)\times 10^{-6}$
	$-J^2 J_z^2 \times$ DJK	$0.31574(12)\times 10^{-3}$	$0.0303198(21)\times 10^{-3}$
	$-J_z^4 \times$ DK	$0.628\ 648(76)\times 10^{-3}$	$[0.862705\times 10^{-3}]^f$
	$-2J^2(J_x^2-J_y^2) \times$ ODELN	$-0.060514(10)\times 10^{-6}$	$-0.0623674(68)\times 10^{-6}$
	$-\{J_z^2, (J_x^2-J_y^2)\} \times$ ODELK	$-0.023204(36)\times 10^{-3}$	$-0.022551(15)\times 10^{-3}$
	$\gamma\{J_z, (J_+^3+J_-^3)\} \times$ GZJ3	–	$0.00030773(61)\times 10^{-3}$
4022	$J^2 \times$ WAG2J	0.000012493(51)	0.000001786(26)
	$(J_x^2-J_y^2) \times$ WAGBC[g]	-0.000019827(54)	-0.0000217525(69)
	$J_z^2 \times$ WAG2K	0.0049756(56)	0.0044477(13)
5212	$P_\gamma\sin 3\alpha J_z \times$ WS3APG	-0.06189(28)	0.0
5032	$P_\gamma\{J_y, J_z^2\} \times$ WCPGK	$0.002908(71)\times 10^{-3}$	0.0
5302	$P_\gamma\{P_\alpha, \sin 3\alpha\} \times$ WPGS3	0. 04353(26)	-0.0032152(41)
6420	$(1-\cos 6\alpha)J^2 \times$ ANV	-0.00002144(44)	-0.000515585(45)
	$P_\alpha^4 J_z^2 \times$ BK1	$-0.0011407(55)\times 10^{-3}$	$0.0045914(25)\times 10^{-3}$
	$(1-\cos 6\alpha)(J_x^2-J_y^2) \times$ C11	–	-0.00037596(18)
	$P_\alpha^4 J^2 \times$ AMV	–	$0.034865(94)\times 10^{-6}$
6402	$P_\alpha^4 \times$ WAK4	0.0000426(15)	0.000016369(92)
	$\cos 6\alpha \times$ WCOS6	–	0.30313(42)
6330	$P_\alpha^3 J^2 J_z \times$ AK3J	$-0.02939(42)\times 10^{-6}$	$-0.09069(21)\times 10^{-6}$

Table A.1: continued.

ntrw[c]	Parameter × Operator[d]	Value(unc) from previous fit[e]	Value(unc) from present fit[e]
	$P_\alpha^3 J_z^3 \times$ AK3K	$0.002682(15) \times 10^{-3}$	[-0.000006508][f]
6312	$P_\alpha^3 J_z \times$ WAK3	-0.0000987(30)	-0.00001807(25)
6240	$(1-\gamma\cos 3\alpha)J^4 \times$ OFV	$0.01504(15) \times 10^{-6}$	$0.012634(19) \times 10^{-6}$
	$(1-\gamma\cos 3\alpha)J^2 J_z^2 \times$ AK5J	$0.128(13) \times 10^{-6}$	$-1.0766(13) \times 10^{-6}$
	$(1-\gamma\cos 3\alpha)J^2(J_x^2 - J_y^2) \times$ C2J	$0.00569(12) \times 10^{-6}$	$0.007165(36) \times 10^{-6}$
	$(1-\gamma\cos 3\alpha)\{J_z^2, (J_x^2 - J_y^2)\} \times$ C2K	$0.863(17) \times 10^{-6}$	0.0
	$P_\alpha^2 J^4 \times$ GVJ	$0.0007172(91) \times 10^{-6}$	$0.0003411(11) \times 10^{-6}$
	$P_\alpha^2 J^2 J_z^2 \times$ AK2J	$0.08167(86) \times 10^{-6}$	$0.09305(24) \times 10^{-6}$
	$P_\alpha^2 J_z^4 \times$ AK2K	$-0.002274(17) \times 10^{-3}$	$0.00502932(90) \times 10^{-3}$
	$\sin 3\alpha\{J_z, (J_+^3 - J_-^3)\} \times$ S3Z3	–	$0.04912(24) \times 10^{-6}$
6510	$P_\alpha^5 J_z \times$ AK3B	–	$-0.0016609(31) \times 10^{-3}$
6600	$P_\alpha^6 \times$ AK4B	–	$0.0002405(12) \times 10^{-3}$
	$\frac{1}{2}(1-\gamma\cos 9\alpha) \times V_9$	[32.9134][f]	[-0.087806][f]
6222	$\cos 3\alpha\{J_x, J_z\} \times$ WODAB	$-0.1309(63) \times 10^{-3}$	0.0
	$\sin 3\alpha\{J_y, J_z\} \times$ WS3AC	$-0.00380(23) \times 10^{-3}$	$0.01303(11) \times 10^{-3}$
	$P_\alpha^2 J_z^2 \times$ WAK2	0.0000791(19)	-0.00002106(26)
	$P_\alpha^2 J^2 \times$ WGV	–	$-0.0001860(11) \times 10^{-3}$
	$2P_\alpha^2(J_x^2 - J_y^2) \times$ WC1	–	$-0.00011844(19) \times 10^{-3}$
6150	$P_\alpha J^4 J_z \times$ OLV	$-0.001148(12) \times 10^{-6}$	$-0.0003594(17) \times 10^{-6}$
	$P_\alpha J^2 J_z^3 \times$ AK1J	$-0.07904(66) \times 10^{-6}$	$-0.04550(13) \times 10^{-6}$
	$P_\alpha J_z^5 \times$ AK1K	$0.0008177(80) \times 10^{-3}$	$-0.00201816(35) \times 10^{-3}$
6132	$P_\alpha J^2 J_z \times$ WALV	$0.0001479(19) \times 10^{-3}$	$0.0003005(12) \times 10^{-3}$
	$P_\alpha J_z^3 \times$ WAK1	-0.00002176(42)	0.00003544(12)
	$P_\alpha\{J_z, (J_x^2 - J_y^2)\} \times$ WC4	–	$0.10614(20) \times 10^{-6}$
6042	$J^4 \times$ WAG2JJ	$0.000641(18) \times 10^{-6}$	$0.0003878(16) \times 10^{-6}$
	$J^2 J_z^2 \times$ WAG2JK	$-0.1177(14) \times 10^{-6}$	$-0.14392(43) \times 10^{-6}$
	$J_z^4 \times$ WAG2KK	–	-0.000012280(23)
	$(J_+^4 + J_-^4) \times$ WAJ4	$-0.000246(12) \times 10^{-6}$	0.0
6060	$J^6 \times$ HJ	$-0.000600(5) \times 10^{-9}$	0.0
	$J^4 J_z^2 \times$ HJK	$0.0004579(61) \times 10^{-6}$	$0.00011487(80) \times 10^{-6}$
	$J^2 J_z^4 \times$ HKJ	$0.02533(19) \times 10^{-6}$	$0.009285(28) \times 10^{-6}$
	$J_z^6 \times$ HK	$-0.1032(15) \times 10^{-6}$	$[0.3296476 \times 10^{-6}]$[f]
7322	$P_\gamma\{P_\alpha, \sin 3\alpha\}J_z^2 \times$ WPGS3K	$0.04814(17) \times 10^{-4}$	[0.000005145][f]
8440	$(1-\cos 6\alpha)J^2 J_z^2 \times$ BK2J	$-0.4030(81) \times 10^{-6}$	0.0
	$(1-\cos 6\alpha)J_z^4 \times$ BK2K	–	$0.0005581(29) \times 10^{-3}$
8422	$P_\alpha^4 J^2 \times$ WMV	$0.0000183(35) \times 10^{-6}$	$-0.005912(42) \times 10^{-6}$
	$P_\alpha^4 J_z^2 \times$ WBK1	–	$0.003706(10) \times 10^{-6}$
	$(1-\cos 6\alpha)J_z^2 \times$ WBK2	–	-0.00047000(96)
	$(1-\cos 6\alpha)J^2 \times$ WNV	–	-0.000021572(56)
8152	$P_\alpha J^2 J_z^3 \times$ WAK1J	$-0.0000302(21) \times 10^{-6}$	$0.002588(14) \times 10^{-6}$
8242	$P_\alpha^2 J^2 J_z^2 \times$ WAK2J	–	$-0.010096(56) \times 10^{-6}$
	$P_\alpha^2 J_z^4 \times$ WAK2K	–	$-0.0034899(99) \times 10^{-6}$
8332	$P_\alpha^3 J_z J^2 \times$ WAK3J	–	$0.013237(83) \times 10^{-6}$
8080	$J^2 J_z^6 \times$ ALJKK	$-0.015(1) \times 10^{-12}$	0.0
	$J^4\{J_z^2, (J_x^2 - J_y^2)\} \times$ OHJK	$-0.06510(68) \times 10^{-9}$	0.0
10802	$\cos 12\alpha \times$ WCOS12	–	-0.9862(65)

Notes. [a]The product of the parameter and operator from a given row yields the term used in the torsion-rotation-tunneling Hamiltonian, except for F, ρ, and A, which occur in the Hamiltonian in the form $F(P_\alpha - \rho P_a)^2 + AP_a^2$, where γ in these operators is shorthand for $\gamma/\langle R|\gamma|R\rangle$ and so its matrix elements give only a ± sign to the final matrix element of the full operator expression (see Kleiner & Hougen (2015)). Operators of species B_1 in G_{12} (such as cos3α) are not allowed in the Hamiltonian. Such operators can be made A_1 in G_{12} by multiplying them by the wagging coordinate γ (which is also B_1 in G_{12}). [b]All parameters are given in cm^{-1} except for RHORHO, which is unitless. The parameter value given in square parentheses (such as F and V_9) was fixed in our final fit at a value taken from an earlier fit where it was floated. [c]The symbols t and r give the order of the torsional part and the rotational part of the operator, as defined in (Kleiner & Hougen 2015); w gives the wagging order, n = t + r + w gives the total order of the operator. [d]The column contains the operator used in the hybrid Hamiltonian multiplied by the parameter adjusted in the least-square fit. [e]This column contains the value of the parameter determined in the fit, with one standard uncertainty in units of the last digits given in parentheses. [f]Value fixed in the fit. [g]This parameter was erroneously named FWAGBC in the previous paper (Kleiner & Hougen 2020).

Appendix B: Assigned microwave and FIR transitions of methylamine

Table B.1: A part of the table available in CDS, with measured pure rotational transitions of methylamine.

v_t'	J'	K_a'	K_c'	Γ'	v_t''	J''	K_a''	K_c''	Γ''	Obs. freq. (MHz)	Uncertainty (MHz)	obs.-calc. (MHz)	Incl.	Ref.
1	21	5	17	B2	1	20	6	14	B1	163610.558	0.060	1.425	0	1
0	2	1	2	B1	0	1	0	1	B2	169447.508	0.100	0.010	1	2
1	10	2	8	E2	1	9	3	7	E2	169533.747	0.100	-0.222	1	1
0	2	-1	1	E2	0	1	0	1	E2	171035.274	0.100	-0.044	1	2
1	10	1	9	E1	1	9	2	8	E1	171816.649	0.060	0.166	1	1
1	23	4	20	E1	1	22	5	17	E1	172601.330	0.060	0.101	1	1
0	2	-1	2	E1	0	1	0	1	E1	173267.798	0.100	-0.068	1	2
1	4	0	5	B2	1	3	1	2	B1	174950.669	0.100	-0.483	0	4
1	4	1	4	A1	1	3	1	3	A2	175338.833	0.100	-0.026	1	4
1	4	1	4	B1	1	3	1	3	B2	175340.894	0.100	0.023	1	4
2	4	1	3	E1	2	3	1	2	E1	176314.060	0.100	0.233	1	1
2	4	0	4	E1	2	3	0	3	E1	176394.935	0.100	0.153	1	1

References. (1) this study; (2) Motiyenko et al. (2014); (3) Ohashi et al. (1989); (4) Kręglewski & Wlodarczak (1992); (5) Motiyenko (priv. comm.)

Table B.2: A part of the table available in CDS, with measured rovibrational transitions of methylamine.

v_t'	J'	K_a'	K_c'	Γ'	v_t''	J''	K_a''	K_c''	Γ''	Obs. freq. (cm^{-1})	Uncertainty (cm^{-1})	obs.-calc. (cm^{-1})	Incl.	$K_a = 2$ flag
2	40	-9	32	E1	1	40	-10	30	E1	165.6057	0.0008	-0.0123	0	
2	21	-3	18	E2	1	21	-4	18	E2	165.6144	0.0008	0.0009	1	
2	13	2	11	A2	1	13	5	8	A1	165.6243	0.0008	-0.0001	1	L
2	13	2	12	A1	1	13	5	9	A2	165.6243	0.0008	-0.0000	1	L
1	23	-11	12	E2	0	24	-12	13	E2	165.6243	0.0008	0.0013	0	
1	16	14	0	B	0	17	15	0	B	165.6280	0.0008	-0.0006	1	
2	16	2	15	B2	1	16	5	12	B1	165.6330	0.0008	0.0007	1	
2	16	2	14	B1	1	16	5	11	B2	165.6330	0.0008	0.0004	1	
1	18	-13	5	E2	0	19	-14	6	E2	165.6801	0.0008	-0.0002	1	
2	12	2	10	A1	1	12	5	7	A2	165.6934	0.0008	-0.0000	1	L
2	12	2	11	A2	1	12	5	8	A1	165.6934	0.0008	-0.0000	1	L

Appendix C: ReMoCA detection of methylamine in its torsional ground state

Figure C.1 shows the rotational transitions of methylamine in its torsional ground state that are covered by the ReMoCA survey and contribute significantly to the signal detected toward Sgr B2(N1S). The spectroscopic entry used to produce the synthetic spectra of methylamine accounts for the hyperfine structure, which was not the case for the synthetic spectra shown in Fig. A.5 of Kisiel et al. (2022).

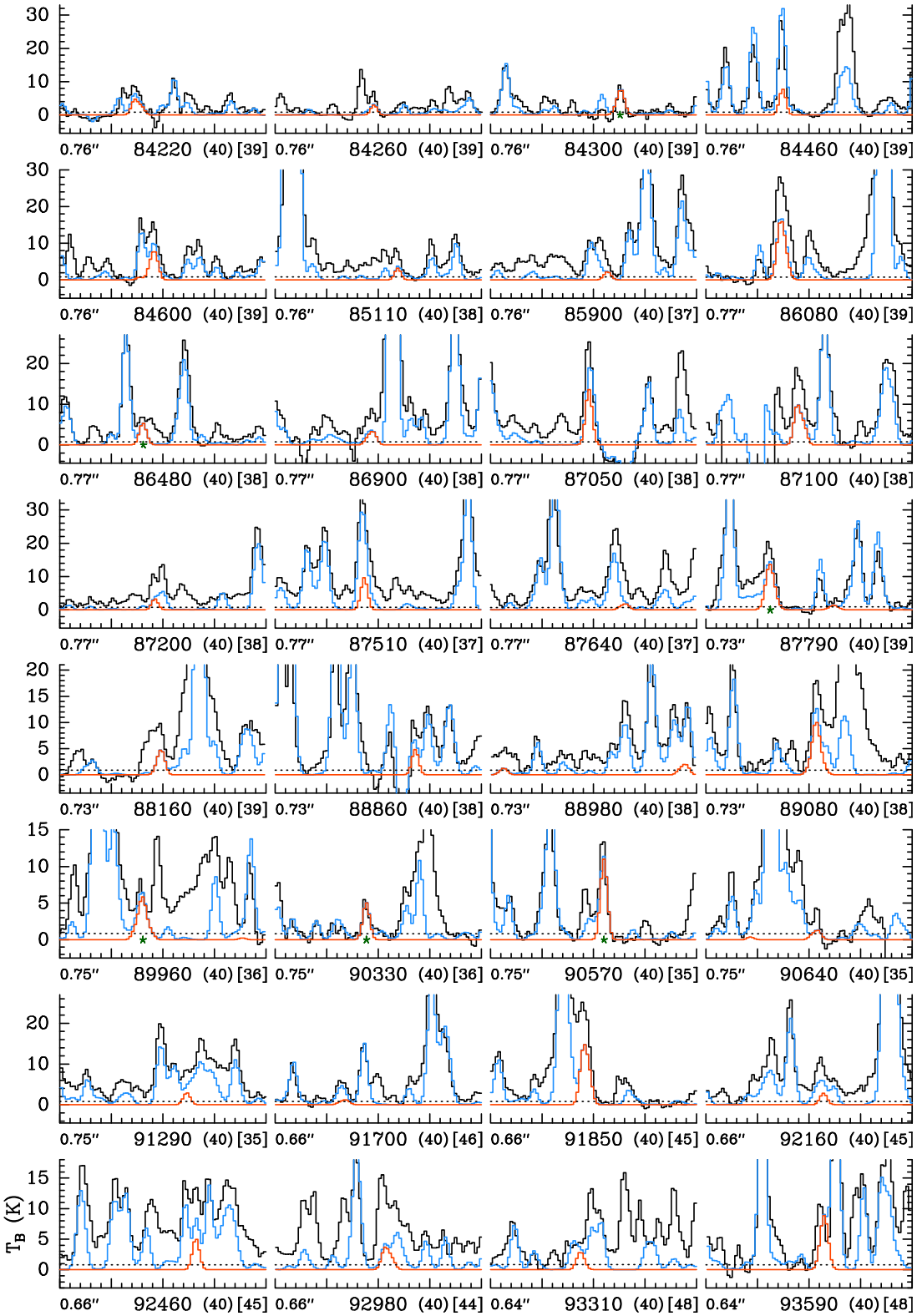

Fig. C.1: Same as Fig. 4 but for CH_3NH_2, $v = 0$.

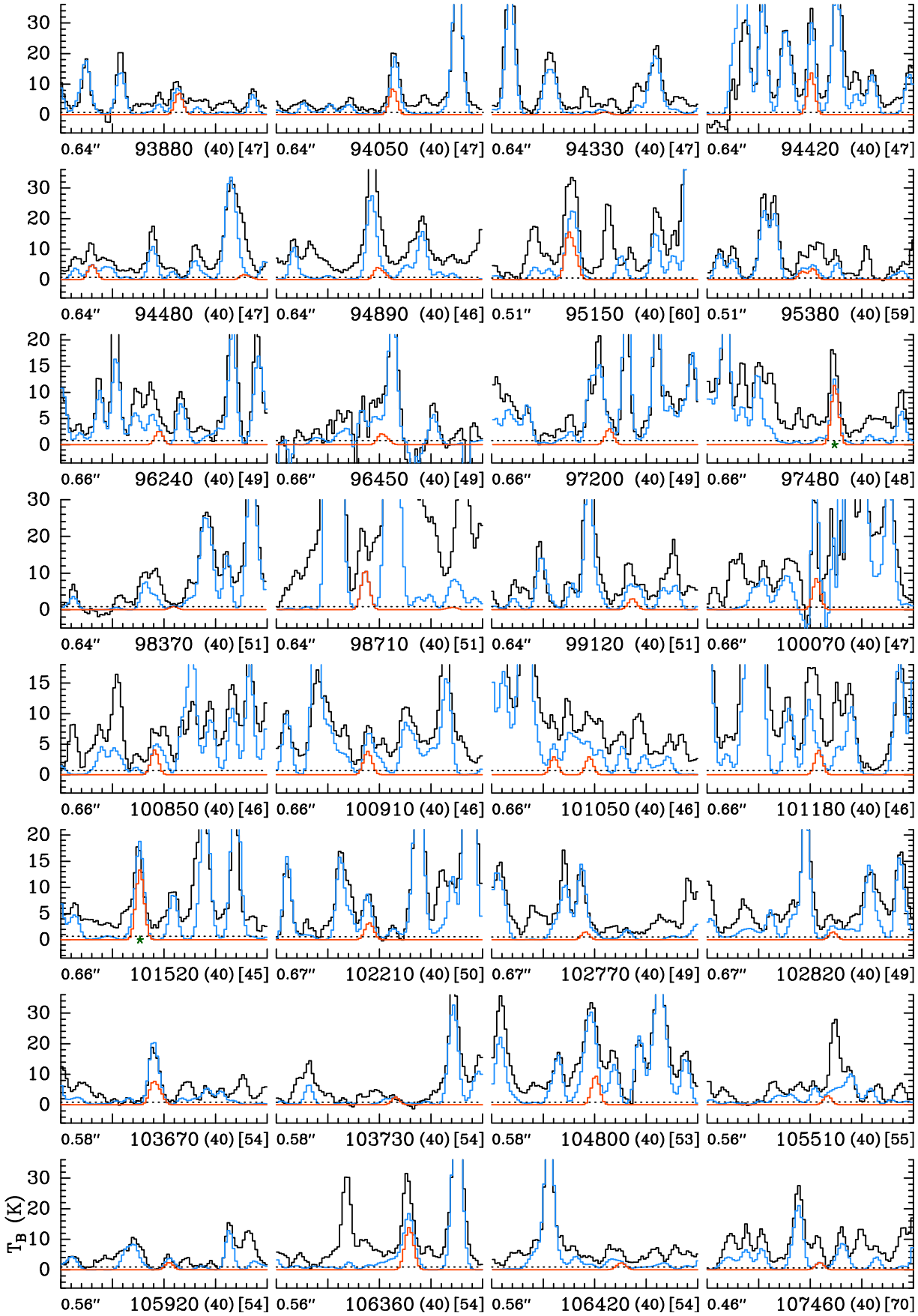

Fig. C.1: continued.

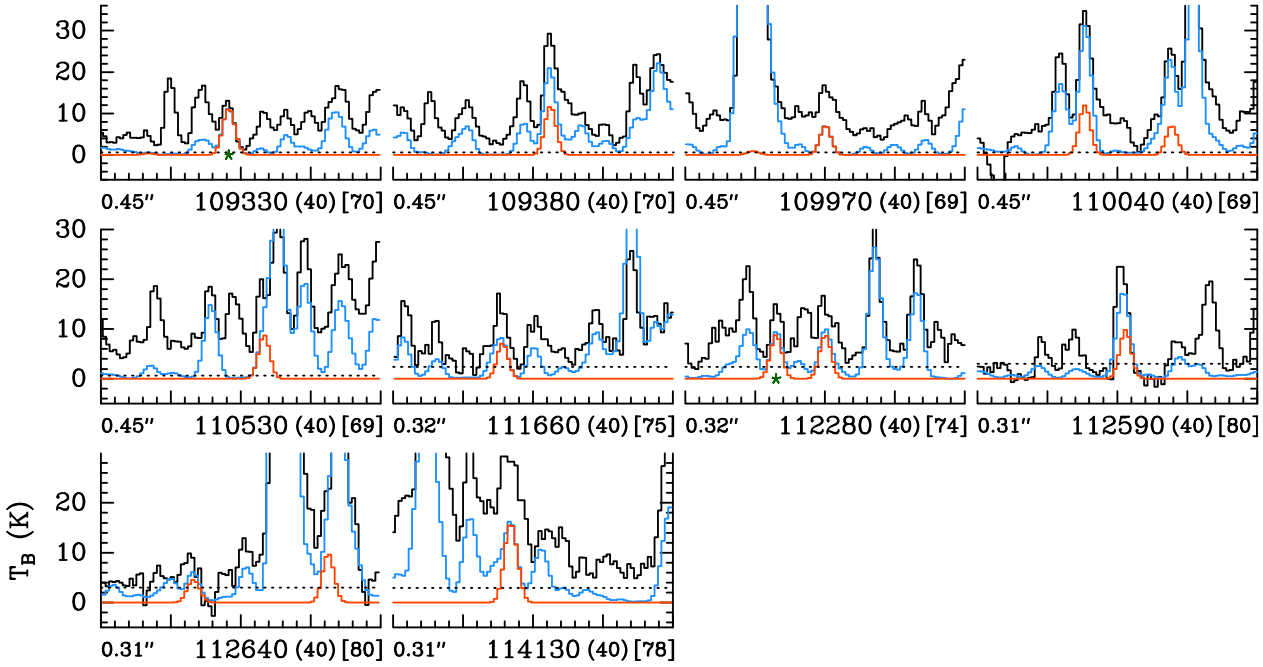

Fig. C.1: continued.

Spectroscopie térahertz de molécules et de complexes moléculaires d'intérêt atmosphérique présentant des mouvements de grande amplitude

Résumé

L'atmosphère est composée d'un large éventail de molécules et d'espèces. Parmi celles-ci, la vapeur d'eau et ses complexes jouent un rôle important dans le phénomène du réchauffement de la planète et du changement climatique. L'analyse spectroscopique de ces complexes est essentielle pour comprendre divers processus atmosphériques. Cependant, les connaissances sur les complexes d'eau à faible liaison dans le domaine des ondes térahertz sont encore limitées en raison de leurs caractéristiques spectrales complexes et des défis expérimentaux. La complexité spectrale résulte souvent des mouvements de grande amplitude limités par de faibles barrières de potentiel. Nous présentons le développement d'un spectromètre d'émission à jet pulsé destiné à l'étude des complexes moléculaires dans la gamme des térahertz. Les développements expérimentaux ont été accompagnés d'une analyse comparative des modèles de mouvements de grande amplitude sur les molécules d'intérêt atmosphérique. Nous avons commencé avec des halogénures d'acétyle présentant un mouvement de torsion périodique du groupe méthyle. Nous avons obtenu des modèles précis des spectres de rotation du chlorure d'acétyle et du bromure d'acétyle avec une précision expérimentale. Nous avons ensuite étudié les spectres de rotation de la méthylamine dans son premier état excité de torsion. La méthylamine est caractérisée par deux mouvements de grande amplitude : la torsion et l'inversion. Le spectre rotationnel de la méthylamine a été analysé à l'aide du modèle dit "hybride" qui, pour la première fois, a permis d'attribuer et de modéliser avec précision les états de torsion excités les plus bas. Enfin, les spectres rotationnels à haute résolution du complexe à faible liaison ammoniac-eau ont été mesurés à l'aide du nouveau spectromètre. Pour l'analyse du complexe l'ammoniac-eau qui présente deux mouvements de grande amplitude similaires à ceux de la méthylamine, nous avons également appliqué l'approche "hybride" démontrant ainsi son avantage dans l'application aux états excités et aux cas à faible barrière.

Mots clés: spectroscopie d'ondes mm/sub-mm, mouvements de grande amplitude, haute résolution, rotation interne, complexe à faible liaison, impulsion de jet, impulsion chirpée

Laboratoire de Physique des Lasers, Atomes et Molécules (PhLAM)
Bat - P5 campus Cité Scientifique - 59655 Villeneuve d'Ascq Cedex - France

Terahertz spectroscopy of molecules and molecular complexes of atmospheric interest exhibiting large amplitude motions

Abstract

The atmosphere comprises a diverse array of molecules and species. Among these, water vapor and its complexes have a significant role in the phenomenon of global warming and climate change. Spectroscopic analysis of such complexes is essential for understanding various atmospheric processes. However, there is still a limited knowledge on weakly bounded water complexes in the terahertz wave range due to their complex spectral features and experimental challenges. Spectral complexity often results from the large amplitude motions limited by low potential barriers. We present the development of pulsed-jet emission spectrometer intended for studies of molecular complexes in the terahertz range. Experimental developments were accompanied by benchmarking large amplitude motions models on the molecules of atmospheric interest. We started with acetyl halides exhibiting a periodic torsional motion of methyl group. We obtained accurate models of the rotational spectra of acetyl chloride and acetyl bromide within experimental accuracy. Subsequently, the rotational spectra of methylamine in its first excited torsional state were studied. Methylamine is characterized by two large amplitude motions: torsion and inversion. The rotational spectrum of methylamine was analyzed using the so-called "hybrid" model that for the first time allowed accurate assignment and modeling of the lowest excited torsional states. Finally, the high-resolution rotational spectra of ammonia-water weakly bounded complex were measured using the newly built spectrometer. For the analysis of ammonia-water which exhibits two large amplitude motions similar to methylamine, we also applied the "hybrid" approach demonstrating thus its advantage in the application to excited states and low barrier cases.

Keywords: mm/sub-mm wave spectroscopy, large-amplitude motions, high-resolution, internal rotation, weakly bounded complex, pulse jet, chirped pulse

Laboratoire de Physique des Lasers, Atomes et Molécules (PhLAM)
Bat - P5 campus Cité Scientifique - 59655 Villeneuve d'Ascq Cedex - France